Reactive oxygen and hydrogen species generation in radio-frequency atmospheric pressure plasmas

- Experimental and Numerical Investigations -

Sandra Schröter

PhD

UNIVERSITY OF YORK
PHYSICS

May 2017

Abstract

Atmospheric pressure plasmas (APPs) are known to be effective sources for reactive oxygen and nitrogen species (RS), making them potentially suitable for applications in biomedicine, where these species are believed to play a crucial role. However, in order to fully establish plasma sources in biomedicine, detailed characterisation of the RS produced is required. This is particularly challenging at atmospheric pressure, because of high collision rates among particles leading to fast de-excitation of excited states (quenching), complex gas mixing, and the small physical dimensions of the investigated systems, which effectively limits the accurate application of several commonly used diagnostic techniques applicable in low pressure systems. The motivation of this work is therefore to investigate the chemical kinetics in APPs, using a combination of simulations and experimental diagnostics, which are able to overcome the above-mentioned challenges.

Experimentally, absolute RS species densities such as O, OH, H_2O_2, N, and NO, are determined using absorption spectroscopy in the UV and VUV spectral range, a technique independent on quenching and providing high spectral resolution. Spatially resolved two-photon absorption laser-induced fluorescence with sub-nanosecond temporal resolution enables the determination of atomic species densities (O and H) in the plasma effluent. Experimental values are benchmarked against zero-dimensional plasma-chemical kinetics simulations, which are used to investigate the principal reaction mechanisms leading to the formation and consumption of the investigated species. It is generally found that formation pathways depend strongly on the concentration of molecules in the feed gas, and the position in the plasma jet, as well as potential impurities being present in the feed gas, which is an important aspect for consideration for the applications of APPs. The results are used to propose possible tailoring schemes to optimise RS productions in APPs.

Contents

List of Tables

List of Figures

Acknowledgements

First of all, I would like to thank my PhD advisor Dr. Deborah O'Connell, for all her support during the last years. Without her, writing this thesis would not have been possible. I would also like to thank her for all the opportunities (and challenges) I was offered during my time as a PhD candidate, which has allowed me to grow both professionally and personally.

Secondly, I would like to thank Prof. Timo Gans, Dr. James Dedrick, and Dr. Erik Wagenaars for always having an open door and always being helpful whenever I had a problem or question.

My sincere thanks also go to Dr. Kari Niemi for all the help with designing and setting up experiments, as well as many fruitful discussions and lots of advice. Additionally, I would like to thank him for proof-reading of some parts of this thesis.

I am grateful to my collaborators Dr. Jean-Paul Booth and Dr. Mickaël Foucher, Dr. Svetlana Starikovskaia, and Nikita Lepikhin (LPP, Ecole Polytechnique, Palaiseau,), Dr. Nelson de Oliveira, Dr. Denis Joyeux, and Dr. Laurent Nahon (SOLEIL synchrotron, Gif-sur-Yvette), and Dr. Yury Gorbanev and Dr. Victor Chechik (Department of Chemistry, University of York), for hosting me and allowing me to occupy their lab space and using both their resources as well as their valuable time. I would also like to thank Prof. Mark Kushner for providing the GlobalKin code.

Additionally, thanks to all my fellow PhD candidates and PostDocs working at the York Plasma Institute. They are a sociable and fun group to be with, and made me feel at home immediately, despite moving to a different country. In particular I would like to thank Team TALIF members Dr. Jérôme Bredin and Dr. Andrew West for their time and patience to teach me everything they know about lasers. I would also like to thank them for proof-reading parts of this thesis. Many thanks also to Dr. Apiwat Wijaikhum, who allowed me to use his experimental setup for a while, and was always very helpful.

For technical assistance, I would like to thank Richard Armitage and the whole team working at the technical workshops of the University of York. Many thanks also to Abigail Storey for her endless patience and great skill when it comes to everything made of glass.

I would like to thank the members of our administrative and finance team (both current and former), for the countless occasions of helping out. They are truly indispensable.

In addition to all my colleagues and collaborators, I would like to thank for the funding during my PhD studies, in particular from the York-Paris Collaborative International Research Centre. Further funding was received from the UK EPSRC, and the LABEX Plas@par project. Finally, I would like to thank AVS, IOP, and the York Plasma Institute, for granting me travel funding for various conference visits during my time as a PhD candidate.

In particular I would like to thank Andrew, not only for all of his help with plasma simulations and generally being a great physicist, but also for his emotional support during all of this time.

Zuletzt möchte ich mich noch bei meiner ganzen Familie bedanken, insbesondere bei meinen Eltern, Sabine und Jörg Schröter, sowie meinen Großeltern, ohne deren durchgehende Unterstützung und Zuspruch ich sicherlich niemals so weit gekommen wäre.

Declaration

I declare that this thesis is an original report of my research, has been written by me and has not been submitted for any previous degree. The experimental and simulation work is almost entirely my own work. Where data was obtained or evaluated by other people, it is explicitly acknowledged in the text. I interpreted all presented results, unless it is stated otherwise in the text or in this declaration. Some of the data was obtained within collaborations. I have driven the discussed collaborations and personally brought together the results to form the overall picture presented in this work. My specific contributions to each collaboration are discussed below.

The experiment described in section 3.2.3 to measure the plasma power was originally designed by Dr. Andrew West. For all plasma power measurements in this work, I planned, set up, conducted and evaluated the experiments myself. For the evaluation I used a script which was written jointly by Dr. Andrew West and myself.

Parts of the results for the measurement of hydroxyl radicals and all measurements of nitric oxide described in chapter 4 were obtained in collaboration with Dr. Mickaël Foucher and Dr. Jean-Paul Booth (École Polytechnique, Palaiseau, France), who were involved in planning and setting up the experiment. The measurements were taken jointly by Mickaël Foucher and myself. I had a major contribution in planning the experiment and evaluating the data. I was also to a large extent involved in setting up the experiment.

Other hydroxyl radical density measurements were taken in collaboration with Dr. Apiwat Wijaikhum, who had set up the absorption spectroscopy setup previously. I had a major contribution in taking and evaluating the obtained data.

For the evaluation of all data involving the measurement of hydroxyl radicals, an automated fitting simulation was used, which was written by Dr. Kari Niemi.

The measurements of atomic oxygen and atomic nitrogen using VUV-FTAS at the synchrotron SOLEIL facility described in chapter 4 were taken in a collaboration with Dr. James Dedrick, Dr. Kari Niemi, Dr. Erik Wagenaars, Dr. Deborah O'Connell, Dr. Nelson de Oliveira, Dr. Laurent Nahon, Dr. Denis Joyeux, Dr. Jean-Paul Booth, and Prof. Timo Gans. I was involved in conducting and also partially in maintaining the experiments.

The laser system used for the ps-TALIF setup was to a large extent set up by Dr. Jérôme Bredin, Dr. Andrew West, Dr. James Dedrick, and Dr. Kari Niemi. All experimental measurements were planned, taken and evaluated by myself. For the evaluation of the ps-TALIF data I used a script which was originally written by Dr. Jérôme Bredin. I made significant changes to this script whenever my specific experimental conditions required that.

The measurements of hydrogen peroxide described in chapter 6 were a collaboration with Dr. Yury Gorbanev and Dr. Victor Chechik. I had a large contribution in planning and setting up the experiment, and a major contribution in conducting and evaluating the obtained data.

The GlobalKin code used for plasma chemical simulations in this work was developed

by Prof. Mark Kushner and coworkers. I set up and evaluated all simulations shown in this work using GlobalKin.

1. Introduction

The use of non-thermal plasmas in modern technologies is vast, with the number of different areas of applications still increasing. The term "non-thermal" or "non-equilibrium" plasma is derived from the feature that not all particles produced in the plasma are in thermal equilibrium. Typically, the very light electrons are accelerated in fast changing electric fields, reaching high temperatures of some 10,000 K, while the heavier ions and neutral particles stay at or close to room temperature. Typical ionisation degrees of non-thermal plasmas at atmospheric pressures are in the order of $10^{-8} - 10^{-6}$. The benefit of these plasmas for applications is the low gas temperatures, enabling treatment of temperature sensitive surfaces, as well as a rich chemistry of reactive species due to the active electron dynamics, which leads to excitation, ionisation and dissociation of molecules present in the gas.

One of the largest areas of non-thermal plasmas is industrial processing, where plasmas are used for surface modification and etching, for example for the production of electronic components. Other applications, which have been arising in the last few decades are biomedical applications, treatment of textiles, materials synthesis, lighting, or even in food processing to prolong the shelf-life of different products.

There are numerous reasons why plasmas are so successful in all these very different applications: first of all, plasmas often offer a more environmentally friendly alternative to commonly used approaches relying on aggressive chemicals, which have to be disposed of. Secondly, plasmas can be set-up in a very cost-effective way, treating large areas of substrates in a short amount of time. Finally, the design and parameters of plasmas can be varied over a large range, so that plasma sources can be tailored to their various applications.

In this thesis, the use of non-thermal plasmas will be discussed from the point of view of biomedical applications. However, there is no doubt that results obtained in this work can be applied in other applications, too.

1.1. The potential of plasmas for biomedical applications

A major motivation for the usage of non-thermal plasmas in biomedicine to offer an adjuvant or even substitutional therapy for many traditional therapies in medicine. A prominent example for this is the growth of multi-drug resistant bacteria, which are resistant to even strong medication and sterilisation procedures. The destructive effect of non-thermal plasmas on bacteria, even of multi-drug resistant nature, has been shown on various occasions [1–3]. It has been found that plasma treatment of bacteria leads to damage of the cell membrane, and breakage of DNA strands in the cell. Similar results were obtained in cancer cells [4, 5] and plasmid DNA [6], leading to a sudden cell death, which is usually referred to as *necrosis*. On the other hand, plasmas have also been proven to be able to trigger a programmed cell death (*apoptosis*) [7]. The type of cell death and response of cancer cells to plasma treatment has been found to be dependent on the investigated cells and plasma conditions [8, 9]. Having this effect on different kinds of cells, plasmas are very attractive as potential adjuvant therapies, or combinatorial or even substitutional treatment methods in areas like decontamination and sterilisation [10–12], cancer treatment [13–15], wound healing [16–18], and electro-surgery [19]. Various review articles exists that explore the different applications of plasmas in medicine [20–22].

Clearly, the effects of plasmas on biomedical samples can be beneficial, however, the exact mechanisms of how plasmas and biological samples interact are poorly understood. Several properties of plasmas, which are important for interactions with biological tissue have been identified, which are plasma chemistry and reactive species (RS) produced in the plasma, electric fields, (high energy) radiation, and gas temperature. In certain systems, some of these effects can be isolated. In most plasma interactions with biological tissue, great care is usually taken to eliminate the effect of thermal influences by keeping the plasma temperature below biomedically relevant temperatures at the position of treatment, such as body-temperature. This can be achieved by limiting the power input (low voltage amplitudes or pulsing of the plasma), or increasing the distance between plasma source and sample.

Another important aspect in plasma interactions with biological samples is the plasma chemistry and high energy radiation. Privat-Maldonado et al. [2] treated samples of S. typhimurium with two different atmospheric pressure plasmas (APPs), and came to the conclusion that the plasma chemistry, particularly reactive oxygen species (ROS), are most likely be the driving force behind observed effects on their samples. They ruled out the effects of high energy radiation by blocking the flux of ROS towards the sample using an MgF_2 window, which is transparent for UV radiation (200-400 nm). For one plasma configuration, they also ruled out the effects of electric fields by preventing plasma break-

down by stopping the gas flow but powering the generator. It was found by others [23–25] that although UV or vaccuum UV (VUV, 100-200 nm) radiation usually has a small effect on the deactivation of bacteria on its own, the combination of RS with (V)UV photons is more effective, and can also exceed the effects of treating samples with RS only. This was attributed to indirect photochemical effects taking place in the plasma effluent instead to a direct effect of the radiation.

The theory behind the effectiveness of reactive oxygen and nitrogen species (RONS) is that a lot of these species naturally serve as signalling agents in important cell functions through oxidation-reduction biochemistry [26]. For example, it was found in a numerical study that radicals such as O and OH could potentially change the lipid composition of the skin [27], which might have potential for future applications of these plasmas in dermatology. Therefore, if beneficial RONS could be produced in a controlled way by plasmas, useful biological responses would be triggered that could lead to desired effects. These effects might depend on the specific RONS, or on the quantities of RONS delivered to the specimen. Therefore, in order to make plasmas applicable in therapeutics, the plasma systems have to be thoroughly characterised, particularly with regards to the reactive species produced.

However, this does not mean necessarily that the influence of other aspects such as high electric fields can always be neglected. Since the electric potential across cell membranes is important for controlling their permeability, it is no surprise that high external electric fields can disrupt their functioning. This effect is called *electroporation*. It was observed that very high electric fields can lead to an increased conductivity, and a rearrangement of the membrane [28]. Norberg et al. [29] investigated the effect of a helium APPJ pulsed with kV pulses on liquid covered cells using a 2D simulation. They found that for most of their conditions, the electric fields in the cells produced by the plasma were not high enough to cause electroporation, but also emphasized that this might not be true generally.

Taking all of these effects into account, plasma sources used for the treatment of biomedical tissue have to be carefully characterised and investigated, before they can be established in therapeutics. In the next section, several prominent plasma designs will be discussed.

1.2. Plasma jets

When looking at the literature, a large variety of plasmas have been developed to investigate biomedical applications. One of the more prominent types are atmospheric pressure plasma jets (APPJ). In these sources, the plasma is ignited in a gas flow. The positioning of the electrodes in relation to the flow and therefore the orientation of the electric field is crucial for the perfomance of the jet: If the gas flow is perpendicular to the electric field, only RS and radiation can escape the active *plasma bulk* into the *effluent region*, while charged particles rapidly decay due a lack of electric field in the effluent. An example for such a configuration is the COST μAPPJ [30], which is the source used in this work, and which will be described later in chapter 2. This jet is investigated by several research

groups within the European COST collaborative project [31], and is therefore one of the best characterised atmospheric pressure plasma sources to date. Examples for a jet in the parallel configuration are the kINPen [32] and the plasma gun [33]. Here, the active plasma can extend beyond the dimensions of the electrodes, and an active *plasma plume* can interact with samples. Although the general voltage characteristics in the two sources are different (sinusoidal kHz voltages in the case of the kINPen vs. ns pulses in the case of the plasma gun), the formation mechanism of this active plasma plume relies on the formation of *plasma bullets* in the sources in both cases. These plasma bullets were found to propagate long distances in thin tubes [33], creating great potential for a use of these sources inside the human body.

Often, APPJs are operated with a sinusoidal radiofrequency (RF) voltage in the kHz or MHz frequency range. This choice of voltage waveform requires the source to run in a rare gas background to ensure electrical breakdown, and small amounts of molecules can be added to promote the production of RS via their dissociation. Ignition in purely molecular gas mixtures is possible by increasing the discharge voltage and decreasing its rise-time, for example by using ns-pulsed plasmas

Other types of discharges include direct current plasmas (DC) and microwave plasmas. A general overview of different types of atmospheric pressure plasmas can be found in reference [34].

1.3. Use of atmospheric pressure plasmas in real-life conditions and the influence of humidity

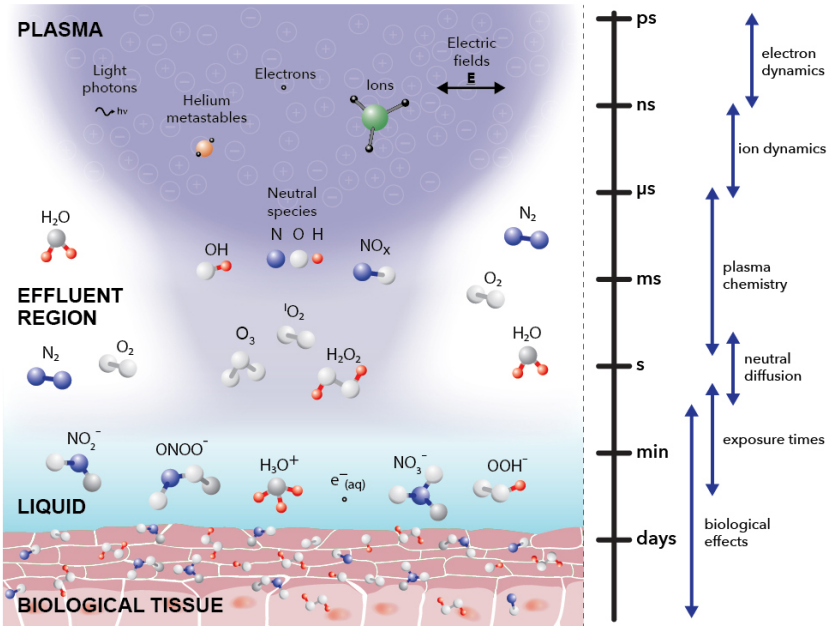

Fig. 1.1: Schematic of plasma interaction with a biological sample. Adapted from reference [35].

Using atmospheric pressure plasmas, a variety of RONS can be produced. The specific species and absolute quantities can be controlled to a certain extent by choosing appropriate plasma conditions. For example, reactive N_xO_y species, which have been found to play a role in many biological responses, are commonly produced by using air or air containing plasmas [36–38]. Similarly, hydrogen containing species such as atomic hydrogen or hydroxyl radicals are produced from humidity in the feed gas [39,40]. A schematic of a typical interaction of a plasma with biological tissue is shown in fig. 1.1[1]. Reactive species are produced in the plasma core by dissociation of admixed molecules. They can subsequently diffuse into the plasma effluent region and further interact with (liquid-covered) biological tissue.

However, certain aspects do not lie in control within a change of plasma parameters, but still have to be taken into account when treating biological matter. One important aspect is the influx of ambient air into the plasma or plasma effluent as indicated in fig. 1.1, causing impurities, which might affect the results of the plasma treatment. Additionally, ambient air usually contains a certain amount of humidity, which can lead to the formation of reactive oxygen and hydrogen containing species (ROHS) such as atomic hydrogen (H), hydroxyl radicals (OH), and hydrogen peroxide (H_2O_2). The amount of impurities coming from ambient air can be controlled by using a shielding gas around the plasma gas flow, as it was implemented in the kINPen [41]. However, it was found that impurities can also arise from the gas supply itself [42, 43], leading to the production of charged high order water clusters ($H^+ \cdot (H_2O)_n$ and $OH^- \cdot (H_2O)_m$).

A way to investigate the production of ROHS is by deliberately admixing water molecules into the feed gas, which has been done both in experimental [44–51] and simulation work [39, 52–58]. In some occasions, the influence of a (liquid-covered) surface on absolute number densities has also be investigated [59, 60]. In the work of Yonemori and Ono [60], the densities of OH and O in the gas phase were dependent on the wetness of the treated surface. Gorbanev et al. [59] investigated the origin of species in plasma treated liquid, and found that most reactive species found in the liquid after plasma treatment originated from the gas phase. Other experimental work includes the detection of OH, O, H_2O_2, and positively and negatively charged water clusters ($H^+ \cdot (H_2O)_n$ and $OH^- \cdot (H_2O)_m$), and will be discussed in the next section.

A plasma can also be ignited directly in the liquid by using very short high voltage pulses, or in aerosol containing plasmas or gas bubbles. However, these applications go beyond the scope of this work. An overview of most plasma-liquid interactions can be found in reference [61].

[1] Many thanks to Phil Roberts (Department of Biology, University of York) for generating the schematic used in fig. 1.1.

1.4. Understanding reactive species production - state of the art and challenges

As previously mentioned, in order to make plasma sources applicable for biomedical and technological applications, a careful characterisation of the respective source is necessary. An important aspect is the quantification of reactive species in the source. In this section, the state-of-the-art experimental and numerical approaches are discussed, as well as current challenges, which will be tackled in this work.

1.4.1. Experimental investigations

In order to quantify absolute species densities, optical diagnostics have been proven to be very effective. Several review papers on the usage of optical diagnostics in APPs exist [62, 63].

A relatively straight-forward method to measure the densities of different species is absorption spectroscopy. This technique relies on the absorption of light generated by an external source by exciting the atom or molecule in the plasma via a resonant transition. One of its main advantages is its independence on collisional de-excitation (*quenching*) of species, which plays a crucial role at high pressures. Using absorption spectroscopy, line-of-sight averaged species can be measured, while the technique can still offer a high spatial resolution in the other two dimensions, depending on the optics and light source used in the individual experiment. The main limitations of the technique lie in the signal strength, which depends on the concentration of species and the absorption length, which is sometimes difficult to define, as well as the availability of absorption cross sections in the literature.

Absorption spectroscopy has been used in the past to detect absolute densities of molecules in APPs such as OH, nitric oxide (NO), and ozone (O_3) [37, 38, 40, 64, 65]. The quantification of atomic species however is challenging, since the wavelengths required to excite resonance transitions from the ground state lie in the VUV spectral range. At atmospheric pressure, light in that wavelength regime gets absorbed quickly, creating the necessity to place the investigated atmospheric pressure plasma source into a low pressure environment. However, for example through the use of state-of-the-art synchroton light sources, it is possible to measure densities of certain atomic species, such as N and O [66]. More details about the absorption spectroscopy technique will be provided in chapter 4. Absorption spectroscopy in the UV spectral range has also been used in combination with a cavity ringdown setup to measure OH [44, 67] in the effluent of an APPJ. This technique can drastically enhance the signal strength and is therefore useful at low species densities or small absorption lengths. However, the necessity of a laser cavity around the investigated jet adds to the complexity of the experimental setup.

Another technique based on the principle of absorption spectroscopy is Fourier-transform infrared spectroscopy (FTIR), which was previously used to detect absolute H_2O_2 densities in an APPJ [68]. The advantage of FTIR spectroscopy typically lies in a better spectral

resolution without having to implement an entrance slit to the used device (in comparison to dispersive techniques), which would decrease the intensity of the probed light. However, spatially resolved measurements e.g. in a plasma jet setup is challenging, since the investigated jet has to be installed in the FTIR spectrometer.

It is also possible to use absorption spectroscopy to probe species in the liquid phase, which typically is an indirect method of measurement. The detection of H_2O_2 in plasma treated water is a common example [51, 59, 68], and will be further described in chapter 6.

A more commonly used and direct diagnostic to quantify absolute densities of atomic ground state species is two-photon absorption laser induced fluorescence (TALIF). This technique relies on the absorption of two laser generated photons, and observation of fluorescence emission from the resulting excited states. The detailed working principle of the technique will be discussed later in chapter 5. TALIF offers a good spatial resolution (absolute densities are not line-averaged), which is only limited by the beam-size of the used laser and the detection system. The main limitations of the technique lie in the temporal resolution of the experimental setup, because in contrast to the previoulsy discussed absorption spectroscopy technique TALIF depends on collisional quenching, and the availability of two-photon excitation cross sections in the literature, as well as their accuracy.

In APPs, TALIF is used to detect atomic species such as O, N, and H [44, 60, 69–85]. As previously mentioned, the temporal resolution of the experimental setup plays a crucial role. Most TALIF setups have laser pulse lengths on the order of nanoseconds, which limits their temporal resolution to the nanosecond range. This is the same range as the lifetimes of excited states at atmospheric pressure due to the high collision rates of these excited states with ambient gas particles. Since the lifetime of the laser-excited state is of great importance in the calculation of absolute densities, it is often calculated assuming a certain gas mixture and the rate of collisional de-excitation of the excited states (quenching coefficients). This procedure relies on knowledge of the gas composition and the values of the associated quenching coefficients, and as a result can lead to large uncertainties, especially when gas impurities are present, or a gradual gas mixing from the ambient air into the plasma or plasma effluent is taking place. In order to reduce the impact of possible feed gas impurities, sometimes diagnostics are run in a protected atmosphere [44]. However, with treatment of living patients in mind, this is usually not feasible under the conditions of actual applications.

In order to circumvent this problem, the usage of shorter laser pulses and faster detection systems is favourable [86]. In recent work, lasers with femtosecond (fs) resolution have been used to detect H produced in flames used for combustion [87]. However, due to the temporal restriction of the detection system, lifetimes still had to be calculated in this work using simulated species densities distributions and quenching coefficients from the literature. Fs-TALIF was also used to detect H and O in a DBD-type plasma jet [88] at atmospheric pressure, and in a ns-pulsed pin-to-pin plasma with O_2 and H_2 admixtures at 100 torr pressure [89]. In the latter publication, the used detection system enabled

the active measurement of quenching coefficients of excited states of atomic oxygen and hydrogen.

A very similar technique is laser-induced fluorescence (LIF), where only one photon is absorbed. This technique has been used in the past to detect molecular species, such as OH and NO [36, 48, 60, 77, 90–93]. In a more advanced setup using a second laser, absolute H_2O_2 densities were obtained by photo-dissociation and subsequent detection of the OH fragments [94].

Both LIF and TALIF are reliant on a calibration to obtain absolute species densities, making these diagnostics less direct than absorption spectroscopy.

Finally, a technique which is used to detect absolute species densities mainly of ionised species is mass spectrometry. This technique has been used to investigate absolute densities of ions such as water clusters in APPs containing oxygen and humidity [49, 50, 95], but also to investigate the ion and neutral dynamics under different plasma conditions [96], or to investigate the role of gas mixing and impurities in these sources and their effluents [43, 97, 98]. However, the application of mass spectrometers to APPs often involves a complex multi-stage pumping system to bridge the transition from atmospheric pressure to the low operating pressures of mass spectrometers.

1.4.2. Simulations

Experimental diagnostic techniques provide information about absolute species densities of many species which are of interest for applications. However, the actual plasma chemistry and reaction mechanisms for the production and destruction of these species are not revealed. Understanding the fundamental plasma chemistry, especially under parameter variations, is of great importance if one wants to understand how to tailor plasmas for applications.

A very useful tool to investigate the plasma dynamics are numerical simulations. The most basic type of simulations are volume-averaged global simulations or 0D simulations [99]. These models usually include a thorough description of the plasma chemistry, but general do not have any spatial information. They only require short computational times, therefore allowing complex plasma chemistries to be taken into account including tens of species and thousands of chemical reactions. This is a great advantage when it comes to representing the complex plasma chemistries typically present in APPs. However, because of the missing spatial information, they can only be used to model spatially homogeneous plasma systems.

Global models have been used for a variety of radio-frequency driven APPs in helium and argon with different molecular admixtures, such as O_2, N_2, H_2O and air [39, 52–56, 100–105]. Using these models, absolute species densities of RS produced in the plasma sources can be quantified. In some of the work [54–56, 106], the influence of feed gas impurities was investigated, such as coming from ambient air or humidity.

The limitations of global models lie in their capability to only generate spatially averaged quantities such as species densities, limiting their accuracy when used to model

highly spatially inhomogeneous plasmas. Additionally, the reliability of calculated species densities is dependent on the accuracy of the proposed reaction mechanisms including the used reaction rates for bulk and wall chemical reactions [104].

Higher dimensional simulations can also take into account spatial distributions of species and gas flow patterns, for example over treated surfaces [107, 108]. Additional physics can be included to for example simulate the interaction of plasmas and a treated liquid [109]. However, they are also computationally expensive, and are therefore typically not used with extensive plasma chemical reaction mechanisms.

1.4.3. Combination of simulations and experiments

When investigating plasma properties using simulations, a verification of RS densities predicted by the simulations is of great importance. Therefore, a combination of simulation and experiments is a powerful tool. However, in most work, simulations and experiments are treated separately, partially because of the challenges associated with measuring RS densities under atmospheric pressure conditions, as described before. On some occasions, however, a successful benchmark of experiments and simulation was achieved. Some examples relevant to this work will be discussed below.

Waskoenig et al. [110] investigated the production of atomic oxygen densities in a previous version of the COST-μAPPJ and found good agreement in qualitative trends for atomic oxygen densities in experiment and a 1D simulation. The model was then used to identify the main formation mechanisms for atomic oxygen. A modified reaction chemistry set was later used to compare simulated and experimental densities of helium metastable atoms [101]. The spatial distribution of helium metastables has been also investigated as a function of electrode distance in other work [111] with both a 2D simulation and tunable diode laser absorption spectroscopy. Spatially resolved numerical and experimental helium metastable densities were found to be in good agreement.

Willems et al. [96] investigated the chemical kinetics of the COST-μAPPJ using a 2D model to explain trends of species such as OH, H_2O_2 and HO_2 observed in experiments using mass spectrometry in the effluent.

For the same jet, Kelly et al. [112] measured gas flow patterns and electrode temperatures, and found good qualitative and quantitative agreement with a complex multi-dimensional modelling approach, which accounts for plasma dynamics (1D), gas and heat dynamics (3D), and heating via enthalpy changed due to interaction of reactive species (2D).

Van Gaens et al. [106,113] investigated RONS densities in APPs using both experimental laser diagnostics and a global model. Absolute densities obtained with both techniques were largely in good agreement. A similar chemistry set was later used by Wende et al. [9], who investigated the effect of an APPJ on growth media and eukaryotic epithelial CRFK cells. It was found that although NO_2^- and NO_3^- were present in the gas phase chemistry according to the simulation, none of these species could be measured in the treated solution, which might be an effect of gas flow or more complex chemical dynamics.

1.5. Aims of this work and thesis outline

In the previously outlined literature review, several current challenges can be identified, and proposed solutions are as following:

1. Absolute species density measurements exist for various different plasma sources. The difficulty is to measure as many reactive species as possible in the very same plasma source, to sufficiently characterise the source with regard to their RS production, ideally under several parameter variations. In this work, four different ROHS are measured in comparable plasma sources containing humidity, which are O, H, H_2O_2 and OH. Additionally, N and NO are also measured in the same source in a gas mixture containing N_2 and O_2.

2. Novel and improved diagnostic techniques are used for these absolute species densities measurements in order to provide the most accurate possible data. Absolute O densities are quantified using VUV-Fourier-transform absorption spectroscopy under a variation of the H_2O content in the feed gas, using synchrotron radiation and and ultra-high resolution spectrometer (chapter 4). For the measurement of absolute OH and NO densities, an ultra-stable broad-band light source is used.

   Additionally, a ps-TALIF technique is presented for the measurement of atomic species such as O and H. This technique enables the measurement of excited species lifetimes (chapter 5). This means that the previously mentioned problem of having to calculate excited state lifetimes using assumed gas mixtures and quenching coefficients can be circumvented. Using this technique we can also gain insight into the gas mixing into the plasma effluent region.

3. Finally, a revised reaction mechanism is proposed to model the plasma chemistry in H_2O containing APPs (chapter 3). Using a 0-D plasma simulation, this reaction mechanism is benchmarked against the experimental measurements of O, H, OH, and H_2O_2. After obtaining a sufficient agreement between simulations and experiments, formation and consumption for these and other species of interest is investigated (chapters 4 to 6).

2. Experimental setup

2.1. Plasma jets

In the following sections, the two plasma sources which are used throughout this thesis are described.

2.1.1. The Micro Atmospheric Pressure Plasma Jet (μAPPJ)

The micro atmospheric pressure plasma jet (μAPPJ) is a prototype, a standardised atmospheric pressure plasma source used within the COST European Collaborative Project [31] and by different European research groups both for experimental [81, 85] and simulation studies [56,101,103,108]. The final aim of establishing such a source in the APP community is to provide a well characterised plasma source, which allows for similar measurement conditions, and more comparable results between different research institutions. The relative simple design allows for optical access to the plasma bulk necessary to probe it with optical diagnostics. Additionally, it has a very simple geometry suitable for plasma simulations, and allows interactions with biological samples.

A schematic and photograph of the version of the μAPPJ used in this work is shown in fig. 2.1 (a) and (b), respectively. The jet consists of two modules, which are the electrode configuration and gas supply, and a housing. Two electrodes are placed in parallel between two quartz glass plates, leaving a channel of (1×1) mm^2 cross section, and 3 cm length. The electrodes form a tip at the end of the channel, enabling the insertion of the setup into the cavities of a 24 well titer plate. The configuration is attached to a gas supply tube. The parallel-plane geometry of the jet contains the electric field inside the discharge gap, therefore only allowing neutral species and (V)UV light to exit the jet, while charged

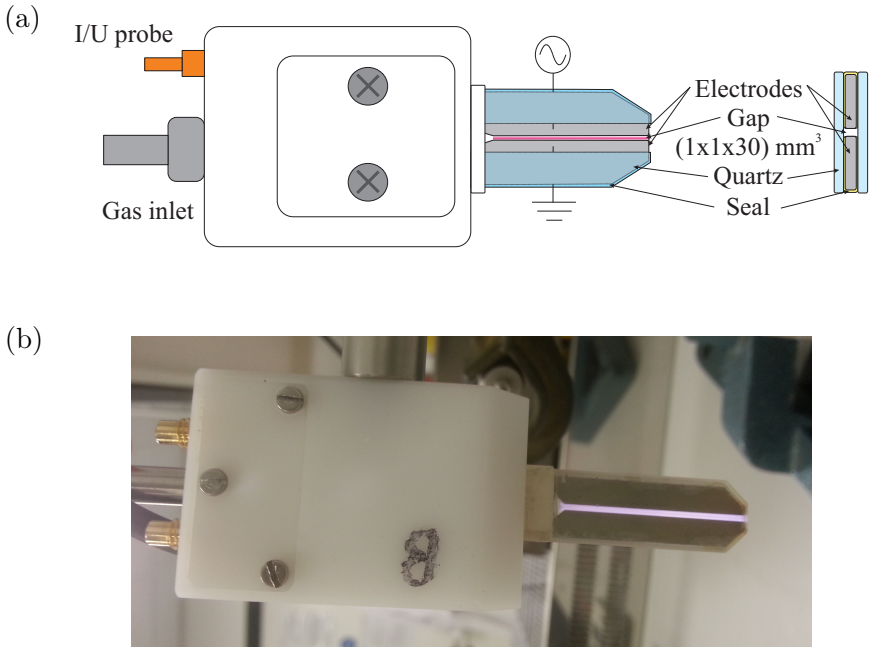

Fig. 2.1: Schematic (a) and photograph (b) of the μAPPJ

species like ions and electrons are contained within the electrodes. Therefore, possible effects on biological matter after plasma treatment can be related to these two effects only.

Gas is introduced into the confined discharge channel, and exits the channel into open air. High purity He (99.996% purity) serves as a buffer gas, and small amounts of molecular gases (up to a few % depending on the gas) can be admixed in order to create RS due to dissociation of these molecules. Typical flow rates range between a few hundred standard cubic centimetre per minute (sccm) and few standard litres per minute (slm). Before using the jet, gas is typically flowed through the channel for at least half an hour to remove any residual impurities which may have entered the channel since the previous use. The plasma is ignited by applying a sinusoidal voltage in the radio-frequency regime, typically 13.56 MHz, to one of the electrodes, whereas the other electrode is grounded. Typical powers coupled into this device lie between 0.2 and 2 W [30], depending on the applied voltage and gas mixture. Gas temperatures can be kept under 37°C at low powers, which is a critical temperature for treatment of biological tissue. Steady-state temperatures are usually reached within the first thirty minutes of plasma operation [30].

The design is an early design of the current COST-μAPPJ as described in reference [30], but without the internal transformer coil, safety-gap and electrode shielding. However, the basic geometry is the same as described in reference [30], so that all plasma properties are the same when operated at the same conditions as the source described in this reference.

2.1.2. Sealed plasma jet (mod-μAPPJ)

For certain diagnostic techniques, such as absorption spectroscopy in the vacuum ultraviolet spectral range, the plasma jet has to be inserted into a vacuum vessel at the DESIRS

beamline at the synchrotron SOLEIL [114]. Therefore, a modified sealed version of the μAPPJ was designed specifically for this purpose, which is referred to here as the mod-μAPPJ. A schematic an a photograph of this plasma source are shown in fig. 2.2 (a) and (b), respectively.

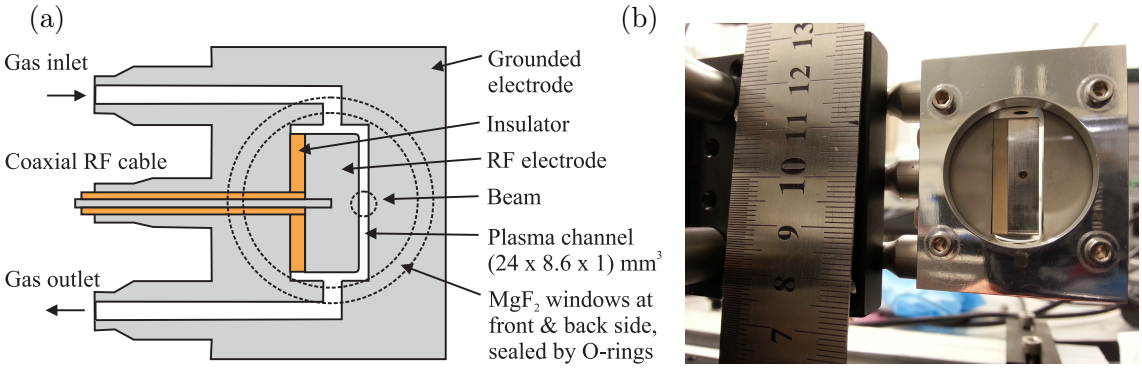

Fig. 2.2: Schematic (a) and photograph (b) of the mod-μAPPJ

The dimensions are chosen to resemble the μAPPJ: The jet has one powered electrode with an area of (8.6×24) mm^2. The whole metal casing of the jet serves as the grounded electrode. Between the two electrodes, the plasma is ignited in a gap of 1 mm width similar to the μAPPJ. The wider electrodes allow for a longer absorption length for AS measurements in order to enhance the signal strength. A very similar source has previously been described by Niemi et al. [66]. However, compared to the source used in this work, the absorption length and channel length in the source described in reference [66] are longer, being 1.1 cm and 3 cm, respectively.

The plasma can be optically probed through two round and 1 mm thick MgF_2 windows (Crystan Limited), which are partially transparent into the UV and VUV range. The transmission of the windows is about 66% at 130 nm, which is the wavelength used for the VUV absorption measurements described in chapter 4 for atomic oxygen, and over 90% for wavelengths over 190 nm. They are shaped like wedges (angle within 0.025 mrad) for a better control of a possible beam displacement, as it is shown in fig. 2.3. By rotating the two windows in opposite directions, the position of the beam can be adjusted. This is necessary because beam paths in the synchrotron facility are large, resulting in a large displacement of the beam if not properly aligned. More details about this experiment will be revealed in section 4.4.

Additionally, the source is completely vacuum-sealed, allowing measurements with atmospheric pressure inside the channel and vacuum outside, and the VUV beam to pass without being absorbed in ambient air. Similarly, the source is well sealed against possible air impurities intruding the source when operated in a common lab environment at atmospheric pressure. Additionally, the gas outlet is far away from the plasma channel, preventing a possible backflow of air into the jet under these conditions.

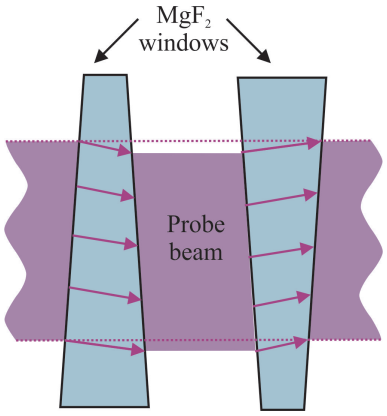

Fig. 2.3: Path of the probe beam going through the two wedge-shaped windows of the mod-μAPPJ

2.2. Plasma operation

2.2.1. General considerations

Although plasma operation depends on the plasma source and plasma conditions for the various different experiments, several general rules are followed when operating the source to increase reproducibility of results. At the beginning of any series of measurements, the plasma is operated at least for half an hour with the desired starting gas mixture. This is to establish equilibrium conditions, in which the gas and electrode temperatures reach steady-state [30], and many gas impurities, which get into the plasma source when not used, are flushed out.

The source is powered by either a fixed frequency power generator, or a combination of function generator and amplifier. In order to maximise the power coupled into the plasma, a matching box is connected between the power supply and the plasma source. The matching network is used to tune the overall impedance of the system close to 50 Ω, which is the ideal output impedance for the rf-power generators. Different combinations of power supply and matching units are used for different experiments carried out in this work. In order to obtain reproducible results, the applied voltage is always monitored using an external voltage probe attached between the matching box and the plasma source. The lengths of all cables between matching box, voltage probe, and plasma source, as well as the numbers of the electrical connections, was kept constant within the experiments involving either of the two plasma sources.

When conducting a parameter sweep, such as a gas mixture variation, a waiting time of 5 mins (in the case of O_2 and N_2 gas admixtures) or 10 mins (when the H_2O admixture is changed) was applied before taking the next measurement point, to ensure that the gas mixture has reached a steady-state condition by the start of the measurement. This is done in addition to the previously mentioned 30 min warming-up tome of the plasma jet.

2.2.2. Gas humidification

For the measurements presented in this work, helium (He) serves as the feed gas, and small amounts of molecules (typically up to 1.5%) are admixed to create a reactive chemistry. For most gases, the desired flow can be obtained by using mass flow controllers (MFC) connected directly to the corresponding gas bottles. However, for the admixture of H_2O vapour another approach has to be used, since MFCs cannot be used with humid gases. As a result, humidity is added to the feed gas by splitting the main He flow into two flows using two MFCs, where one gas flow is bubbled through a bubbler. A similar approach has been used in other work [40, 44, 47]. The bubbler consists of a 120 cm long domed glass adapter (Biallec GmbH), which can be clamped to a KF40 flange using an O-ring. This setup makes it easy to fill and empty the bubbler, and prevents air impurities entering the gas flow during the measurements. Two stainless steel pipes are welded to the flange, providing a gas in- and outlet. A schematic of the MFC setup is shown in fig. 2.4. For results presented in chapter 5, an additional filter was installed in the dry part of the He gas supply to filter out humidity coming from gas impurities. This prevents impurities having an impact on results when the intentional molecular admixture is low.

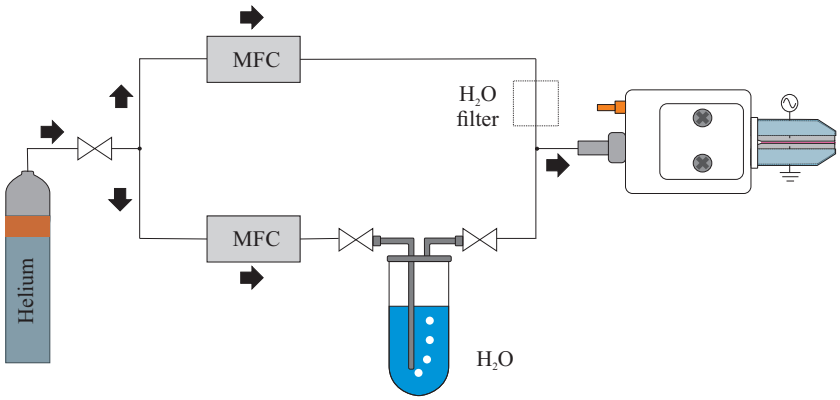

Fig. 2.4: Setup for humidifying the He feed gas. The amount of H_2O vapor is controlled by changing the ratio of dry He and the He guided through the bubbler.

Assuming that the He is saturated after passing through the bubbler, the total amount of water in the vapour phase can be calculated using the vapor pressure $p^{\text{vap}}_{H_2O}$ of H_2O [115] and the flow rate of the He through the bubbler $F^{\text{bubbler}}_{\text{He}}$, as has been described elsewhere [44]:

$$p^{\text{vap}}_{H_2O} = 6.112 \times 10^{-3} \exp\left(\frac{17.62 T_C}{243.12 + T_C}\right) \text{ bar} \tag{2.1}$$

$$F_{H_2O} = F^{\text{bubbler}}_{\text{He}} \frac{p^{\text{vap}}_{H_2O}}{p_{\text{atm}} - p^{\text{vap}}_{H_2O}} \tag{2.2}$$

where T_C is the temperature in °C. In order to check if the He is saturated with water after passing through the bubbler, the weight loss of water is measured over long time periods. Using the flow rate, weight loss, and bubbling time, a value for the absolute humidity is calculated. Measured absolute humidities can be found in fig. 2.5 as a function of gas flow

rate through the bubbler[1].

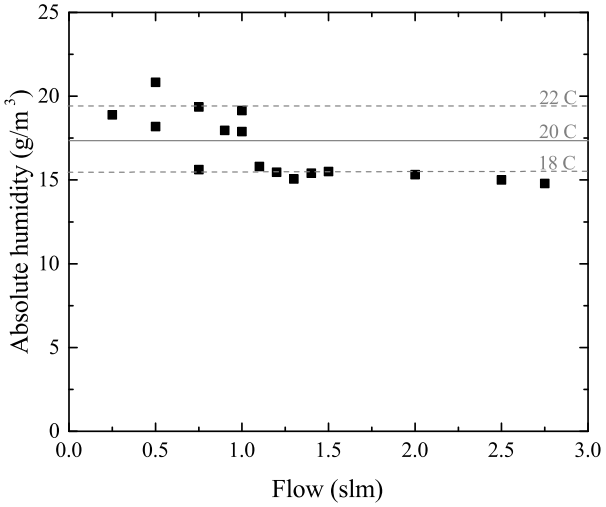

Fig. 2.5: Measured water content in the gas phase over the amount of He through the bubbler, and calculated values for different temperatures.

The gas temperature varies slightly with the He flux through the bubbler. Additionally, a day-to-day variation can occur, which is likely due to temperature fluctuations in the laboratory. However, most absolute humidity values can be described by assuming a $t = (20 \pm 2)$°C, as it is shown in fig. 2.5. Therefore, if not otherwise stated, a typical error bar of 2°C is assumed when calculating the humidity for a given set of experiments. For most measurements in chapter 5, the bubbler was placed in a water bath to regulate the temperature to 18°C. For these measurements, a smaller error bar of 1°C for the temperature fluctuation of the water in the bubbler is assumed.

Other methods have been used previously by other groups to quantify the content of humidity in their feed gas. These methods include molecular beam mass spectrometry [44, 96], tunable diode laser absorption spectroscopy [116], or using hygrometers [42]. These techniques could be implemented in future work to measure the water content in the feed gas more accurately.

[1]Data points in fig. 2.5 were taken by Nicolas Minesi

3. Plasma modelling

Plasma simulations are very useful tools to investigate plasma systems that are difficult to access experimentally, and together with experiments they offer a means to interpret experimental data. In this work, the 0-dimensional plasma-chemical kinetics code GlobalKin [109, 117] is used, together with the pathway analysis tool PumpKin [118]. Together with an extensive chemistry set, these tools are used to investigating the complex reaction chemistry in APPs, while keeping the computational time low. Both the μAPPJ and the mod-μAPPJ produce homogeneous spatial density profiles for most species of interest when operated in α-mode, making the use of a global model justified.

The aim of the establishment of such a model is two-fold. First of all, a comparison between model and experiments can help to benchmark the model to determine if it is describing the plasma dynamics correctly, and to find the relevant formation pathways for species of interest. Secondly, if good agreement is obtained between simulation and experiments, the model can be used to predict other parameters which are not easily accessible, such as additional species densities of interest.

3.1. Principles of the GlobalKin code

Globalkin is a 0-dimensional plasma-chemical kinetics code, which is widely used to simulate different kinds of plasma systems. It has been used to investigate various applications [109, 117, 119, 120], such as the investigation of formation of $O_2\left(^1\Delta\right)$, surface modification of polymers, or plasma remediation in combustion processes. The code is described in detail in the cited publications, and only its main features will be summarised here.

GlobalKin consists of 3 parts; a chemistry module, a two-term Boltzmann equation solver to calculate the electron energy distribution function (EEDF), and an ordinary differential equation solver. It solves mass balance equations (3.1) for all the species included in the reaction scheme and, in addition, the electron energy balance equation (3.2).

$$\frac{dn_i}{dt} = \frac{S}{V}\left(-\frac{D_i n_i \gamma_i}{\gamma_i \Lambda_D + \frac{4D_i}{v_{th,i}}} + \sum_j \frac{D_j n_j \gamma_j f_{ij}}{\gamma_j \Lambda_D + \frac{4D_j}{v_{th,j}}}\right) + S_i \tag{3.1}$$

$$\frac{d}{dt}\left(\frac{3}{2} n_\mathrm{e} k_\mathrm{B} T_\mathrm{e}\right) = P_\mathrm{d} - \sum_i \frac{3}{2} n_\mathrm{e} \nu_{mi} \left(\frac{2m_\mathrm{e}}{m_i}\right) k_\mathrm{B} \left(T_\mathrm{e} - T_i\right) + \sum_l n_\mathrm{e} k_l n_l \Delta\epsilon_l \tag{3.2}$$

Here n_i denotes particles densities of species i, m_e and m_i the masses of electrons and heavy particles, and T_e, T_i and T_g the electron, heavy particle and gas temperatures, respectively. Λ and D_i are the diffusion length and coefficients for species i, γ_i and f_{ij} the wall recombination ("sticking") coefficients and return fractions, S_i a source term of species from chemical reactions, P_d is the coupled power into the plasma, ν_{mi} the collision frequency, k_l the reaction rate coefficient for electron inelastic collisions with particles l, and $\Delta\epsilon_l$ the internal energy difference.

Equation (3.1) is the continuity equation for species and describes how species densities change as a function of time. The different terms on the right hand side of eq. (3.1) account for diffusion to and recombination of species at the wall (first two terms in brackets) and changes in gas temperature that lead to changes in species densities at fixed pressure (last term). Since all simulations are carried out at a constant $T_\mathrm{g} = 315$ K in this work, the latter is not taken into account here. The source term S_i describes production and loss of species due to chemical reactions, and will be described in more detail later in section 3.2.

Equation (3.2) is the electron energy balance equation. It describes the change of electron temperature due to power coupled into the system (first term on right hand side) and power losses due to elastic (second term on right hand side) and inelastic collisions (third term on right hand side) with heavy particles. The power P_d is the average power deposited into the system over many RF cylces, and therefore temporally averaged.

3.2. Model inputs

3.2.1. Geometry

GlobalKin is a 0-dimensional chemical kinetics code, therefore, all quantities such as species densities and temperatures are calculated as a function of time and not necessarily space. However, GlobalKin also incorporates a pseudo-one-dimensional plug flow [117]. In systems like APPJs, this allows a specific volume of gas to be followed while it travels along the discharge gap. This allows for the simulation of plasma parameters spatially as the gas propagates through the discharge gap. In order to convert the temporal change in species densities and temperatures shown in eq. (3.1) and eq. (3.2) into a spatial change,

GlobalKin takes into account the flow velocity in the mass flux conservation equation [117]

$$\frac{dv_\mathrm{x}}{dt} = -\frac{v_\mathrm{x}}{\rho}\frac{d\rho}{dt} \tag{3.3}$$

The flow velocity v_x is calculated by using the cross sectional area A_flow, through which the gas is flowing, and the gas flow rate F in sccm

$$v_\mathrm{x} = \frac{F}{A_\mathrm{flow}}\frac{n_0}{n_\mathrm{g}} \tag{3.4}$$

where n_g is the gas density under plasma operating conditions, and n_0 is the gas density at standard conditions ($T_\mathrm{g} = 273.15$ K and atmospheric pressure). By default, this plug flow is calculated assuming a plasma formed in a cylindrical tube geometry in GlobalKin. In this case A_flow and the diffusion length Λ are calculated using a given radius r of the discharge:

$$A_\mathrm{flow} = \pi r^2 \tag{3.5}$$

$$\Lambda = \frac{r}{2.405} \tag{3.6}$$

However, because the plasma sources investigated in this work have rectangular cross sections instead of circular ones, A_s and V_p are manually calculated from the plasma dimensions and used as inputs for the model. The diffusion length Λ for a rectangular cross section is also manually calculated using [121]

$$\Lambda = \left(\sqrt{\left(\frac{\pi}{x}\right)^2 + \left(\frac{\pi}{y}\right)^2}\right)^{-1} \tag{3.7}$$

where x and y are the width and height of the plasma channel. A list with all relevant parameters used for the simulations can be found in table table 3.1.

Tab. 3.1: Dimensions used for plasma simulations

Source	**μAPPJ**	**mod-μAPPJ**
Dim. (cm^3)	$0.1 \times 0.1 \times 3$	$0.1 \times 0.86 \times 2.4$
A_flow (cm^2)	0.01	0.086
Λ (cm)	0.0225	0.0316
A_s (cm^2)	1.2	4.608
V_p (cm^3)	0.03	0.2064
F_He (sccm)	500	5000

3.2.2. Initial particle densities

All experiments in this work are carried out in a He background gas with small deliberate molecular admixtures up to 1.5%, such as H_2O, O_2, and N_2.

In the simulations, a total gas flow is defined, as well as the mole fractions of different

species contributing to this gas flow. With the gas flow mainly consisting of He, mole fraction for He is set to 1 and the initial mole fraction for H_2O or other deliberately admixed molecules is typically set to values between 10^{-6} to 10^{-2}, depending on the investigated admixture. For all other not deliberately admixed species, chosen mole fractions of the inital gas mixture are $10^{-12} - 10^{-10}$ for neutral species, 10^{-12} for ions, and 10^{-11} for electrons.

3.2.3. Plasma power

An important input parameter for the simulation is the plasma power. The power can be measured by measuring current I and voltages U of the plasma source, as well as the phase shift φ between them

$$P = \frac{UI}{2}\cos(\varphi) \tag{3.8}$$

However, measuring the plasma power is not very easy in rf plasmas at atmospheric pressure, because the power deposited is typically small. Therefore, the phase shift between voltage and current is small and difficult to measure accurately.

In this work, the power is measured dependent on the H_2O content in the feed gas by determining current, voltage and phase shift using a current (Ion Physics Corp. CM-100-L 1 V/A) and voltage probe (Tektronix, 1000:1). The procedure is described in much detail elsewhere [122]. The probes are installed between matching unit and plasma source.

Power losses into the plasma source and surrounding electronics are accounted for by measuring the power deposited in the system without a gas flow, so that the ignition of the plasma is inhibited. We then use the power subtraction method for a given current [123]

$$P_{\text{net}}(I^2) = P_{\text{on}}(I^2) - P_{\text{off}}(I^2) \tag{3.9}$$

The net power P_{net} is the difference between the power measured with and without plasma, P_{on} and P_{off}, respectively. The measured powers can be transformed to power densities p by taking into account the volume of the plasma

$$p = \frac{P_{\text{net}}}{V_{\text{plasma}}}. \tag{3.10}$$

The instrumental phase shift from the electronics is determined using an air capacitor with a known phase shift (MFJ 282-2018-1). For the calibration measurement, the plasma source and cable between source and matching box are replaced by this capacitor.

Current and voltage waveforms are recorded by a fast oscilloscope (WaveSurfer10, 10 GS/s sample rate, LeCroy). From the data, the three parameters in eq. (3.8) were obtained by performing a fast Fourier transform.

Tab. 3.2: Species considered in the simulation. N containing species are only taken into account on an impurity level in chapter 5. All other simulations in this work only take into account O and H containing species, as well as He and electrons (species printed in bold).

Species	**neutral**	**positive**	**negative**
He	He, He^*, He_2^*	He^+, He_2^+	
O-species	O, $O(^1D)$, $O(^1S)$, O_2, $O_2(a^1\Delta)$, $O_2(b^1\Sigma)$, O_3	O^+, O_2^+, O_4^+	O^-, O_2^-
H-species	H, H_2		H^-
N-species	N, $N(^2D)$, $N(^2P)$, N_2	N^+, N_2^+, N_4^+	
OH-species	OH, HO_2, H_2O, H_2O_2	OH^+, $H_2O^+(H_2O)_{n=0,1}$, $H^+(H_2O)_{n=1..9}$, $O_2^+(H_2O)$	$H_2O_2^-$, $OH^-(H_2O)_{n=0..3}$
NO-species	NO, NO_2, N_2O, NO_3	NO^+	
NH-species	NH, NH_2, NH_3		
NOH-species	HNO, HNO_2, HNO_3		
Electrons			e

3.2.4. Reactive species and reaction set

One aim of this work is to establish a chemistry set which describes accurately the dynamics in a He-H_2O atmospheric pressure plasma (with some potential air impurities) by benchmarking its results to those of experimental measurements. Several previous studies have been developed on reaction sets either in He or argon (Ar) with various molecular admixtures. Liu et al. [39] developed a large reaction mechanisms for a He-H_2O atmospheric pressure plasma, taking into account 46 species and 577 reactions. Other work was carried out to elaborate further on this chemistry, e.g. by admixing additional species such as O_2 [52, 53]. Recently, also chemistry sets for plasmas containing humid air have been developed [54, 105, 124]. The reaction set used in this work is based on the work of Liu et al. [39] and Murakami et al. [54], with additional and revised rate coefficients.

Table 3.2 shows all 61 species taking into account in this work. For all simulations, O and H containing species (in bold in table 3.2) are taken into account. The respective reactions can be found in chapter A. For simulations carried out in chapter 5, some additional N-containing species are added to the chemistry set that could potentially arise from air impurities, because the source modelled in that section is in contact with ambient air. The additional reactions taken into account in chapter 5 can be found in chapter B. The reader should note that the chemistry set used is not necessarily designed to represent plasmas with high nitrogen or air content, because several species, which are known to play an important role in these kinds of plasmas, are missing from the set presented in this work. Examples for these species are vibrationally or electronically excited states of N_2 and O_2.

In the following paragraphs, the four different types of reactions, which must be considered when developing a reaction set, will be discussed. These are electron impact reactions, mutual ion-ion-recombination, ion-neutral collisions and reactions between neutrals. All

551 reactions taken into account are listed in chapters A and B, where the latter lists additional N-containing reactions for simulations carried out in chapter 5. In general, GlobalKin accepts reaction rates for all four types of these reactions in Arrhenius form

$$k = A_{\mathrm{A}} T_{\mathrm{e}}^{n} e^{-E_a/T_e} \tag{3.11}$$

$$k = A_{\mathrm{A}} T_{0}^{n} e^{-E_a/T_g} \tag{3.12}$$

Where A_{A} is the Arrhenius A coefficient in the units s^{-1}, $\mathrm{m}^3\mathrm{s}^{-1}$, or $\mathrm{m}^6\mathrm{s}^{-1}$ for 1-,2- or 3-body reactions, respectively, and E_{a} is the activation energy of the reactions. Equation (3.11) is for electron reactions, therefore T_{e} and E_{a} are in eV. Equation (3.12) is for heavy particle collisions, with $T_0 = \frac{T_g}{300\ \mathrm{K}}$, T_g and E_{a} in K.

Radiative reactions are not taken into account in this work, although it is known that several species occuring in the plasma under the investigated conditions, such as He_2^* excimers, can be strong sources for UV radiation, which could lead for example to dissociative processes. However, including radiation would require a radiative transfer model, taking into account excitation into these radiative states as well as competition with quenching processes, and would highly add to the complexity of the present model. The addition of radiative process could be a task for future investigations.

Electron collisions

All electron reactions taken into account in the simulations are listed in tables A.1 and B.1 given in the appendices. As stated previously, GlobalKin incorporates an internal Boltzmann solver, which calculates rate coefficients and EEDFs from sets of electron impact cross sections for the species contained in the plasma. This is the case for the electron scattering and momentum transfer cross sections, most electron impact excitation cross sections, and some of the dissociative processes. However, some cross sections are not well known. In that case, rate coefficients are either deduced from known processes, or estimated using similar processes. Whenever rate coefficients are not calculated using the internal solver and/or cross sections are approximated, this is noted in footnotes in tables A.1 and B.1. However, some specific examples will be discussed in the next few paragraphs.

For the calculation of rate coefficients for electron impact of excited states, such as the O_2 metastable states ($\mathrm{O}_2(\mathrm{a}^1\Delta)$ and $\mathrm{O}_2(\mathrm{b}^1\Sigma)$), the equivalent cross section for the ground state species is used as a basis for estimating the electron impact cross section for the excited state. However, the threshold energy for these processes is shifted according to the energy difference between the ground and excited states. Additionally, the cross sections are scaled by taking into account the excitation threshold of the reaction. For super-elastic collisions, the electron impact cross section is calculated from the inelastic process using the principle of detailed balancing.

For some reactions electron impact cross sections cannot be found in the literature, in these cases well-known approximations are used to calculate cross sections or rate coefficients. One example for this is the approximation of electron ionisation cross sections

for the ionisation of atoms (in this work for the ionisation from atomic oxygen metastable states O(^{1}D) and O(^{1}S)), using equations derived by Gryzinski and Vriens [125, 126]. Another way is to assume the same cross sections as for a species with similar energy level distribution. An example here is OH. For the dissociation of OH, the same cross sections as for the dissociation of CO are assumed.

Sometimes there is no cross section data available, and rate coefficients are estimated in the literature. A typical example for this is the neutral dissociation of H_2O_2 by electron impact, resulting in two OH radicals. Soloshenko et al. [127] have calculated the rate coefficient for this from the electron impact dissociation cross sections for O_2, and doubling the threshold energy. This rate coefficient is used by other authors [39], but it is a very rough estimate, and results obtained by using this rate, especially when analysing the most important pathways in a reactions set, should be treated carefully. Later in this work in chapter 6, the effect of this rate coefficients on the absolute densities on H_2O_2 densities will be discussed. H_2O_2 densities are generally small compared to densities of admixed species such as He or H_2O, so it is assumed that this pathway does not significantly influence electron energy losses and that its main purpose is in determining the densities of H_2O_2 and OH.

Ion-ion recombination

Of the four types of possible reactions described in this section, ion-ion recombination reactions are perhaps the least investigated in the literature. However, these reactions play an important role especially in electro-negative gases, as they are one of the main mechanisms to limit the charge density in these kinds of plasmas [128]. As pointed out in several publications [129–131], reaction rates generally depend on the gas pressure, where three pressure regimes are distinguished. At very low pressures, at the zero-pressure limit, mutual neutralisation reactions (with rate coefficient k_{MN}) are binary in nature.

$$A^+ + B^- \rightarrow C + D \tag{3.13}$$

Reactants A and B can either be atoms, in which case the products of this reactions $C = A$ and $D = B$, or molecules. In the latter case, this reaction typically leads to dissociation of the reactants or rearrangement of molecules due to the high potential energy of the positive ion, which typically lies above the needed dissociation energies of most molecules. It has been found that these reaction rates also depend on the gas density [130, 131]. However, the exact dependence is not known for most ions.

Towards higher pressures (the "Thomson regime", up to a few atmospheres), another mechanism that can enhance the overall reaction rate is three body recombination (with rate coefficient k_{R})

$$A^+ + B^- + M \rightarrow AB^* + M \tag{3.14}$$

$$\rightarrow A + B + M \tag{3.15}$$

Here reactants A and B (of which at least one is a molecule) recombine to form a highly excited complex, which could potentially decompose back into the original particles, unless the excess energy is taken away by the background gas. Therefore, this reaction rate increases strongly towards higher pressures.

At very high pressures (the "Langevin regime"), the ambient gas starts to interfere with the ions and the rate coefficient becomes diffusion limited. Therefore, the reaction rate decreases again with increasing pressure. The rate coefficient in this regime can be expressed by

$$\begin{aligned} k_{\mathrm{L}} &= 4\pi e(\mu_1 + \mu_2) \\ &= \frac{4\pi e^2}{kT}(D_1 + D_2) \end{aligned} \tag{3.16}$$

where D and μ are the diffusion constant and mobilities of the different particles, respectively. As shown in the previously mentioned publications [129–131], and also other experimental work [132, 133], the transition between the Thomson and the Langevin regimes typically lies around atmospheric pressure, with recombination rate coefficients of $k_{\mathrm{R}} \approx 10^{-6}$ cm^{3}s^{-1}. In early work by Kossyi [134], the rate coefficient

$$A^- + B^+ + M \rightarrow AB + M \qquad (k = 2 \times 10^{-25} T_0^{-2.5}\ \mathrm{cm^6 s^{-1}}) \tag{3.17}$$

$$\rightarrow A + B + M \qquad (k = 2 \times 10^{-25} T_0^{-2.5}\ \mathrm{cm^6 s^{-1}}) \tag{3.18}$$

for several atoms and molecules was proposed for the modelling of air plasmas, where M is a third body species such as O_2 or N_2. At atmospheric pressure and room temperature, the effective rate coefficient, obtained by multiplying by the gas density, is in the order of 10^{-6} cm^{3}s^{-1}.

Values for the binary ion mutual neutralisation reactions k_{MN} have been measured for several rare gas cations reacting with different di- and polyatomic anions by Miller et al. [128]. They found that for these reactions, k_{MN} is given by the following expressions

$$k_{\mathrm{MN}} = 3.2 \times 10^{-8} T_0^{-1.1} m_{\mathrm{r}}^{-0.01} \varepsilon_{\mathrm{a}}^{-0.04} \text{ (diatomic)} \tag{3.19}$$

$$k_{\mathrm{MN}} = 2.8 \times 10^{-7} T_0^{-0.9} m_{\mathrm{r}}^{-0.5} \varepsilon_{a}^{-0.13} \text{ (polyatomic)} \tag{3.20}$$

Therefore, these reaction rates are one to two orders of magnitude smaller than the three body processes at atmospheric pressure and close to room temperature. It is also worth to mention that the measurements by Miller et al. have been conducted at low pressures (at 1 Torr), but that it was observed in other work [130, 131] that these reaction rates can strongly depend on pressure. However, in the work presented here, ion-ion neutralisation reactions are treated as three-body reaction with the rate constant shown in eqs. (3.17) and (3.18).

All ion-ion reactions for this work can be found in table A.2 and B.2.

Ion-neutral reactions

Most second order ion-neutral reaction rates taken into account in this work to describe the kinetics of positive ions are simple charge transfer reactions or charge transfer involving rearrangement or dissociation of species:

$$A^+ + B \rightarrow A + B^+ \tag{3.21}$$

$$\rightarrow C + D^+ \tag{3.22}$$

Many bimolecular reaction rates of this type for the species considered in this work can be found in the UMIST database for Astrochemistry [135], and the kinetic database for Astrochemistry (KIDA) [136].

Some charge exchange (or excitation transfer in the equivalent case for neutral excited species) reactions involving rare gas metastable states and ions, reaction rates have been found to consist of a combination of bi- and termolecular reactions [137–140], the latter becoming more important towards higher pressures.

Another process taken into account is three body association, where an ion and a neutral form a new highly unstable complex, which is subsequently stabilised by a collision with the background gas. Examples from this work are the association reactions which form large protonated H_2O clusters by collisions between smaller water clusters and H_2O molecules which are stabilised by the background gas. The forward and reverse reactions are denoted as

$$H^+(H_2O)_n + H_2O + He \rightleftarrows H^+(H_2O)_{n+1} + He \tag{3.23}$$

The reaction rate for these processes are both temperature and pressure dependent, and therefore have to be calculated for the specific temperature and pressure conditions in the system of interest. Details can be found elsewhere [124]. At low pressures, the association reaction can be expressed as a sequence of two binary reactions, where in a first step the two colliding partners combine to form a highly excited and loosely bound state, which can decompose back into the original particles if the excess energy is not taken away by a collision with a third body.

$$H^+(H_2O)_n + H_2O \rightleftarrows (H^+(H_2O)_{n+1})^* \tag{3.24}$$

$$(H^+(H_2O)_{n+1})^* + M \rightarrow H^+(H_2O)_{n+1} + M \tag{3.25}$$

In this low pressure limit, rate coefficients are then expressed as for a three-body reaction (k_0 in unit cm^6s^{-1}), and the effective rate increases linearly with pressure at constant temperature. At high pressures, the third body density is high enough that all excited species are stabilised before they can decompose back into the original particles. The reaction rate coefficient in this high pressure limit becomes two-body in nature (k_∞ in unit cm^3s^{-1}). Figure 3.1 shows the dependence of the effective two-body rate coefficient k_{eff} on the pressure, calculated from expressions that can be found in Sieck et al. [124].

It shows that, at atmospheric pressure, for low n k_{eff} approaches k_∞, while for high n k_{eff} approaches k_0. This highlights the importance of calculating the effective rate coefficient correctly for the pressure range to be studied by the model.

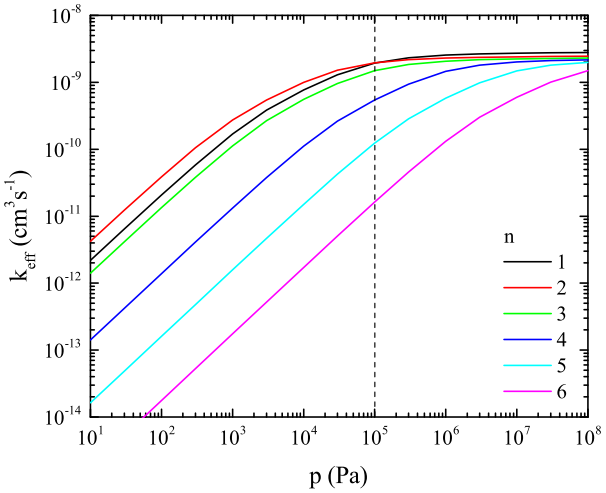

Fig. 3.1: Dependence of the effective rate coefficient for the reaction $H^+(H_2O)_n + H_2O(+He) \rightarrow H^+(H_2O)_{n+1}(+He)$ on the pressure at 315 K. For low n, the rate coefficient approaches k_∞ at atmospheric pressure (dashed line), while for high n, the rate coefficient is still described by k_0.

The efficiency of eq. (3.25) depends on the nature of the third body. Where the third body is stated to be O_2 or N_2 in the original source, k_0 is multiplied by a factor 0.38 to account for the effect that He is a much less efficient quenching species. This a rough estimation, because the effectiveness of stabilisation via He could change for different reactions. However, it is in accordance with previous work [141].

In order to use these rate coefficients in GlobalKin, which requires reaction rate coefficients in Arrhenius form (eqs. (3.11) and (3.12)), k_{eff} has to be calculated for the relevant experimental conditions. This is done by calculating k_{eff} using the expressions given by Sieck et al. [124] for atmospheric pressure and a temperature variation between 280 and 350 K, and fitting an Arrhenius expression to the data, where possible. This means of course that k_{eff} calculated in this way can only be used under these operating conditions and might not be valid at other pressure or temperature regimes. Figure 3.2 shows the dependence of the rate coefficients for the association reaction of different sized H_2O clusters on the temperature at atmospheric pressure. It can be seen that for the association reaction, k_{eff} decreases with increasing T_{gas}. The opposite is the case for the decomposition reaction (not shown). Figure 3.2 also shows the Arrhenius fit to the calculated data. Although the expressions given by Sieck et al. [124] are not strictly in an Arrhenius form, the data can be represented well by the fit in the regime of interest for most the experimental conditions considered in this work. For most decomposition reactions, the data is not represented satisfactory by an Arrhenius fit. Therefore, the rate coefficient has to be calculated specifically for the respective temperature, in this case $T_{\text{g}} = 315$ K. Table 3.3 shows calculated k_{eff} for for the association and decomposition reactions considered in this

work.

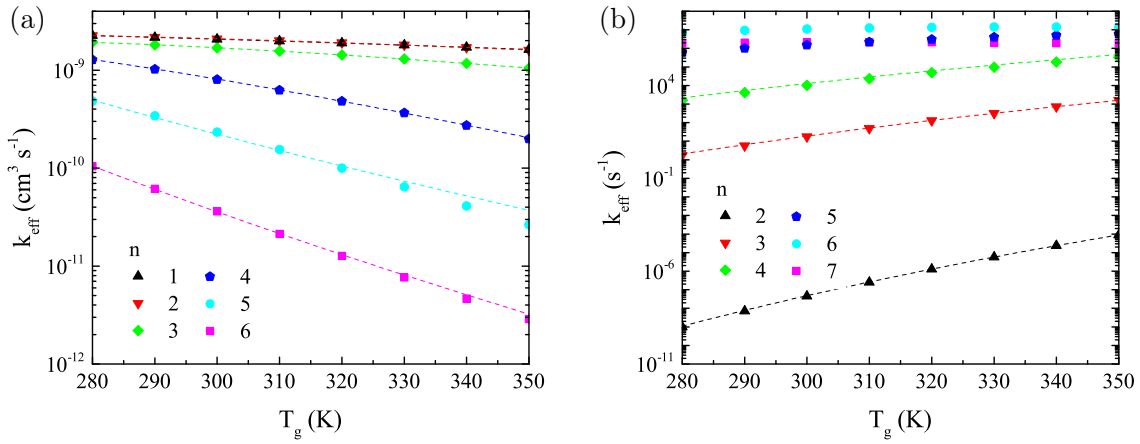

Fig. 3.2: Calculated rate coefficients for the reactions $H^+(H_2O)_n + H_2O(+He) \rightleftarrows H^+(H_2O)_{n+1} + He$ for different n under a variation of the gas temperature (Symbols) at atmospheric pressure using data from Sieck et al [124]. (a) Association reactions. (b) Decomposition reactions. The dashed lines represent an Arrhenius fit to the calculated data.

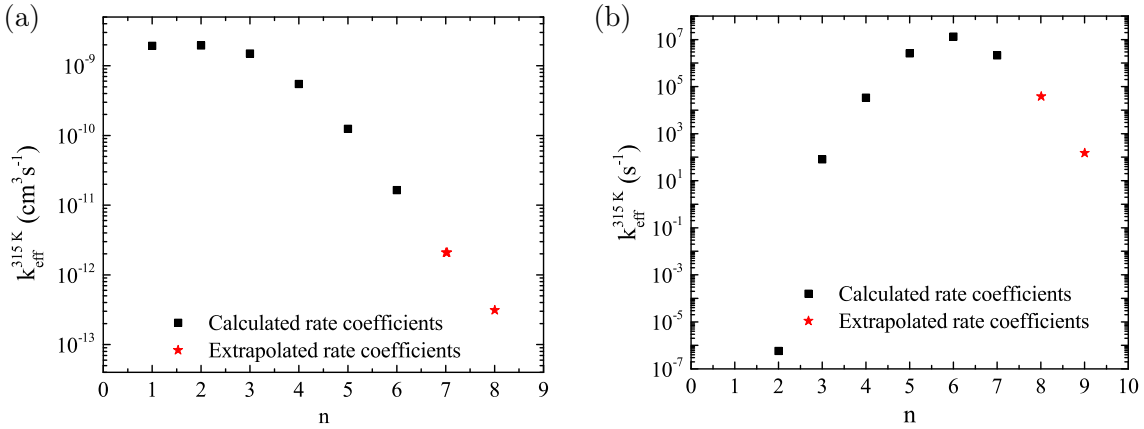

Fig. 3.3: Calculated rate coefficients for the same reactions as in fig. 3.2 at atmospheric pressure for a fixed gas temperature of 315 K (black dots). For higher n, rate effective rate coefficients are extrapolated (red stars). These values are used in the model.

Sieck et al. only provide low and high pressure limit rate coefficient for clusters up to $n = 7$ for decomposition and $n = 6$ for association reactions. In order to obtain k_{eff} for bigger clusters, the data for the known k_{eff} is extrapolated to higher n. The results can be seen in fig. 3.3 (a) and (b).

All ion-neutral reactions for this work can be found in tables A.3 and B.3.

Neutral chemistry

Similar to the ion-neutral reactions, all reactions for the neutral-neutral chemistry are either binary reactions, or association reactions which require a third body for the sta-

Tab. 3.3: Effective rate coefficient for decomposition and association reactions obtained from an Arrhenius fit to the data by Sieck et al. [124]. k_{eff} is either in s^{-1} for decomposition or in m^3s^{-1} for association reactions. The number in the left column is the row number according to table table A.3 in the appendix. Where an Arrhenius fit could not reproduce the calculated data, the rate coefficients are calculated for 315 K.

No	Reaction	k_{eff}
Decomposition reactions ($T_g = 315$ K)		
253	$H^+\cdot(H_2O)_2$ (+ He) → $H^+\cdot(H_2O)$ + H_2O (+ He)	$3.91 \times 10^{15} e^{-15829/T_g}$
254	$H^+\cdot(H_2O)_3$ (+ He) → $H^+\cdot(H_2O)_2$ + H_2O (+ He)	$5.88 \times 10^{14} e^{-9321/T_g}$
255	$H^+\cdot(H_2O)_4$ (+ He) → $H^+\cdot(H_2O)_3$ + H_2O (+ He)	$2.64 \times 10^{26} T_0^{-34} e^{-13979/T_g}$
256	$H^+\cdot(H_2O)_5$ (+ He) → $H^+\cdot(H_2O)_4$ + H_2O (+ He)	2.60×10^{6}
257	$H^+\cdot(H_2O)_6$ (+ He) → $H^+\cdot(H_2O)_5$ + H_2O (+ He)	1.33×10^{7}
258	$H^+\cdot(H_2O)_7$ (+ He) → $H^+\cdot(H_2O)_6$ + H_2O (+ He)	2.14×10^{6}
259	$H^+\cdot(H_2O)_8$ (+ He) → $H^+\cdot(H_2O)_7$ + H_2O (+ He)	3.81×10^{4}
260	$H^+\cdot(H_2O)_9$ (+ He) → $H^+\cdot(H_2O)_8$ + H_2O (+ He)	1.49×10^{2}
279	$O_2^+\cdot H_2O$ (+ He) → O_2^+ + H_2O (+ He)	$1.41 \times 10^{12} e^{-6629/T_g}$
Association reactions		
299	$H^+\cdot(H_2O)$ + H_2O (+ He) → $H^+\cdot(H_2O)_2$ (+ He)	$4.44 \times 10^{-14} T_0^{-4.4} e^{-919/T_g}$
300	$H^+\cdot(H_2O)_2$ + H_2O (+ He) → $H^+\cdot(H_2O)_3$ (+ He)	$8.47 \times 10^{-13} T_0^{-7.3} e^{-1800/T_g}$
301	$H^+\cdot(H_2O)_3$ + H_2O (+ He) → $H^+\cdot(H_2O)_4$ (+ He)	$1.65 \times 10^{-10} T_0^{-13.7} e^{-3450/T_g}$
302	$H^+\cdot(H_2O)_4$ + H_2O (+ He) → $H^+\cdot(H_2O)_5$ (+ He)	$1.07 \times 10^{-6} T_0^{-28.4} e^{-6300/T_g}$
303	$H^+\cdot(H_2O)_5$ + H_2O (+ He) → $H^+\cdot(H_2O)_6$ (+ He)	$2.22 \times 10^{-16} T_0^{-11.6}$
304	$H^+\cdot(H_2O)_6$ + H_2O (+ He) → $H^+\cdot(H_2O)_7$ (+ He)	$3.58 \times 10^{-17} T_0^{-15.6}$
305	$H^+\cdot(H_2O)_7$ + H_2O (+ He) → $H^+\cdot(H_2O)_8$ (+ He)	2.08×10^{-18}
306	$H^+\cdot(H_2O)_8$ + H_2O (+ He) → $H^+\cdot(H_2O)_9$ (+ He)	3.10×10^{-19}
307	O_2^+ + H_2O (+ He) → $O_2^+\cdot H_2O$ (+ He)	$1.19 \times 10^{-15} T_0^{-2.4}$
308	O_2^+ + O_2 (+ He) → O_4^+ (+ He)	$7.13 \times 10^{-17} T_0^{-3.3}$

bilisation of the products, and therefore appear as three-body reactions at low pressure. All reaction rates accounted for in this work can be found in tables A.4 and B.4 in the appendix.

Most three-body association rates are still in the low-pressure limit even at atmospheric pressure, and can be described accurately by k_0, the three-body reaction rate. Wherever the reaction approaches the transition between the low and high pressure limits, and the effective rate coefficient deviates more than 10% from k_0, the effective rate coefficient is calculated as described by Atkinson et al. [142]. These rate coefficients can be found in table 3.4.

An example for such a pressure dependent reaction is the association reaction for the formation of H_2O_2

$$2OH(+M) \rightarrow H_2O_2(+M) \tag{3.26}$$

Tab. 3.4: Effective rate coefficients for different association reactions, where k_{eff} is in m^3s^{-1}. k_{eff} is calculated using data from the IUPAC database [142]. The number in the left column is the row number according to tables A.4 and B.4 in the appendix.

No	Reaction	k_{eff}
Association reactions		
365	(He +) H + O_2 → HO_2 (+ He)	$3.50 \times 10^{-19} T_0^{-2.1}$
366	(He +) 2OH → H_2O_2 (+ He)	$3.60 \times 10^{-18} T_0^{-2.9}$
511	OH + NO_2 (+ He) → HNO_3 (+ He)	$6.11 \times 10^{-18} T_0^{-2.8}$

The effective rate coefficient for this particular reaction has been measured by Forster et al. [143], and the results are shown in fig. 3.4. At lower pressures, k_{eff} increases linearly with the third-body density, while at higher pressures, k_{eff} approaches k_∞ and stays constant with pressure. The offset shown at very low pressures is the rate coefficient for another product channel

$$2OH \rightarrow H_2O + O \tag{3.27}$$

which is a pressure independent reaction with a bimolecular reaction rate.

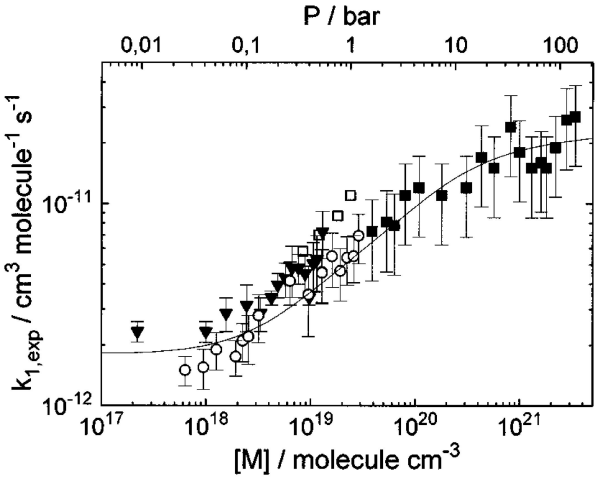

Fig. 3.4: Dependence of the effective rate coefficient for the reaction $2OH(+He) \rightarrow$ *products* on the pressure at 298 K. Reprinted from R. Forster et al., *J. Chem. Phys.* **103** (1995) 2949-2958 [143], with the permission of AIP Publishing.

Wall reactions

Additionally to the previously discussed plasma bulk reactions, reactive particles can also stick to the plasma reactor walls with a certain probability γ, which is usually referred to as the surface recombination or "sticking" coefficient, be absorbed, and return into the plasma bulk as another particle. γ depends on the plasma properties (temperature, gas mixture, pressure, and potential ion bombardment of surfaces) as well as the specific wall material. Some of these coefficients are measured in low pressure systems under specific

conditions, however, the measurements of these coefficients at higher pressures is very challenging. Therefore, γ is not well known for most discharge conditions, especially at atmospheric pressure. Additionally, if the plasma is run in humid conditions, as for most experiments in this work, several monolayers of water could potentially build up on the reactor wall, and change the surface sticking coefficients and reactions taking place at the surface.

In order to test the sensitivity of the simulation results to the surface loss probability the effect of varying the surface loss probability has been investigated. For the same discharge conditions (mod-µAPPJ, 5 slm He, 5000 ppm H_2O and 13.6 Wcm^{-3} power density), the sticking coefficient for atomic hydrogen γ_H is systematically changed. Atomic hydrogen as the lightest of the reactive neutral species is generally found to have the highest loss towards the wall. More details about this will be given in section 5.4.1. The H atoms which stick to the walls are assumed to undergo recombination and return to the plasma as hydrogen molecules:

$$H \xrightarrow{\text{wall}} \frac{1}{2} H_2 \tag{3.28}$$

Therefore, the absolute density of both H and H_2 depend on γ_H. Figure 3.5 shows simulated densities of these species at the end of the plasma channel under a varying γ_H. The highest H densities are found when the sticking coefficient is lowest, because no H is lost to the wall. Absolute H densities are then decreasing with increasing γ_H, and approach a steady-state at higher γ_H. Here, the loss of H is only limited by the amount of H that can actually reach the wall via diffusion processes.

The trend in the H_2 densities is opposite, because one of the important formation mechanisms for H_2 is via eq. (3.28). Therefore, less H_2 is produced when γ_H is low, and no recombination reactions for H take place at the walls. With increasing γ_H, more H_2 is produced via recombination reactions at the walls, and the absolute H_2 densities increase. Other species can also be affected by the variation of γ_H, as shown in table 3.6. Generally all species densities, except H, increase with increasing γ_H, because H as a very reactive species and plays a role in the consumption of many particles. For example O_3, which shows an increase of 159%, is directly consumed by collisions with atomic hydrogen

$$O_3 + H \rightarrow OH + O_2 \tag{3.29}$$

For O_2, the most important reaction for destruction under the investigated conditions is

$$H + O_2 + He \rightarrow HO_2 + He \tag{3.30}$$

Therefore, O_2 densities increase with increasing γ_H due to a decreasing H density. The metastable states $O_2(a^1\Delta)$ and $O_2(b^1\Sigma)$ also increase because they are directly produced from O_2 via electron impact excitation.

For the simulations presented in this work, the following assumptions are made regarding wall reactions: Neutral species in the ground state as well as negative ions are not reacting with the wall. Positive ions generally react at the wall with $\gamma = 1$, and return as their

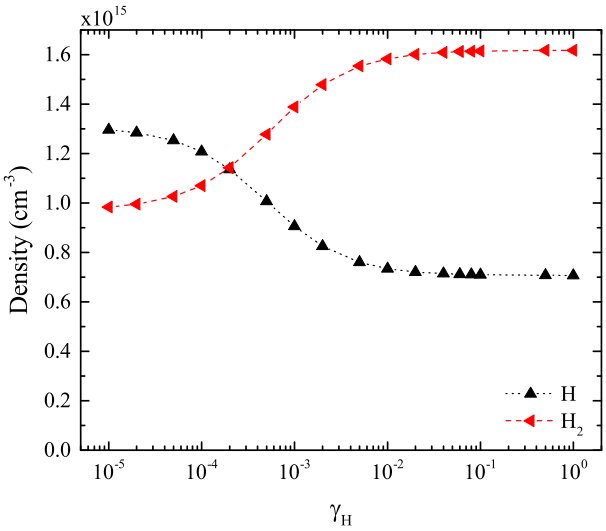

Fig. 3.5: Absolute H and H_2 densities at the end of the channel in the mod-µAPPJ at 2.4 cm as a function of γ_H. Simulation conditions are 5 slm He, 5000 ppm H_2O and 13.6 Wcm^{-3} power density.

Tab. 3.5: Change in species densities when γ_H is changed from 0 to 0.1.

Species	He*	He_2^*	O	$O(^1D)$	$O(^1S)$	O_2	$O_2(a^1\Delta)$
Change in density (%)	0.0	0.1	9.1	13.7	0.8	32.6	21.9
Species	$O_2(b^1\Sigma)$	O_3	H	H_2	OH	HO_2	H_2O_2
Change in density (%)	30.3	159	-46	66	3.0	17.1	7.3

neutral counterpart. For positive ion clusters of size $H^+\cdot(H_2O)n$, the return species are $H + n \times H_2O$. Electronically excited species, such as He or oxygen containing metastables, also react with the wall with $\gamma = 1$, and return as their ground state counterpart. Electrons are lost to the wall with $\gamma = 1$, with a return fraction $f = 0$. Table 3.6 lists all exceptions from these rules. The reader should note that sticking coefficients in table 3.6, where not estimated (indicated as est.) have usually been determined in low pressure systems, which makes their accuracy at atmospheric pressure questionable, particularly in He-H_2O plasmas with a possible wall coverage of the reactor surfaces with H_2O. However, these wall coefficients are adapted from Liu et al. [39] for consistency.

3.3. Pathway analysis

Using a plasma simulation helps in calculating absolute species densities for the simulated conditions, and additionally is a useful tool to investigate the formation of species. In this work, the pathways analysis tool PumpKin [118] is used to undertake this task. PumpKin is described in detail in other work [118], and only the main aspects are discussed here.

PumpKin is a pathway analysis tool based on the algorithm developed by Lehmann [146]. It uses output files from the GlobalKin simulations, including a list of species, *elementary*

Tab. 3.6: Wall sticking coefficients and return fractions for various species considered in this work.

Species	γ	**Return species**	**Reference**
He_2^*	1.00	2 He	est.
O	0.02	0.5 O_2	[39, 144]
$O_2(a^1\Delta)$	0.0004	O_2	[39]
$O_2(b^1\Sigma)$	0.02	O_2	[39, 144]
H	0.03	0.5 H_2	[39, 145]
N	1.00	0.5 N_2	est.
He_2^+	1.00	2 He	est.
O_4^+	1.00	2 O_2	est.
N_4^+	1.00	2 N_2	est.
$O_2^+(H_2O)$	1.00	O_2 + H_2O	est.
$H_2O^+(H_2O)$	1.00	2 H_2O	est.

reactions, and reaction rates at different positions in the channel. Based on these inputs, it calculates effective lifetimes for the different species averaged within an interval in the plasma source that can be defined by the user. In a second step, it builds reaction *pathways* from the elementary reactions, effectively eliminating short lived species, and sorts these pathways by the magnitude of their effective reaction rate. The time scale τ_p that defines if a species is short-lived or not, can be set by the user. Short lived species, whose lifetime is shorter than τ_p, are referred to as *branching point species*.

This is further illustrated with the example of the formation of O_2 in a He-H_2O plasma. The main elementary reaction responsible for the O_2 production under certain conditions is found to be

$$OH + O \rightarrow O_2 + H \tag{3.31}$$

However, it might be of interest to also investigate the formation of OH and O necessary from this reaction step. In order to do this using PumpKin, τ_p is set to value that is larger than the effective lifetime of O and OH. Specifying τ_p like this, O and OH are considered branching point species, and have to be recycled when a pathway is built. The resulting pathway can be written as

$$\begin{aligned} 3 \cdot (e + H_2O &\rightarrow H + OH + e) \\ 2OH &\rightarrow O + H_2O \\ OH + O &\rightarrow O_2 + H \\ 4 \cdot (H &\rightarrow \frac{1}{2} H_2) \\ \hline 2H_2O &\rightarrow 2H_2 + O_2 \end{aligned}$$

It is obvious that the sum of O and OH on the left and right hand sides of the set of elementary reactions is equal, effectively resulting in a zero net production of these species. The same is valid for H, whose effective lifetime is also shorter than τ_{p}. By balancing both sides of the elementary reactions, the net production pathway can be obtained as $2H_2O \rightarrow 2H_2 + O_2$. Additionally to the formation reaction of O_2, formation pathways of OH and O are also revealed, leading back to the initial dissociation of H_2O by electron impact. This of great interest, because it reveals all intermediate steps from the initial H_2O dissociation to the point where O_2 is created from by-products.

4. Reactive oxygen and nitrogen species production in a sealed APPJ containing humidity

As already discussed in chapter 1, atmospheric pressure plasmas are sources for reactive species, which are typically produced by dissociating molecules admixed to the feed gas. Reactive species, particularly reactive oxygen species, have been found to play a key role in many biological functions [26]. In order to make plasmas suitable for applications such as in biomedicine, the quantification of these species is of great importance.

The measurement of reactive species in atmospheric pressure plasmas is often challenging due to additional diagnostic challenges which are not present in low pressure systems. In particular, the small dimensions of the investigated systems makes the use of certain diagnostic techniques, such as electrical probes, which are used in low pressure systems, impossible. Optical diagnostic techniques on the other side are powerful tools, which allow for non-invasive investigations of plasma properties. However, these diagnostic techniques also have limitations, especially at high pressures where excited particle lifetimes are short (typically in the order of ns) due to fast collisional de-excitation (quenching) and the densities of the quenching partners is often unknown. A technique which is independent of collisional quenching is absorption spectroscopy, which has been used previously for the determination of line-of-sight averaged densities of several species in atmospheric pressure plasmas [62]. A common example is OH [40, 44, 47]. However, absorption spectroscopy on ground state atomic species is challenging, since the energy gaps between ground state and excited states of the atoms are large and the required excitation wavelengths typically lie

in the vacuum ultra-violet (VUV) range. Since these wavelengths are strongly absorbed by air, the application of VUV spectroscopy at atmospheric pressure is challenging.

In this chapter, absolute densities of OH, O, NO, and N are investigated experimentally using UV broadband absorption spectroscopy and vacuum ultraviolet high resolution Fourier-transform absorption spectroscopy. These species are of particular interest because of their high reactivity and therefore their prominent role in the chemical kinetics of the plasma. They are also precursors for longer-lived species such as hydrogen peroxide (H_2O_2), which is an important signalling agent in cells [26, 147], and ozone (O_3). In high concentrations both of these species can also have a toxic effect on biological material. Absolute species densities of OH, O, NO and N are measured under different parameter variations such as the humidity, oxygen, and air content in the plasma, or a variation of the power, with the aim to find parameters that can assist to tailor the reactive species production.

The experimental results are compared to those obtained from a 0-dimensional chemical kinetics model, which is also used for the identification of the most important formation mechanisms of the experimentally measured species. Further to this, the formation of other species produces in water containing plasmas is investigated using this model, such as the hydroperoxy radical, O_2 and H_2 molecules, and metastable states of He, O and O_2, which were not investigated experimentally.

4.1. Plasma operation

All experiments in this chapter are performed on the sealed plasma source described in section 2.1.2 (mod-μAPPJ), except the measurements described in section 4.6.2 and section 4.3. In these sections, a previous version of the mod-μAPPJ has been used, with slightly larger dimensions (discharge channel: $0.1 \times 1.1 \times 3$ cm instead of $0.1 \times 0.86 \times 2.4$ cm in the mod-μAPPJ), but with a similar surface-to-volume ratio. The source has been described in [66].

The mod-μAPPJ has been specifically designed to operate inside a vacuum chamber, while retaining atmospheric pressure inside the source, thus facilitating VUV spectroscopy. During all measurements, a fixed frequency matching network and a high voltage probe are used in order to monitor the applied voltage across the gap. Typically, the generator power is set so that the voltage measured by the voltage probe reads 510 V_{pp} in pure He at the start of the measurement. At higher voltages, the plasma tends to extend around the powered electrode when run in pure He, and a small bright discharge starts to form at one of the electrode corners, which could potentially damage the source. For a parameter sweep, such as a variation of the molecular content in the plasma, the generator power is then kept constant. An increase of the molecular admixture sometimes lead to an increase of the observed voltage, which was not more than 10% for most measurements. The power coupling is very likely dependent on the combination of power supply and matching box used, as well as the power deposition in cables and electronic connections. Because several

different combinations of power supplies and matching boxes were used for measurements described in this chapter, the measured voltage was always recorded as a more reliable parameter. The cable length was kept at 50 cm and numbers of connectors between voltage probe and plasma was kept constant to minimise the effect of a variation of deposited power in the plasma external electrical circuit. It will be shown in section 4.7 and sections 4.9.2 and 6.2.2, that the change of most investigated species densities is generally low under a variation of power.

For the measurements of atomic oxygen using VUV Fourier-transform absorption spectroscopy (VUV-FTAS), the source was enclosed in a vacuum vessel with restricted optical access, where visual identification of the transition of the source into the arc mode was not possible. In these cases, measurements were carried out at a lower voltage of 470 V_{pp} to ensure the "arc" mode was not reached to avoid damage to the source. For some measurements in this chapter, a higher voltage is chosen deliberately to increase the signal-to-noise ratio of the measurements.

4.2. Plasma Power

A large part of this chapter will be on the production of reactive species from deliberately admixed humidity in the feed gas. It is therefore of great interest, how a change in humidity content affects the power that is coupled in to the plasma under a variation of the humidity content. The measured powers are later used as an input for the GlobalKin simulations.

The actual rf-power deposited in the plasma P_{net} is calculated for different H_2O admixtures and fixed generator power as described in section 3.2.3, by subtracting the measured power in the plasma off case from the plasma on case. The results are shown in fig. 4.1 (a). It is found that by varying the H_2O content while keeping the generator power constant, a peak in P_{net} is reached at a certain H_2O admixture, the value of which depends on the generator power. These results are shown in fig. 4.1 (b). The variation of P_{net} with H_2O content is generally less than 15%, and close to the statistical error associated with the measurement. Therefore, when the densities of O and OH are investigated numerically (section 4.6), average model input powers are chosen as 2.11 W and 2.76 W, respectively, as indicated in fig. 4.1 (b) by grey lines.

4.3. Plasma emission

To get a first idea of species produced in the plasma, it is often helpful to look at the optical plasma emission. Here, a spectrometer (HR4000CG-UV-NIR, Ocean Optics) is used to measure the plasma emission at different positions in the jet. The calibrated spectral range of the spectrometer is 300 - 1050 nm.

Figure 4.2 (a) shows a typical emission spectrum in a He plasma containing 4750 ppm water. The measurement is calibrated to obtained the irradiance, and then normalised

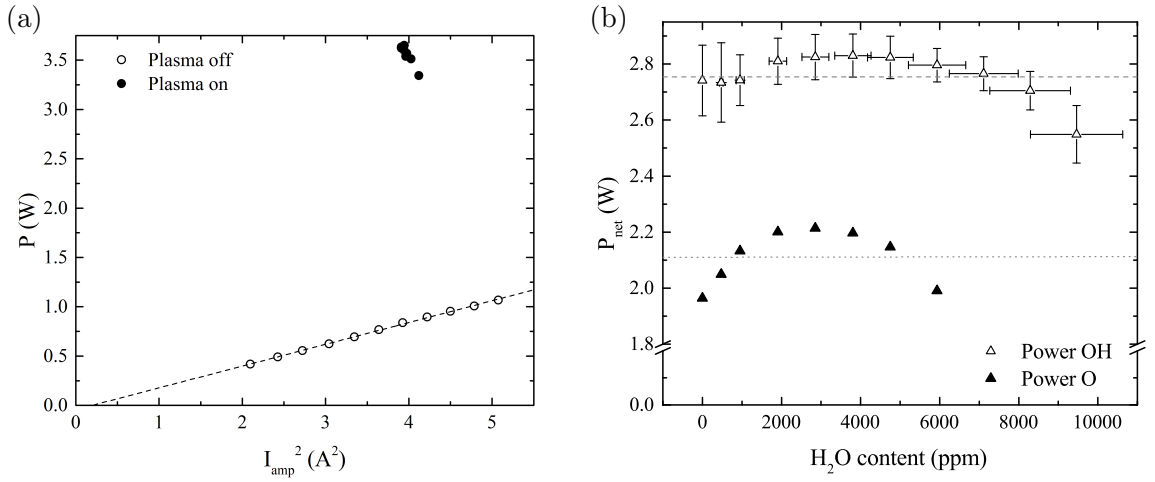

Fig. 4.1: (a) Measured powers with (black circles) and without active plasma (white circles) as a function of I^2. It can be seen that the power with plasma off is dependent on the current amplitude squared. (b) Powers for two different operating voltages. White triangles are measured for the voltage used for OH absorption measurements (around 510 V_{pp}), while the O VUV-FTAS was conducted at slightly lower voltages (around 480 V_{pp}, black triangles).

to the emission of He atoms at 706 nm ($3s\ ^3S_1 \rightarrow 2p\ ^3P_{J=1,2,3}$). The strongest emission comes from OH molecules resulting from rotational emission bands around 306 nm, followed by optical emission lines of H at 656 nm, which will be discussed in more detail later in chapter 5 and are listed in table 5.1, and the He emission lines at 706 nm. Weaker emission intensities for He and H are observed at other wavelengths, as well as from O, at 777 nm ($3p\ ^5P_{J=3,2,1} \rightarrow 3s\ ^5S_2$) and 844 nm ($3p\ ^3P_{J=0,2,1} \rightarrow 3s\ ^3S_1$), respectively. Therefore, the most prominent species emitting in the visible spectral range are excited states of He, OH, H, and O.

The measured line intensity ratios with respect to the He 706 nm emission line yield a first indication of the variation of the other species densities as a function of distance along the plasma channel. This approach assumes that the electron energy distribution function stays constant over the discharge gap, and that the densities of the emitting states of H and O are directly proportional to the grounds state densities. The first point is probably a valid assumption, since a stable electron temperature and density is reached quickly in the GlobalKin simulations. The second point is more difficult to address, since the excited states of H and O are not necessarily only produced via direct electron impact excitation from the ground state, but also via dissociative processes from water, O_2 and H_2 [148–150]. Although the two latter species are not directly added to the gas flow, it will be later shown using simulations (section 4.6.4) that there is a continuous build-up of the molecular oxygen and hydrogen densities, that can exceed the corresponding atomic densities. Therefore, it is important to keep in mind that the plasma emission is not necessarily only dependent on the ground state atomic densities.

Figure 4.2 (b) and (c) show the spectrally integrated H 656 nm, O 777 nm and O 844 nm relative emission intensities, normalised to the He 706 nm emission, as a function of po-

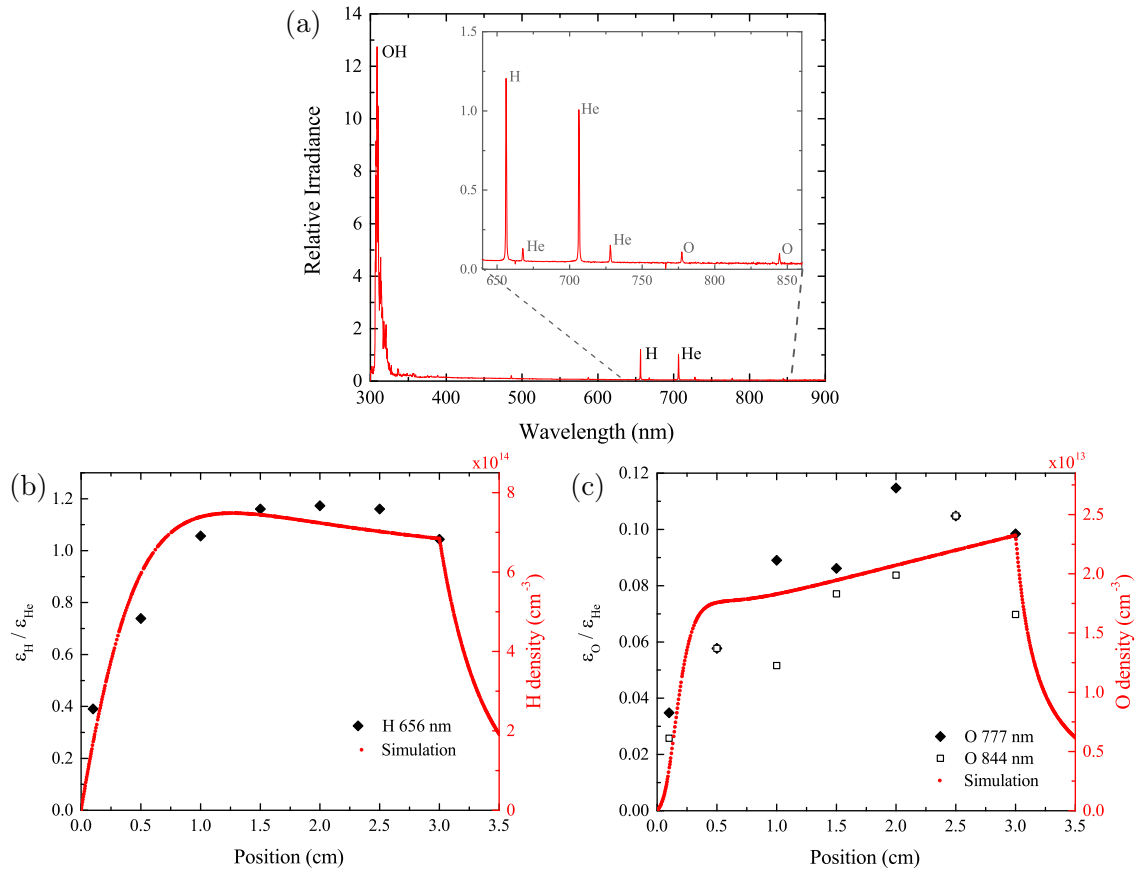

Fig. 4.2: (a) Optical emission spectrum from the centre of the discharge. Plasma parameters are 530 V_{pp} and 4750 ppm H_2O in 5 slm total He flow. (b) Measured under the same plasma conditions: The ratio of the H 656 nm line emission versus He 706 nm line emission as a function of the axial position in the jet. Also shown is the simulated absolute H atom density dependence for a plasma power density of 13.6 Wcm^{-3} and the same H_2O content as in the experiment. (c) same representation as (b) for measured O 777 nm (black diamonds) and O 844 nm (white diamonds) line emission versus He 706 nm line emission, as well as simulated absolute O density density trend.

sition in the plasma. The H 656 nm emission is increasing as the gas travels through the channel, and is approaching a steady-state value towards the end of the channel. The slight decrease in the H emission at the very end can be explained by the spatial resolution of the measurement, which is a few millimetres, and that this point was possibly partially taken in the effluent of the jet, where no electrons are present to excite hydrogen atoms and therefore the emission decreases rapidly to zero. The experimental trend matches roughly the simulated H densities in the channel, which are also shown in fig. 4.2 (b). Simulation and experiments are normalised to the experimental value taken at the end of the channel at $x = 3$ cm.

For atomic oxygen, as shown in fig. 4.2 (c), the experimental data is very scattered due to the low signal from the O 777 nm and O 844 nm emission lines. Therefore, it is difficult to say how well experimental data and simulation match, although a continuous

increase of O and its emission can be observed in both experiment and simulation for almost all investigated points, showing that the plasma does not reach a steady-state operation within the length of the channel. However, in order to compare the trends of both plasma emission and simulated densities fully, the number of atoms in the emitting states produced via dissociative excitation from molecules has to be fully quantified, which is not done in this work.

4.4. Vacuum ultra-violet high resolution Fourier-transform absorption spectroscopy

Absolute line-integrated O and N densities are measured by VUV-FTAS, using synchrotron radiation at the DESIRS beamline at the synchrotron SOLEIL [114], which features an ultra-high resolution spectrometer [151]. The atomic oxygen transition O($2p^4$ $^3P_{J=2,1,0}$ →3s $^3S_1$) and atomic nitrogen transition N($2p^3$ $^4S_{3/2}$ →3s $^4P_{J=\frac{1}{2},\frac{3}{2},\frac{5}{2}}$) for atomic nitrogen are investigated in this work.

The measurement and analysis procedure is described in detail in reference [66]. The spectrometer yields a transmission spectrum S_T, which is a convolution of the plasma transmission T and the instrumental "sinc" function $\Phi(\lambda') = \frac{sin(\pi(\lambda'-\lambda))}{\pi(\lambda'-\lambda)}$ of the spectrometer

$$S_T(\lambda') = S_0(\lambda')[\Phi(\lambda' - \lambda) * T(\lambda)] \tag{4.1}$$

The transmission (T) through the plasma is described by Beer-Lambert's law

$$T(\lambda) = \exp(-A(\lambda)) = \exp(-\alpha(\lambda) \cdot l) = \exp(-\sigma(\lambda) \cdot l \cdot n), \tag{4.2}$$

where λ is the wavelength of the transition, n the line-averaged species density, α the absorption coefficient, l the absorption length, and $\sigma(\lambda)$ the absorption cross section, including the spectral line "Voigt" profile, which takes into account the Doppler and pressure broadening of the spectral line, the statistical weights g_J for the different states and the transition probabilities (see Niemi et al. [66] for more details).

A typical transmission spectrum for O is presented in fig. 4.3. Due to the fine structure of the ground state, three transitions from the resulting ground state sub-levels to the higher excited state are observed in atomic oxygen. To obtain absolute ground state densities, first the sub-level ground state densities for $J = 2, 1, 0$ are obtained from the three transmission lines. If the transmission lines are strong enough without entering an optically thick regime, the total ground state density can be obtained by summing up the densities from the three ground sub-levels.

In this work, a slightly different approach is chosen. Where possible, three values for the absolute ground state density are obtained by evaluating the transition from each sub-level,

and applying a Boltzmann factor to obtain the total ground state density $\sum_J n_J$

$$\frac{n_J}{\sum_J n_J} = \frac{g_J \exp\left(-E_j/k_B T_g\right)}{\sum_J g_J \exp\left(-E_j/k_B T_g\right)} \tag{4.3}$$

where E_j is the energy of the state, k_B is the Boltzmann constant, and T_g is the gas temperature. The three values for the absolute ground state density are then averaged, and the standard deviation is used as the uncertainty of the measurement.

For O densities obtained from admixing H_2O to the feed gas, transmission signals are generally weak, and only the $J = 2$ state can be evaluated, which has the lowest energy of the three sub-levels. It is therefore populated highest, resulting in the highest absorption signal, as shown in fig. 4.3. To obtain the total ground state density in the case of a H_2O containing plasma, the Boltzmann factor eq. (4.3) has to be applied. In general, when absolute densities of ground state atomic oxygen are discussed in this work (obtained both in experiment and simulation), the abbreviation "O" is used for the sum of densities in all ground-state sub-levels of atomic oxygen $O(2p^4\ ^3P)$.

The gas temperature is set to 315 K as determined by thermocouple measurements in the plasma effluent region of the μAPPJ [30] at a similar voltage. Although the μAPPJ is a different source, it has similar critical dimensions as the source used in these investigations. It is therefore assumed that the gas temperature is comparable for the same power density. Gas temperatures could not be measured directly in the mod-μAPPJ because the gas region is not accessible with a thermocouple.

In the case of atomic nitrogen, the absolute ground state N density can be obtained from each of the three transmission lines from the unsplit ground state to the sub-levels $J = \frac{1}{2}, \frac{3}{2}, \frac{5}{2}$ of the upper 3s state. The values presented in this work are the mean values obtained from the three transitions and their standard deviation is shown as an error bar.

Since the measurements of atomic oxygen presented in this section take place in the optical VUV range using radiation from a synchrotron, the plasma source has to be placed in a vacuum vessel. Absorption measurements were then carried halfway along the discharge channel, as indicated in fig. 2.2.

Photodissociation of H_2O

H_2O is dissociated by electron-impact only, or also through photolysis by the energetic radiation of the synchrotron beam itself. If the two rates were in a comparable order of magnitude, it would not be distinguishable if the measured atomic N and O densities would be produced in the plasma itself or because of the VUV beam, and absolute densities would be over-estimated. The dissociation rates by electron impact and photo-dissociation are therefore calculated and compared for the specific conditions of 5000 ppm water content.

The corresponding electron impact dissociation rate is calculated using an electron density $n_e = 3.7 \times 10^{10}$ cm^{-3} and the electron impact dissociation rate coefficient $k^e_{H_2O} = 3 \times 10^{-10}$ cm^{3}s^{-1} (for an electron temperature of 2.7 eV). Both of these values are taken from GlobalKin simulations for this particular H_2O content. The resulting electron impact

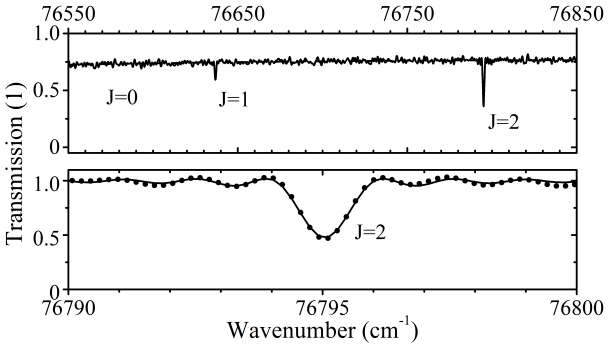

Fig. 4.3: Example spectrum for the measured transition $O(2p^4\ ^3P_J) \rightarrow O(3s\ ^3S_1)$ using VUV-FTAS: Broad spectral range (top) and zoom into the $O(2p^4\ ^3P_2) \rightarrow O(3s\ ^3S_1)$ transition, which was used for the measurements presented in this work. The spectrum was taken with 4.6 slm dry He and 0.4 slm humidified He. The density obtained from this spectrum is 2.7×10^{13} cm^{-3}.

dissociation rates is

$$R^{\mathrm{e}}_{\mathrm{H_2O}} = k^{\mathrm{e}}_{\mathrm{H_2O}}\, n_{\mathrm{H_2O}}\, n_{\mathrm{e}} = 1.2 \times 10^{18}\ \mathrm{cm^{-3}s^{-1}} \tag{4.4}$$

To compare the value for the electron impact dissociation rate with the photo dissociation rate $R^{\mathrm{ph}}_{\mathrm{H_2O}}$, one needs the absorption cross section of water $\sigma_{\mathrm{H_2O}}$, the spectral photon flux F_{ph}, the quantum yield $\phi = \frac{\#\text{ of dissociated molecules}}{\#\text{ of absorbed photons}}$, and the area of the beam A.

$$R^{\mathrm{ph}}_{\mathrm{H_2O}} = k^{\mathrm{ph}}_{\mathrm{H_2O}}\ n_{\mathrm{H_2O}} = \int \left(\frac{F_{\mathrm{ph}}(\lambda)}{A}\ \phi(\lambda)\ \sigma_{\mathrm{H_2O}}\ (\lambda)\ d\lambda \right)\ n_{\mathrm{H_2O}} \tag{4.5}$$

The size of the synchrotron beam is $A = (0.2 \times 0.4)$ cm^2, with a spectrally integrated photon flux of about 4×10^{15} ph/s at 130 nm.

An upper limit of the photolysis rate is calculated by taking an over-estimated value of 1×10^{-17} cm^2 for the absorption cross section $\sigma_{\mathrm{H_2O}}$ [152, 153] at 130 nm, and assuming full photo-dissociation yield $\phi = 1$. The result amounts to:

$$R^{\mathrm{ph}}_{\mathrm{H_2O}} = \frac{F_{\mathrm{ph}}}{A}\ \phi\ \sigma_{\mathrm{H_2O}}\ \ n_{\mathrm{H_2O}} \tag{4.6}$$

$$= 5.5 \times 10^{16}\ \mathrm{cm^{-3}s^{-1}} \tag{4.7}$$

It is therefore concluded that dissociation of H_2O molecules via photolysis is small compared to electron impact dissociation under our experimental conditions.

4.5. Ultra-violet broadband absorption spectroscopy

In addition to the quantification of atomic oxygen using VUV-FTAS, absolute ground state densities of ($OH(X\ ^2\Pi_i, v' = 0)$) are determined in the mod-µAPPJ using UV broadband absorption spectroscopy (UV-BBAS). The setup is presented in fig. 4.4 (a). Light

from an ultra-stable broad-band plasma lamp (Energetiq EQ-99) is guided through the centre of the plasma channel and focused on the entrance slit of a 0.32 m spectrograph (Isoplane SCT320) with a 2400 mm^{-1} grating. Spectra are recorded using a photodiode array detector (Hamamatsu S-3904). In order to calculate the absorbance in eq. (4.2), four signals are required: Plasma on and light source on ($I_{P,L}$), Plasma on only (I_P), light source on only (I_L) and a background with both plasma and light source off (I_0). Each signal is integrated over 50 ms, after a stabilisation time of 4 s beforehand. A schematic of the experimental setup and an illustration of the triggering/timing scheme is presented in fig. 4.4 (a) and (b), respectively. An example spectrum of the OH absorbance is shown in fig. 4.5. More detailed descriptions of the UV-BBAS setup including all components and the measurement procedure are given elsewhere [154]. Additionally, the light was focused into the plasma using two additional parabolic mirrors, allowing for a better signal-to-noise ratio. For the spectrograph, a slit width of 50 µm was chosen, allowing for a spectral resolution of about 56 pm.

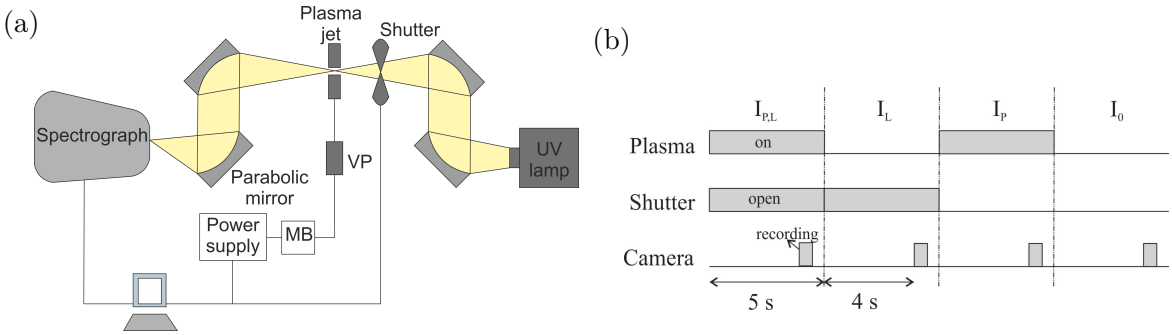

Fig. 4.4: (a) Setup used for the UV-BBAS measurements of OH. (b) Time scales for the UV-BBAS absorption measurements.

For comparative measurements, and also to widen the measurement regime, measurements are repeated using a similar in-house UV-BBAS setup, incorporates a UV LED (UVTOP-305-FW-TO18, Roithner Lasertechnik GmbH) as light source, a 0.5 m spectrograph (Andor SR-500i), and a CCD camera (Andor Newton 940) as detector. The measurement procedure is as described before, but with a longer exposure time due to the lower detection limit of this setup, which will be discussed at the end of the next section.

OH density evaluation

Measured OH rotational absorbance spectra of the transition OH(X $^2\Pi_i$,$\upsilon' = 0$) $\rightarrow$ OH(A $^2\Sigma^+$,$\upsilon'' = 0$) are fitted by a simulation in order to obtain absolute OH(X $^2\Pi_i$,$\upsilon' = 0$) densities. Under the experimental conditions at relatively low gas temperatures (typically 300 - 350 K), excitation into vibrational states is driven by electron impact. Additionally, due to the high pressure, quenching of vibrational states is high. Therefore, it is assumed that the population of highly vibrationally excited states OH(X $^2\Pi_i$,υ') is low [40], and that densities of OH(X $^2\Pi_i$,$\upsilon' = 0$) are equal to the total ground state densities of OH(X).

Generally, the notation for different states in molecules are described by

$$^{2S+1}\Lambda_{\Omega} \tag{4.8}$$

where S is the electron spin, Λ the projection of the orbital angular momentum onto the internuclear axis, and Ω the projection of the total angular momentum onto the internuclear axis.

The programme used for the fitting of OH spectra is based on the theory described by Dieke and Crosswhite [155]. In a first step, rotational energy levels for the Π ground state (rotational energies are denoted as f) and the upper Σ state (rotational energies are denoted as F) are calculated on the basis of known molecular constants describing the quantum mechanics and angular momentum coupling of the involved states. While the Σ state with a projection of the electronic orbital momentum $\Lambda = 0$ onto the internuclear axis and an electronic spin $S = \frac{1}{2}$ is a typical Hund's case (b), the lower Π state with $\Lambda = 1 \neq 0$ represents a transition from Hund's case (a) to (b). For both states, the rotational energy levels can be calculated as function of the angular momentum $N = J \pm S$, where J is the total angular momentum, and S is the electron spin, using several diatomic constants for OH. For each J, two energy states exist due to $S = \frac{1}{2} \neq 0$, which are $J = N \pm \frac{1}{2}$. Energy states are typically denoted by f_1 for $J = N + \frac{1}{2}$ and f_2 for $J = N - \frac{1}{2}$ for the lower states, and F_1 and F_2 for the higher states accordingly.

In a second step, relative intensities are calculated for 12 possible branches according to the selection rules for the quantum numbers J and N, using expressions derived by Earls [156]. An experimental value for the radiative lifetime of the $F_1(N' = 0, J' = 0.5)$ state of OH has been determined as 0.688 µs [157]. Therefore, calculated relative Einstein coefficients using the in-house simulation are normalised to this value. The resulting Einstein coefficients for other transitions are in good agreement with literature values [158].

Similar to work by Dilecce et al [47], the simulation also takes into account the instrumental function, which leads to a broadening of the measured spectra. The instrumental broadening is dependent on the spectral resolution of the spectrometer, which again depends on different parameters such as the pixel size of the detector array, the optical grid and the slit width at the entrance of the spectrograph. In the simulation, the spectrometer function is implemented as a a convolution of the theoretical molecular emission spectrum with a Gaussian instrumental function.

An example for a measured and simulated absorbance spectrum can be found in fig. 4.5 (black dots and blue dashed line).

In order to prove the working principle of the automated fitting simulation, the software PGOPHER [159] is used. PGOPHER is a programme to simulate rotational, vibrational and electronic spectra, and also calculates absorption coefficients using vibrational and rotational constants for the specific species.

Constants of diatomic molecules from the NIST Chemistry WebBook [160] are used to calculate the input parameters for the PGOPHER simulations. These input parameters are in particular the origin of the band E, the rotational constant B, the spin-orbit coupling

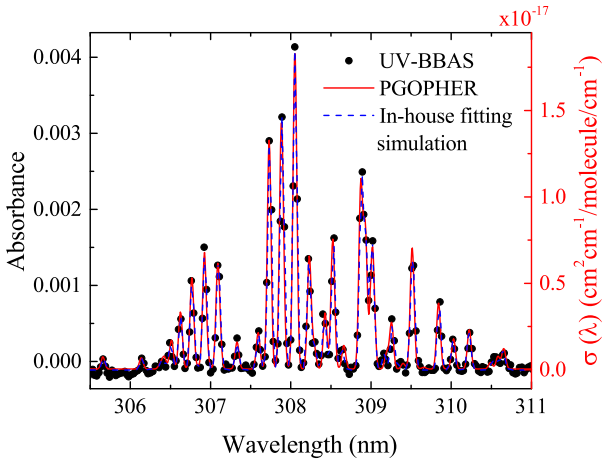

Fig. 4.5: Example spectrum for the measured (black dots) using UV-BBAS and fitted rotational bands for OH(X $^2\Pi_i$,$v' = 0$) $\rightarrow$ OH(A $^2\Sigma^+$,$v'' = 0$), for a He flow of 5 slm and a humidity content of (4460 $\pm$ 600) ppm H_2O. The blue line is the absorbance fitted with the in-house simulation. The red line is the absorbance calculated using PGOPHER (at 315 K and Gaussian instrumental function with 56 pm width). For this simulation also the cross section $\sigma(\lambda)$ is shown on the right hand side axis. Calculated OH(X $^2\Pi_i$,$v' = 0$) density obtained from this spectrum is 2.6×10^{14} cm^{-3}.

constant (A), the spin rotation coupling constant (γ_s), the Lambda doubling constants (p and q), and the centrifugal distortion constants (D and H), which are listed in table 4.1. E, B, and D are calculated using the following expressions

$$E_v = T_e + \omega_e(v + \frac{1}{2}) - \omega_e x_e(v + \frac{1}{2})^2 \tag{4.9}$$

$$B_v = B_e - \alpha_e(v + \frac{1}{2}) + \gamma_e(v + \frac{1}{2})^2 \tag{4.10}$$

$$D_{v',X} = D_e - 0.43 \times 10^{-4}(v' + \frac{1}{2}) + 0.024 \times 10^{-4}(v' + \frac{1}{2})^2 \tag{4.11}$$

$$D_{v''=0,A} = 0.0024, \quad D_{v''=1,A} = 0.0021, \quad D_{v''=2,A} = 0.0013, \quad D_{v''=3,A} = 0.0018 \text{ [161]} \tag{4.12}$$

where T_e is the minimum electronic energy, the terms including ω_e are the different terms of the vibrational constant, B_e is the equilibrium rotational constant, α_e the first term of the rotational constant, γ_e the rotation-vibration interaction constant, and D_e is the centrifugal distortion constant. All of these constants have the unit (cm^{-1}) and are available from the NIST Chemistry Webbook [160].

Absolute species densities were calculated as following: After setting up PGOPHER with the respective constants, Einstein coefficients A_{ik} are calculated. A_{ik} from the simulation for the particular transition P11(J"=2.5) (or $P_1(2)$), which is well isolated and relatively strong, was normalised to the literature value of $A = 5.777 \times 10^5$ s^{-1} [158] by adjusting the "Strength" parameter in the simulation, which is a measure for the dipole transition moment. As done previously for the in-house fitting simulation, the lifetime of

Tab. 4.1: Input parameters for the PGOPHER simulations. The constants are the state origin (E), the rotational constant (B), the spin-orbit coupling constant (A), the spin rotation coupling constant (γ_s), the Lambda doubling constants (p and q), and the centrifugal distortion constants (D and H). E, B, A and D are calculated using eqs. (4.9) to (4.12) and constants from the NIST chemistry Webbook, while γ_s, p, q, and H are taken directly from the NIST chemistry Webbook [160].

Species	E	B	A	γ_s	p	q	D	H
$OH(X^2\Pi_i, v' = 0)$	1847.726	18.55	-139.21	0	0.235	-0.0391	0.001917	1.47×10^{-7}
$OH(A^2\Sigma^+, v'' = 0)$	34250.07	16.96	0	0.201	0	0	0.00204	8.7×10^{-8}

the state $F_1(N' = 0, J' = 0.5)$ was compared to the experimental determined OH lifetime of 0.688 µs [157] and found to be in good agreement. Einstein coefficients for some other transitions were cross-checked and also found to be in good agreement. The simulation is then used to calculate the cross sections $\sigma(\lambda)$ from these Einstein coefficients, which is proportional to the absorbance, as shown in eq. (4.2).

Figure 4.5 shows OH absorbance spectra simulated using PGOPHER (red line), for the same density 2.64×10^{14} cm^{-3} as obtained previously using the in-house simulation. The absorbance spectra is manually fitted in this case, using a gas temperature of 315 K and an instrumental Gaussian width of 56 pm. $\sigma(\lambda)$ calculated with PGOPHER are shown on the right hand side axis. It can be seen that both simulated absorbance spectra (using the in-house simulation and PGOPHER) agree very well, which provides a validation of the working principle of the in-house fitting model.

A typical statistical error for the measurement of OH densities is obtained to be 7%. The systematic error of OH densities can be obtained by differentiation of

$$n = \frac{A(\lambda)}{\sigma(\lambda) l} \tag{4.13}$$

The uncertainty in the calculation of $\sigma(\lambda)$ is estimated as 10%. The uncertainty related to the absorption length l is neglected. For the UV-BBAS II setup (LED), the noise level is relatively high and can reach 3×10^{-4} in the measured absorbance A, leading to a peak uncertainty in absolute densities of 3.6×10^{-13} cm^{-3}. This value is therefore taken as the detection limit for the UV-BBAS II setup. For the UV-BBAS I setup (ultra-stable broad band light source), the noise level is very low (typically an order of magnitude lower than for the UV-BBAS II setup), and is therefore neglected in the error calculation. Absolute densities shown in figures are the sum of the statistical and systematic errors.

4.6. Reactive species densities under a variation of the humidity content

In this section, the extent to which the production of reactive species can be tailored by changing the gas composition, particularly the H_2O content in the feed gas, will be investigated using a combination of GlobalKin simulations and experimental measurements.

4.6.1. Destruction pathways for H_2O

The first step in the creation of reactive oxygen and hydrogen species is the dissociation of H_2O molecules. Therefore, the consumption pathways for H_2O are investigated using GlobalKin together with PumpKin for different humidity contents. For the PumpKin simulations, it is chosen not to build complex reaction pathways, but to have a look at the most fundamental reaction mechanisms. The number of branching point species, whose function has been described in section 3.3, is therefore set to 0.

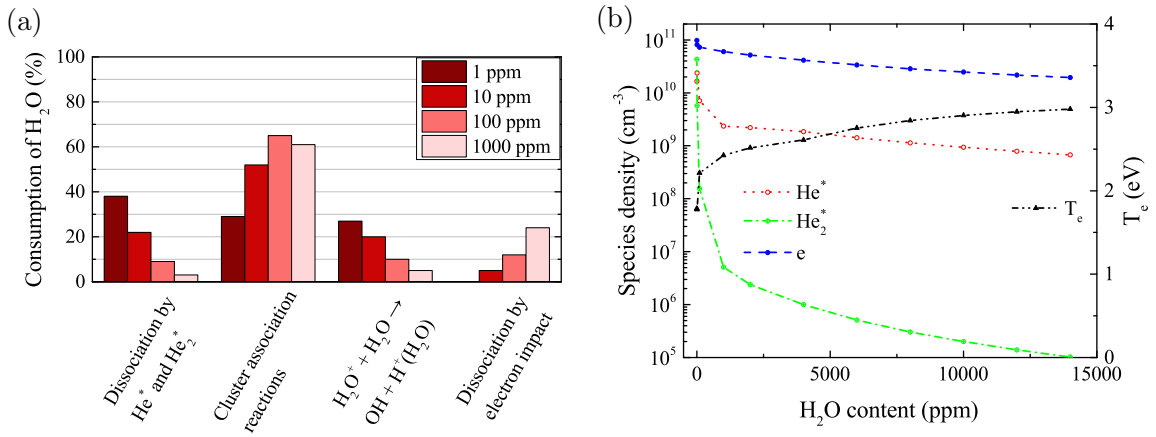

Fig. 4.6: (a) Consumption pathways for H_2O at different humidity contents in the feed gas. Simulations are carried out at a power density of 13.6 Wcm^{-3} and 5 slm total He flow. (b) Simulated densities of He^*, He_2^*, and electrons (coloured lines) dependent on the humidity content. The simulated electron temperature is also shown (black line).

Using PumpKin, three major pathways can be identified for the destruction of water molecules, which are shown in fig. 4.6 (a). The first pathway is the dissociation and ionisation of H_2O molecules by collisions with He metastables. The main mechanisms here are

$$He^* + H_2O \rightarrow He + H_2O^+ + e \tag{4.14}$$

$$He_2^* + H_2O \rightarrow 2He + H_2O^+ + e \tag{4.15}$$

$$He^* + H_2O \rightarrow He + OH^+ + H + e \tag{4.16}$$

These reactions are important particularly at lower H_2O contents in the feed gas, where densities of He metastables are highest. The He metastable densities as a function of the water content of the feed gas are shown in fig. 4.6 (b). Towards higher water admixtures, a rapid decay of He metastables, particularly He_2^*, which decreases by several orders of magnitude, can be observed. He_2^* is produced by the three-body association reaction

$$He^* + 2He \rightarrow He_2^* + He \tag{4.17}$$

and mainly destroyed by collisions with water molecules (eq. (4.15)).

Therefore, the decrease of He_2^* with increasing humidity content can be explained both by the decreasing amount of He^* and the increasing amount of water molecules. The decrease of He^* can be similarly explained by collisions with an increasing amount of available water molecules (eqs. (4.14) and (4.16)). However, the rate for the He^* production increases with increasing humidity content

$$e + He \rightarrow He^* + e \tag{4.18}$$

probably due to the increasing electron temperature, as shown in fig. 4.6 (b). Therefore, the drop in He^* densities is not as pronounced as in the case of He_2^*.

Another important consumption mechanism for H_2O is the formation of high-order protonated water clusters

$$H^+ \cdot (H_2O)_n + H_2O + He \rightarrow H^+ \cdot (H_2O)_{n+1} + He \tag{4.19}$$

Especially at high H_2O content, this becomes the dominant loss mechanism for H_2O. Clusters become higher order with higher water content, as has been observed previously in other work [39, 49, 50]. Figure 4.7 shows simulated water cluster densities as a function of H_2O content. Smaller clusters with size $n \leq 4$ decrease with increasing humidity, while larger clusters $n \geq 6$ increase in density. This trend has also been observed in experimental measurements of water clusters in a similar plane-to-plane geometry in a He-H_2O plasma, obtained using mass spectrometry [49]. Trends shown in the experiments from reference [49] and simulations from this work show good agreement, particularly for higher mass clusters the trend agrees very well, taking into account the high uncertainty in the cluster formation reaction rates, and the fact that the plasma source used in reference [49] differs from the source used in this work.

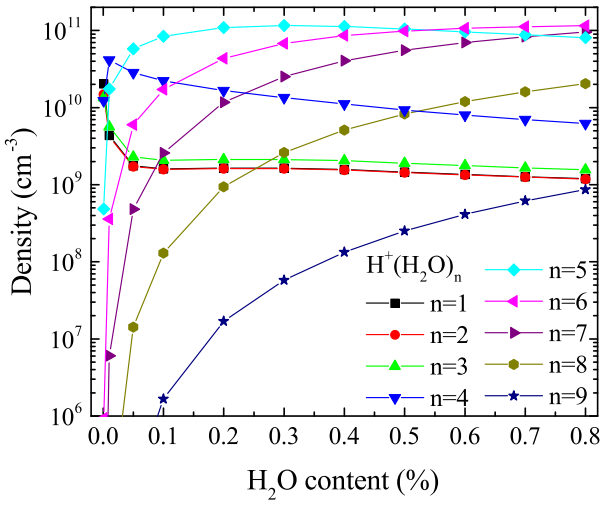

Fig. 4.7: Simulated densities of positive water clusters from n=1 to n=9 as a function of the humidity content of the feed gas.

A first step for the creation of higher order water clusters is the reaction

$$H_2O^+ + H_2O \rightarrow OH + H^+ \cdot (H_2O) \tag{4.20}$$

which is an additional loss mechanism for H_2O molecules, particularly at lower water contents. Finally, water is also consumed by electron impact dissociation reactions

$$e + H_2O \rightarrow OH + H + e \tag{4.21}$$

$$\rightarrow OH + H^- \tag{4.22}$$

This consumption mechanism becomes more important at higher water contents because of the increasing electron temperature, as shown in fig. 4.6 (b).

4.6.2. Hydroxyl radicals

Figure 4.8[1] shows the spatial development of the OH density in the 3 cm long plasma channel for a humidity content of 5400 ppm and a plasma power density of 17.5 Wcm^{-3}. The experimental measurements show a fast increase of the OH density within the first 2 mm of the channel, after which the density remains approximately constant between 3.5 and 4.0×10^{14} cm^3 until the end of the channel. A small increase of the densities can be observed, but this is within the error bar of the measurement. Experimental and modelling results agree very well both in trend and absolute densities within the estimated uncertainties of the experiment. In order to asses the uncertainties arising from the simulation, a full sensitivity analysis has to be carried out, which takes into account all the uncertainties associated with the reaction rate coefficients used. This has for example been done by Turner [103] for a He-O_2 plasma, who found that for several species produced in this plasma and under certain conditions, simulated species densities could vary within a factor up to ten. Although a sensitivity analysis is not carried out in this work, it would certainly be a valuable task for future work to assess the uncertainty associated with the modelling results.

A pathway analysis is performed in the three regions of interest highlighted in fig. 4.8 using PumpKin. These regions correspond to a fast formation of OH at the start of the plasma channel (0 - 0.2 cm), a steady-state region (2 - 2.5 cm) and the decay of OH in the plasma effluent (3.3 - 3.5 cm). The dominant reaction and consumption pathways for OH are shown in fig. 4.9. τ_P, the timescale of interest for the PumpKin simulations (see section 3.3 for more detail), is chosen such that all species with a lifetime shorter than He^* are considered branching point species.

At the start of the discharge channel (0 - 0.2 cm), the gas mainly consists of the initial gas mixture plus some rapidly forming species such as ions and electrons. Therefore, the main production channel for OH is through electron impact with the added water vapor,

[1] Experimental data in fig. 4.8 was taken and evaluated by Helen Davies

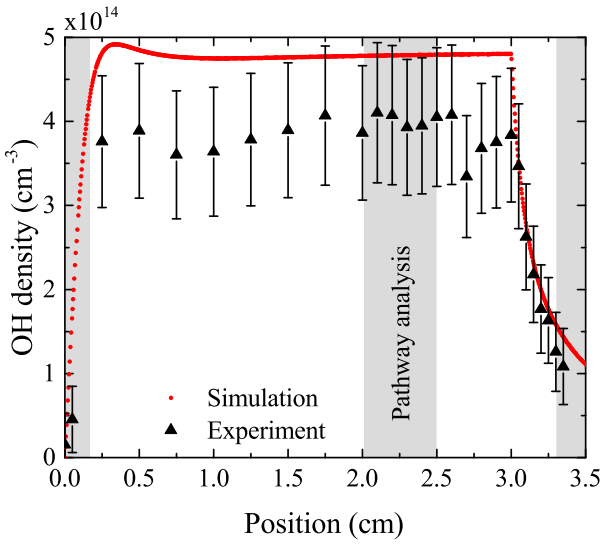

Fig. 4.8: Absolute densities of OH as a function of the position in the discharge channel, where 0 cm corresponds to the beginning and 3 cm to the end of the channel. Experimental results (black triangles) are taken at 17.5 $\mathrm{Wcm^{-3}}$ plasma power density and 5400 ppm humidity. Simulation results (red dots) are calculated for the same power. Grey areas indicate locations for the PumpKin pathway analysis.

forming either OH and H (dissociation) or OH and H^- (dissociative attachment):

$$e + H_2O \rightarrow OH + H + e \qquad (67\%) \tag{4.23}$$

$$\begin{aligned} e + H_2O &\rightarrow OH + H^- \\ H^- + H_2O &\rightarrow OH^- + H_2 + e \end{aligned} \qquad (11\%) \tag{4.24}$$

$$\begin{aligned} e + H_2O &\rightarrow OH + H^- \\ H^- + He &\rightarrow H + He + e \end{aligned} \qquad (3\%) \tag{4.25}$$

Note that the last two pathways are calculated separately by PumpKin, although the formation pathway for OH is the same. This is because H^- is a branching point species, and therefore has to be effectively consumed, which happens either by a dissociative process involving water molecules (eq. (4.24)), or by electron detachment via collisions with He (eq. (4.25)).

Another relevant production mechanism is through the destruction of charged water clusters, as was previously discussed by Ding and Lieberman [57]. The formation of these clusters is generally a multistep process. For positive clusters, this process usually begins through direct ionisation of H_2O either through electron impact or Penning ionisation with He^*. These water ions then collide with water molecules and form $H^+(H_2O)$, which

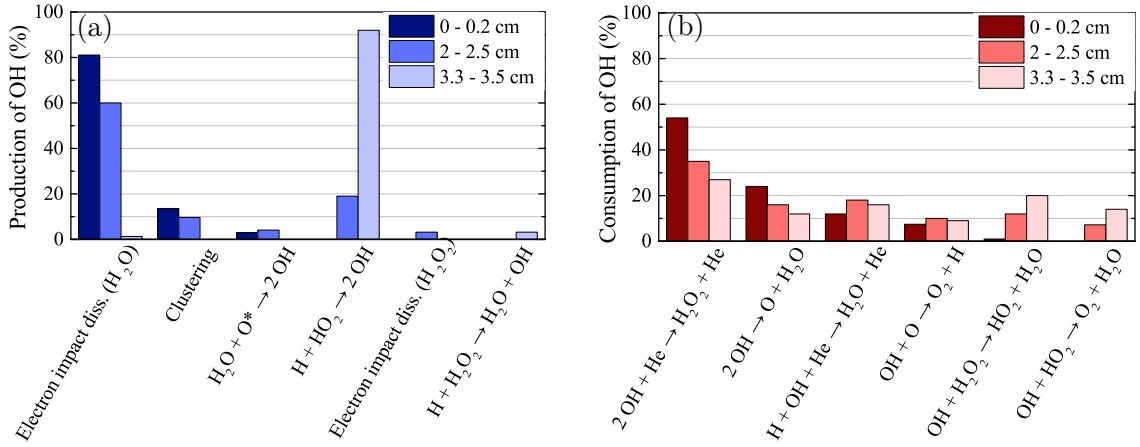

Fig. 4.9: Production (a) and consumption (b) pathways of OH at different positions in the discharge, as indicated in fig. 4.8.

accumulates additional water through a series of reactions:

$$\begin{aligned} H_2O^+ + H_2O &\rightarrow OH + H^+(H_2O) \\ H^+(H_2O)_n + H_2O + He &\rightarrow H^+(H_2O)_{n+1} + He \end{aligned} \tag{4.26}$$

Similar processes should also happen for negative ion clusters, however, rate coefficients for clusters such as $OH^-(H_2O)_n$ are currently not known for $n > 3$ and are therefore not included in the simulation. In particular at higher H_2O admixtures, it can be expected that the formation of higher mass negative clusters may play an important role in defining the plasma characteristics by increasing its electronegativity. It has been shown recently through mass spectrometry [50], that these negative clusters follow very similar trends to the positive clusters for changing water admixtures. However, the role of higher mass negative ion clusters has not been investigated in this work due to the lack of data concerning their production and destruction.

The main consumption pathway for OH in the first 2 mm of the plasma channel is the formation of H_2O_2, but recombination to water also plays a role:

$$2OH + He \rightarrow H_2O_2 + He \quad (54\%) \tag{4.27}$$

$$2OH \rightarrow H_2O + O \quad (24\%) \tag{4.28}$$

$$H + OH + He \rightarrow H_2O + He \quad (12\%) \tag{4.29}$$

Further into the plasma channel (2 - 2.5 cm), the previously discussed pathways are still dominant. However, longer lived species, which are generated in the source over longer timescales, start to play an important role. For example, OH is now also formed by the interaction of atomic hydrogen with hydroperoxy radicals (HO_2):

$$H + HO_2 \rightarrow 2OH \quad (19\%) \tag{4.30}$$

and consumed by interaction with HO_2 and hydrogen peroxide (H_2O_2):

$$OH + H_2O_2 \rightarrow HO_2 + H_2O \quad (12\%) \quad (4.31)$$

$$OH + HO_2 \rightarrow O_2 + H_2O \quad (7\%) \quad (4.32)$$

In the afterglow (3.3 - 3.5 cm), a fast decay of the OH density is observed both in the experiments and simulations. Short lived species such as ions, electrons or He metastable species are not present in this region due their fast recombination and the lack of a significant production channel outside of the plasma. Therefore, the chemistry in the plasma effluent is dominated by longer lived neutral species. In this region, OH is produced mainly by interaction of atomic hydrogen with stable species:

$$H + HO_2 \rightarrow 2OH \quad (92\%) \quad (4.33)$$

$$H + H_2O_2 \rightarrow OH + H_2O \quad (3\%) \quad (4.34)$$

However, in this region the rate of destruction of OH exceeds its rate of production leading to a fast decay of the OH density in the effluent. The main destruction pathways are through interaction with H_2O_2, as shown in eq. (4.31), and recombination resulting in formation of H_2O_2, as shown in eq. (4.27)

OH densities under a variation of the humidity content

Figure 4.10 shows the density of OH measured by UV-BBAS in the centre of the discharge channel using the two experimental setups described earlier under a variation of the H_2O content in the feed gas. It is observed that the measured OH densities increase non-linearly with increasing H_2O content. The error bars shown in the x-direction represent the approximate uncertainty in the H_2O content of the feed gas. It was observed that especially at higher flow rates, the water in the bubbler is cooled down due to the fast evaporation rate, and as such it is useful to view the H_2O content of the feed gas at high H_2O mixtures critically. On the other hand, when the H_2O content in the gas phase is high, the measured OH densities do not vary strongly with changing H_2O content. The absolute OH densities measured with both experimental setups agree well within the error bars of the measurements.

Figure 4.10 also shows the simulated OH densities as the H_2O content of the feed gas is varied. In general, very good agreement in the trends of experimental and simulation results is observed. Absolute OH densities agree very well at the low end of investigated H_2O contents. Towards higher H_2O contents, simulated densities tend to be higher than those measured experimentally. The largest difference of a factor 1.7 is found at the highest investigated H_2O content. This can be regarded as good agreement, taking into account the large uncertainties typically associated with global models and the reaction rate coefficients used in them [104], as previously discussed at the beginning of section 4.6.2. This further emphasizes the need of a full sensitivity analysis for the simulation results to judge their accuracy better.

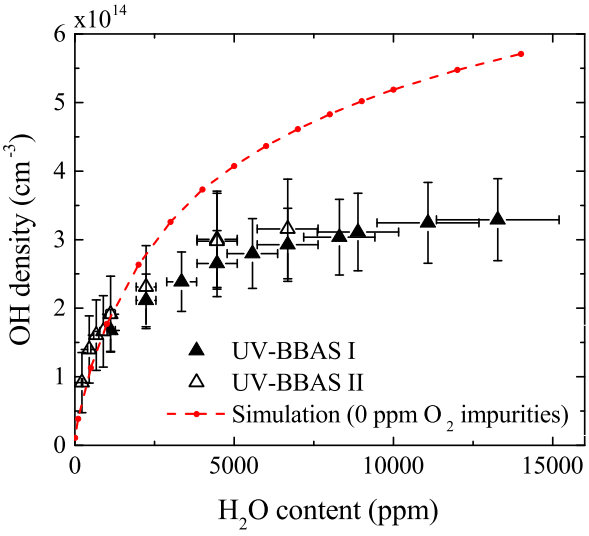

Fig. 4.10: Absolute densities of OH as a function of the H_2O content of the He feed gas. Triangles represent the experimental values and the dashed lines the simulation results. The simulations are run with 13.6 Wcm^{-3} power density. OH is measured with two different UV-BBAS setups, one incorporating an ultra-stable BB light source and a photodiode array (UV-BBAS I) and the other using a UV LED and CCD camera (UV-BBAS II), as described in the text.

The main production and consumption pathways for OH at different H_2O admixtures are shown in fig. 4.11. Two production pathways dominate for all investigated H_2O admixtures. The pathway that is dominant at lower H_2O contents is the dissociative charge transfer reaction of H_2O^+ and H_2O forming OH and $H^+{\cdot}(H_2O)$ (eq. (4.26)). The H_2O^+ in this reaction is produced mainly via Penning ionisation with He^* or He_2^*, as discussed previously. The clustering reactions (second line in eq. (4.26)) continue until a cluster is reached whose lifetime is larger than the defined τ_P in the PumpKin simulations (typically $n = 4$ or $n = 5$ depending on the H_2O admixture). At any stage of the clustering process, the clusters can be destroyed by electron impact dissociation.

$$e + H^+(H_2O)_n \rightarrow H + n \times H_2O \tag{4.35}$$

Towards higher H_2O concentrations, direct electron impact dissociation (eq. (4.23)) and dissociative electron attachment (eqs. (4.24) and (4.25)) of H_2O gradually begin to replace the clustering processes as the dominant formation pathway of OH.

Towards higher H_2O admixtures, OH is also increasingly formed via reaction of H with HO_2 (eq. (4.30)), because of increasing densities of HO_2 and H, which will be shown in section 4.6.4.

The dominant destruction pathway of OH for all investigated H_2O contents is 3-body recombination of H_2O_2 via eq. (4.27), although this reaction becomes slightly less important at higher H_2O admixtures. Other important pathways for the destruction are recombination of two OH to form O and H_2O (eq. (4.28)), recombination of OH and H to form H_2O

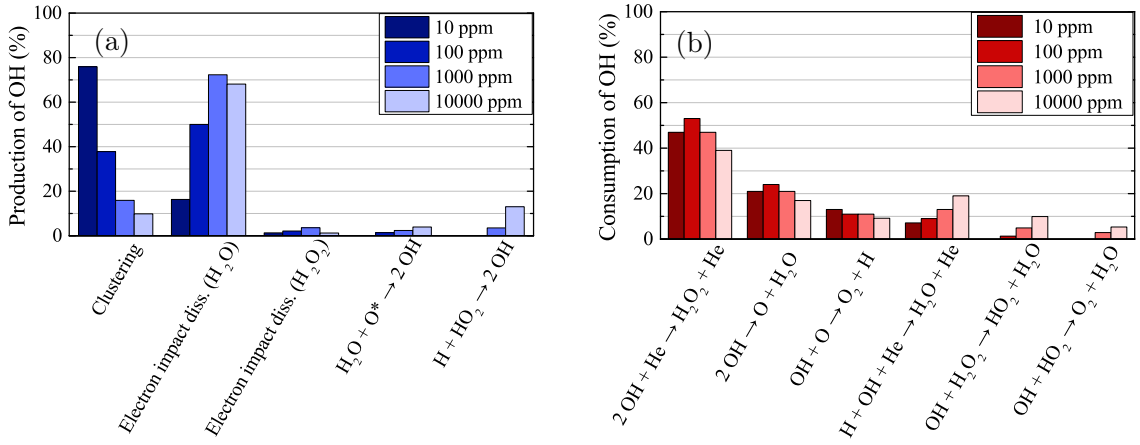

Fig. 4.11: Dominant production (a) and consumption (b) mechanisms for OH for different admixtures of H_2O. The rates from which percentages are calculated are averaged over the whole discharge time (0 - 2.4 cm, without effluent region).

(eq. (4.29)), as well as the reaction

$$OH + O \rightarrow O_2 + H \tag{4.36}$$

At higher H_2O content, reactions with H_2O_2 and HO_2 also become important due to the increasing densities of these species.

4.6.3. Atomic oxygen

Figure 4.12 shows absolute densities of O measured by VUV-FTAS in the center of the discharge (triangles)[1]. O densities are increasing with increasing H_2O content and level off at higher H_2O contents. The simulated O densities (red line in fig. 4.12) also show an increase towards higher H_2O admixtures, however, the simulations continue to increase more significantly at higher H_2O contents than the experimental results. The simulated O densities are around a factor 2 lower than experimentally determined values.

One possible explanation for the difference between simulation and experiment could lie in the fact that O is not directly produced from H_2O due to electron or heavy particle impact dissociation. As a result O must be formed in a process taking at least two steps. Therefore, uncertainties in the rate coefficients for the reactions involved in the production and consumption of O add up. As shown in fig. 4.13, the dominant production mechanism is via recombination of two OH molecules to form H_2O and O, respectively. At lower H_2O contents, O is also formed through processes involving positive ion water clusters:

$$\begin{aligned} OH^+ + H_2O &\rightarrow H^+(H_2O) + O \\ H^+(H_2O) + n \cdot H_2O + He &\rightarrow H^+(H_2O)_n \end{aligned} \tag{4.37}$$

[1]Experimental data in fig. 4.12 has been evaluated by Dr. Kari Niemi

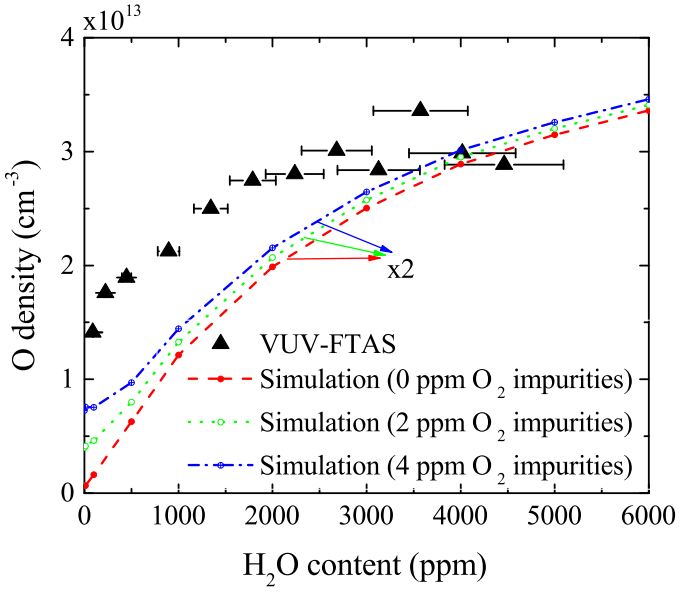

Fig. 4.12: Absolute densities of O as a function of the H_2O content of the He feed gas. Triangles represent the experimental values and the dashed lines the simulation results, which have been multiplied by 2 to show a better comparison of the trends in simulation and experiment. Simulations are also shown for different concentrations of O_2 which is potentially present in the feed gas as an impurity. The plasma power density for the simulations is 10.2 Wcm^{-3}.

With increasing H_2O admixture the formation of O_2 also increases. As a result, electron impact dissociation of O_2 becomes a more important production pathway for O:

$$e + O_2 \rightarrow 2O + e \qquad (6\text{ eV}) \qquad (4.38)$$

$$e + O_2 \rightarrow O + O(^1D) + e \qquad (8.4\text{ eV}) \qquad (4.39)$$

O is mainly consumed by reactions involving OH forming O_2 and H (eq. (4.36)).

At lower admixtures, wall losses of O and electron impact excitation into higher excited states also play a minor role, while at higher admixtures reactions with H become slightly more important.

In fig. 4.12 it is also observed that significant densities of O are present even when only very small quantities of H_2O are admixed to the feed gas. This could be explained by oxygen containing impurities coming from the gas bottle or the feed gas line. Therefore, fig. 4.12 also shows the simulated O densities for two different non-zero O_2 impurity concentrations in the order of typical impurities originating from the feed gas supply. Particularly at low H_2O contents, these impurities lead to an increase of atomic oxygen compared to the gas mixture without impurities. Because the density of O produced from H_2O is very small, typically a few ppm, even small amounts of oxygen containing impurities can significantly influence the O density produced in the plasma. The slightly increased production of O at higher H_2O and impurity contents (5000 ppm H_2O and 4 ppm O_2) originates from increased dissociation of O_2. Both rates for the reactions eq. (4.38) and eq. (4.39) increase

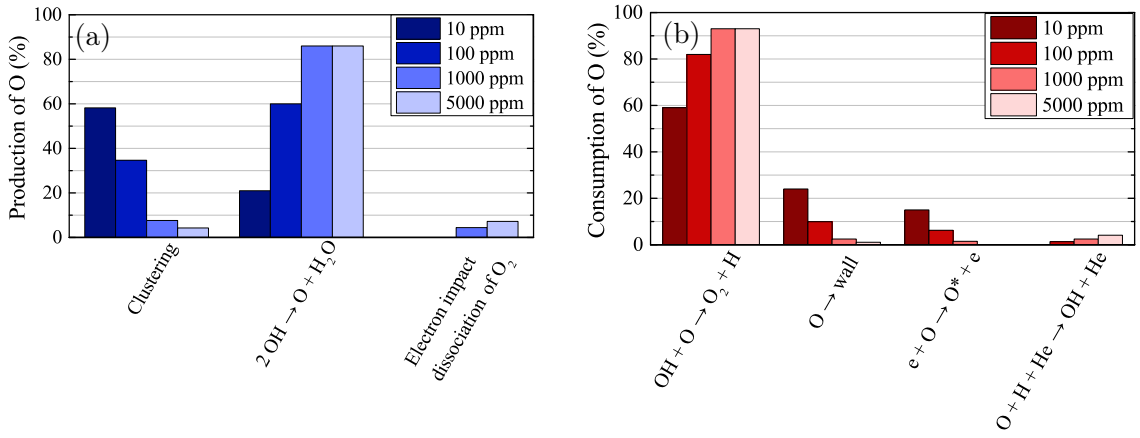

Fig. 4.13: Dominant production (a) and consumption (b) mechanisms for O for different admixtures of H_2O into the feed gas. The rates from which percentages are calculated are averaged over the whole discharge time (0 - 2.4 cm, without effluent region).

about 45% from 0 to 4 ppm O_2 impurities at 5000 ppm H_2O content.

The influence of small O_2 admixtures on OH densities was found to be negligible (not shown).

4.6.4. Determination of additional species by global modelling

In fig. 4.8 it has been shown that the OH density reaches a steady-state value well before the end of the plasma channel in both simulation and experiment. This is as a result of the fact that, particularly at higher H_2O content, OH is primarily produced by direct electron impact dissociation of H_2O in a one step process, and consumed via reactions with other OH molecules. The same is valid for atomic hydrogen, 77% of which is produced via the same channel at a water content of 5000 ppm, and whose main consumption process is via recombination at the reactor walls. However, other species treated in the simulation do not reach a steady state over the 2.4 cm plasma channel and instead continuously increase in density until they exit the plasma. This is particularly true for slowly forming, long-lived species such as O_2, H_2O_2 and H_2, and is illustrated in fig. 4.14. The formation mechanisms for these species is more complex than for H and OH.

First, atomic oxygen is considered. The density of O does not reach a steady state value in the simulation within the plasma channel for most investigated conditions using a He-H_2O gas mixture. A long timescale for the simulation to reach a steady-state value has been also found by others [58] and is in contrast to results found when the µAPPJ is run in a He-O_2 mixture instead of a He-H_2O mixture [162]. In the work described in reference [162], O densities were approaching a steady-state value towards the end of the plasma channel of the µAPPJ. It is therefore suggested that a He-H_2O chemistry reaches a steady-state much slower. This was indicated earlier in the spatially resolved emission of excited states of O

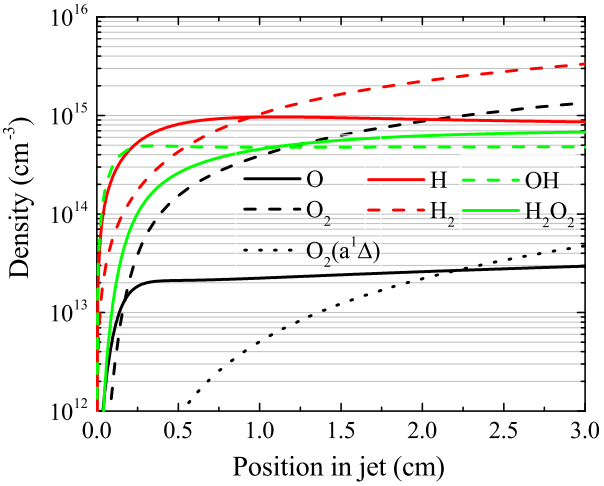

Fig. 4.14: Development of several species of interest as a function of position in the plasma channel, under the same conditions shown in fig. 4.8.

(fig. 4.2). In fig. 4.14, O densities are increasing sharply within the first few millimetres of the channel, and then at a lower rate until the end of the channel. Therefore, O densities follow a very similar dependence to the OH densities, which are also shown in fig. 4.14. This is not surprising when looking at the main production and consumption pathways for O (eqs. (4.28) and (4.36)), which are production via re-arrangement of two OH molecules to form H_2O and O, and consumption of O via collision with OH to form O_2 and H, and are therefore both related to OH. The fact that O is still building up within the channel, while OH approaches a steady-state value, is due to the continuous build-up of O_2 in the channel. Electron impact dissociation of O_2 (eqs. (4.38) and (4.39)) provides an additional formation mechanism for O further into the channel, although eqs. (4.28) and (4.36) are still the dominant production and consumption pathways for O.

The build-up of O_2 is a complex multi-step process, and the dominant pathways for the formation of O_2 for different humidity contents are investigated using PumpKin. Since O_2 is a slowly forming species, we look at the dominant production and consumption pathways for longer timescales than previously. The time scale of interest is chosen in such that only He, H_2O, O_2, O_2^*, H_2, and H_2O_2 are treated as long-lived species, in accordance with previous studies [57].

The two main net production pathways for the formation of molecular oxygen are found to be

$$2H_2O \rightarrow 2H_2 + O_2 \tag{4.40}$$

$$H_2O_2 \rightarrow H_2 + O_2 \tag{4.41}$$

Many different pathways are possible in order to obtain these net production pathways. A few examples of the more detailed mechanisms are

$$
\begin{aligned}
3 \cdot (e + H_2O &\rightarrow H + OH + e) \\
2OH &\rightarrow O + H_2O \\
OH + O &\rightarrow O_2 + H \\
4 \cdot (H &\rightarrow \frac{1}{2} H_2) \\
\hline
2H_2O &\rightarrow 2H_2 + O_2
\end{aligned}
\tag{4.42}
$$

$$
\begin{aligned}
3 \cdot (e + H_2O &\rightarrow H^- + OH) \\
3 \cdot (H^- + He &\rightarrow H + He + e) \\
2OH &\rightarrow O + H_2O \\
OH + O &\rightarrow O_2 + H \\
4 \cdot (H &\rightarrow \frac{1}{2} H_2) \\
\hline
2H_2O &\rightarrow 2H_2 + O_2
\end{aligned}
\tag{4.43}
$$

$$
\begin{aligned}
3 \cdot (e + He &\rightarrow He^* + e) \\
3 \cdot (He^* + H_2O &\rightarrow He + H_2O^+) \\
3 \cdot (H_2O^+ + H_2O &\rightarrow OH + H^+(H_2O)) \\
3 \cdot (H^+(H_2O)_n + H_2O + He &\rightarrow H^+(H_2O)_{n+1} + He) \\
3 \cdot (H^+(H_2O)_n + e &\rightarrow H + n \times H_2O) \\
2OH &\rightarrow O + H_2O \\
OH + O &\rightarrow O_2 + H \\
4 \cdot (H &\rightarrow \frac{1}{2} H_2) \\
\hline
2H_2O &\rightarrow 2H_2 + O_2
\end{aligned}
\tag{4.44}
$$

$$
\begin{aligned}
2 \cdot (e + H_2O &\rightarrow H + OH + e) \\
OH + H_2O_2 &\rightarrow HO_2 + H_2O \\
OH + HO_2 &\rightarrow O_2 + H_2O \\
4 \cdot (H &\rightarrow \frac{1}{2} H_2) \\
\hline
H_2O_2 &\rightarrow H_2 + O_2
\end{aligned}
\tag{4.45}
$$

Note that eqs. (4.42) to (4.44) have effectively the same net production pathway, although the intermediate steps towards the formation of O_2 are different. Equations (4.42) and (4.43) both start with the electron impact dissociation of H_2O molecules, either by direct dissociation, or via the dissociative attachment process. The reaction of OH with OH and O leads to the formation of O_2. The H atoms formed recombine at the wall to form H_2.

Equation (4.44) is the same net pathway as eqs. (4.42) and (4.43), however, the step-by-step analysis reveals a completely different production mechanism. H_2O molecules are first ionised via Penning ionisation with He^*. H_2O^+ ions then start accumulating more H_2O molecules in a clustering process, where OH is eventually produced. As previously, the reaction of OH with OH and O lead to the formation of O_2. The produced cluster ions are consumed by electron impact dissociation, and atomic hydrogen which is formed in that process is lost to the wall. Other pathways exists that involve the formation of clusters, but are not explicitly discussed here. The production of O_2 in a reaction chain involving clusters is found to be more important at lower H_2O admixtures (100 ppm).

Equation (4.45) has a different net production pathway than eqs. (4.42) to (4.44). OH produced from electron impact dissociation of H_2O reacts with H_2O_2 to form reactive HO_2, which then forms O_2 after reacting with more OH.

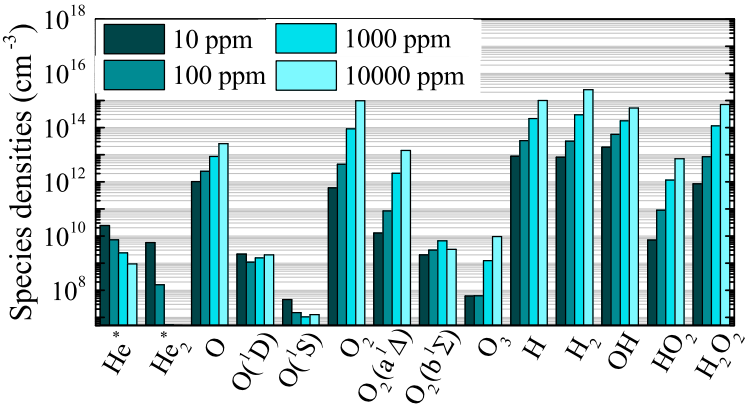

Fig. 4.15: Neutral species densities at the end of the channel in the mod-µAPPJ with 13.56 Wcm^{-3} plasma power and different humidity contents.

Figure 4.15 shows all neutral species produced in the plasma at different water admixtures. As discussed previously, He metastables strongly decrease with increasing humidity content. Most other investigated species increase, except O(^{1}S), which generally has very low densities in water containing plasmas. At high H_2O contents, the dominant species are H_2, H_2O_2, H, O_2 and OH, all having densities greater than 10^{14} cm^{-3}. Purely oxygen containing species such as O(^{1}D), $O_2(b^1\Sigma)$ and O_3, have very low densities. The excited oxygen metastable $O_2(a^1\Delta)$ as well as atomic oxygen still have significant densities.

4.7. Hydroxyl densities for a power variation

As shown in the previous section, OH densities could be tailored through varying the humidity content in the feed gas. Another parameter that could potentially be used for tailoring species densities is the plasma power or applied voltage. It is therefore investigated in this section to what extent the applied voltage can influence the hydroxyl radical densities.

Figure 4.16 shows absolute OH densities for two different water contents as a function of the applied voltage. OH densities increase with increasing voltage, however, the dependence of OH densities on the voltage is not very strong. For the higher water admixture of 11100 ppm (measurement taken with UV-BBAS I setup including the ultra-stable broad band light source), densities increase 45% when the voltage is increased by a factor of 1.7 over the whole measurement range. For the measurement at the lower water content (measurement taken with UV-BBAS II setup including the LED), the increase occurs within the error bar of the measurements. It is therefore concluded that a variation of plasma power is not as effective in tailoring the OH densities as a variation of the humidity content.

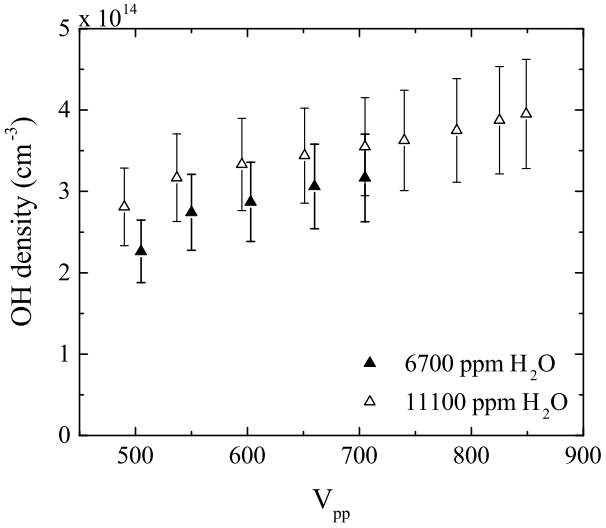

Fig. 4.16: OH densities as a function of applied voltage for two different H_2O admixtures.

4.8. Hydroxyl densities under a variation of O_2, N_2 and H_2O content

In this section it is investigated how additional molecular admixtures such as O_2 or dry air (N_2:O_2 4:1) could potentially influence, or even enhance the OH production in the APPJ. Therefore, the amount of admixed H_2O and O_2 is changed simultaneously. The experimental results are shown in fig. 4.17 (a). Several regions of interest can be identified.

When no H_2O is admixed (O_2 only), the OH density is generally below the detection limit of the experiment, with exception of the point where 0.2% O_2 is admixed. However, since it is most likely that OH is produced from impurities in this case, the measured OH density is very low. By increasing the H_2O content, the OH density increases as discussed previously for fig. 4.10. Increasing the amount of O_2 at the same time, the OH density peaks around 0.2% O_2 admixture for all H_2O contents. At high molecular admixtures between 1.2 and 1.4% the plasma extinguishes. In general, it is found that the dependence of OH densities on the O_2 admixture is less pronounced than on the H_2O content.

Figure 4.17 (b) shows the simulation results for similar conditions compared to fig. 4.17 (a) and an average power of 2.76 W at 1.2 cm into the discharge channel. Simulated OH densities are generally a little lower than experimental values, as it has been discussed previously for the case of pure H_2O admixtures in fig. 4.10 (note the different scaling in fig. 4.17 (a) and (b)). In particular for low H_2O admixtures, experimental and simulation results agree very well. Figure 4.17 (c) shows the comparison of simulation and experiments for a fixed H_2O content of 2380 ppm (black triangles and red dashed line). It can be observed both in experiment and simulation, that OH densities increase slightly at first to peak around 0.2-0.4% O_2 admixture and decrease again with higher admixtures. It should be noted however, that the total variation at this particular H_2O content is less than 18%, which is close to the uncertainty in the experimental measurements.

Figure 4.18 shows the dominant production and consumption pathways for OH for the same conditions as fig. 4.17 (c) (O_2 admixture). The dominant pathways change drasti-

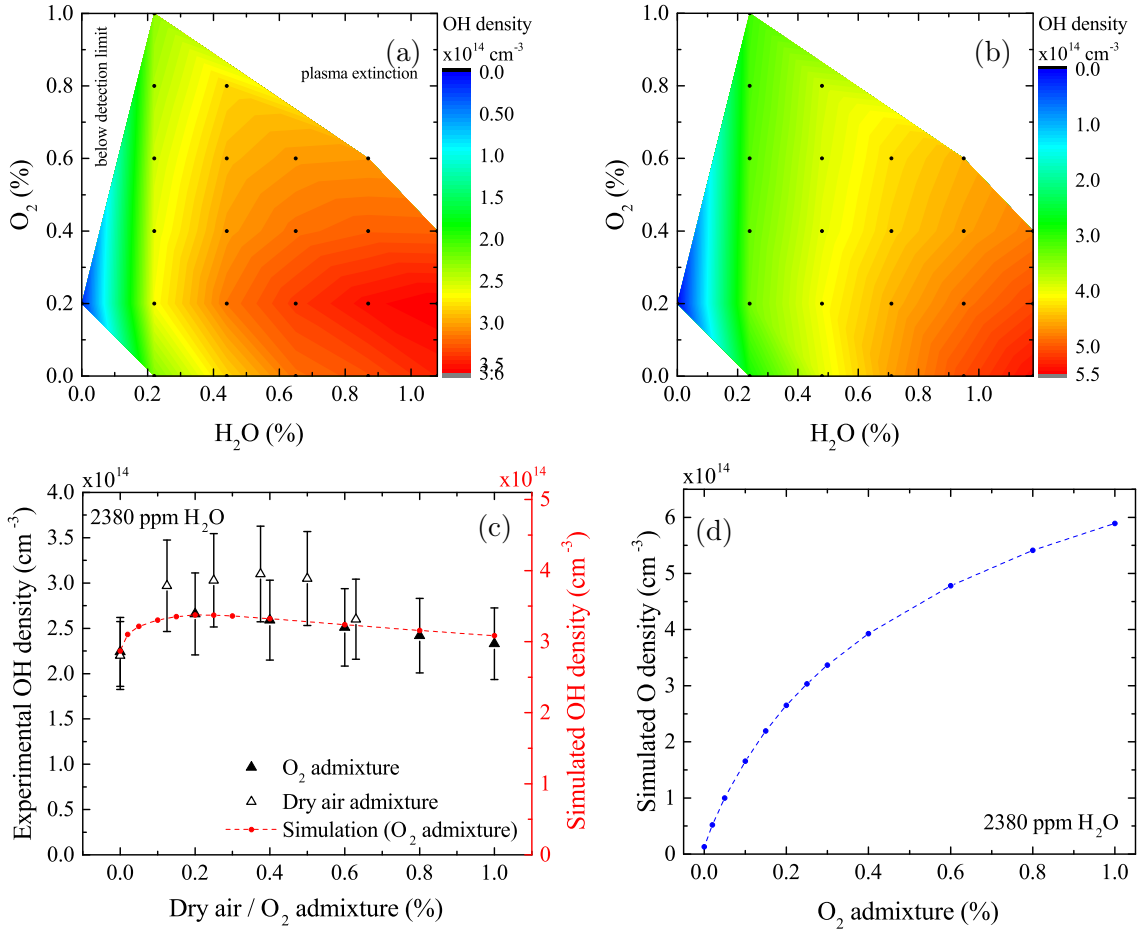

Fig. 4.17: Absolute OH densities under a variation of H_2O and O_2 content. Experimental (a) and simulation (b) results are in good agreement especially at low molecular admixtures (note different scaling of the colour bars). Black dots indicate measurement/simulation points. In the experiment, the total He flow is 5 slm, and the applied voltage varies between 527 and 587 V_{pp} dependent on the admixture. For the simulation, an average power of 2.78 W is assumed, which was measured previously in section 4.7 for a voltage of 510 V_{pp}. (c) Absolute OH densities under a variation of O_2 and dry air at a fixed H_2O content of 2380 ppm. (d) Absolute simulated OH densities under a variation of O_2, conditions are the same as in (c).

cally when O_2 is admixed, especially from 0 to 0.2% admixture, although the change in OH densities is not very pronounced. For the production of OH at 0% O_2 content, electron impact dissociation of H_2O and dissociative attachment as well as clustering are the dominant pathways with a total contribution of more than 80%. At 0.2% O_2 admixture, these pathways only contribute 13% of the total production, while the dissociation of H_2O by collisions with $O(^1D)$ and dissociation of HO_2 by collisions with O contribute 63%. This transition from a water to oxygen dominated reaction chemistry becomes even more dominant at higher O_2 admixtures.

A similar trend can be observed for the dominant consumption pathways for OH. When no O_2 is admixed, the main consumption pathways are reactions with OH itself to produce

H_2O_2 or H_2O, or with H to produce H_2O. These three reactions contribute 78% to the total consumption of OH. At 0.2% O_2 admixture the dominant consumption pathways change significantly. Now the previous channels only contribute 19% of the total consumption, and reactions of OH with O and HO_2 become dominant.

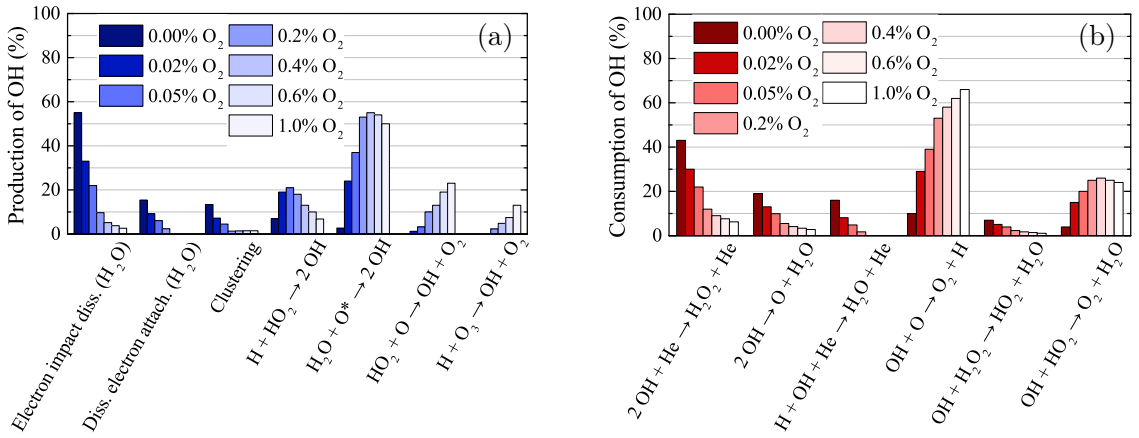

Fig. 4.18: Main production (a) and consumption (b) pathways for OH under an O_2 variation with fixed H_2O content of 2380 ppm. The pathways are averaged between 0 and 2.4 cm.

Figure 4.17 (d) shows atomic oxygen densities obtained from simulations under a variation of the O_2 content and the same conditions as fig. 4.17 (c). O densities increase more than one order of magnitude with increasing amount of admixed O_2, in contrast to OH densities, which stay almost constant, as was discussed previously (fig. 4.17 (c)). A combined admixture of H_2O and O_2 therefore offers potential for an independent tuning of both O and OH densities.

Figure 4.17 (c) also shows a variation of OH content with air admixture (white triangles). By increasing the air admixture, OH densities increase above those measured under an O_2 variation. This seems counter-intuitive because if OH production increased with increasing density of atomic oxygen in the O_2 admixture case, it should result in less OH in the dry air admixture case because there is five times less O_2 present in the discharge and one would therefore also expect less O in the plasma. In order to investigate the dominant pathway for the formation of OH under these conditions, a more complex plasma chemistry also involving nitrogen containing species with densities higher than on the scales of impurities has to be implemented into the simulation. However, this goes beyond the scope of this thesis, and is left for future investigations.

4.9. Nitric oxide densities under a variation of O_2 and N_2

Nitric oxide (NO) has been found to be an important signalling agent in cells [163], and is therefore important in different biomedical applications such as wound healing [164–166]. The interest in producing NO using plasmas has therefore grown significantly in

the last years, and there has been a recent effort to quantify NO in different atmospheric pressure plasma jets using different diagnostic techniques, such as LIF [36] or absorption spectroscopy in the infrared range [37, 38].

In this work, absolute NO ground state densities are measured using UV-absorption spectroscopy on the NO($X^2\Pi_i$,$v = 0$) → NO($A^2\Sigma^+$,$v' = 0$) transition at 226 nm. Absorbance spectra are taken for this transition using the setup described in section 4.5, with the only difference being the wavelength region investigated.

NO data evaluation

PGOPHER is used to calculate absolute ground state NO densities using a similar method to that described for OH. Coefficients from the NIST Chemistry WebBook [160] are used, and the different quantum-mechanical constants listed in table 4.2 are calculated from these coefficients. After putting these coefficients into PGOPHER, Einstein coefficients are calculated and normalised to Einstein coefficients calculated by Reisel et al. [167].

Tab. 4.2: Constants used in PGOPHER for the calculation of the transition spectra for NO. The constants are the state origin, the rotational constant (B), the spin-orbit coupling constant (A), the spin rotation coupling constant (γ_s), the Lambda doubling constants (p and q), and the centrifugal distortion constants (D and H).

Species	Origin	B	A	γ_s	p	q	D	H
NO($X^2\Pi_i, v = 0$)	1068.11	1.71	123.162	0	0.0117	6.7×10^{-5}	5.3×10^{-6}	0
NO($A^2\Sigma^+, v' = 0$)	45150	1.987	0	-0.002765	0	0	0	0

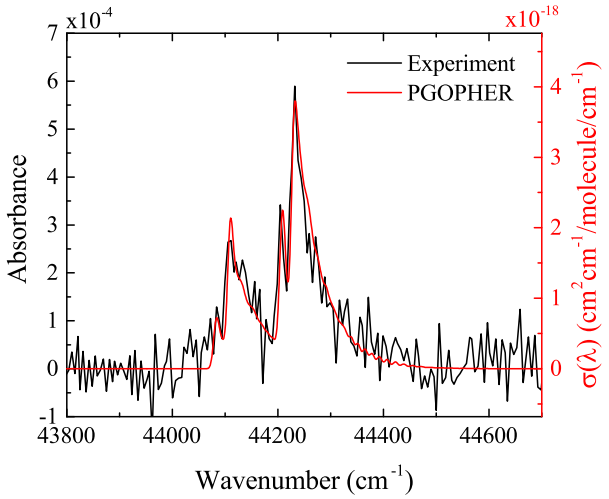

Fig. 4.19: Experimental and simulated PGOPHER spectrum for NO. The NO(X) density obtained from this spectrum is 1.8×10^{14} cm^{-3}.

Figure 4.19 shows experimental results and a simulated absorbance spectrum as well as absorption coefficients obtained from PGOPHER for NO. The baseline was manually removed in order to account for additional absorbance due to other species in the plasma such as O_3 and NO_2, which have continuous absorption bands in the same wavelength

region. It is observed that in general, the absorbance signal for NO is much weaker compared to OH, leading to a worse signal to noise ratio. The standard deviation of the noise is calculated from the distribution of absorbance signal in the wavenumber range 43000 - 44000 cm^{-1} as $\Delta A = 3.6 \times 10^{-5}$. The error bar for the absolute densities can be calculated by deviation of eq. (4.13) and will be shown in the following plots.

For the operation parameters 10 slm He flow, 0.5% dry air admixture, and $V_{pp} = 660$ V, an absolute NO density of 0.9×10^{14} cm^{-3} is measured (data not shown). This is in the same order of what was measured previously by Douat et al. [37] in the μAPPJ using quantum-cascade laser absorption spectroscopy under comparable operating conditions (1.4 slm He, 0.35% N_2 and about 500 ppm O_2).

4.9.1. NO densities under a variation of N_2 and O_2 in the feed gas

Figure 4.20 (a) shows the measured atomic oxygen and nitrogen ground state densities obtained by VUV-FTAS as described previously [66] under a variation of the gas mixture composition. The total amount of molecular admixture is kept at 0.1% in a He flow of 10 slm, while the ratio N_2/O_2 is varied.

It is observed in fig. 4.20 (a), that both atomic oxygen and nitrogen densities increase with increasing admixture of O_2 and decreasing admixture of N_2[1]. While it would be expected that O densities increase with increasing O_2 and decreasing N_2 admixture, intuitively one would expect the opposite trend for N. A possible explanation for this phenomenon could be the presence of electronically and highly vibrationally excited states of N_2, which have been found to play a major role in plasma systems operating at lower pressures [168–171]. In particular the reactions of highly vibrationally excited states of N_2 with atomic oxygen has been found to be the dominant process for the formation of NO and N in low pressure DC glow discharges:

$$N_2(X, \upsilon > 13) + O \rightarrow NO(X, \upsilon = 0) + N \tag{4.46}$$

This reaction mechanism could potentially explain the increase of N densities with decreasing N_2 admixture, showing that the produced N could increase with increasing amount of O present in the discharge, although the amount of N_2 is decreasing. A possible counter-argument to this would be if the electron energy distribution function were to change on decreasing N_2 admixture and increasing O_2 admixture such as to more effectively excite the N_2 vibrational states required for eq. (4.46). The development of a model describing all the necessary reaction mechanisms is complex, because of the large number of excited species and reactions to be considered, but could be a task for future investigations.

Figure 4.20 (b) shows absolute NO densities under similar conditions to fig. 4.20 (a). The applied voltage and therefore coupled power is higher for the NO absorption measurement due to the weak absorption signal. Absolute NO densities peak approximately when the amount of admixed O_2 and N_2 is the same.

[1] Experimental data in fig. 4.20 (a) has been evaluated by Dr. Kari Niemi

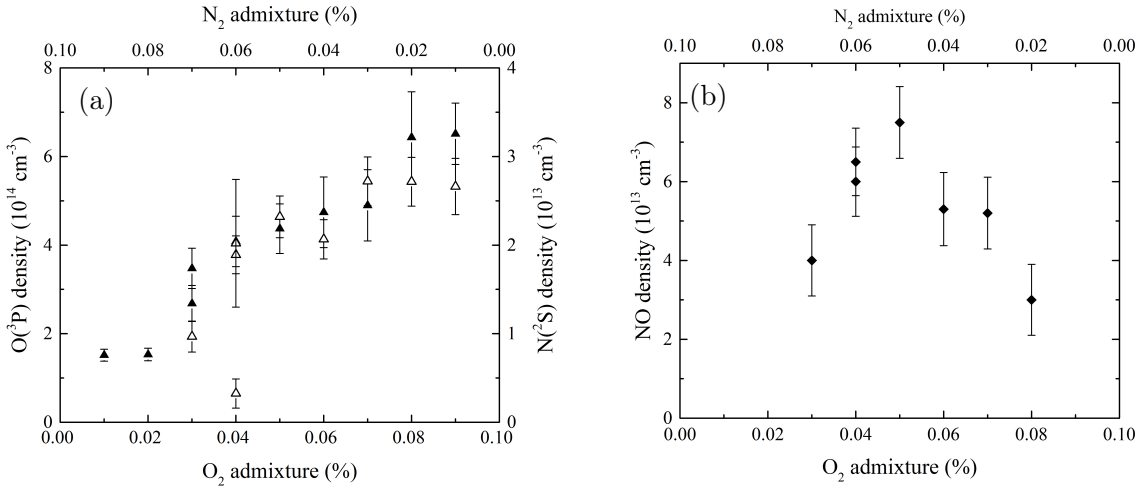

Fig. 4.20: (a) Absolute values of O (black triangles) and N (white triangles) measured by VUV-FTAS with a total He flow of 10 slm and $V_{\mathrm{pp}} = 455$ V. (b) Absolute NO densities under the same conditions as (a), but with $V_{\mathrm{pp}} = 665$ V.

4.9.2. NO densities under a variation of plasma power

Figure 4.21 shows the development of NO densities under a variation of the applied peak-to-peak voltage. NO densities increase linearly with increasing power coupled into the plasma source. The dependence on power is much stronger than in the previously discussed case of OH. Higher powers in general lead to higher electron densities in the plasma source and therefore higher dissociation rates of molecules. However, higher powers lead to higher gas temperatures, which are usually not desirable from the point of view of applications of these types of plasmas. Therefore, even though NO densities are strongly affected by the power coupled into the plasma, using increasing power in order to tailor reactive species densities is quite likely limited for plasma medicine or heat sensitive applications by the requirement to have low gas temperatures.

4.10. Key results

In this chapter, both experimental and numerical approaches were used to characterise different species densities under a variation of several plasma parameters. Of particular interest is the question, which parameter variation enables optimum tuning of RS production in the plasma. Generally, simulation and experiment showed good agreement in the case where benchmarking was possible.

OH. Absolute OH densities are strongly dependent on the H_2O content in the feed gas, and only weakly depend on the coupled power. The main production mechanisms for OH in a pure He and H_2O plasma were found to be electron impact dissociation with H_2O molecules and clustering processes, while the main consumption pathways are due to collisions with other OH molecules, O, and H. Formation pathways are dependent on the position in the plasma channel. Air and O_2 admixtures only slightly affect absolute OH

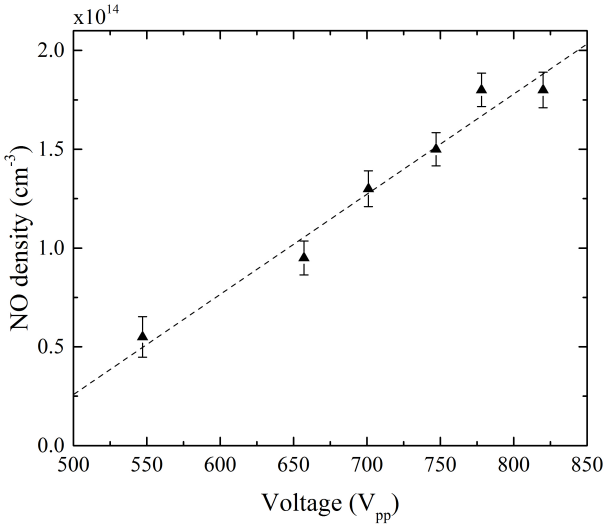

Fig. 4.21: Absolute NO densities under a variation of the plasma power. The plasma conditions are 40 sccm N_2 and 10 sccm O_2 with a total He flow of 10 slm. The N_2:O_2 ratio is chosen to represent dry air.

densities, however, as shown in the case of O_2 admixtures, formation pathways can change significantly, with dissociation of water by O(^{1}D) becoming an important production pathway for OH towards higher O_2 admixtures. Surprisingly, adding air leads to slightly higher OH densities than an addition of pure O_2. A possible reason might be that a similar dissociation process by N metastables might be even more effective due to a higher potential energy compared to O(^{1}D). However, in order to investigate this further, a more complex plasma chemistry involving N species has to be implemented, which goes beyond the scope of this work.

O. Atomic oxygen densities produced from H_2O are about an order of magnitude lower than OH densities. The production and consumption of O is strongly coupled to OH due to the pathways $OH + OH \rightarrow H_2 + O$ and $OH + O \rightarrow O_2 + H$. At high H_2O contents and towards the end of the plasma channel, electron impact dissociation of O_2, which is continuously accumulating over time, starts to enhance O production, meaning that absolute O densities do not reach equilibrium within the channel. Therefore, changing the length of the plasma source could enable a tuning of O densities while species such as OH and H stay constant.

N and NO. Absolute densities of N and NO were measured while increasing the O_2 content and decreasing the N_2 content. Surprisingly, N increased with increasing O_2 content and decreasing N_2 content in the gas phase. NO was found to peak when the N_2 and O_2 admixtures were approximately equal. In order to investigate these trends in more detail, a more complex plasma chemistry model is needed. NO shows a stronger dependence on applied voltage than OH, making the power a suitable parameter for tailoring the density of NO, only limited by a possible increase in gas temperatures.

Generally, for all species investigated numerically in this work, a very valuable task for future work would be the development of a full sensitivity analysis for the plasma simu-

lations. Such an analysis could provide typical error bars associated with the modelling results, and therefore help to develop a better understanding the magnitude of these uncertainties, as well as their origin.

5. Atomic oxygen and hydrogen production in the μAPPJ containing humidity

As discussed in the previous chapter, the detection of many reactive species and their quantification is challenging under the typical experimental conditions provided by APPs. So far, absolute species densities were detected in the sealed source in a "protected" atmosphere, which means there was no direct contact between the investigated gas volume and ambient air. Therefore, the previously discussed measurements were not influenced by any effects of for example ambient gas mixing. However, the plasma sources used for biological applications are typically operated in ambient air to allow for interaction of plasma produced particles with biological samples, making gas entrainment particularly in the plasma effluent, inevitable. Due to this gas mixing, measurements of reactive species in these types of plasmas, or their effluents, are challenging, because entrained ambient air can influence the gas dynamics, for example by quenching of excited state lifetimes [80]. Additionally, the length of the absorbing medium is poorly defined and spatially dependent, causing additional problems when using line integrated absorption spectroscopy.

In this section, an advanced technique for the investigation of absolute species densities is introduced, which enables absolute measurements of spatially resolved species densities and effective lifetimes in the plasma effluent region. The technique is Two-photon Absorption Laser Induced Fluorescence, with sub-nanosecond temporal resolution (ps-TALIF).

5.1. Two-photon absorption laser induced fluorescence with sub-nanosecond temporal resolution

Laser induced fluorescence (LIF) or two-photon absorption laser induced-fluorescence (TALIF) are techniques based on the absorption of one or two laser generated photons, typically by the ground state of a molecule or atom. The resulting excited state can de-excite via radiative and, at elevated pressures, collisional de-excitation processes. The general concept of LIF and TALIF is to obtain absolute ground state densities of molecules by measuring this fluorescence signal. The working principle of TALIF has been described in much detail in the literature [71, 172–174], so only the main steps for the derivation of the "TALIF equation", which describes the dependence of absolute ground state species densities on the fluorescence signal, will be mapped out here. For all derivations in this work it is assumed that the laser energy is sufficiently small to avoid any saturation effects, which will be discussed later.

5.1.1. Principles of TALIF

Fluorescence signal

A schematic of the two-photon laser excitation and fluorescence is shown in fig. 5.1. Two incoming photons excite the molecule from a lower state 0 with density n_0, which in this case is assumed to be the ground state of the molecule, to a higher state 1. In the case of purely radiative de-excitation processes, this state has a limited lifetime defined by the Einstein coefficient $A_i = \sum_k A_{ik}$ for spontaneous emission, taking into account all possible lower states k. In the example shown in fig. 5.1, the atom goes from state 1 to state to state 2 with a probability denoted by the Einstein coefficient A_{12}, emitting a photon. Because the excitation by two photons usually goes via an intermediate "virtual" state, both, the transition from the ground state to this virtual state and from the virtual state to the higher excited state have to follow one-photon excitation rules. This means that in contrast to LIF, the transition back into the ground state emitting one photon with half the wavelength of the two excitation photons is spectroscopically forbidden for TALIF. The general selection rules for TALIF are that the parity $(-1)^{\sum_i l_i}$ (here $l = 0, 1, 2...$ denotes the angular momentum quantum number for s, p, d... states) for lower and excited states are the same [175]. This allows fore example for $s \rightarrow s$ and $s \rightarrow d$ transitions, which are not allowed with only one photon. An additional general selection rule for the total angular momentum of the electron J is $J \rightarrow J$, $J \pm 1$, $J \pm 2$ (except $J : 0 \leftrightarrow 1$ if the two photons originate from the same laser) [175]. For a one-photon transition, the rule $J \rightarrow J \pm 2$ is not possible. A full list with selection rules for two-photon excitation can be found in [172, 175].

The aim of this section is to derive an expression which links the intensity of the fluorescence signal, which is a measurable quantity, with the ground state density. We start by looking at the absorption process from the ground state 0 to the higher state 1. The probability for absorption is given by the Einstein coefficient B_{01}. Generally, B_{ik} is related

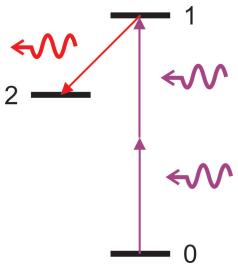

Fig. 5.1: Schematic of TALIF excitation scheme.

to the absorption cross section $\sigma_{ik}(\lambda)$ of the transition

$$\sigma_{ik}(\lambda) = \frac{h}{\lambda} B_{ik}(\lambda) \tag{5.1}$$

Note that $B_{ik}(\lambda) = B^0_{ik}\Phi(\lambda)$ contains the normalised line-shape function $\int \Phi(\lambda)d\lambda = 1$. Using the Einstein B_{ik} coefficient, the rate of change of the lower state can be expressed as

$$\frac{dn_0}{dt} = -B_{01} n_0 \rho(t) = -\frac{dn_1}{dt} \tag{5.2}$$

where $\rho(t)$ is the spectral energy density of the incoming radiation.

Equation (5.2) shows that the absorption process is populating the higher state 1. Several processes exist that can lead to the de-population of this particular state. The first process is spontaneous emission, where the change of population in the upper state 1 can be expressed by the Einstein coefficient A_{12} for spontaneous emission into the lower state 2, as previously discussed. The second possibility for depopulation of state 1 is via radiationless de-excitation due to collisions (quenching), which becomes more important at elevated pressures. A measure for the quenching efficiency of a quenching species q with density n_q is given by the quenching rate coefficient k^1_q. Together with the previously discussed absorption, the total change in the excited state 1 densities can be expressed as

$$\frac{dn_1}{dt} = B_{01} n_0 \rho(t) - (\sum_k A_{1k} + \sum_q n_q k^1_q) n_1 \tag{5.3}$$

$$= R_{01}(t) n_0 - (A_1 + Q_1) n_1 \tag{5.4}$$

where the first term on the right hand side describes a gain in density of n_1 due to excitation from the ground state, and the last two terms describe a loss in density of n_1 due to spontaneous emission into all possible lower states ($A_1 = \sum_k A_{1k}$) and quenching ($Q_1 = \sum_q n_q k^1_q$). The product $B_{01}\rho(t)$ has the unit s^{-1} and can therefore be denoted as a rate R_{01}. From eq. (5.4) it is obvious that without any active excitation process ($R_{01} = 0$, for example after the laser pulse), n_1 decreases exponentially with the effective decay time

$$\tau_{\text{eff}} = \frac{1}{A_1 + Q_1} \tag{5.5}$$

For a two-photon excitation process, the excitation rate is proportional to the two-photon

excitation cross section $\sigma^{(2)}(\lambda)$, as well as the square of the laser intensity [173, 174]

$$R(t) = G^{(2)}\sigma^{(2)}(\lambda)\left(\frac{I(\boldsymbol{r},t)\lambda_{\mathrm{L}}}{hc}\right)^2 \tag{5.6}$$

$G^{(2)}$ is the photon statistic factor, which depends on the temporal correlation of the radiation fields, and λ_{L} is the wavelength of the laser with intensity $I(\boldsymbol{r},t)$. The square dependence of the rate on the intensity results from the absorption of two identical photons from the same laser. From eq. (5.4), n_1 can be expressed as [174]

$$n_1(t) = n_0 \int_0^t R_{01}(t')e^{(A_1+Q_1)(t-t')}dt' \tag{5.7}$$

Integration over the total fluorescence time and volume gives the number of fluorescence photons at a particular wavelength [172, 174]

$$N_{\mathrm{F}}(\lambda) = A_{12}\int_V\int_0^\infty n_1(t)dt\,dV \tag{5.8}$$

$$= a_{12}n_0G^{(2)}\sigma^{(2)}(\lambda)\int_V\int_0^\infty\left(\frac{I(\boldsymbol{r},t)\lambda_{\mathrm{L}}}{hc}\right)^2 dt\,dV \tag{5.9}$$

where $a_{12} = \frac{A_{12}}{A_1+Q_1}$ is the branching ratio.

In the experimental setup, not all fluorescence photons will be detected. First of all, only photons emitted within a solid angle $\Delta\Omega$ can reach the detector. Photons can also be absorbed or reflected by any material between the point of emission and the detector, such as optical lenses, filters, or windows. The transmission $T(\lambda)$ of these components therefore has to be taken into account. Finally, the quantum efficiency $\eta(\lambda)$ of the detector, which describes the response of the detector to an incoming photon, is wavelength dependent. The signal s measured by the detector can be expressed by

$$s(\lambda) = \eta(\lambda_{\mathrm{F}})T(\lambda_{\mathrm{F}})\frac{\Delta\Omega}{4\pi}N_{\mathrm{F}}(\lambda) \tag{5.10}$$

Spectral integration of eq. (5.10) gives the absolute intensity of the TALIF signal, which is proportional to the ground state density n_0

$$S_F = \int s(\lambda)d\lambda$$

$$= \eta(\lambda_{\mathrm{F}})T(\lambda_{\mathrm{F}})\frac{\Delta\Omega}{4\pi}a_{12}G^{(2)}\sigma^{(2)}n_0\int_V\int_0^\infty\left(\frac{I(\boldsymbol{r},t)\lambda_{\mathrm{L}}}{hc}\right)^2 dtdV \tag{5.11}$$

Therefore, using eq. (5.11), absolute ground state densities can be calculated. However, in order to solve the integral in eq. (5.11), one has to know the exact intensity profile, both in time and space, of the laser. The observation angle $\Delta\Omega$ has to be determined accurately. Additionally, two-photon excitation cross sections $\sigma^{(2)}$ are very difficult to measure due to their low values, and are not available for all species in the literature. A solution for

this problem would be to compare S_F with the signal obtained for a known amount of the species of interest, but atomic species such as O, N, or H are highly reactive, and therefore difficult to produce in a controlled manner. An alternative is a calibration with noble gases, if similar excitation and fluorescence schemes to that in the species of interest can be found. This method will be discussed in the next section.

Calibration with noble gases

The general principle of calibration with noble gases is to compare the fluorescence signal of the species x of interest after excitation with the fluorescence signal of a species with known density n_{cal}. This procedure has been described in more detail in the literature [70, 173]. Absolute species densities n_x can be calculated by rearranging the following equation

$$\frac{S_{F,x}}{S_{F,cal}} = \frac{\eta_x(\lambda_{F,x})}{\eta_{cal}(\lambda_{F,cal})} \frac{T_x(\lambda_{F,x})}{T_{cal}(\lambda_{F,cal})} \frac{a_{12,x}}{a_{12,cal}} \frac{\sigma_x^{(2)}}{\sigma_{cal}^{(2)}} \frac{n_x}{n_{cal}} \frac{i_x}{i_{cal}} \tag{5.12}$$

where i is the short form notation for the integral in eq. (5.11). If the temporal and spatial characteristics of the laser beam are equal for both the measurement and calibration wavelength, then i can be substituted by the spatially averaged beam energy E

$$\frac{S_{F,x}}{S_{F,cal}} = \frac{\eta_x(\lambda_{F,x})}{\eta_{cal}(\lambda_{F,cal})} \frac{T_x(\lambda_{F,x})}{T_{cal}(\lambda_{F,cal})} \frac{a_{12,x}}{a_{12,cal}} \frac{\sigma_x^{(2)}}{\sigma_{cal}^{(2)}} \frac{n_x}{n_{cal}} \left(\frac{E_x}{E_{cal}} \frac{\lambda_x}{\lambda_{cal}} \right)^2 \tag{5.13}$$

$$\frac{S_{F,x}}{S_{F,cal}} = C \frac{a_{12,x}}{a_{12,cal}} \frac{n_x}{n_{cal}} \tag{5.14}$$

where all quantities that depend on the experimental system are summarised in the parameter C. The term in brackets on the very right hand side of eq. (5.13) is the laser pulse energy divided by the photon energy, and therefore represents the number of laser photons.

Several requirements have to be fulfilled in order to go from eq. (5.11) to eq. (5.13). First of all, as already mentioned, the temporal and spatial laser beam profiles for measurement and calibration have to be identical. Optics that are used for directing and potentially focussing the laser beam should have similar optical characteristics (e.g. transmission, focal length for lenses) for both the fluorescence and calibration measurement. Because of this, the calibration species are usually chosen in a way such that the excitation wavelength of the two species are very close. The same principle has to be applied for the optics used to capture the fluorescence light. Therefore, calibration species are chosen in a way such that the fluorescence light is emitted at a similar wavelength compared to the investigated species. Equation (5.13) has the advantage that the angle of observation $\Delta\Omega$ cancels out, if the experimental system is not changed between measurement and calibration. Additionally, even if two-photon excitation cross sections are not available for a species of interest in the literature, the ratios of cross sections have been measured [76, 173].

Figure 5.2 shows the calibration schemes for the species investigated in this work. Data for the schematics have been taken from other publications [76, 173] and the NIST Atomic Spectra Database [176], and have been previously discussed and used in other work [69,

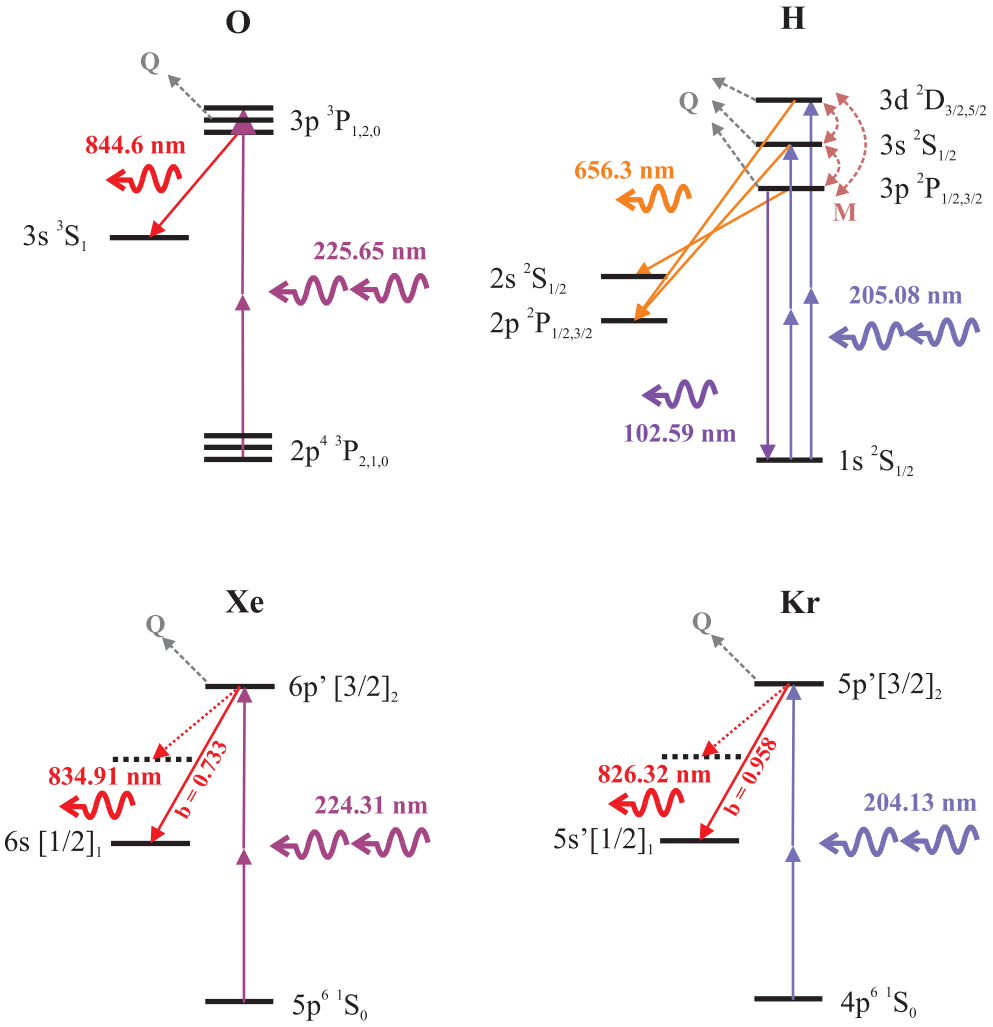

Fig. 5.2: TALIF schemes for the investigated species O and H and corresponding calibration gases, which are Xe and Kr, respectively. All level specifications are taken from the NIST Atomic Spectra Database [176] and [76, 173]. Schematics for noble gases are in Racah notation.

71, 79, 89]. Here, only some particulars of the different species are discussed.

In *atomic oxygen*, both the ground and the LIF excited state (O($2p^4$ ^3P_J) and O(3p ^3P_J), respectively) are split into three fine structure energy sub-levels $J = 0, 1, 2$. While the ground state levels have a distinct energy gap in the order of a few hundred wavenumbers, the upper states lie energetically very close within one wavenumber. Therefore, excitation from any ground state level leads to a population of all $J = 0, 1, 2$ upper state levels, because the spectral width of the laser used in this work (roughly 4 cm^{-1}) is greater than this energy difference.

Xenon is typically chosen as a calibration gas for O, since both the excitation and fluorescence wavelengths are in close proximity. The excited Xe state can decay into several sublevels. The purely optical branching ratio $b = \frac{A_{12}}{A_1}$ for the transition into the 6s state with a wavelength of 834.9 nm is 0.733 [76, 177].

In this work, the following two-photon absorption cross section ratio is used for O and

Xe [76]

$$\frac{\sigma^{(2)}_{\mathrm{Xe}}}{\sum_{J'} \sigma^{(2)}_{\mathrm{O},J\to J'}} = 1.9(\pm 20\%) \tag{5.15}$$

which takes into account all possible transitions into the upper excited states of atomic oxygen. In the measurements presented in this work, usually only the $J = 2$ sub-level of the electronic ground state of O is probed. Particularly for measurements where humidity is added to the gas flow, the fluorescence signal from the other sub-levels is very weak due to low O densities. In order to calculate the absolute density of all ground state sub-levels, a Boltzmann factor as in eq. (4.3) is applied. To test the validity of this approach O densities are measured when O_2 is mixed into the feed gas to give higher O densities so that the fluorescence signal from the $J = 0$ and $J = 1$ states is high enough to be measured. Figure 5.3 shows the densities of each of the three sub-levels as a function of the O_2 content in the feed gas. Absolute ground state O densities calculated from the different O sub-levels lie within 10%.

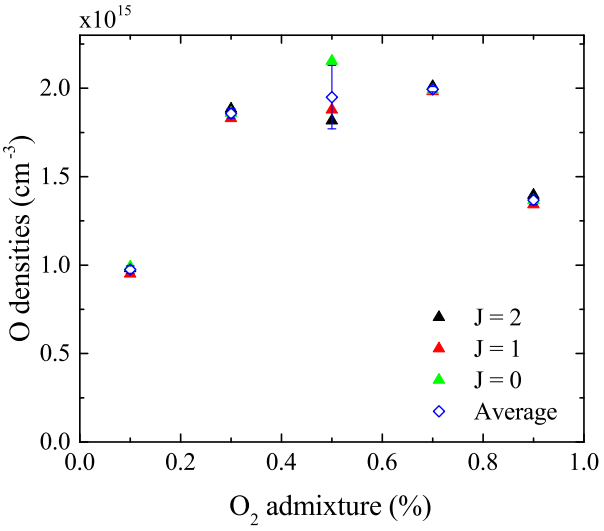

Fig. 5.3: Absolute atomic oxygen densities under a variation of the O_2 content in the plasma. Plasma parameters for the ps-TALIF measurements are 1 slm He and 600 V_{pp}. Densities are obtained from probing the three ground sub-levels and applying a Boltzmann factor.

For the calibration, the plasma jet is replaced with a Starna Spectrosil Fluorometer Cuvette, which is filled with Xe at 10 torr pressure. This pressure is chosen in a way such that the detected TALIF signal in the Xe gas is high enough to give a good signal-to-noise ratio, but not so high as to mean the excited state is strongly quenched by background Xe. Before filling the cuvette with Xe, the cell is pumped down for several hours below 10^{-2} torr to minimise the impact of impurities on the Xe lifetime and signal.

Atomic hydrogen has two levels which are populated by 205.08 nm radiation according to the selection rules for two-photon absorption transitions, if the laser is spectrally wider than the separation of these levels of roughly 0.15 cm^{-1} (as previously mentioned, the laser used in this work has a spectral bandwidth of roughly 4 cm^{-1}). These two states

Tab. 5.1: Detailed information about energy levels and allowed transitions in the H atom. Einstein coefficients A_{ik} are taken from the NIST Atomic Database [176].

Lower state	Higher state	A_{ik} (1/s)
H(1s $^2S_{1/2}$)	H(3p $^2P_{1/2,3/2}$)	1.6725×10^8
H(1s $^2S_{1/2}$)	H(3s $^2S_{1/2}$)	forbidden
H(1s $^2S_{1/2}$)	H(3d $^2D_{3/2,5/2}$)	forbidden
H(2p $^2P_{1/2,3/2}$)	H(3p $^2P_{1/2,3/2}$)	forbidden
H(2p $^2P_{1/2}$)	H(3s $^2S_{1/2}$)	2.1046×10^6
H(2p $^2P_{3/2}$)	H(3s $^2S_{1/2}$)	4.2097×10^6
H(2p $^2P_{1/2}$)	H(3d $^2D_{3/2}$)	5.3877×10^7
H(2p $^2P_{3/2}$)	H(3d $^2D_{3/2}$)	1.0775×10^7
H(2p $^2P_{1/2,3/2}$)	H(3d $^2D_{5/2}$)	6.4651×10^6
H(2s $^2S_{1/2}$)	H(3p $^2P_{1/2,3/2}$)	2.2448×10^7
H(2s $^2S_{1/2}$)	H(3s $^2S_{1/2}$)	forbidden
H(2s $^2S_{1/2}$)	H(3d $^2D_{3/2,5/2}$)	forbidden

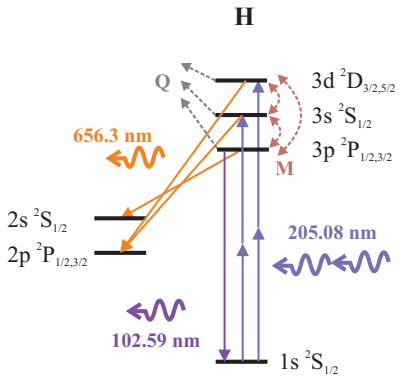

are the 3s and 3d state. The ratio of the excitation cross sections $\frac{\sigma_d^{(2)}}{\sigma_s^{(2)}}$ into these two states is 7.56 [178], and the effective lifetimes for the two states are 15.6 ns and 159 ns for the 3d and 3s state, respectively [178, 179]. As discussed previously, the higher state population decreases due to spontaneous emission from the excited states and collisional quenching with other particles. In atomic hydrogen, a third loss mechanism has to be taken into account, which is known as L-state mixing, and which acts as an additional contribution to the quenching of the species. L-state mixing is effectively a redistribution of the population in the higher excited levels of atomic hydrogen, and is observed to be dependent on the pressure [178]. It can, for example, lead to a population of the 3p state, which would be otherwise prohibited by the two-photon absorption selection rules. This 3p state can radiatively decay back into the 1s state, and radiation from the 656.3 nm emission line would get lost, effectively reducing the lifetime of the higher excited state. Another prossible radiative transition would be into the 2s state, with a mean lifetime of 5.4 ns [179]. The branching ratio $b(\frac{2s}{1s})$ can be calculated as 0.12, which means that transition into the 1s state is favourable. All possible transitions and Einstein coefficients relevant in this scenario are listed in table 5.1.

Preppernau et al. [178] have developed a model for the calculation of absolute decay rates taking into account L-state mixing, additionally to radiative decay times and quenching. In chapter C, this model is applied for conditions typical for experiments carried out in this work (He background gas at atmospheric pressure and $T_g = 315$ K). Taking into account all three de-excitation mechanisms, the equilibrium calculated lifetime is 1.2 ns. An effective lifetime of 0.97 ns is determined experimentally (result is shown in section 5.2), when the lifetime of H(n=3) is measured in a pure He flow and the detected H is produced from impurities only. The equilibrium excited lifetime calculated using the model in chapter C does also not significantly change dependent on if L-state mixing is included in the calculations or not. However, when applying the model, certain aspects are difficult to assess. For example, it is not clear if, or to what extend, the plasma is optically thick for the VUV-radiation emitted from the 3p state after L-mixing induced redistribution of the

upper state population. Therefore, in this work, lifetimes measured using the ps-TALIF system are used for absolute density calculations for H ground state atoms.

Krypton is a gas that is typically used for the absolute calibration measurements with atomic hydrogen. Similar to the Xe-O calibration, the excitation wavelengths of Kr and H are spectrally close, as shown in fig. 5.2. However, the wavelengths for the fluorescence signals lie almost 200 nm apart. This results in a change of the focal length of approximately 50 μm for the particular lens used in the ps-TALIF setup. The setup will be described in the next section.

For the two-photon excitation cross section ratio, the following value is used [173]

$$\frac{\sigma^{(2)}_{\mathrm{Kr}}}{\sigma^{(2)}_{\mathrm{H}}} = 0.62(\pm 50\%) \tag{5.16}$$

Similar to Xe, a cuvette is filled with Kr for the calibration measurement. The pressure in the calibration cell is chosen as 1 torr. At higher pressures, a significant contribution of Amplified Spontaneous Emission (ASE) to the fluorescence signal has been observed previously [122]. ASE leads to a population inversion between the two excited states, and can influence the lifetime measurement if the laser energy or ground state density of Kr is chosen too high. The purely optical branching ratio for the Kr transition of interest is $b = 0.953$ [180].

For the discussion of results, the following abbreviations are used when mentioning different states: When results for absolute ground state densities are presented, the notation "O" is used for the sum of the densities in all atomic oxygen ground state sub-levels $\sum_J \mathrm{O}(2\mathrm{p}^4\ {}^3\mathrm{P}_J)$ and "H" for the $\mathrm{H}(1\mathrm{s}\ {}^2\mathrm{S}_{1/2})$ ground state. For the discussion of quenching of laser excited states, which are discussed in more detail in section 5.2, the abbreviations H^* for the H(n=3) state, and O^* for the $\sum_J \mathrm{O}(3\mathrm{p}\ {}^3\mathrm{P}_J)$ (or short: $\mathrm{O}(3\mathrm{p}\ {}^3\mathrm{P})$) are used.

5.1.2. ps-TALIF setup and parameters

TALIF at atmospheric pressure is challenging due to the high de-excitation rates of the excited states caused by collisional quenching. This leads to very short lifetimes of these states, which are typically shorter than the nanosecond laser pulse duration or the temporal resolution of the detection system in conventional TALIF setups. With such systems, effective lifetimes cannot be directly measured, but have to be calculated from the natural lifetimes of the excited states, and quenching with all possible quenching partners, as indicated in eq. (5.5).

In order to circumvent this problem, the laser and detection system can be chosen in a way that the timescales of interest are shorter than the effective lifetimes, even at high pressure. In this work, a picosecond laser system (EKSPLA) is used to generate laser pulses with a duration of approximately 32 ps. Because of the short length of the pulses, the excitation process of the atoms is much shorter than the effective lifetimes of the excited states, which for gas mixtures used here typically lie in the order of a few nanoseconds for

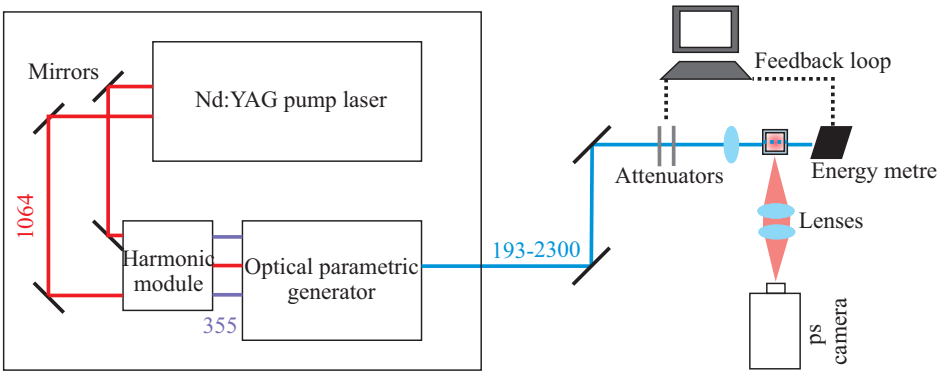

Fig. 5.4: Laser setup as used for the TALIF measurements.

O* and a few hundreds of picoseconds for H* at atmospheric pressure. Excitation therefore happens almost instantaneously, and excitation by the laser beam and de-excitation are not temporally convoluted.

The laser system, as shown in fig. 5.4, consists of three components, which are an Nd:YAG pump laser (EKSPLA PL2251, 10 Hz), an amplifier and harmonic generator (EKSPLA APL 2100 and H400), and a solid state optical parametric generator (EKSPLA PG411). The laser wavelength can be tuned continuously between 193 and 2300 nm. Typical output laser energies are in the range of a few hundreds of μJ, and are further reduced in order to avoid any saturation effects, which will be discussed later. Depending on the desired output energy, either a set of two variable attenuator plates, or one attenuator plate and a compensator (Layertec), are used for the attenuation. The attenuator plate has an anti-reflective coating, the attenuation of which is dependent on the incident angle of the laser beam. Therefore, to control the laser beam energy, the components are mounted on counter-rotational stages (Zaber T-NM17A04). The use of two components and the rotational stages ensures that a possible offset of the beam after travelling through the first attenuator is corrected for by the second component, so that its position is not dependent on the attenuation. The output laser energy is monitored by an energy meter (Gentec-EO, QW8SP-B-MT), and fed into a LabView PID energy control feedback loop. This allows the laser energy to be controlled precisely, and ensures that potential long-term drifts in the laser energy, which can occur when measuring over a number of hours, are counteracted. The standard deviation of the short-term shot-to-shot laser energy has an upper limit of 8%, and signals are accumulated over 64 or 128 laser shots (depending on the signal strength). Finally, the laser beam is focussed to a spot size of about a few hundreds of micrometres into the volume to be observed, i.e. the plasma effluent region. The small spot size of the beam allows for spatially resolved measurements with a spatial resolution in the same order.

The fluorescence light emitted is detected by a fast iCCD camera (4Picos dig Stanford Computer Optics, 780×580 pixels, (8.3×8.3) μm^2 pixel size, S25IR photo cathode), which is set up in a 90° angle to the laser beam. Synchronisation between camera and laser is achieved using the pre-trigger laser output as an external trigger for the camera. The signal

is imaged on the iCCD chip using two achromatic lenses (Thorlabs, AC050-010-B-ML) with a focal length of 8 cm each, so that the effective focal length is decreased to approximately 4 cm, resulting in a higher collection angle and therefore higher signal-to-noise ratio. The theoretical transmission of these lenses for all four fluorescence wavelengths of interest (O^*, H^*, Xe(6p'[3/2]$_2$) and Kr(5p'[3/2]$_2$), as indicated in fig. 5.2, is 99%. Optical filters for 845 nm, 656 nm, 835 nm, and 825 nm, respectively, with a spectral bandwidth of 10 nm each, are fitted in front of the cameras during the detection of the detection signals for the different species.

TALIF signal measurement

In order to obtain absolute species densities, several quantities in eq. (5.14) have to be measured. One of these parameters is S_F which is the temporally, spatially, and spectrally integrated fluorescence signal.

The spatial integration is performed by choosing a defined region of interest (ROI) from the camera image, and taking the sum of the signal within this region. This means that the spatial resolution is limited by the choice of ROI. Figure 5.5 (a) shows the fluorescence signal of O^* at 844 nm, at the strongest excitation wavelength of 225.65 nm. A bright region is visible in the middle of the picture where the laser beam intersects with the jet effluent region, leading to excitation of O from the ground state, and subsequent emission of fluorescence light. Similarly, fig. 5.5 (b) shows the fluorescence signal obtained from the calibration with Xe at 835 nm and a laser wavelength of 224.30 nm. The calibration cuvette containing the Xe gas has much larger dimensions compared to the 1 mm discharge gap of the μAPPJ, therefore, the fluorescence signal is visible over the whole width of the CCD chip. For both measurements, the same ROI is chosen, as indicated in the figures.

The temporal integration is performed by choosing the camera gate width long enough to collect almost all of the fluorescence light from the exponential fluorescence decay after the laser pulse (>98% under all measurement conditions). The relation for this long-gate measurement is schematically shown in fig. 5.6. The species with the longest effective lifetime of the four species of interest is Kr(5p'[3/2]$_2$), due to the long natural lifetime of the excited state, and the low pressure of 1 Torr in the reference cell. The measured lifetime for Kr(5p'[3/2]$_2$) under these conditions is 21.4 ns. Therefore, a camera gate width of 100 ns is chosen, which means that 98-99% of the fluorescence signal is captured, depending on the camera start delay. The same gate width is chosen for all other species, leading to a light capture higher than 99.9%.

Temporal and spatial integration of the fluorescence signal gives $s(\lambda)$, the spectrally dependent fluorescence signal. $s(\lambda)$ is measured for different wavelengths by tuning the laser wavelength over the resonant transition. The wavelength step is 0.01 nm, which is also the minimum possible gate step for the particular laser used in this work. For the wavelength scan, usually 4 points before and after the central wavelength are measured, resulting in 9 measurements for each wavelength scan. Additionally, a measurement of the background signal is performed by manually closing the shutter of the laser output. By

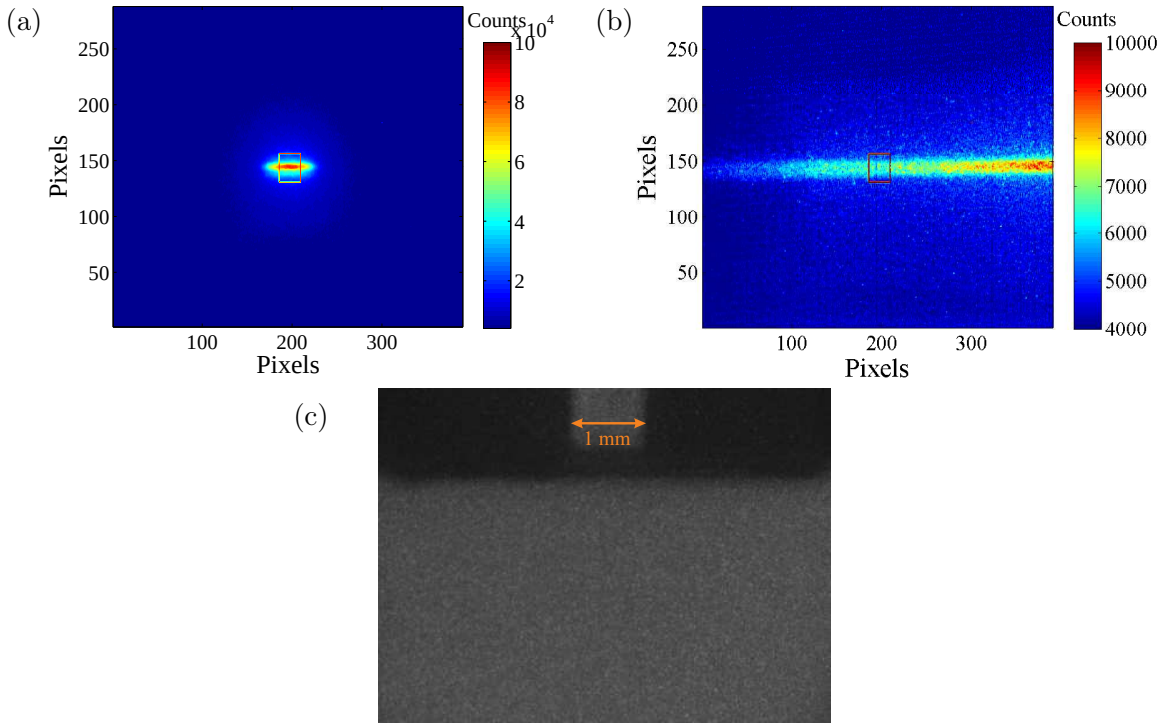

Fig. 5.5: Example fluorescence images for O (a) and Xe (b) measured with the ICCD camera. (c) Image taken with a background light to determine the distance between laser beam and jet nozzle.

subtracting this background signal, potential background light from the plasma source is accounted for, as well as base noise from the detector. Spectral integration of $s(\lambda)$ results in the absolute fluorescence signal S_F. Typical wavelength scans for atomic hydrogen and oxygen are shown in fig. 5.7.

The spectral integration is performed by fitting a Gaussian function to $s(\lambda)$, and integrating under the curve. The Gaussian fitting function is chosen because the main line broadening mechanism under the experimental conditions is because of instrumental broadening due to the relatively large spectral bandwidth of the laser, and it is assumed that the spectral profile of the laser is Gaussian. Because of the short laser pulses of about 32 ps, the minimum of the spectral laser width is limited by the Fourier limit

$$\Delta\lambda\Delta t \geq \frac{\lambda^2}{c}C \tag{5.17}$$

where C is a constant, which depends on the temporal shape of the laser pulse. Assuming a Gaussian shaped line profile ($C = 0.44$ [181]), we obtain $\Delta\lambda \geq 2.3$ pm. As previously mentionded, the bandwidth as stated by the laser manufacturer is 4 cm^{-1} ($\Delta\lambda = 0.02$ nm). Equation (5.17) also shows that the laser used in this work is naturally spectrally wider than lasers used in typical ns-TALIF setups, due to the shorter pulse duration.

Other broadening mechanisms, such as Doppler and pressure broadening, are much smaller under our experimental conditions. For atomic oxygen, the Doppler broadening

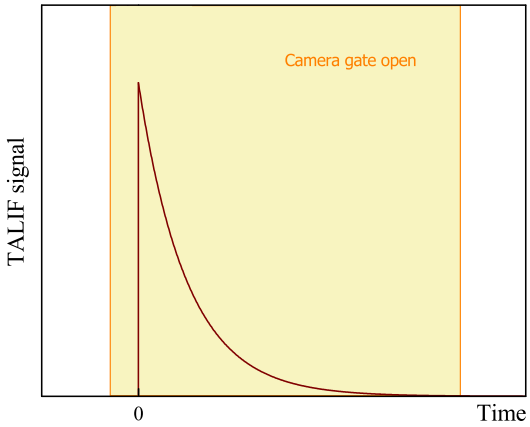

Fig. 5.6: Schematic of long gate width measurement. The camera gate (orange area) is chosen long enough to capture most of the emitted light from the fluorescence decay.

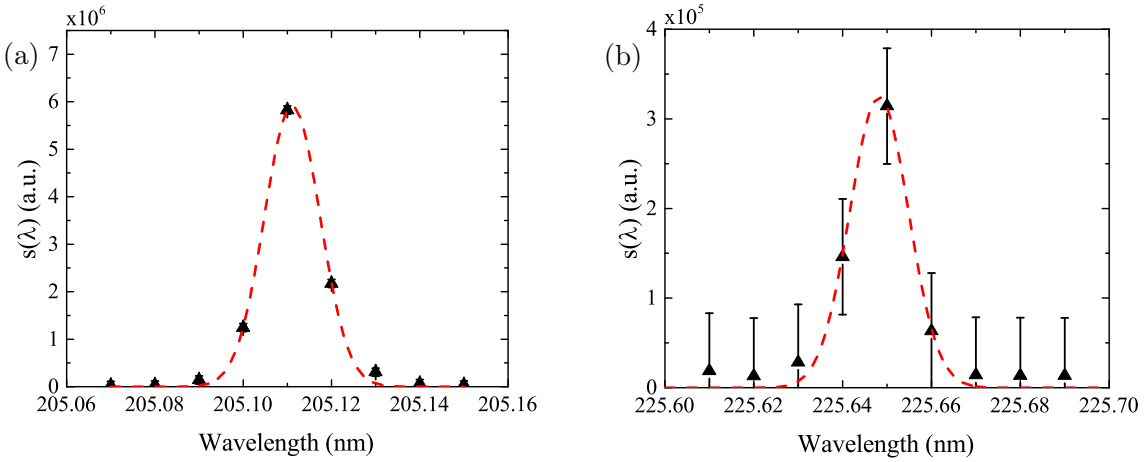

Fig. 5.7: Normalised fluorescence signal for (a) H* and (b) O* 500 sccm He with a H_2O content of 1240 ppm, 510 V_{pp}. Error bars show the standard deviation of the noise. The data is fitted with a Gaussian function.

$\Delta\lambda_D$ can be calculated as

$$\Delta\lambda_D^O = \frac{\lambda}{c}\sqrt{\frac{8k_B T_g \ln(2)}{m_O}} = 0.35 \text{ pm} \tag{5.18}$$

where $T_g = 315$ K and $\lambda = 112.8$ nm as half the excitation wavelength for atomic oxygen, which is in good agreement with measured values [182]. For atomic hydrogen, $\Delta\lambda_D^H = 1.3$ pm, which is still more than a factor 10 smaller than the laser bandwidth.

Pressure broadening coefficients for O by He and O_2 were determined in reference [182]. For 1 bar, pressure broadening by the background He can be calculated as

$$\Delta\lambda_L^O = 0.59 \text{ pm} \tag{5.19}$$

assuming that pressure broadening is dominated by the He background gas. Therefore,

both Doppler and pressure broadening are much smaller compared to the laser line width.

The quality of the signal measurement strongly depends on the investigated species and the experimental circumstances, and the signal-to noise ratio, which is defined here as

$$SNR = \frac{s - s_0}{\Delta noise} \tag{5.20}$$

where $\Delta noise$ is the standard deviation of the measured noise, and $s_{\mathrm{net}} = s(\lambda) - s_0$, which means the signal integrated over the ROI minus the background s_0. For example, when measuring atomic hydrogen under a H_2O variation, the measured H fluorescence signal is strong since H densities produced from H_2O are high. Figure 5.7 (a) shows normalised fluorescence signal of H^* as a function of the laser wavelength. The SNR for this measurement is good, resulting in a small $\Delta noise$ (shown as error bars) compared to the signal strength. On the contrary, for a measurement of O under a H_2O admixture, the signal to noise ratio is small, because the O densities produced from H_2O are low. This is shown in fig. 5.7 (b).

As discussed previously, the laser steps are limited to 0.01 nm, resulting in typically 4-5 possible measurements where a signal is obtained for each wavelength scan. Although a Gaussian function can be usually fitted to the experimental data with no difficulties, the fact that only so few points are available for the fit makes it difficult to assess the accuracy of the fitting procedure, particularly when the SNR is low.

TALIF lifetime measurement

In addition to the total fluorescence signal S_{F}, the branching ratio

$$a_{12} = \frac{A_{12}}{A_1 + Q_1} = b\frac{\tau_{\mathrm{eff}}}{\tau_{\mathrm{nat}}} \tag{5.21}$$

and therefore the effective lifetime τ_{eff} of the excited state, including radiative and quenching-induced contributions towards the decay, has to be determined, in order to calculate absolute species densities from eq. (5.14). The natural lifetimes for O^*, H^*, Xe(6p'$[3/2]_2$), and Kr(5p'$[3/2]_2$) are 34.7 ns, 17.6 ns, 40.8 ns, and 34.1 ns, respectively [76, 173]. In the case of atomic oxygen, this lifetime takes into account all sub-levels of the excited state. In the case of atomic hydrogen, the stated lifetime was obtained as an effective lifetime of the 3s and 3d state. The purely optical branching ratios b are 1 for O^* and H^*, and 0.733 and 0.953 for Xe(6p'$[3/2]_2$) and Kr(5p'$[3/2]_2$), respectively, as stated in the previous section.

In order to measure τ_{eff} with the ps-TALIF setup, the gate width of the camera is fixed, and the camera delay is increased incrementally, so that the fluorescence signal $s(\lambda)$ at different times after the laser pulse is obtained. A schematic of this is shown in fig. 5.8.

The choice of the gate step is generally dependent on the lifetime of the different excited species. For Kr(5p'$[3/2]_2$) with the longest lifetime of 22 ns, the gate width is chosen as 3 ns. The species with the shortest lifetime is H^*. Under high molecular admixtures, the H^* lifetime drops well below 1 ns, therefore, the gate step is chosen as 0.2 ns. Finally, the gate step for the measurement of O^* and Xe(6p'$[3/2]_2$) lifetimes, which typically lie in the

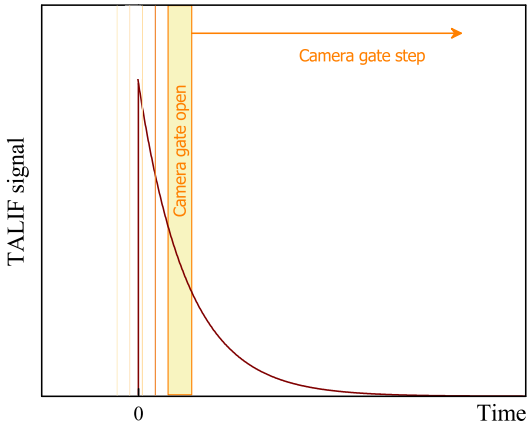

Fig. 5.8: Schematic of the lifetime measurement. By changing the camera delay, the camera gate is open at different times during the exponential decay of the fluorescence signal. By scanning over the whole decay, the lifetime of the excited state can be measured.

order of a few ns, is chosen to be 1 ns.

The choice of the camera gate width, for the lifetime measurement, does not have an impact on the measured lifetimes, as illustrated in fig. 5.9. Figure 5.9 (a) shows the measured signal of the O* fluorescence dependent on the camera delay for different gate widths. The plasma is operated with 1 slm He and 0.5% O_2. The laser pulse occurs at approximately $t = 0$. For images taken at $t < 0$ ns, the camera is not detecting any signal, or the fluorescence signal is partially detected by the camera. For example, for a camera gate width of 20 ns, the camera does not detect any fluorescence signal at $t < 20$ ns. At $-20 < t \leq 0$ ns, the camera starts to detect fluorescence signal, because the laser pulse lies within this time interval. Therefore, the signal increases with increasing delay time. At $t > 0$ ns, the laser pulse has excited the atoms, the camera detects the fluorescence signal without any "dead time" before the laser pulse. In this interval, the signal is decaying exponentially, and the decay time can be determined by fitting an exponential decay function. By plotting the log of the signal, the exponential nature of the decay is verified for all lifetime measurements (not shown here). All lifetimes obtained from fig. 5.9 (a) lie within $\tau_{\text{eff}} = (4.38 \pm 0.11)$ ns.

Similarly, fig. 5.9 (b) shows measured lifetimes of O* for a plasma operated in 500 sccm He and a H_2O content of (5390 ± 326) ppm. Again, all measured lifetimes lie in the range $\tau_{\text{eff}} = (3.18 \pm 0.12)$ ns. Therefore, it is shown that the measured effective lifetime is independent of the gate width. Generally, long gate widths are chosen for the measurements in this work in order to maximise signal. The gate widths used are 2 ns for H and Xe, and 10 ns for O, whose emission signal is weak when H_2O is admixed. For the lifetime measurement of Kr, a very long gate width of 20 ns is chosen. Due to the long lifetime, low pressure and low laser energy chosen for these measurements, the fluorescence signal is very weak. The choice of laser energy for the different species will be discussed in the next section.

As for the signal measurements, the quality of the lifetime measurement strongly depends

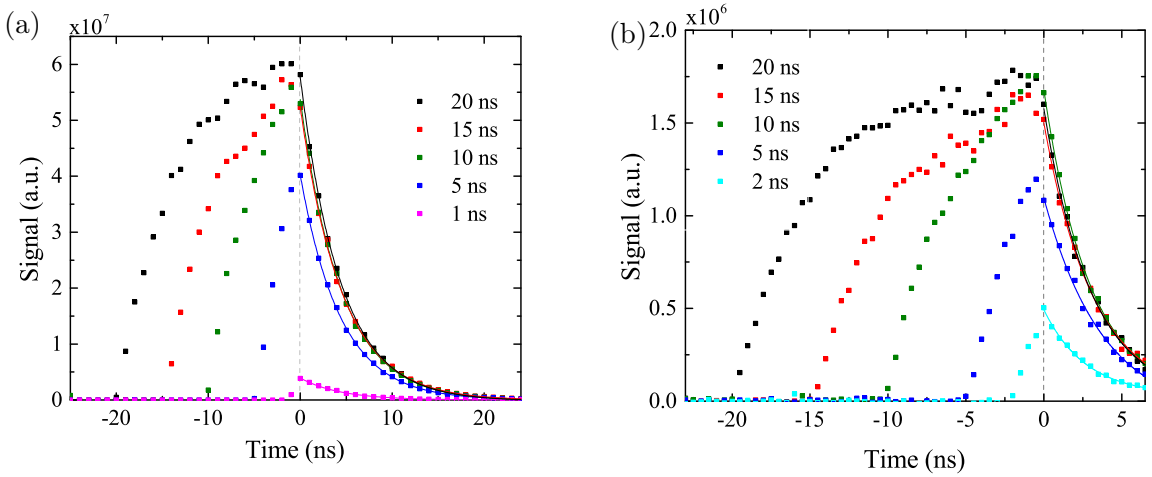

Fig. 5.9: Influence of the gate width on the measured lifetime of species. (a) Lifetime of O(3p ^{3}P) with 1 slm He flow rate and 0.5% O_2 admixture. (b) Lifetime of O(3p ^{3}P)) with 0.5 slm He flow rate, and a H_2O content of (5390 ± 326) ppm.

on the investigated species and the experimental circumstances, and the signal-to-noise ratio. The lifetime of the excited species can be obtained by fitting an exponential decay to the measured TALIF signal. This is shown for measurements of the atomic oxygen fluorescence for two different conditions in fig. 5.10. Atomic oxygen is produced in large quantities from O_2 (fig. 5.10 (a)), resulting in a good signal-to-noise ratio, whereas O densities produced from H_2O are much smaller (fig. 5.10 (b)), and $\Delta noise$ is large compared to the fluorescence signal. However, a large number of points is generally taken, and the fluctuation of the measurement is small. The decay can be easily fitted by an exponential decay. Using a 95% confidence band, errors are determined from the goodness of the individual fits. The effective lifetimes for Xe(6p'$[3/2]_2$) and Kr(5p'$[3/2]_2$) (at 10 Torr and 1 Torr pressure) have been measured each time an absolute calibration was performed. The lifetimes and their uncertainties are therefore calculated as average and standard deviations from multiple measurements as $\tau_{\text{eff}}^{\text{Xe(6p'[3/2]}_2)} = 6.5 \pm 0.5$ ns and $\tau_{\text{eff}}^{\text{Kr(5p'[3/2]}_2)} = 21.4 \pm 0.8$ ns, respectively.

Another influence that can have an effect on the measured lifetimes are impurities present in the gas flow. It is found that even in a "pure" He flow without any deliberate addition of molecules, weak TALIF signals of O* and H* can always be obtained. Impurities can enter the feed gas either through leaks in the gas supply line, or diffuse into the plasma effluent region from the ambient air. In the latter case, the amount of impurities is gradually decreasing towards the central axis of the APPJ. Because of this effect, the choice of ROI most likely influences the measured lifetime, with the lifetime becoming smaller with larger ROI. With good SNR, the lifetime does not change more than 10%, if the ROI is increased "radially" from 280 μm to 1 mm.

It can be estimated how high the unwanted admixture of air has to be to significantly influence the measured lifetimes. For H, quenching coefficients with He, O_2 and N_2 are $k_{\text{He}}^{\text{H}^*} = 0.317 \times 10^{-10}$ cm^{3}s^{-1} [89], $k_{\text{O}_2}^{\text{H}^*} = 32.6 \times 10^{-10}$ cm^{3}s^{-1} and $k_{\text{N}_2}^{\text{H}^*} = 20.1 \times 10^{-10}$ cm^{3}s^{-1} [76],

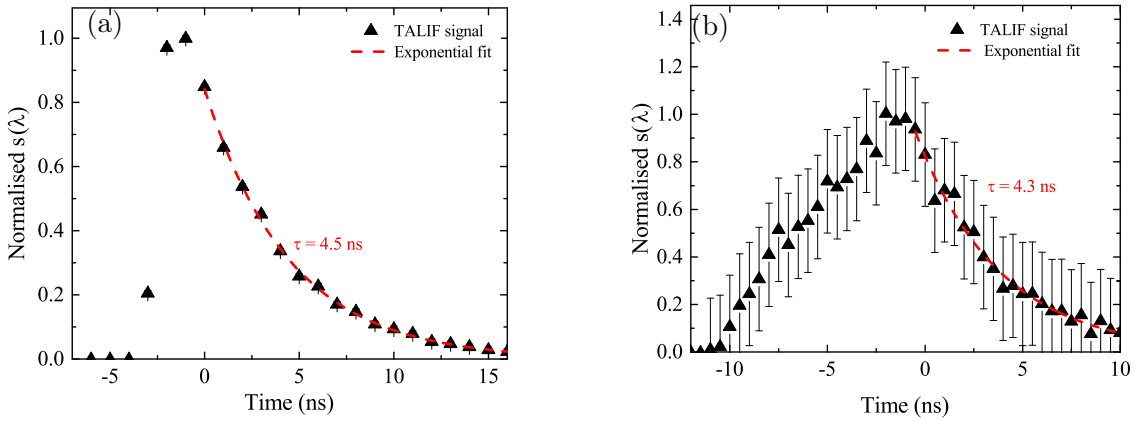

Fig. 5.10: Normalised measured fluorescence decay for (a) O* at 500 sccm He, 2.5 sccm O_2, 600 V_{pp} and (b) 500 sccm He with an H_2O content of 3800 ppm, 510 V_{pp}. Error bars show the standard deviation of the noise.

respectively. In pure He and at atmospheric pressure ($T_g = 315$ K), the lifetime of H* can be calculated as 1.26 ns. To obtain an effective decrease in this lifetime of 1 or 10%, the air admixture has to be in the order of 150 or 1700 ppm, respectively. Since these are relatively large concentrations of air, it is assumed that any small impurities being present in the gas do not have an impact on measured lifetimes, as long as measurements are carried out close to the the nozzle of the plasma jet, and the ROI is chosen small enough to not extend into regions of the effluent where gas mixing starts to play a role.

Energy saturation curves

From eq. (5.13) it is known that the observed TALIF signal depends on the square of the laser pulse energy. However, while deriving this term it was assumed that the laser energy is weak enough to only excite a small amount of the ground state atoms, and not disturb the system otherwise. In reality, several effects could be observed if the laser energy is chosen too high, such as photo-dissociation of molecules being present in the gas, or photo-ionisation when a third photon is absorbed by the excited atom. These effects would lead to a deviation of the square dependence of the TALIF signal and the laser pulse energy. This can be easily checked by varying the laser pulse energy, and plotting the spectrally integrated TALIF signal S_F against the squared laser pulse energy.

Figure 5.11 shows the spectrally integrated TALIF signals S_F for O (a), H (b), Xe (c), and Kr (d), as a function of laser pulse energy squared. For O, Xe, and Kr, S_F increases linearly with increasing squared laser pulse energy. At high energies, saturation effects start to play a role, and the deviations from this linear trend occur. H on the other hand shows a linear dependence on the squared laser energy over the whole investigated energy range. For all measurements, laser energies in the linear regime are used, and are exemplarily shown as red stars in fig. 5.11.

As shown in fig. 5.11, typical laser energies for ps-TALIF measurements are in the order of tens of microjoules, and even smaller for the calibration species Xe and Kr. This is

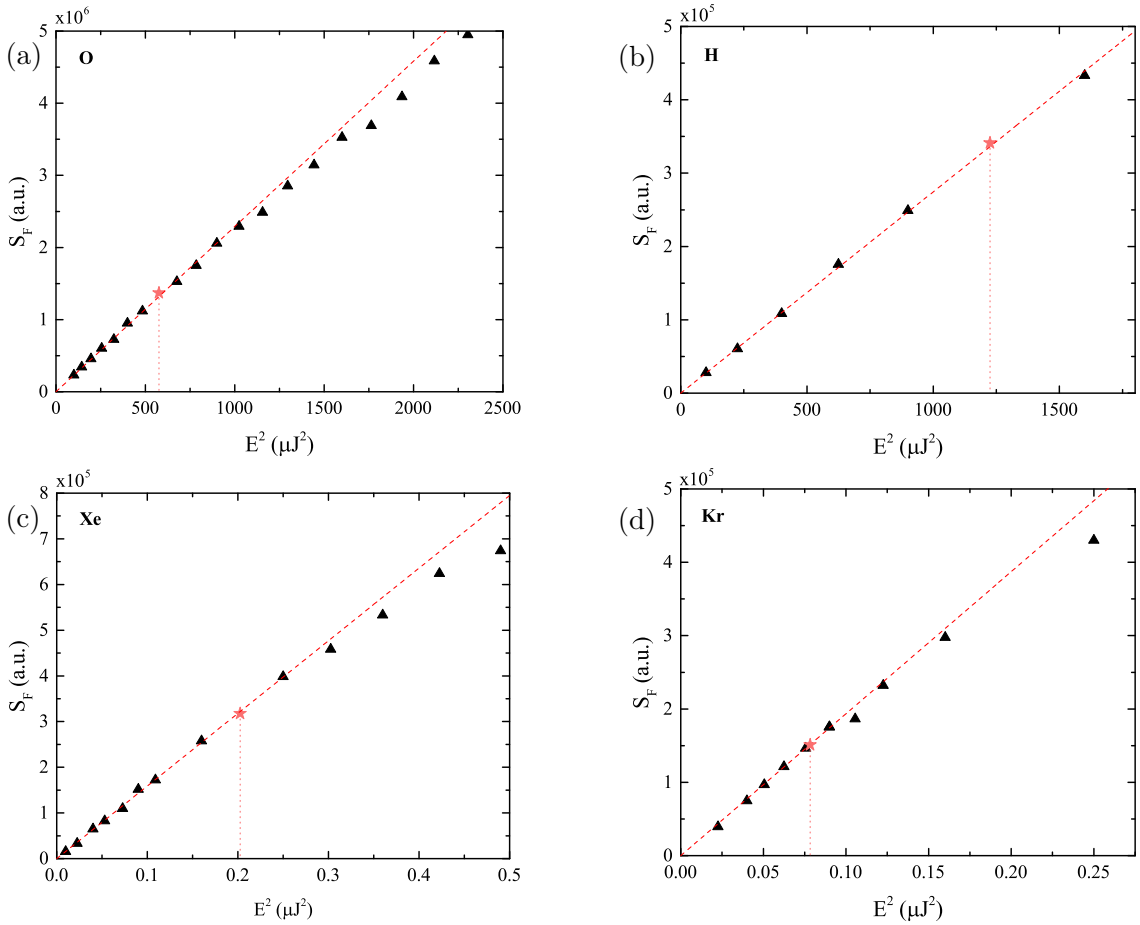

Fig. 5.11: Energy saturation curves for O (a), H (b), Xe (c), and Kr (d). All species except H show a deviation from the square dependence at high laser pulse energies. Red stars show typical laser energies used for the measurements.

much lower compared to ns-TALIF setups, where typical laser energies lie in the range of millijoules for lasers with a 10 Hz repitition rate [76, 82]. Therefore, comparing the ps-TALIF setup with a standard ns-TALIF setup, average powers are lower for the ps-TALIF setup, assuming the same excitation frequency. Pulse peak powers of the two systems are about in the same order of magnitude ($\sim 10^5$ W).

5.1.3. Constants and error estimation

Table 5.2 shows values used together with eq. (5.13) to calculate absolute densities of O and H. Values for the natural lifetimes as well as branching ratios have been taken from references [76, 173]. As discussed previously, the laser energy is usually monitored using an energy meter. Values for the quantum efficiency were taken as stated by the manufacturer of the detector. The spectral transmission of the optical filters were previously measured using a Shimadzu UV-1800 UV-VIS spectrophotometer with 0.1 nm resolution [122]. Transmissions for the calibration cuvette were obtained by measuring the transmitted laser energies using the energy meter at the respective wavelengths.

Tab. 5.2: Constants used for calculation of absolute densities using eq. (5.13) for the excitation wavelength λ_L, the natural lifetime τ_{nat}, the purely optical branching ratio b, the laser energy E_L, the quantum efficiency η, and transmissions of several optics. T_f, T_c^L and T_c^F are the transmissions of the optical filter, and the calibration cuvette for the laser and fluorescence signals, respectively.

Species	λ_L (nm)	τ_{nat} (ns)	b	E_L (μJ)	T_f (%)	T_c^L (%)	T_c^F (%)	η (%)
O	225.65	34.7	1	24	83.7	-	-	9.10
H	205.11	17.6	1	35	88.9	-	-	13.23
Xe	224.31	40.8	0.733	0.45	62.9	92	94	9.65
Kr	204.13	34.1	0.953	0.28	73.7	90	94	10.35

Table 5.3 shows an estimation of several errors associated with the calibration of absolute densities. The uncertainty of the transmission of the reference cell for both for the laser and fluorescence wavelength is 3% for both of the calibration gases. The error for the laser energy is assumed to be 8%, which was the maximum standard deviation of the shot noise observed in the experiment. The uncertainties of the cross section ratios and natural lifetimes are taken from references [76, 173]. Uncertainties for τ_{eff} are calculated from a 95% confidence interval of the fit of the exponential fluorescence decay. Typical error bars for different experimental conditions are shown in table 5.3. The uncertainty of τ_{eff} for the calibration gases is calculated as the standard deviation of several independent measurements, as discussed previously.

Tab. 5.3: Estimated relative uncertainties (in %) for several quantities in eq. (5.13), as well as resulting relative uncertainties for absolute densities measured under different conditions, which are O densities under an admixture of O_2 and H_2O, as well as H densities under an admixture of H_2O .

		T_c	E_L	$\frac{\sigma_{cal}^{(2)}}{\sigma_x^{(2)}}$	τ_{nat}	τ_{eff}	S_F	n
Species	O		8		5		-	
	H		8		10		-	
	Xe	3	8		5	7	10	
	Kr	3	8		10	4	10	
Measure-ment	O-O_2			20		4	5	**34**
	O-H_2O			20		11	15	**39**
	H-H_2O			50		5	5	**58**

The resulting uncertainties for the calculation of absolute species densities under several experimental conditions are calculated from the various error bars in table 5.3. The highest error of 58% is associated with the measurement of H in H_2O containing plasmas due to the high uncertainty of the two-photon excitation cross section ratio.

5.2. Excited species lifetimes and quenching rates

One of the key features of ps-TALIF over conventional ns-TALIF is the ability to actively measure lifetimes of the excited species at atmospheric pressure. This enables the measurement of quenching coefficients at high pressure. In this section, several quenching coefficients are measured for the quenching of O(3p ^{3}P) and H(n=3) with H_2O and O_2, respectively. All measurements are carried out within 1 mm distance of the plasma jet, so that the mixing with ambient air is minimal. At distances closer to the jet, shadowing effects start to play a role, and part of the fluorescence light is clipped by the plasma jet.

The plasma is operated at 510 V_{pp}. The only exception is the measurement of the quenching coefficient $k^{O^*}_{O_2}$, which was carried out at 600 V_{pp}. For the measurement of $k^{O^*}_{O_2}$, $k^{O^*}_{H_2O}$, and $k^{H^*}_{H_2O}$, variable concentrations of H_2O and O_2 are admixed to a total He flow of 500 sccm. For the measurement of $k^{H^*}_{O_2}$, 20 sccm of the total He flow is constantly humidified so that H is produced in the plasma, while the amount of O_2 is varied. Whenever the gas in humidified, the temperature of the bubbler is controlled to be 18°C, so that the amount of H_2O in the gas phase is constant. Since the laboratory is also temperature controlled at 21°C, it is assumed that the lower temperature of the H_2O bubbler prevents condensation of H_2O vapour on the surfaces of the gas tubes.

From the camera image, the ROI is chosen as an area of approximately 267×267 μm^2 (16×16 pixels on obtained images with binning 2x2) in the centre of the fluorescence signal. It was found that the choice of ROI does not lead to changes in the quenching coefficients within 4%, although the measured lifetimes can decrease significantly with increasing ROI due to the fact that quenching through impurities plays a more important role at the sides of the plasma effluent, as discussed previously. But since the inflow of air into the effluent region is the same at all gas mixtures for one particular admixture variation, this effect cancels out when calculating the quenching coefficients.

Quenching coefficients can be obtained by plotting the measured H* or O* decay frequency as a function of O_2 or H_2O admixture. Quenching coefficients are calculated from the slope of the linear fit. An estimate for the uncertainty is given by the standard deviation of the linear fit. Figure 5.12 shows decay frequencies of H* and O* under a variation of the O_2 and H_2O variation in the feed gas. The linear fit is instrumentally weighted with the error bars from the individual decay rate measurements. Table 5.4 shows a comparison of quenching coefficients measured in this work and values obtained from the literature.

In order to calculate densities of all quenching species correctly, the gas temperature was measured using a thermocouple at the jet exit for the different plasma conditions. All measured gas temperatures lie between 35 and 42°C. For some gas mixtures, a slight variation of temperature is observed when the gas mixture is changed. For example, for a He-O_2 plasma (0.5 slm gas flow) operated at 600 V_{pp}, the gas temperature decreases a few degrees when the O_2 content of the plasma increases. A variation of the gas temperature within the mentioned upper and lower limit would lead to a maximum error in the quenching coefficient calculations of about 5%, in addition to the uncertainties in table 5.4.

A fluctuation of the bubbler temperature within the error bar of 1°C leads to an uncer-

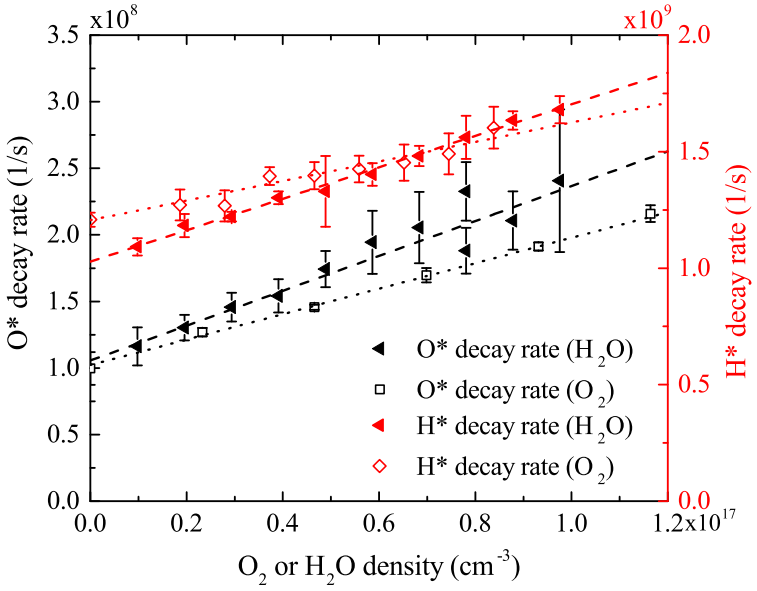

Fig. 5.12: O(3p ^{3}P) and H(n=3) decay frequencies as a function of molecular admixtures. Red: H* decay frequencies as a function of H_2O admixture (triangles) and O_2 admixture (squares). Black: O* decay frequencies as a function of H_2O admixture (triangles) and O_2 admixture (squares). Quenching coefficients for the excited states can be calculated from the slope and are given in table 5.4. O_2 and H_2O admixtures are calculated using $T_g = 315$ K.

tainty of 6%, in addition to the uncertainties in table 5.4.

Tab. 5.4: Measured quenching coefficients and comparison with literature values.

Species	Quenching species	k_q (cm^3s^{-1})	k_q^{lit} (cm^3s^{-1})	Ref.
O(3p ^{3}P)	O_2	9.6×10^{-10} (±3%)	$(9.4 \pm 0.5) \times 10^{-10}$	[76]
O(3p ^{3}P)	H_2O	1.3×10^{-9} (±10%)	$(9.4 \pm 1.5) \times 10^{-10}$	[183]
			$(4.9 \pm 0.3) \times 10^{-9}$	[184]
H(n=3)	O_2	4.2×10^{-9} (±10%)	$(2.6 \pm 0.1) \times 10^{-9}$	[184]
			$(3.3 \pm 0.3) \times 10^{-9}$	[173]
H(n=3)	H_2O	6.8×10^{-9} (±3%)	$(9.1 \pm 1.6) \times 10^{-9}$	[183]
			$(1.1 \pm 0.1) \times 10^{-8}$	[184]

5.2.1. Quenching of O(3p ^{3}P) with O_2

From the ps-TALIF measurement, a quenching coefficient $k_{O_2}^{O^*} = 9.6 \times 10^{-10}$ cm^3s^{-1} is obtained from the slope in fig. 5.12 (white squares and dotted black line), with an uncertainty of 3%. The deviation from the literature value is only 2% and therefore in very good agreement. Dissociation O_2, which could be important to consider when calculating quenching coefficients from the linear fit, typically lies below 10% under the investigated operating conditions of the plasma. Therefore, dissociation of O_2 is neglected.

$k_{O_2}^{O^*}$ has been measured by Niemi et al. [76] using ns-TALIF in a flow-tube reactor at low pressure (thousands of Pa), finding $k_{O_2}^{O^*} = (9.4 \pm 0.5) \times 10^{-10}$ cm^3s^{-1} with an approximate

error of 5%. Therefore, good agreement between the value for $k_{O_2}^{O^*}$ in this work and the work carried out by Niemi et al. demonstrates that quenching coefficients can be obtained accurately by ps-TALIF measurements.

By extrapolating the linear fit to zero O_2 admixture in fig. 5.12, a lifetime of $\tau_{O^*,\mathrm{eff}} = 10.2$ ns is obtained in pure He. Taking the natural lifetime of O^* $\tau_{O^*,\mathrm{nat}} = 34.7$ ns [76], a quenching coefficient for O^* with He can be determined as $k_{He}^{O^*} = 0.03 \times 10^{-10}$ cm^{3}s^{-1} using

$$k_{He}^{O^*} = \frac{\frac{1}{\tau_{O^*,\mathrm{eff}}} - \frac{1}{\tau_{O^*,nat}}}{n_{He}} \tag{5.22}$$

This is well within quenching coefficients $k_{He}^{O^*}$ from the literature, which range from 0.016 to 0.15×10^{-10} cm^{3}s^{-1} [76, 89, 173, 185].

5.2.2. Quenching of O(3p ^{3}P) with H_2O

The quenching coefficient $k_{H_2O}^{O^*} = 1.3 \times 10^{-9}$ cm^{3}s^{-1} is obtained from the slope of measured decay frequencies shown in fig. 5.12 (black triangles and dashed black line) with an uncertainty of 10% from the linear fit.

A literature value for the quenching coefficient of O^* with H_2O has been obtained previously by Quickenden et al. [183] as $k_{H_2O}^{O^*} = (9.4 \pm 1.5) \times 10^{-10}$ cm^{3}s^{-1} using radiolysis of pure water vapour with an electron beam, and detection of fluorescence light using a photo-multiplier. The water vapour was created by heating up a supply of water connected to their experimentation cell. Meier et al. [184] have measured the same quenching coefficient using TALIF in a flow-tube reactor as $k_{H_2O}^{O^*} = (4.9 \pm 0.3) \times 10^{-9}$ cm^{3}s^{-1} under low pressure conditions in the mbar range. Calculated quenching frequencies using these quenching coefficients as well as coefficients for quenching of O^* with He [89] and literature values for the natural lifetime of O^* $\tau_{nat}^{O^*} = 34.7$ ns [76] are shown in fig. 5.13 for atmospheric pressure conditions. Quenching with other species, such as impurities or dissociation products from H_2O is neglected in the calculation. Clearly, the literature values for quenching coefficients for O^* with H_2O do not agree well with each other, resulting in large differences in the slopes of the calculated frequencies in fig. 5.13. The O^* decay measured in this work, which is also shown in fig. 5.13, lies between the two available literature values. It is shown that our experimental data lies closer to the data obtained using the quenching coefficient measured by Quickenden et al. [183], although this is the older of the two cited sources, and a non-linearity between quenching frequencies and H_2O content was observed in their experiment.

A comparison between the measured and calculated decay rates shown in fig. 5.13 shows a difference of the intercept at 0 ppm H_2O admixture. This offset is explained by the uncertainty of measuring the quenching coefficients of O^* with He, as discussed previously.

A partial dissociation of admixed H_2O molecules could provide an additional source of error. The dissociation degree is therefore investigated using GlobalKin. For the experimental conditions (500 sccm total He flow, 0.4 W plasma power), the dissociation degrees shown in fig. 5.14 at the end of the plasma channel at 3 cm are obtained for different H_2O

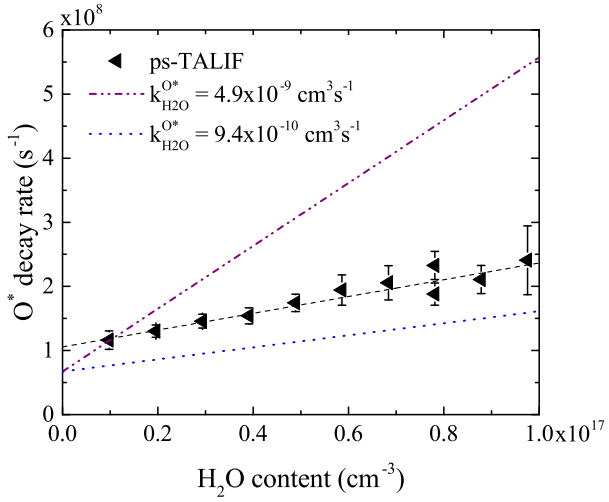

Fig. 5.13: O* decay rates measured with ps-TALIF (black triangles) under a variation of the humidity content. Also shown are calculated quenching coefficients using $\tau_{\mathrm{nat}}^{\mathrm{O}^*} = 34.7$ ns and quenching coefficients from the literature [183, 184].

admixtures.

$$D_{\mathrm{H_2O}} = \frac{n_{\mathrm{H_2O}}(3\ \mathrm{cm})}{n_{\mathrm{H_2O}}(0\ \mathrm{cm})} \times 100 \tag{5.23}$$

At very low H_2O content in the feed gas (1 ppm), up to 33% of the admixed H_2O molecules are dissociated by the plasma by the time they reach the end of the plasma channel. The dissociation degree rapidly decreases with increasing H_2O admixture. For admixtures greater than 500 ppm, the dissociation degree only changes very slightly around a value of 3.8%, which is too small to explain the difference between the quenching coefficients measured in this work and in the literature.

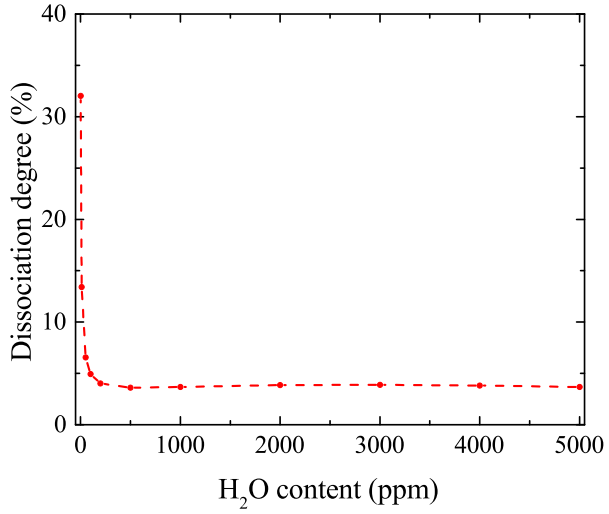

Fig. 5.14: Simulated percentage of dissociated H_2O molecules at the end of the channel. Simulation parameters are 500 sccm total He flow and 0.4 W.

5.2.3. Quenching of H(n=3) with O_2

The quenching coefficient $k_{O_2}^{H^*} = 4.2 \times 10^{-9}$ cm^{3}s^{-1} is obtained with an error of 10% (white diamonds and dotted red line in fig. 5.12). For these measurements, a fixed amount of 20 sccm He was constantly humidified and mixed with 480 sccm dry He. As soon as O_2 is added to the gas flow, the H^* fluorescence signal decreased significantly.

A literature value of $k_{O_2}^{H^*} = (3.3 \pm 0.3) \times 10^{-9}$ cm^{3}s^{-1} was obtained by Niemi et al. [173] using ns-TALIF in a flowtube setup at low pressure (in the range of 1000 Pa). Taking into the 10% uncertainty in the measurement carried out in this work, and the literature value from reference [173], both values are still in reasonable agreement with each other.

5.2.4. Quenching of H(n=3) with H_2O

The quenching coefficient $k_{H_2O}^{H^*} = 6.8 \times 10^{-9}$ cm^{3}s^{-1} is obtained from fig. 5.12 (red triangles) with an uncertainty of 3% from the linear fit. As in the case of the measurement of $k_{H_2O}^{O^*}$, the measured values are significantly smaller than the values obtained from the literature [183, 184], where they have been obtained as $k_{H_2O}^{H^*} = (9.1 \pm 1.6) \times 10^{-9}$ cm^{3}s^{-1} and $k_{H_2O}^{H^*} = (1.1 \pm 0.1) \times 10^{-8}$ cm^{3}s^{-1}, respectively, using the same techniques as described in section 5.2.2.

From the intercept of linear fit in fig. 5.12, an effective lifetime $\tau_{H^*,\mathrm{eff}} = 1$ ns is obtained in pure He. From this, a quenching coefficient $k_{He}^{H^*} = 0.42 \times 10^{-10}$ cm^{3}s^{-1} is calculated, using the literature value $\tau_{H^*,\mathrm{nat}} = 17.6$ ns [89, 173, 178] for the natural lifetime of H^* and eq. (5.22). As previously discussed for the determination of $k_{He}^{O^*}$ in section 5.2.1, a large range of values for $k_{He}^{H^*}$ can be found in the literature, ranging from 0.099 to 0.53×10^{-10} cm^{3}s^{-1} [89,173,178,185]. The value obtained in this work is close to the most recently measured value $k_{He}^{H^*} = 0.317 \times 10^{-10}$ cm^{3}s^{-1} [89].

5.2.5. General discussion

As discussed previously, the comparison between measured quenching coefficients and coefficients obtained from the literature varies strongly depending on the investigated species and the measurement conditions. Quenching coefficients with O_2 for O^* and H^* are in relatively good agreement with literature values, taking into account the different uncertainties in the measurements. Quenching coefficients with H_2O are generally not very well documented in the literature, which makes a comparison with the measured values difficult. Generally speaking, in the case of H_2O admixtures, quenching coefficients are lower than the literature values, with the exception of the value for $k_{H_2O}^{O^*}$ measured by Quickenden et al. [183], who did not observe a linear trend between quenching densities and measured decay rate. Lower measured quenching rates could be explained by an underestimation of the amount H_2O in the feed gas, which would be the case if the He is not saturated with H_2O after passing the bubbler. In the case of $k_{H_2O}^{H^*}$, the measured quenching coefficient would approach the literature value, if the saturation of He with H_2O only reached about 60%. In the case of $k_{H_2O}^{O^*}$, the saturation would be only about 35% to obtain good

comparison with the quenching coefficient proposed by Meier et al. [184]. If an insufficient saturation of the He feed gas with water vapour was the main error, one would expect that this "correction factor" would be similar for the measurements for O^* and H^*. Even if the He is not saturated with H_2O, the saturation degree should at least stay constant within the two measurements.

Additionally, it was discussed already in section 2.2.2, that almost complete saturation was observed for much higher flow rates in the slm region, while flow rates through the bubbler do not exceed 140 sccm during all measurements presented in this section.

One can compare the quenching effectiveness of H_2O and O_2 by taking the ratio $\frac{k^i_{H_2O}}{k^i_{O_2}}$, where i is O^* and H^*, respectively.

$$\frac{k^{O^*}_{H_2O}}{k^{O^*}_{O_2}} = 1.35 \qquad \frac{k^{H^*}_{H_2O}}{k^{H^*}_{O_2}} = 1.61 \tag{5.24}$$

For both species O(3p ^{3}P) and H(n=3), quenching by H_2O is 35% and 61% higher than quenching with O_2.

The measurement of quenching coefficients using ps-TALIF could be improved further in the future for a better comparison with literature values, for example by keeping the gas temperature constant, and investigating the dissociation degree in the plasma more accurately for different measurement conditions. Quenching coefficients in the literature are usually measured at slightly lower gas temperatures (around 300 K). However, the scope of this work was mainly to determine effective lifetimes of excited states for the absolute density calibrations carried out in the next section. The fact that quenching coefficients found in this work partially deviated relatively far from literature values shows the advantage of using ps-TALIF, since the effective lifetimes can be actively measured, and no use of coefficients from the literature is necessary.

5.3. Reactive oxygen densities under plasma parameter variations

5.3.1. Variation of O_2

One of the most studied molecular admixtures in the μAPPJ is O_2. It was found previously both in experimental and simulation work [95, 102, 103, 186], that the atomic oxygen densities peak around 0.5-0.6% O_2 admixture. Recent measurements carried out by Ellerweg et al. [95] in a very similar μAPPJ to the one used in this work, using two different diagnostic techniques, ns-TALIF and molecular beam mass spectrometry (MBMS), also showed this trend.

Figure 5.15 shows absolute atomic oxygen densities measured by ps-TALIF under a variation of the O_2 content in the feed gas (black triangles, data as in fig. 5.3). O densities show a peak between 0.6 and 0.8% O_2 admixture, and the measured trend agrees well with the measurements by Ellerweg et al. [95], which are also shown in fig. 5.15. The ps-TALIF data lies quantitatively between the MBMS data and the ns-TALIF data. Differences can

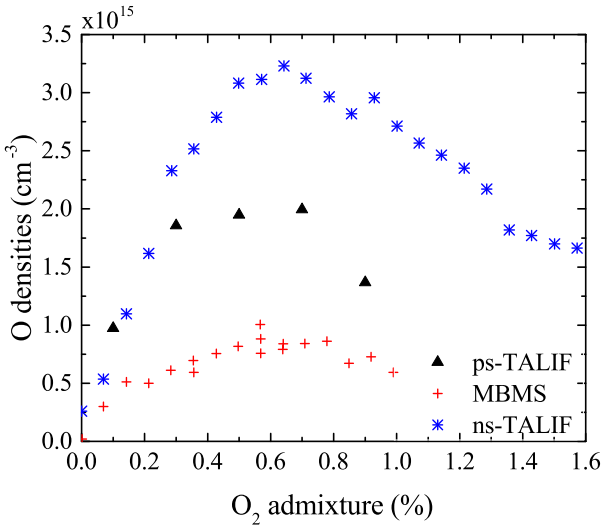

Fig. 5.15: Comparison of absolute atomic oxygen densities obtained with ps-TALIF under a variation of the O_2 content in the plasma with literature values [95]. Plasma parameters for the ps-TALIF measurements (black triangles) are 1 slm He and 600 V_{pp}. The measurements by Ellerweg et al. [95] (MBMS and ns-TALIF) were carried out at 1.4 slm He flow and 650 V_{pp}.

be explained by the slightly different experimental parameters such as gas flow and voltage, and as pointed out in reference [95], the different measurement conditions arising from the different diagnostic techniques, such as the gas flow pattern in the effluent region, and the fact that O can combine on surfaces of the mass spectrometer using MBMS.

The peak O densities measured by Ellerweg et al. using ns-TALIF are about 1.6 times higher than the values measured by ps-TALIF. Ellerweg et al. state the absolute error bar on the reliability of their TALIF measurements to be about 50%. If taking into account the typical error of 34% associated with the ps-TALIF measurements, and the fact that the measurements of Ellerweg et al. were carried out under slightly different experimental conditions, the agreement between the results can still be described as good. Additionally it has to be pointed out that Ellerweg et al. have to rely on calculated quenching coefficients to calculate their excited state lifetimes due to the low temporal resolution of the ns-TALIF setup, introducing an additional uncertainty, while lifetimes are directly measured using the ps-TALIF setup in this work. The large difference between the ns-TALIF and MBMS data by Ellerweg et al. could arise from uncertainties in calculated decay rates.

5.3.2. Variation of humidity

Water molecules are naturally present in ambient air. As a result, they serve as a likely source of impurities in open air plasma sources, meaning that it is important to understand their role in reactive species production. Additionally, when these sources are in contact with biological samples, there is usually some interaction with H_2O coming from liquid surfaces, such as a wound. It is therefore of great interest to investigate the amount of O that can be produced from humidity in the feed gas.

Figure 5.16 shows the O densities produced under a variation of humidity in the feed gas. The black triangles represent those measured by ps-TALIF in this work, while the blue plus symbols are those measured using ns-TALIF by Benedikt et al. [44]. Considering first the ps-TALIF measurements from this work, it can be observed that at admixtures > 100 ppm, O densities are slightly increasing with increasing H_2O content in the feed gas, reaching a plateau around 2000-2500 ppm. This trend agrees with previously discussed O densities measured by VUV-FTAS in section 4.6.3. However, absolute O densities measured with ps-TALIF in the μAPPJ are about a factor 2.3 smaller than O densities measured with VUV-FTAS in the mod-μAPPJ in the plateau region. Possible reasons for this difference could lie in the different surface-to-volume ratios of the two sources, resulting in different recombination probabilities for O at the reactor walls, and the fact that O is measured at different positions in the jet using the two setups (in the centre of the discharge at 1.2 cm in section 4.6.3 and outside the channel in this section). Differences in measured absolute densities can also arise from the two very different diagnostic techniques used here and in the previous chapter (ps-TALIF vs. VUV-FTAS) and the uncertainties associated with them.

O densities are generally about two orders of magnitude lower than in the case of an O_2 admixture, which has been discussed in the previous section. At very low H_2O content, a sharp increase of O densities with decreasing H_2O content is observed. A peak value of 2×10^{13} cm^{-3} is obtained when no H_2O is actively admixed to the He background gas.

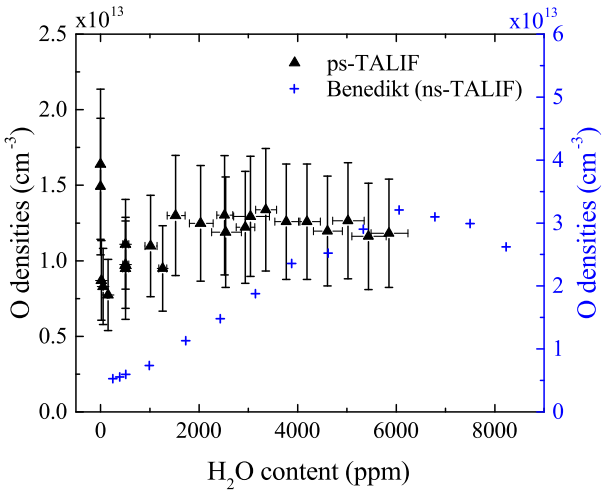

Fig. 5.16: Absolute ground state atomic oxygen densities as a function of humidity content of the He feed gas. Measurements were taken at 500 sccm total gas flow, and 510 V_{pp}. Blue crosses show comparison with reference [44].

The measurements of Benedikt et al have been carried out using ns-TALIF in a controlled He atmosphere. Under their plasma operating conditions (1.4 slm total He flow, 565 V_{pp}), they observed an increase in O up to 3×10^{13} cm^{-3} at 6000 ppm, followed by a short decrease until the plasma extinguished at 8000 ppm, as shown in fig. 5.16. Therefore, their measured peak O densities are about a factor 2.5 larger than the values obained in this work. One possible reason for the large difference lies in the fact that with their ns-TALIF system,

Benedikt et al. are not able to determine their O* lifetimes experimentally. Therefore, they calculate the effective decay rate using the quenching coefficient $k^{O^*}_{H_2O} = 4.9 \times 10^{-9}$ cm^{3}s^{-1} from reference [184]. However, as discussed previously (fig. 5.13), calculating the effective lifetimes from these literature values can lead to large discrepancies compared to measured lifetimes under atmospheric pressure conditions, which manifest when used to calculate absolute densities, since absolute densities depend linearly on the effective decay rates

$$\begin{aligned} n_O &\propto \frac{a_{12}^{Xe}}{a_{12}^{O}} n_{Xe} \\ &\propto b_{12}^{Xe} \frac{A_{nat}^{Xe}}{A_{eff}^{Xe}} \frac{A_{eff}^{O}}{A_{nat}^{O}} n_{Xe} \end{aligned} \tag{5.25}$$

The different magnitudes of $k^{O^*}_{H_2O}$ can lead to both different trends and absolute densities, and could therefore also be a possible explanation for the different trends shown in fig. 5.16. The increase of O with increasing humidity content is much steeper in the work of Benedikt et al., and the peak occurs at a different H_2O admixture. The latter could also be due to the fact that they are using higher powers to sustain their plasma, which could shift the peak slightly towards higher molecular admixtures.

Additionally, using ps-TALIF, a strong increase of O towards very low admixtures is observed. These high O densities at low admixtures are most likely due to impurities in the feed gas, either because of O_2 entering the feed gas through small leaks, or diffusion of O_2 from the ambient air. Benedikt et al. would not observe these high densities at low admixtures, because their measurements were carried out in a He atmosphere.

In order to investigate the influence of impurities and distance to the plasma nozzle further, GlobalKin simulations are carried out for the μAPPJ. The plasma volume is set to the volume of the plasma channel ($3 \times 0.1 \times 0.1$) cm^3. Gas temperature and plasma power are fixed to 315 K and 0.4 W, respectively. The gas temperature was measured close to the nozzle of the jet using a thermocouple. It was found that the temperature stays constant at constant discharge voltage for different H_2O admixtures. The power density is assumed to be the same as in the jet described in the previous chapter, because the applied voltage is the same. This leads to a total power of 0.4 W at 510 V_{pp}. This power value agrees with powers previously measured in the μAPPJ [30]. Figure 5.17 shows simulated absolute atomic oxygen densities together with the measured results for a variation of the humidity content in the feed gas.

Figure 5.17 (a) shows absolute simulated O densities as a function of H_2O content in the feed gas, for different distances from the nozzle, and without any air impurities. Absolute O densities decrease with increasing distance to the nozzle, due to consumption of O in chemical reactions, mainly with OH (eq. (4.36))

$$O + OH \rightarrow O_2 + H$$

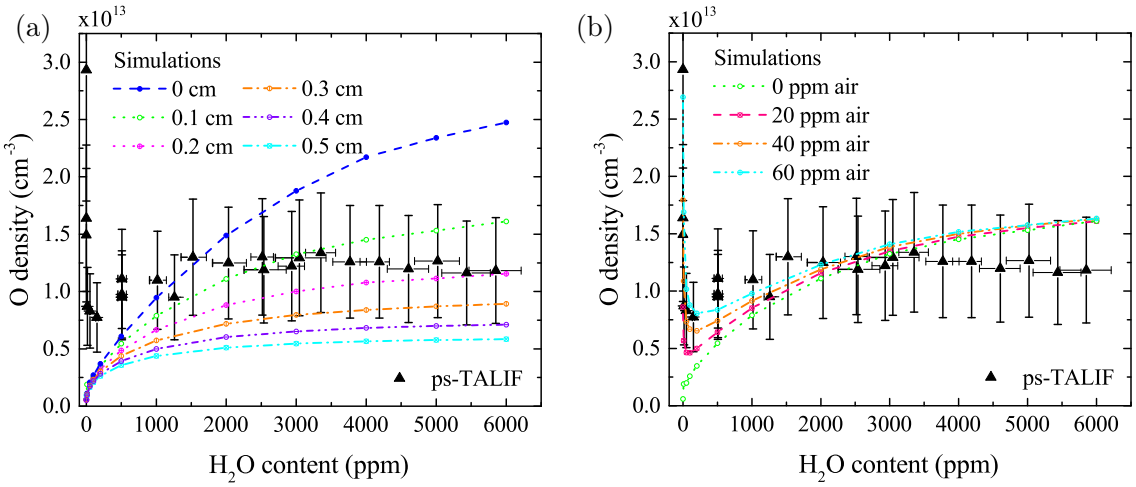

Fig. 5.17: Absolute measured O densities under a variation of the humidity content (triangles), as in fig. 5.16. (a) Simulation results for absolute O densities as a function of H_2O content and distance from the plasma nozzle, for a plasma power of 0.4 W. (b) Absolute simulated O densities as a function of H_2O for different air impurity contents, for a plasma power of 0.4 W and distance 0.1 cm from the nozzle.

Consumption by reactions with HO_2 gain more importance further away from the nozzle

$$O + HO_2 \rightarrow O_2 + OH \tag{5.26}$$

The trends for O densities under a humidity variation depend on the distance from the jet nozzle. While directly at the nozzle at 0 cm (blue line in fig. 5.17 (a)), O densities are constantly increasing with increasing H_2O admixture, O densities a few millimetres away from the nozzle approach a steady-state value at high H_2O admixtures. Ps-TALIF measurements were carried out at approximately 1 mm distance to the plasma nozzle (green line in fig. 5.17 (a)). At this distance, trends in the simulation and experiments are slightly different. In the simulation, O densities clearly increase with increasing H_2O admixture. In the experiment, a plateau is reached at about 1500 sccm. At higher admixtures, O densities stay constant within the error bars of the measurement. Simulated and experimental absolute O densities agree well, particularly considering that the formation of O from H_2O is complex, because it is not directly produced from dissociating H_2O molecules.

In order to investigate the role of impurities in the feed gas flow, different air impurity concentrations are assumed in the initial gas mixture. The amount of air is fixed at 20, 40, and 60 ppm, respectively. As a comparison, the amount of air impurity in a He 4.6 grade bottle is 32 ppm. The absolute O densities simulated under these conditions are shown in fig. 5.17 (b) for a distance of 1 mm from the nozzle. In the simulation, it is easily seen that at very low H_2O admixtures, < 100 ppm, O densities sharply increase towards decreasing H_2O admixtures, as observed in the experiments. It is therefore likely that the trend from the experiment is due to air impurities being present in the feed gas. At high humidity admixtures, the addition of air impurities only makes a small difference to absolute O

densities. It is therefore concluded that plasmas can be operated in a more controlled way by purposefully admixing molecules into the feed gas, because the produced RS are not strongly influenced by ambient conditions, which are susceptable to change if the plasma is not operated in a shielding gas atmosphere.

Because of the excellent agreement between simulations and experiments, the production and consumption pathways for different H_2O admixtures can be investigated using PumpKin. In the following discussion, production and consumption pathways are averaged over the whole discharge channel, and the pathway analysis is carried out for an impurity content of 40 ppm because of the good agreement between simulation and experiment at this admixture. An overview of the different pathways can be found in fig. 5.18.

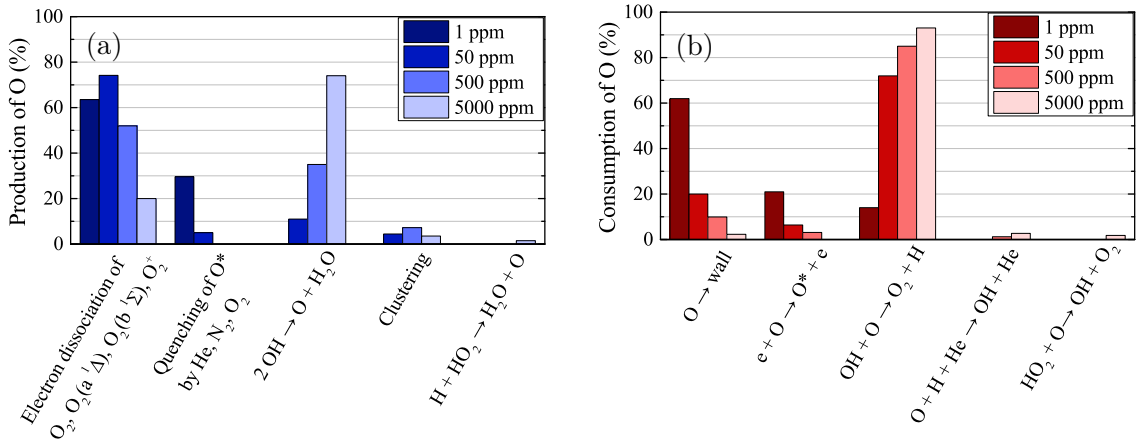

Fig. 5.18: Formation (a) and consumption (b) pathways for O at different humidity contents and a fixed air admixture of 40 ppm, 0.4 W and 500 sccm total He flow, averaged over the whole channel length of 3 cm.

The production pathways for O at different H_2O contents are shown in fig. 5.18 (a). At a H_2O admixture of only 1 ppm, the plasma chemistry is completely dominated by the oxygen and nitrogen reactions originating from air impurities. O is mainly produced by electron impact dissociation of molecular oxygen (eqs. (4.38) and (4.39))

$$e + O_2 \rightarrow O + O(^1D) + e$$
$$e + O_2 \rightarrow 2O + e$$

and the equivalent processes from the $O_2(a^1\Delta)$ and $O_2(b^1\Sigma)$ states. Further O is produced via quenching of excited $O(^1D)$

$$O(^1D)(+He, N_2, O_2) \rightarrow O(+He, N_2, O_2) \tag{5.27}$$

As the H_2O content increases, these processes become less relevant, and are increasingly replaced by reactions including hydrogen species. Particularly eq. (4.28)

$$2OH \rightarrow H_2O + O$$

which was found to be important for the formation of O in chapter 4, is found to play a keyrole in the formation of O under these conditions as well, and becomes the dominant production mechanism at high H_2O admixtures. Dissociation of O_2 remains one of the dominant production mechanisms also at high H_2O admixtures, since O_2 is actively formed in H_2O containing plasma, as discussed in section 4.6.4. On the other hand, densities of $O(^1D)$ decrease rapidly with increasing admixture of water, therefore, quenching of $O(^1D)$ becomes less important for the production of O at higher H_2O contents.

The O consumption pathways are shown in fig. 5.18 (b). The main loss mechanism for O at low H_2O admixtures are losses to the wall. This is reasonable as with low molecular admixtures, less chemical reactions take place in the plasma bulk. Wall losses decrease significantly at higher molecular content due to the formation of reactive species such as OH, H, and HO_2, which readily react with O in the gas phase. The pathways shown in eqs. (4.36) and (5.26)

$$O + OH \rightarrow O_2 + H$$
$$O + HO_2 \rightarrow OH + O_2$$

as well as the reaction

$$O + H + He \rightarrow OH + He \tag{5.28}$$

become important reactions at higher H_2O contents, with eq. (4.36) being the dominant consumption pathway.

5.4. Atomic hydrogen densities under plasma parameter variations

So far, the production and consumption of O under different molecular admixtures was discussed. In addition to atomic oxygen, the quantification of absolute H densities is also possible with ps-TALIF. This section will discuss several parameter variations, and also include a measurement of the spatial distribution of H in the plasma effluent region.

5.4.1. Variation of humidity

Figure 5.19 shows absolute H densities as a function of H_2O admixture in the feed gas (black triangles). H densities increase with increasing humidity content over the whole measurement range. At very high admixtures, H densities seem to reach a plateau just before extinction of the plasma.

Similar to fig. 5.17 for atomic oxygen, the dependence of H densities on the distance to the plasma jet nozzle and air impurity content is investigated. From fig. 5.19 (a) it is obvious that the simulations carried out at a distance between 0 and 1 mm from the plasma jet are closest to the measured values, depending on the humidity content in the feed gas. As discussed previously, this distance matches best the distance measured in the experiment. Therefore, experiment and simulations are in excellent agreement. Figure 5.19 (b) shows

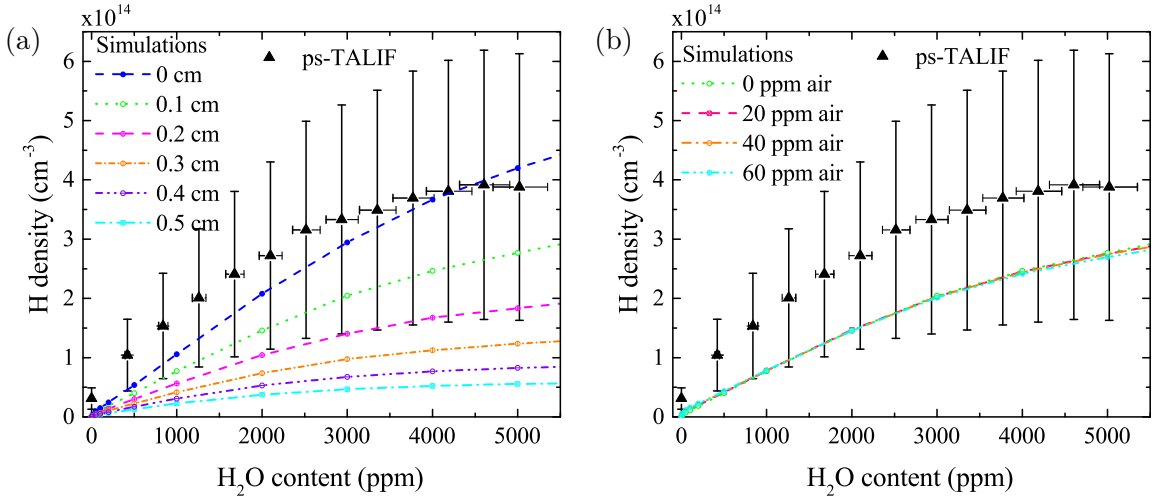

Fig. 5.19: Absolute ground state atomic hydrogen densities as a function of gas humidity content (black triangles). Also shown are simulation results for different distances to the jet nozzle (a), and different air impurity contents (b). Measurements were taken at 500 sccm total gas flow, and 510 V_{pp}. The input power for the simulations is 0.4 W.

H densities for different air impurity contents in the feed gas. From the results it is clear that H densities do not depend significantly on the amount of impurities in the plasma, in contrast to the trends found for O, where impurities had a large influence on O densities at low water admixtures.

The good agreement between simulation and experiment allows for the investigation of the most important formation pathways for H. The dominant pathways for production and consumption are shown in fig. 5.20 (a) and (b), respectively.

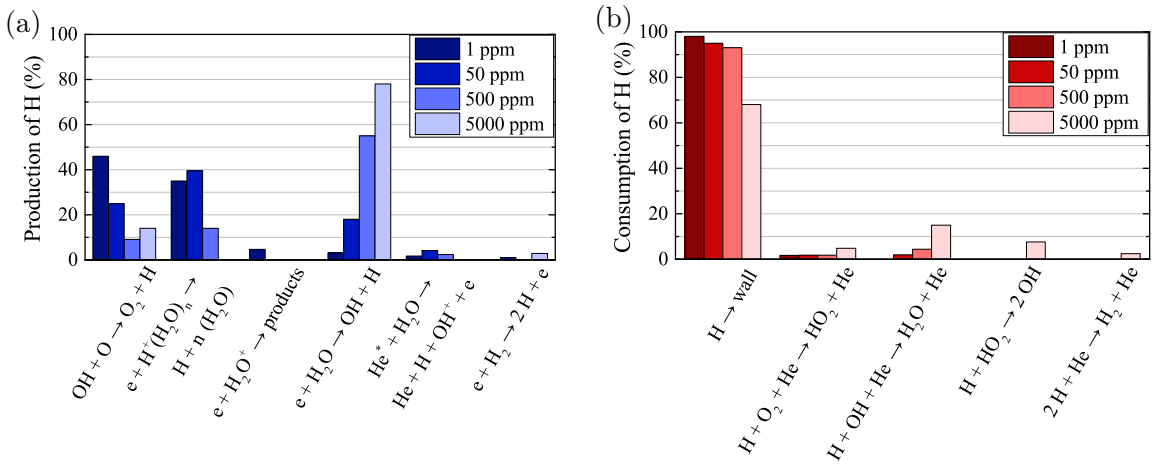

Fig. 5.20: Formation (a) and consumption (b) pathways for H at different humidity contents and a fixed air admixture of 40 ppm, 0.4 W and 500 sccm total He flow.

H production pathways vary strongly with humidity content. The dominant production pathway at low H_2O admixture is via collisions of OH and O (eq. (4.36)). At higher H_2O

admixtures, the relevance of this pathway decreases, and slightly increases again at the highest H_2O admixture investigated. Another important production mechanism for H at low H_2O admixtures is the destruction of protonated water clusters (eq. (4.35)) and H_2O^+ via dissociative recombination with electrons

$$e + H^+(H_2O)_n \rightarrow H + n \cdot H_2O$$
$$e + H_2O^+ \rightarrow H + OH \tag{5.29}$$
$$e + H_2O^+ \rightarrow 2H + O \tag{5.30}$$

At low H_2O admixtures, the plasma is electro-positive, and then becomes more electro-negative at higher H_2O contents. The electro-negativity β is defined as

$$\beta = \frac{n_-}{n_e + n_-} \tag{5.31}$$

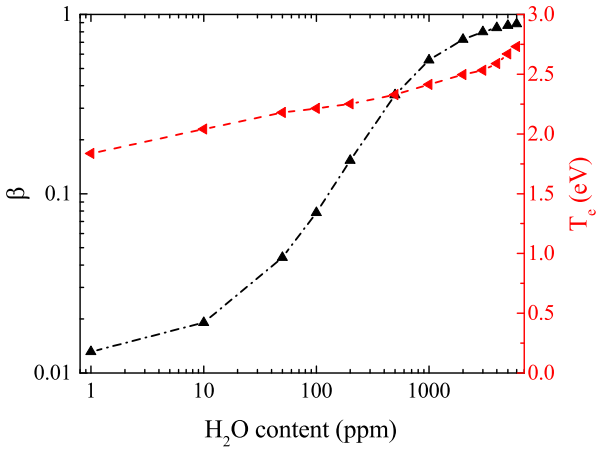

Fig. 5.21: Electro-negativity (black) and electron temperature (red) as a function of H_2O content in the feed gas at the end of the channel. Plasma parameters are 0.4 W, $T_g = 315$ K.

At low H_2O contents, electron densities are in the order of 9.2×10^{10} cm^{-3}, and H_2O^+ is the dominant positive ion after O_2^+ and $O_2^+ \cdot (H_2O)$, followed by $H^+(H_2O)$. Absolute densities of H containing cluster ions (including H_2O^+) are in the order of 10^{10} cm^{-3}. The ions build up quickly in the plasma channel, and electron-ion recombination reaction rates are generally higher than reactions involving neutrals.

At higher H_2O admixtures, H is predominantly produced by electron (eq. (4.23)) and He* (eq. (4.16)) impact dissociation of water molecules

$$e + H_2O \rightarrow H + OH + e$$
$$He^* + H_2O \rightarrow He + H + OH^+ + e$$

and also to a small extent via dissociation of H_2 by electrons.

$$e + H_2 \rightarrow 2H + e \tag{5.32}$$

The dissociation of ions and small ion clusters become less relevant. This is due to the fact that more water is available for electron impact dissociation. From 1 to 5000 ppm, the H_2O content increases by 3 orders of magnitude, while the number densities of cluster ions available for dissociation only increases by a factor of 6. Additionally, high densities of negative ion clusters of the form $OH^-(H_2O)_n$ are formed, leading to an increasing electro-negativity β of the plasma.

From 1 ppm to 5000 ppm humidity content, the electro-negativity increases from 0.013 to 0.88, as shown in fig. 5.21. Simultaneously, the electron temperature is increasing with increasing humidity from 1.84 to 2.73 eV, further enhancing the dissociation of H_2O by electron impact.

As for the consumption of H, the dominant process at all humidity contents is recombination at the wall to form H_2, as shown in fig. 5.20 (b).

$$H \rightarrow \frac{1}{2} H_2 \tag{5.33}$$

This is reasonable because of the high diffusion coefficient of H atoms, which is inversely proportional to the mass of the particle

$$D = \frac{k_B T_g}{m \nu_\mathrm{m}} \tag{5.34}$$

where ν_m is the collision frequency, and the lack of gas phase reactions. The reaction of H with H_2O has a high activation energy, so that the main reaction partners for H would be other reactive species, which are only present in low densities. Of course the loss of H to the wall is determined by the sticking coefficient γ_H and the return fraction f_H that is assumed in the simulation. However, as already discussed in section 3.2.4, these coefficients are usually not measured under similar experimental conditions to those used in this work. Their accuracy should therefore be judged carefully.

While at low H_2O admixtures, almost all H is consumed by losses to the wall, additional loss mechanisms involving chemical reactions with bulk species become more important at higher H_2O contents. In particular, collisions with OH, HO_2, O_2, and with H itself lead to destruction in the plasma bulk and formation of various short and long-lived species, such as H_2O and H_2.

5.4.2. Variation of gas flow

Similar to the investigations of OH in section 4.6.2, it is interesting to investigate the build-up of H in the plasma channel, and look into different production and consumption pathways at different positions in the jet. However, spatially resolved measurement in the channel using TALIF is challenging. In order to conduct these measurements, the jet has to

have a 45° angle towards the camera and laser beam. Under these conditions, shadowing effects of the laser and fluorescence light caused by the plasma electrodes can have an impact on absolute densities calculations. Additionally, since the jet is placed close to the laser focus, energy densities of the laser are high at the point of measurement, which leads to a damage of the jet windows by interaction with the laser.

In order to get an idea of the spatial distribution of H in the plasma channel, absolute H densities are measured under a variation of the total feed gas flow, with a constant admixture of H_2O. Changing the flow velocity and therefore the residence time of the gas, one can get an idea of how the densities are evolving within the channel. The relation between gas flow rate f and position x in the jet is

$$x = l\frac{500\ \text{sccm}}{f} \tag{5.35}$$

where l is the length of the jet. From the He flow rate and the length of the jet, the residence time of the gas in the channel is calculated. These values are then translated into a position in the jet, assuming a total gas flow of 500 sccm. Therefore, the point measured at 0.5 slm He flow corresponds to 3 cm in the jet. Figure 5.25 (a) shows absolute H densities at the end of the plasma channel, as a function of He flow rate (red triangles and top x-axis) position in the jet (black triangles and bottom x-axis). H densities increase with decreasing flow rate and increasing position in the jet. They are compared to simulated H densities along the channel for a total gas flow of 500 sccm (black dots). Absolute H densities increase with increasing position in the jet, to approximately 2 cm in the experiment, and then decrease slightly again. The same trend can be observed in the simulation, however, the build-up of H occurs quicker, and the maximum is reached at 1.5 cm. However, the agreement is still good, considering the fact that the method is a very rough approach of measuring the spatial dependence of H densities, and that an actual spatially resolved measurement would still be favourable.

Figure 5.22 (b) shows the lifetimes of excited H atoms measured with ps-TALIF under a variation of the flow and as a position in the channel. Lifetimes slightly increase when the absolute flow rate is decreased, corresponding to a longer residence time of the gas in the jet. This is likely due to a higher dissociation degree and subsequently a decrease in quenching. However, the change in lifetime is smaller than the error bar of the lifetime measurement, indicating that a variation of gas flow is only weakly influencing the H^* lifetime.

Figure 5.22 (c) shows the gas temperature measured just outside the plasma jet as a function of gas flow and position in the jet. The higher the gas flow, the lower the measured gas temperature, because the gas has less time in the channel to heat up.

Different production and destruction mechanisms are investigated at the positions 0-2 mm, 2-2.5 cm, and 3.3-3.5 cm (plasma effluent), as previously done in section 4.6.2 for OH. The results are shown in fig. 5.23 (a) and (b), respectively.

After the gas has just entered the jet (0-0.2 cm), the production of H is dominated by interactions of short-lived species, like electron impact dissociation of H_2O and dissociative

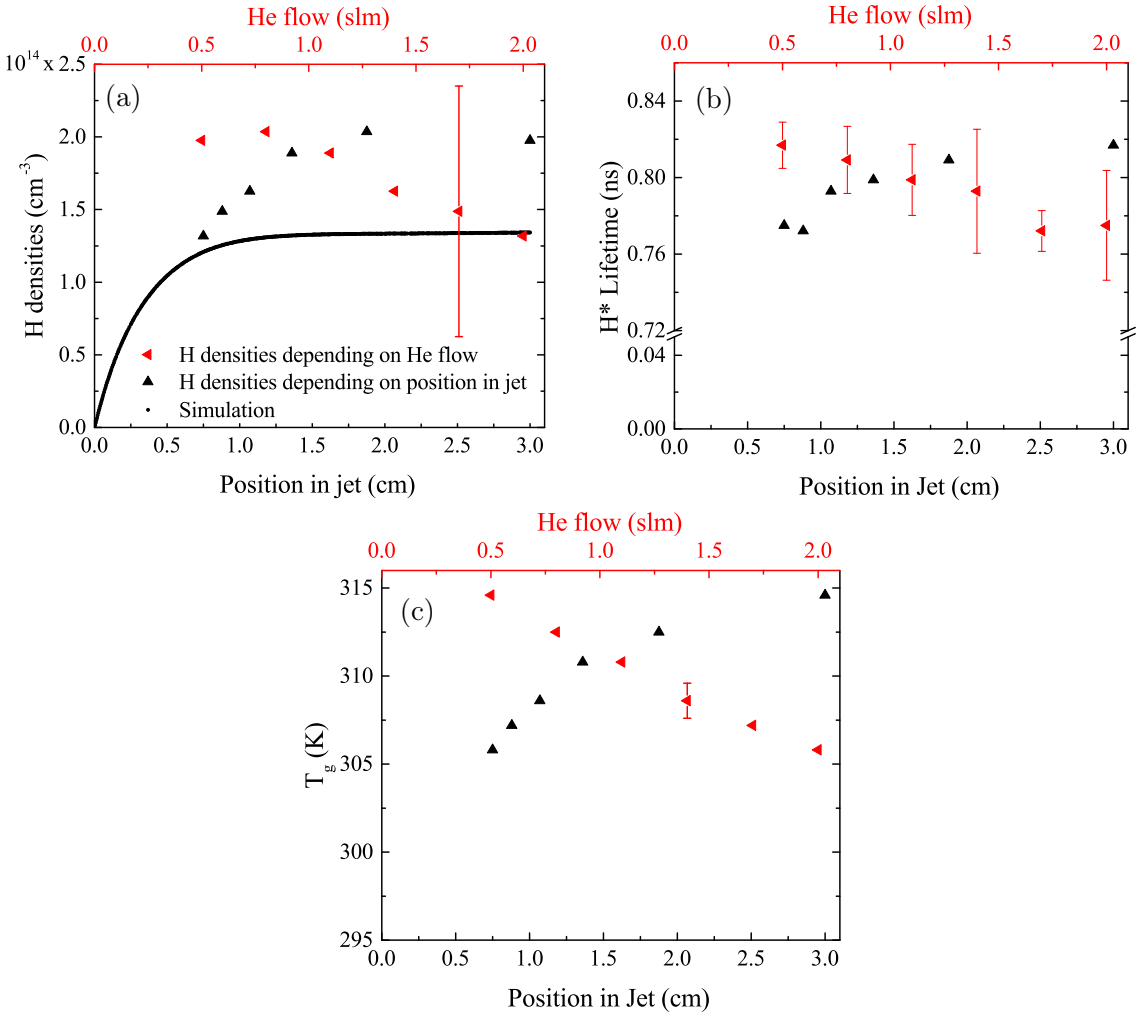

Fig. 5.22: (a) Absolute ground state atomic hydrogen densities as a function of gas flow velocity (red triangles, top x-axis) and position in the jet (black triangles, bottom x-axis) assuming a total gas flow of 500 sccm. Measurements were taken at 1260 ppm humidity content, and 510 V_{pp}. Black dots are simulated H densities for 0.4 W plasma power, 500 sccm gas flow, and 1260 ppm humidity. (b) Measured H lifetimes as function of total He flow (red triangles) and jet position (black triangles, respectively). Conditions are as in (a). (c) Gas temperature measured with a thermocouple at the end of the channel. Conditions are as in (a).

recombination of electrons with protonated water clusters. Further into the channel, other species have had time to form, such as O, OH, and H_2. Chemical reactions of OH and O eq. (4.36) and electron impact dissociation of molecular hydrogen then become important for the formation of H

$$e + H_2 \rightarrow 2H + e \tag{5.36}$$

In the effluent region, the total rate of H formation drops significantly, but small amounts of H can still be formed by reactions of O and OH (eq. (4.36)) and reactions between OH

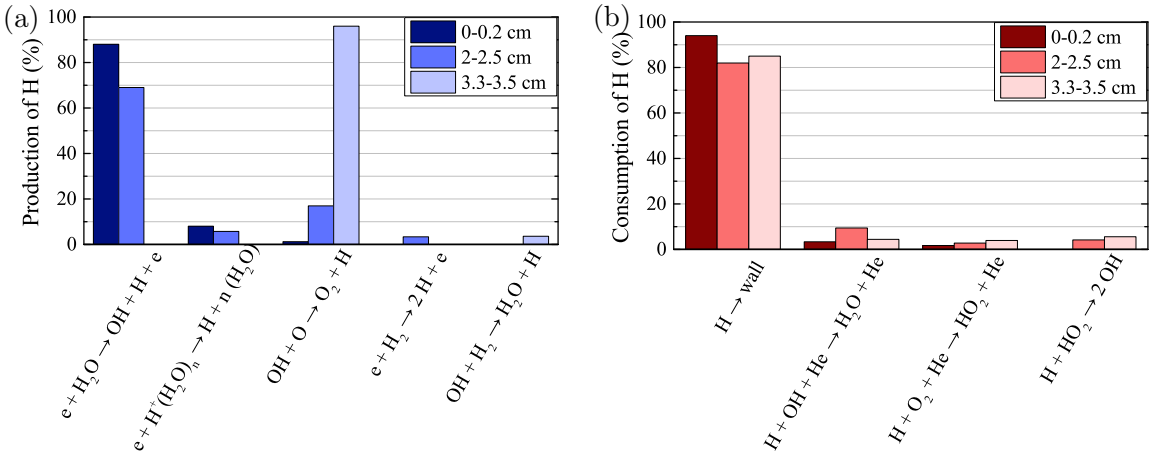

Fig. 5.23: Production (a) and consumption (b) pathways for H at different positions in the jet. Parameters are 500 sccm He, 1260 ppm humidity, and 0.4 W, as in fig. 5.22.

and H_2

$$OH + H_2 \rightarrow H_2O + H \tag{5.37}$$

The main destruction mechanisms for all investigated positions is loss of H to the walls. Further into the channel and in the effluent, H also reacts with long-lived species such as HO_2 and O_2, which are building up within the channel.

5.5. Atomic hydrogen density distribution in plasma effluent

For any application of APPs, knowledge about the distribution of reactive species is crucial in the regions where interaction of plasma and sample take place. As mentioned previously, diagnostics of this region are challenging, particularly as a result of the gradual gas mixing with ambient air. However, because ps-TALIF allows for the direct measurements of excited species lifetimes, spatially resolved measurements can be carried out in the effluent, even when the degree of mixing with ambient air is unknown. Figure 5.24 shows absolute densities of atomic H in the effluent region for two different gas flows.

Absolute densities of H produced in the jet do not vary between measurements with 0.5 and 1 slm total He flow, as shown in fig. 5.24 (a) and (b), respectively. Black dots in fig. 5.24 indicate where the centre of ROI is chosen. (For these particular measurements, seven ROIs of 10×15 pixels are used to divide the fluorescence signal in the horizontal direction, and signals are integrated over these ROIs.) At about 1 mm from the jet nozzle, the H density is 2.2×10^{14} cm^{-3} in both cases. In the grey area between 0 and 1 mm, no measurements were taken due to shadowing effects of the jet, as discussed previously. H densities are decreasing in the axial direction away from the nozzle. In the case of 0.5 slm He flow, H densities can be measured up to 3.5 mm away from the nozzle. Doubling the flow leads to approximately twice the distance that H can travel in the effluent region,

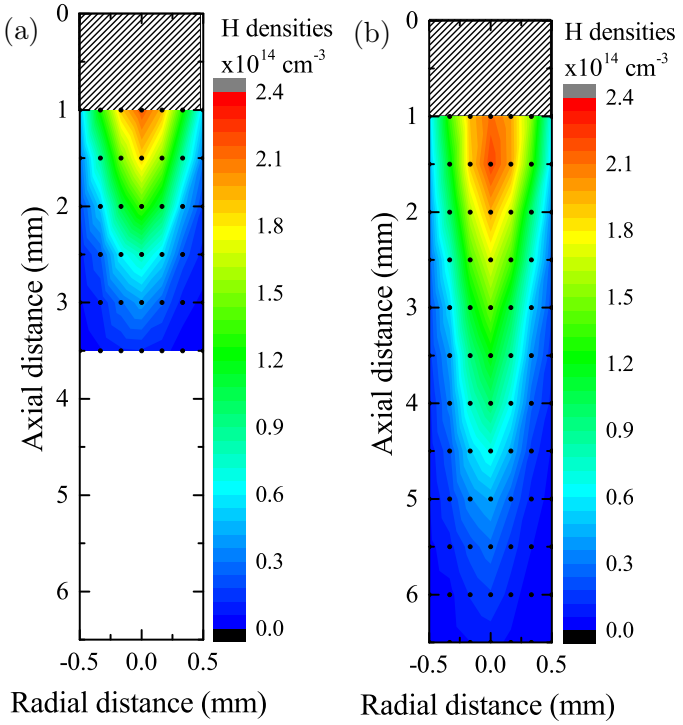

Fig. 5.24: Spatial distribution of ground state atomic hydrogen in the plasma effluent. Plasma parameters are 510 V_{pp}, 1260 ppm H_2O , (a) 0.5 slm total He flow and (b) 1 slm total He flow.

before the densities get too low to be detected by the ps-TALIF setup.

Figure 5.25 shows simulated H densities in the plasma channel (black dots, 0 - 3 cm) and the effluent region (3 - 3.5 cm), together with the experimental data from fig. 5.24 along the central axis, for 0.5 and 1 slm total He flow, respectively. For the higher gas flow shown in fig. 5.24 (b), H densities build up more slowly in the channel due to the shorter residence time of the gas in the plasma. However, in both cases, H densities are close to a steady-state value, leading to similar densities at the end of the channel. In the effluent, experimentally measured H densities are decaying faster in the case of low gas flow (fig. 5.25 (a)).

In both cases, simulated H densities are decaying faster in the experiment than in the simulation. This is likely to be because of gas-mixing of the effluent region with ambient air, which is not taken into account in the simulations. Figure 5.26 shows the H^* lifetimes measured with ps-TALIF in the plasma effluent for a total He flow of 1 slm. H^* lifetimes are constant on the central axis up to approximately 3 mm. Further away from the nozzle, H^* lifetimes decrease along the central axis due to gas-mixing and enhanced quenching with air species. Figure 5.26 (b) shows the spatial densities of air inferred from the measured lifetimes. Air densities are calculated using the following equation

$$n_{\text{air}} = \frac{A_{\text{H}^*} - \tau_{\text{H}^*}^{-1} - n_{\text{He}} k_{\text{He}}^{\text{H}^*} - n_{\text{H}_2\text{O}} k_{\text{H}_2\text{O}}^{\text{H}^*}}{0.2 k_{\text{O}_2}^{\text{H}^*} + 0.8 k_{\text{N}_2}^{\text{H}^*}} \tag{5.38}$$

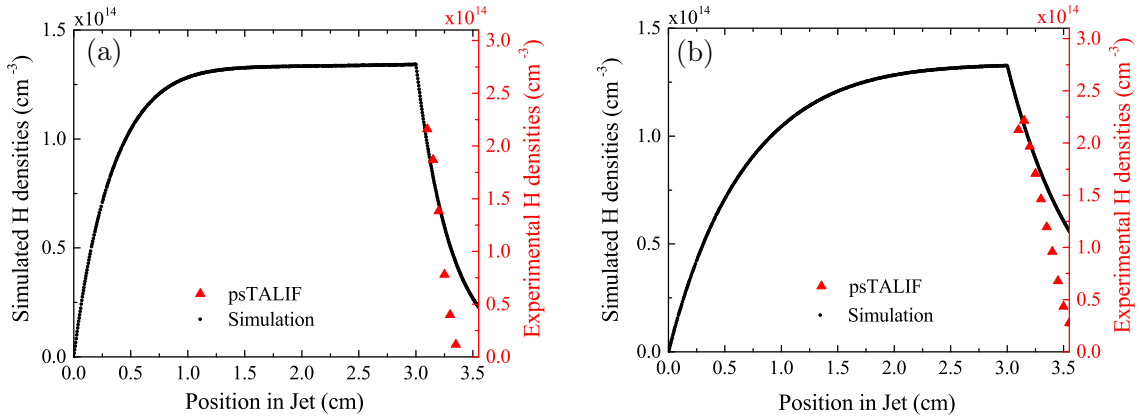

Fig. 5.25: Measured H densities (red triangles) in the plasma effluent and simulated H densities (black dots) in the plasma core and effluent. Plasma conditions are 510 V_{pp} and 1260 ppm H_2O . (a) Total He flow is 500 sccm. (b) Total He flow is 1 slm.

where n_{He} is calculated using the ideal gas law and $T_g = 315$ K, $n_{H_2O} = 1260$ ppm, $\tau_{H^*} = 17.6$ ns [173], $k_{He}^{H^*} = 4.14 \times 10^{-11}$ cm^{3}s^{-1} (calculated from τ_{H^*} , n_{He} and A_{H^*} from fig. 5.12 for 0 ppm H_2O admixture), $k_{O_2} = 3.26 \times 10^{-9}$ cm^{3}s^{-1} [173] and $k_{N_2} = 2.01 \times 10^{-9}$ cm^{3}s^{-1} [173]. The addition of small amounts of H_2O to account for humidity from ambient air (typically 45% relative humidity, which corresponds to 10540 ppm at 293 K) does not have an influence on the calculated air densities and is therefore neglected here.

By comparing fig. 5.26 (a) and (b) it is observed that the highest lifetimes occur where the gas-mixing with ambient air is least, which is close to the nozzle and in the axial centre of the jet. Further away from the jet, gas-mixing is enhanced, with intruding air densities of more than 10000 ppm.

Gas-mixing is also observed moving radially away from the central axis, leading to a decreased H^* lifetime. At high radial distances 0.5 and -0.5 mm, an increase of lifetime is observed again for certain axial positions. These increased lifetimes are likely to be artefacts, which occur because of the low intensity of the measured TALIF signal, leading to a higher uncertainty in the measured lifetimes.

The influence of gas mixing demonstrates the advantage of ps-TALIF compared to conventional ns-TALIF measurements, in which the gas mixture has to be obtained computationally, or the measurements have to be carried out in a protected He atmosphere. Using ps-TALIF, gas-mixing can be taking into account directly by measuring the effective lifetimes of the excited states.

5.6. Reactive species densities as a function of plasma power

In addition to the variation of gas flow velocity and gas mixture, the plasma power is a parameter that could potentially influence the gas chemistry. With respect to applications

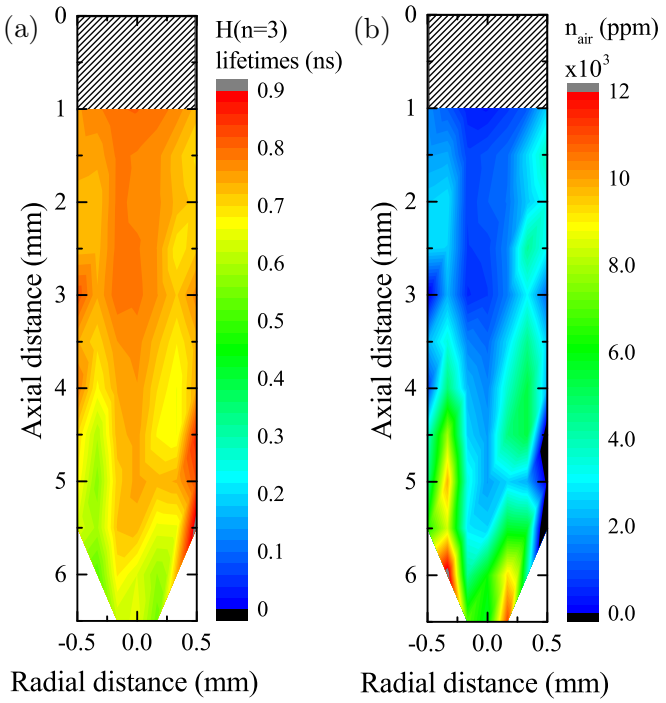

Fig. 5.26: Spatial distribution of H(n=3) lifetimes (a) and gas mixing (b) in the plasma effluent. Plasma parameters are same as in fig. 5.24 (b): 510 V_{pp}, 1260 ppm H_2O , 1 slm total He flow.

of plasmas such as biomedicine, the plasma power is a very limited parameter for tailoring RS densities, since increasing the power typically also leads to an increase in gas temperature [30], which usually is an undesired effect. However, it can be a valuable parameter for tailoring species densities if thermal effects can be neglected, for example for the treatment of less temperature dependent samples.

Figure 5.27 (a) shows simulated relative species densities in a He-H_2O plasma (0.5 slm He flow with 5000 ppm H_2O content) for different power densities. All species densities are increasing with plasma power. Several groups of species can be identified with regard to their response to plasma power. Excited ROS such as atomic and molecular oxygen metastables increase strongest over the investigated power range, with $O_2(b^1\Sigma)$ increasing most by a factor of 73. They are followed by He metastables, and ground state atomic and molecular purely oxygen and hydrogen containing species. Species containing both oxygen and hydrogen are the least affected by a change in plasma power, the increase only being a factor of about 2.5-3 for OH and HO_2, and 2.1 for H_2O_2. However, although the plasma power can have a strong effect on certain species, species density ratios are only weakly affected.

Of specific interest is the question of relative species density ratios are changing with plasma power. This is investigated for the example of OH in fig. 5.27 (b), which is found to be a key species in He-H_2O plasmas. If values in fig. 5.27 (b) are larger than one, it means that the respective species density is increasing faster than the OH density, while values below one mean species densities are increasing slower than the OH density. For

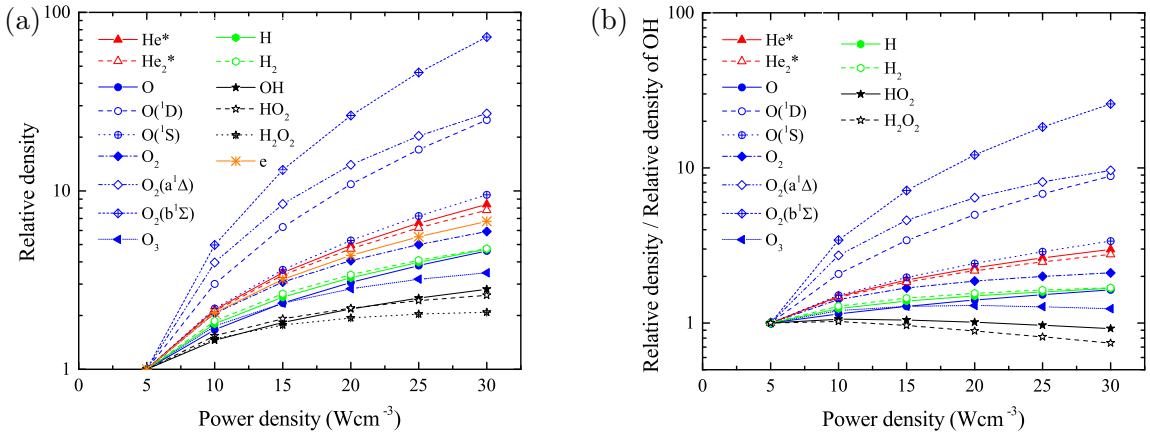

Fig. 5.27: (a) Simulated relative species densities as a variation of plasma power density in the μAPPJ for 0.5 slm He and 5000 ppm H_2O. Densities are normalised to the density obtained at the lowest power. The symbol colours are chosen as red for He metastables, blue and green for purely oxygen and hydrogen containing species, and black for mixed species. Gas temperatures in the simulation are taken from reference [30]. (b) as (a), but relative densities are normalised to the relative density of OH to show how species densities change relatively to OH densities.

example, at the highest investigated power, the density ratio of $O_2(b^1\Sigma)$ to OH is highest, while the H_2O_2 to OH density ratio is lowest. Therefore, if for the plasma application a large density of $O_2(b^1\Sigma)$ to OH is needed, the plasma should be operated at high powers.

5.7. Key results

Absolute densities of ground state atomic hydrogen and oxygen as well as lifetimes of their excited states, were measured using ps-TALIF, in the plasma effluent of the μAPPJ.

Quenching rates. Quenching rates of H(n=3) and O(3p ^{3}P) with O_2 and H_2O were measured. The quenching coefficients obtained for O_2 are in good agreement with literature values, taking into account the uncertainties of the measurement. The agreement of experimental quenching coefficients with H_2O is less good. This could be explained by the fact that a controlled addition of H_2O to the feed gas is more difficult than for gases where the admixture can be simply controlled by mass flow controllers, and that the experiment relies on a full saturation of the He with water. Additionally, at least in the case for quenching of O* with H_2O , the literature values are not in good agreement with each other.

O densities. Absolute densities of ground state atomic oxygen (O(2p^4 ^{3}P)) were obtained at about 1 mm of the nozzle of the μAPPJ. Absolute O densities under a variation of O_2 in the gas phase showed good agreement with previous measurements using molecular beam mass spectrometry and ns-TALIF. O densities were found to not change significantly when the feed gas humidity was changed. However, at very low humidity contents, an in-

crease of O densities was found. Through comparison with a global model, it was revealed that air impurities present in the gas could cause this effect. Generally, when modelling the system, the distance between laser beam and plasma nozzle in the experiment is important, since O decays rapidly in the plasma effluent.

H densities. Absolute H densities were found to increase with increasing humidity content in the gas flow. The dominant pathway for the formation of H was found to be electron impact dissociation of H_2O and with recombination to form H_2 at the wall the dominant destruction pathway, although the latter pathway should be treated with caution due to the lack of an accurate wall sticking coefficient for H under the experimental conditions, as discussed in chapter 3. A flow variation was performed to understand the spatial dependence of H inside the channel, where ps-TALIF measurements could not be carried out. Spatially resolved measurements revealed the H distribution in the plasma effluent, while measurements of H(n=3) lifetimes showed the spatially resolved gas mixing of ambient air into the plasma effluent.

Influence of plasma power. An increase in plasma power was generally found to lead to a faster increase of purely oxygen containing species such as O_2, O, and their respective metastable states, compared to the increase of purely hydrogen or mixed species. Therefore, these relative density ratios could be tuned by changing the power density. Generally, all species densities were found to increase with increasing power.

6. Production of H_2O_2 in the mod-μAPPJ and transfer into a liquid sample

H_2O_2 is a long-lived reactive species which can be created in H_2O containing plasmas and can enter a volume of liquid even after travelling several centimetres in open air. This is particularly interesting from the point of view of biomedical applications of APPs. Biological samples, such as cells, are typically embedded in biological media, which largely consists of water. An example for this is the potential treatment of wounds, which are usually covered in wound fluid, using plasmas. H_2O_2 particularly can readily transfer from the gas to the liquid phase, where it can undergo further reactions with the liquid or the cells. It is known to be an important signalling agent in cells [26], can permeate cell membranes, and is found to trigger cell death when applied in high concentrations. It is therefore important to quantify long-lived reactive species such as H_2O entering liquids after treatment by plasma.

In this chapter, a sample of H_2O is treated by the far exhaust of the mod-μAPPJ described in section 2.1.2, and absolute densities of H_2O_2 in the treated sample are quantified for different parameter variations using absorption spectroscopy in the liquid. Although no spatial information about species distribution can be gained from this diagnostic, it offers the great advantage of an easy calibration procedure with known amounts of H_2O_2 in the solution. Therefore, no calculations from cross-sectional data is necessary to obtained absolute species densities, in contrast to the diagnostics presented in the previous chapters 4 and 5.

From the measurements in the liquid sample, absolute gas phase densities of H_2O_2 can be obtained via a calibration. The comparison of experimental and numerical H_2O_2 densities offers an additional possibility of benchmarking the chemistry model, and gives insight into H_2O_2 formation and consumption pathways.

6.1. Absorption spectroscopy in the liquid phase

The experimental investigations presented in this section are divided into two parts. In a first step, absolute H_2O_2 densities are measured in a 2 ml water sample, which has been treated with the far effluent of the mod-μAPPJ described in chapter 2, using UV-VIS absorption spectroscopy (UV-liqAS). In a second step, a calibration with a known amount of H_2O_2 allows the absolute densities of H_2O_2 in the gas phase to be calculated. These densities are then compared to those obtained from a global model.

6.1.1. Measurements in the liquid phase

In order to investigate the amount of H_2O_2 deposited in the liquid, a small volume (2 ml) of deionised H_2O is treated by the exhaust of the mod-μAPPJ for a treatment time of 5 min. A 22 cm stainless steel metal tube with an elbow is attached to the gas exhaust and pointed onto the surface of a 20 ml beaker containing 2 ml of H_2O. The distance between the exit of the nozzle and the H_2O surface is 2 mm. A schematic of the setup is shown in fig. 6.1.

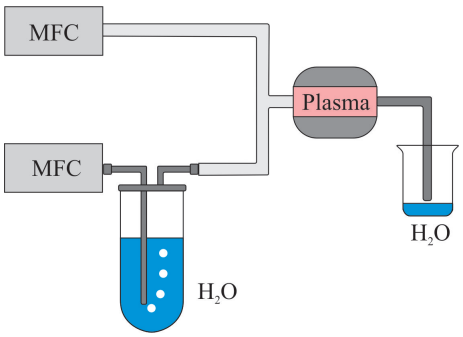

Fig. 6.1: Setup for measuring the deposition of plasma generated H_2O_2 into H_2O. The distance between the plasma and the liquid is 22 cm. The distance between the nozzle exit and the liquid surface is 2 mm.

The treated liquid is analysed by UV-VIS absorption spectroscopy, which has been used for the detection of H_2O_2 in previous work [59]. Directly after the plasma treatment, 300 μl of the H_2O sample is mixed with 500 μl potassium titanium (IV) oxalate solution in optical glass precision cuvettes (10 mm path, Hellma Analytics). As described elsewhere [187], the solution reacts with H_2O_2 in the liquid and forms a complex, which is yellow in colour and absorbs light with a peak absorption at about 400 nm. Typical absorption spectra are shown in fig. 6.2. The absorbance is linear with the concentration of H_2O_2 in the liquid,

as long as all H_2O_2 reacts with the Ti-compound. UV-VIS absorption spectroscopy was perfomed using a UV-VIS spectrophotometer (UV-1800, Shimadzu), which was previously calibrated using H_2O_2 solutions of known concentrations. The ratio 5:3 of Ti-oxalate solution and treated H_2O ensures that an excess of the Ti-oxalate compared to H_2O_2 is present and all H_2O_2 is complexed. The solution was freshly prepared each measurement day, as proposed by Sellers [187] for a maximum absorption signal. 0.885 g of potassium bis(oxalato)-oxotitanate(IV) dihydrate ($K_2[TiO(C_2O_4)_2)]\cdot 2H_2O$, Alfa Aesar) was mixed with 6.8 ml concentrated sulfuric acid (Fluka, purity $> 95\%$). This was diluted with deionised H_2O to a total volume of 25 ml.

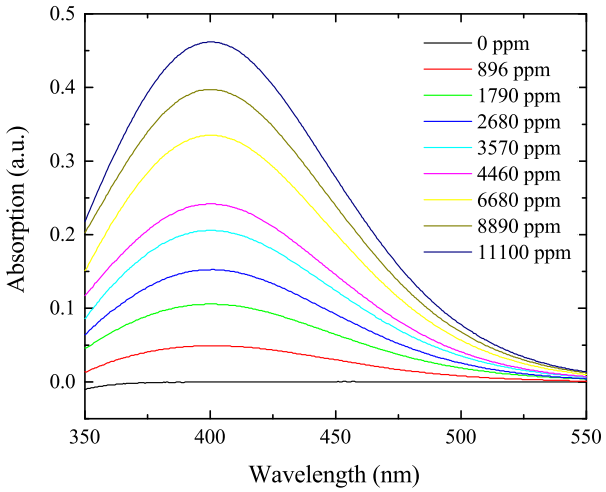

Fig. 6.2: Absorption spectra for the complexed H_2O_2 for different humidity contents in the plasma at 530 V_{pp}.

Using the exhaust of the mod-μAPPJ to treat the liquid sample ensures two prerequisites: the gas is not in contact with ambient air until it exits the metal tube, which reduces the influence of possible gas impurities coming from ambient air, and all short-lived reactive species should decay in the tube, resulting in only stable species reaching the water surface. We test this hypothesis using electron parametric resonance (EPR) spectroscopy and spin trapping. Instead of a H_2O sample, 1 ml of 100 mM solution of the spin trap 5-**die**thoxy**p**hosphoryl-5-**m**ethyl-1-**p**yrroline-N-**o**xide (DEPMPO) is treated by the plasma for 1 min. DEPMPO reacts with free radicals in the liquid, for example OH and $O_2{\cdot}^-$ (superoxide anion), and forms adducts, which can be distuingished via their magnetic spectra using EPR (Bruker EMX spectrometer). Simply, EPR uses the interaction of an applied magnetic field with the spin of an unpaired electron. Due to the Zeeman splitting the electron can exist in two states with opposite spin, which are energetically separated if an external magnetic field is applied. By exiting the electron from a lower to a higher excited state with different spin, parts of the applied electromagnetic radiation is absorbed, leading to distinctive absorption peaks for different radicals. The settings of the EPR spectrometer used to record the spectra are listed in table 6.1.

For the EPR measurement, the plasma is operated with a total He flow of 5 slm, with a H_2O content of (4200 ± 550) ppm, and a peak-to-peak voltage of 530 V. Figure 6.3

Frequency	9.68 GHz
Power	3.17 mW
Modulation frequency	100 kHz
Modulation amplitude	1 G
Time const.	40.96 ms
Conversion time	40 ms
No of scans	5
Sweep width	100 G

Tab. 6.1: Settings used for the EPR measurements.

shows EPR spectra obtained from a sample treated under these conditions (bottom) and an untreated sample (top). Although there are very weak peaks observable, the height of the peaks in the treated sample are of the same order as the peaks in the untreated sample, signifying that no additional radicals are introduced by the plasma. Signals in general are in the order of the noise level, indicating that the concentration of radicals in the liquid phase is very small, and probably originates from impurities in the commercial DEPMPO solution.

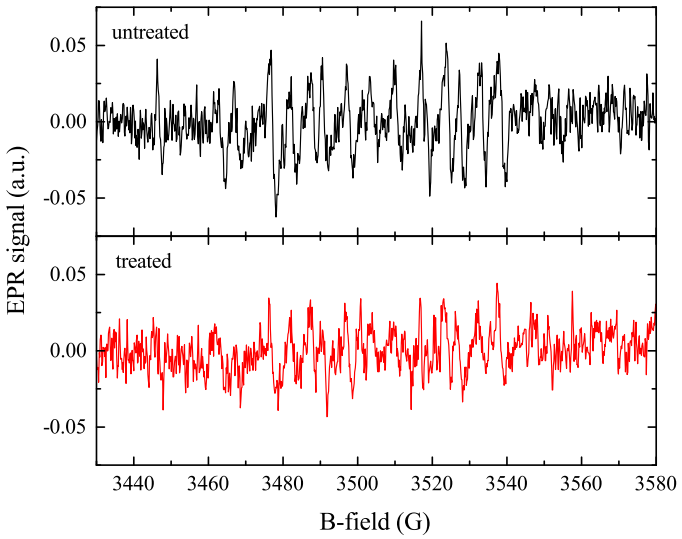

Fig. 6.3: EPR spectrum for an untreated and a plasma treated DEPMPO solution.

6.1.2. Calculations for the gas phase

In order to obtain the concentration of H_2O_2 in the gas phase, the system is calibrated with a known amount of H_2O_2 coming from the gas phase. To do this, the H_2O in the bubbler is replaced with 10% H_2O_2 solution, by diluting commercial H_2O_2 solution ($>$ 30%, Sigma-Aldrich) with deionised H_2O. The concentration of the commercial H_2O_2 was verified using titration with potassium permanganate solution. The exact procedure can be found in chapter D. The calibration then consists of the following 2 steps:

1. Quantification of H_2O_2, which is delivered to the H_2O sample via the gas phase.

2. Quantification of total amount of H_2O_2 in the gas phase.

From these two measurements, it can be calculated what fraction of the H_2O_2 in the gas phase enters the liquid.

Step1. The setup is similar to the one described previously. A schematic is shown in fig. 6.4 (a). Instead of H_2O, the bubbler is filled with 10% H_2O_2 solution. Because H_2O_2 is less volatile than H_2O due to its ten times lower vapour pressure compared to the vapour pressure of water under our experimental conditions [115, 188], a larger bubbler (500 ml) and volume of liquid (420 ml) is used. The gas exits the bubbler and is diluted with a dry He flow, then passes through the plasma source (without the plasma being switched on) and impinges on the liquid. A certain fraction of H_2O_2 will enter the liquid, with the remainder being carried away by the gas flow.

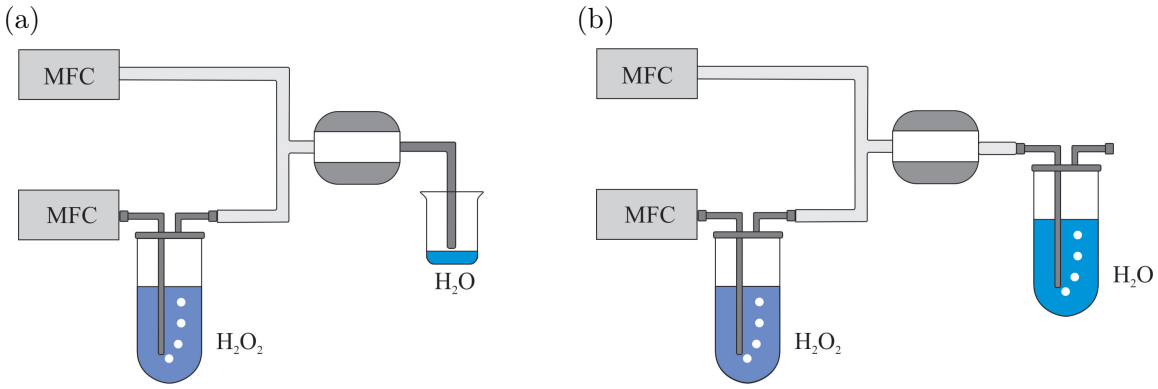

Fig. 6.4: Experimental setups for the H_2O_2 calibration.

Step2. The beaker is replaced by a bubbler (250 ml) filled with deionised H_2O , as shown in fig. 6.4 (b). In this setup all of the H_2O_2 in the gas phase is assumed to be absorbed by the water in the bubbler and the total amount of H_2O_2 in the gas phase is quantified. The complexed H_2O_2 in the liquid $n^{\text{liq}}_{H_2O_2}$ is measured. By taking into account the volume of H_2O V_{H_2O} in the bubbler after the measurement to account for evaporation of the liquid, the treatment time t, and the gas flow F_{He}, a value for the gas phase H_2O_2 can be determined:

$$n^{\text{gas}}_{H_2O_2}\ \left[\text{m}^{-3}\right] = n^{\text{liq}}_{H_2O_2}\ [\text{M}]\ \frac{V_{H_2O}}{tF_{\text{He}}} N_{\text{A}} \tag{6.1}$$

where N_{A} is the Avogrado constant. Using this calculation, a value $n^{\text{gas}}_{H_2O_2} = (44 \pm 6)$ ppm is calculated from 8 independent measurements. By placing a third bubbler filled with H_2O behind the second bubbler in fig. 6.4 (b), it was assured that all H_2O_2 from the gas phase exiting the first bubbler was captured in the second bubbler. It was found that less than 3% of the H_2O_2 escapes the second bubbler, meaning that almost all H_2O_2 gets absorbed by the water in the second bubbler.

By combining step 1 and step 2, the fraction of H_2O_2 which enters the liquid phase from the gas phase in the setup shown in fig. 6.4 (a) can be calculated. This calculation is important, because not all H_2O_2 present in the gas phase is expected to enter the

liquid. Although H_2O_2 has a relatively high solubility, only the surface of a H_2O sample is treated, so that parts of the gas generated H_2O_2 could potentially be carried away by the background He flow before being in contact with the H_2O surface. Therefore, if one would like to calculate the amount of gaseous H_2O_2 from the amount of H_2O_2 in the liquid, the fraction of H_2O_2 entering the liquid from the gas phase has to be known.

Figure 6.5 shows the measured concentrations of H_2O_2 in the beaker after 5 mins of treatment with a total flow of 5 slm, where different He flows have been humidified with the H_2O -H_2O_2 mixture. It is observed that with increasing He flow going through the bubbler, the concentration of H_2O_2 increases linearly. The statistical error obtained from 3 measurements is 11%.

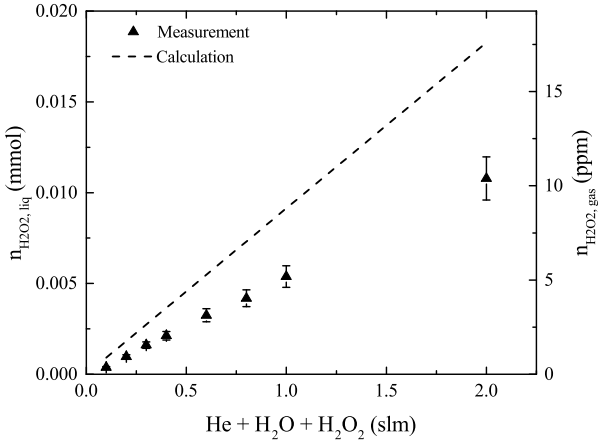

Fig. 6.5: Concentration of H_2O_2 in the treated volume of H_2O after 5 mins treatment with a total flow of 5 slm humidified He (triangles). The initial volume of H_2O before the measurement was 2 ml. The statistical error is 11%. Calculated values using the value from step 1 and the mixing ratio of dry and humidified He are also shown (dashed line).

From these measurements and the absolute value of H_2O_2 in the gas phase, a factor $f_{\text{in}} = (0.56 \pm 0.10)$ can be calculated, indicating that approximately 56% of the H_2O_2 in the gas phase gets diffused into the liquid under the experimental conditions considered here.

6.2. Parameter variations

Using the previously determined correction factor f_{in} and eq. 6.1, the amount of H_2O_2 in the gas phase can be calculated from measured concentrations in the treated sample as the humidity content of the feed gas and the plasma power are varied.

6.2.1. Humidity variation

Figure 6.6 shows the experimentally determined H_2O_2 densities as a function of H_2O content in the feed gas. Measured H_2O_2 densities increase non-linearly up to 10^{14} cm^{-3}

with increasing humidity in our measurement regime. The statistical error obtained from three independent measurements is 6%. Together with the uncertainties arising from the calibration measurements discussed previously, this results in a combined relative uncertainty of 24%.

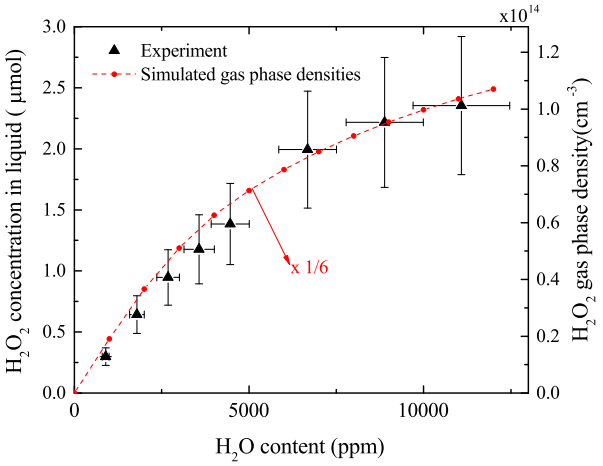

Fig. 6.6: Absolute concentration and densities of H_2O_2 in the liquid and gas under a variation of the H_2O content, measured at 530 V_{pp} (black triangles). Simulation results for the gas phase (dashed line) are carried out for 2.8 W plasma power and 315 K gas temperature. The simulation results have been divided by a factor of 6 in order to better compare with the experimental trend.

H_2O_2 densities are simulated with a plasma power of 2.8 W within the channel length of 2.4 cm and the chemistry set from chapter A, which describes a pure He-H_2O chemistry and does not include air impurities. After 2.4 cm, the power is set to 0 W to simulate the species evolution in the effluent region. The total length of the simulation is 15 cm, combining 2.4 cm active plasma and 12.6 cm effluent. At this point, H_2O_2 densities reach steady-state in the simulation, as shown in fig. 6.7. It is assumed in the simulation that H_2O_2 does not react with the surrounding stainless steel tubes. Comparing the steady-state value obtained from the the simulation for the far plasma effluent with the experimental data accounts for the fact that in the experiment the treated liquid surface is 22 cm away from the plasma, giving reactive species enough time to recombine, as discussed in section 6.1.1.

It it observed in fig. 6.6 that the trends for H_2O_2 densities both in the experiment and simulation agree very well. However, absolute calculated densities in the gas phase are about a factor of 6 higher than densities obtained from the experiments. A similar discrepancy between simulation and experiment was observed by Vasko et al. [51] in a comparable plasma source. In order to validate that H_2O_2 does not undergo decay between the plasma source and the treated liquid, we measured the H_2O_2 concentration in the liquid for three different tube lengths between plasma and treated liquid surface. The results (shown in fig. 6.8) show a slight decrease of H_2O_2 concentrations in the liquid with increasing tube length. However, this decrease is within the typical standard deviation of the experiment of 6%. Additionally, an extrapolation of the data to the end of the plasma channel does not explain the difference of the factor 6 between measurement and

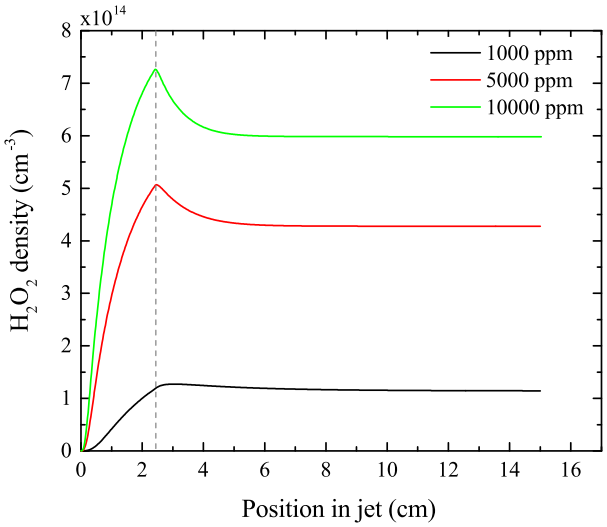

Fig. 6.7: Simulated evolution of absolute densities of H_2O_2 in the plasma channel and afterglow region for different H_2O contents. For all investigated conditions the H_2O_2 densities have reached an equilibrium value at 12.6 cm into the afterglow region. Plasma parameters are 2.8 W and 5 slm total He flow.

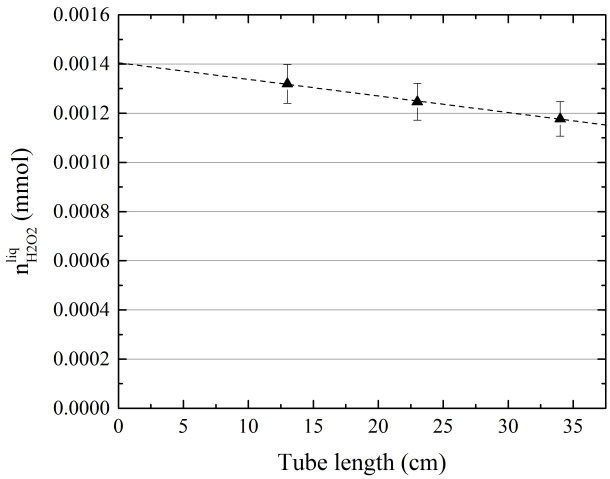

Fig. 6.8: Measured H_2O_2 densities in the liquid with different tube lengths between treated liquid and plasma. The plasma channel exit is at 0 cm. Plasma conditions are 5 slm total He flow with 1 slm humidified He and 530 V_{pp}.

experiment.

Another possible source of error could be the reaction rate coefficients used in the simulation. The main sources for uncertainties for both production and consumption of H_2O_2 are therefore analysed.

H_2O_2 is almost exclusively produced by recombination of two OH molecules

$$2OH + He \rightarrow H_2O_2 + He \tag{6.2}$$

Looking at this reaction, two mechanisms have an influence on the accuracy of the calcu-

lated densities of H_2O_2; the density of OH, from which H_2O_2 is formed, and the reaction rate coefficient. As discussed in section 4.6.2, the simulated OH densities agree well with the experimentally determined ones within a factor 1.7 for all investigated H_2O admixture. The rate coefficient for eq. (6.2) is taken from the IUPAC evaluated database [142], and has been measured on several occasions. Its accuracy is therefore judged as good. Because of this, the production rate of H_2O_2 in the model is assumed to be accurate.

The dominant destruction pathways (averaged over the 2.4 cm discharge channel) of H_2O_2 in the case of 5000 ppm humidity and 2.8 W are

$$OH + H_2O_2 \rightarrow HO_2 + H_2O \quad (84\%) \quad (6.3)$$

$$e + H_2O_2 \rightarrow 2OH + e \quad (10\%) \quad (6.4)$$

$$H + H_2O_2 \rightarrow H_2O + OH \quad (4\%) \quad (6.5)$$

$$e + H_2O_2 \rightarrow OH + OH^- \quad (1\%) \quad (6.6)$$

The rate coefficient for eq. 6.4 is particularly poorly known, because no measured electron impact cross sections exist for this process. The rate coefficient used in this work is taken from reference [189] in which it is stated that in order to calculate the rate coefficient, the cross sections for electron impact dissociation of molecular oxygen are used with twice the threshold energy for that process. Given the lack of a good source for the rate coefficient of eq. (6.4), this coefficient has been artificially varied in the simulation to test its effect on the simulation results. Figure 6.9 shows how different relative species densities simulated for the end of the plasma channel behave with different rate coefficients for eq. (6.4). The x-axis shows the multiplicity of the rate coefficient from table A.1. It is observed in fig. 6.9 that the simulated H_2O_2 at the end of the channel can be reduced by a about 50% when a 30 times higher rate coefficient is used. The influence on simulated OH densities with an increase of 26% and O densities with an increase of 19% is smaller. H densities are only weakly affected and increase 5%. As a result, it is plausible that some of the discrepancy between simulated and measured H_2O_2 densities can be explained by the variation of this rate coefficient. Particularly as this does not significantly affect the agreement of the simulations with the measured densities of the other species.

Additionally the influence of other factors that could lead to dissociation such as dissociation from vibrationally excited states, or photolysis are not accounted for in the model. The dissociation from vibrationally excited states is known to play an important role for certain molecules, such as CO_2 [190, 191]. However, no cross section data or rate coefficients are known for these processes in H_2O_2, and as a result they are not included in the model used in this work.

6.2.2. Power variation

Figure 6.10 shows the absolute H_2O_2 densities both in the liquid and gas phase as a function of the applied voltage to the powered electrode. Generally, measured H_2O_2 densities depend linearly on the applied voltage. This can be explained by the linearly

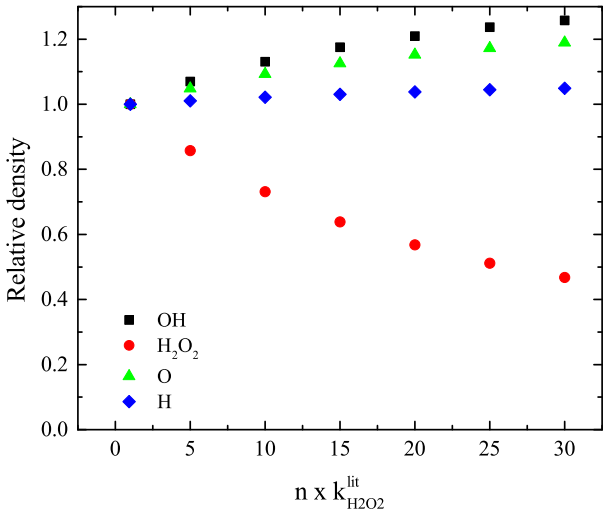

Fig. 6.9: Variation of several relative species densities with the rate coefficient for eq. (6.4). The x-axis shows the multiplicity of the rate coefficient compared to the coefficient listed in table A.1. Simulation conditions are 2.8 W plasma power, 5 slm He flow and 5000 ppm H_2O content.

increasing OH densities, as discussed in section 4.7, and the fact that H_2O_2 production rates dominate over destruction rates under the investigated conditions. This means that H_2O_2 densities are continuously increasing within the active plasma channel, as it was shown previously in fig. 6.7.

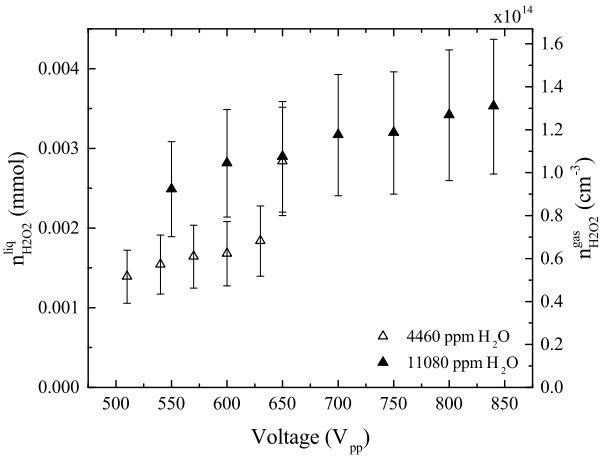

Fig. 6.10: Absolute densities of H_2O_2 dependent on the voltage applied to the plasma source for two different H_2O contents.

Measurements for both H_2O contents were taken from the ignition point of the plasma to the point where the plasma starts extending around the powered electrode. The increase in the density of H_2O_2 is only weakly dependent on power, and the variation stays within the error bar associated with the measurement. For a humidity of 4460 ppm, the point at the highest measured voltage does not fit into the linear trend that is observed for the other points. A possible explanation for this is that during this measurement the plasma started

extending around the powered electrode, effectively enlarging the active plasma volume and residence time of the gas within the plasma, and therefore effectively increasing the H_2O_2 density.

6.3. Key results

Absolute liquid phase concentrations of H_2O_2 in 2 ml H_2O after plasma treatment with the far exhaust of the mod-μAPPJ were measured using UV absorption spectroscopy in the liquid phase. By applying a calibration with a known amount of H_2O_2, absolute gas phase densities of H_2O_2 produced by the plasma could be estimated. It was found that under our specific experimental conditions, about 56% of the H_2O_2 transits from the gas to the liquid phase. Absolute liquid concentrations and gas phase densities depend strongly on the H_2O content in the plasma source, and weakly on the plasma power, making the H_2O content a good parameter to tune the absolute density of H_2O_2 for final applications. Absolute gas phase densities were found to reach up to 10^{14} cm^{-3}. Trends of absolute H_2O_2 densities agreed well with simulation results. However, densities are about a factor 6 higher in the simulation than in the experiment, suggesting poor knowledge of one or more reaction rate coefficients concerning H_2O_2, most likely for one of the dissociation processes, or an important dissociation mechanism not included in the model, such as dissociation via vibrationally excited states, or photolysis.

7. Conclusions

In chapter 1, several goals were identified for this work; fundamental characterisation of the COST μAPPJ (and a variation of that jet that enables measurements in a vacuum environment) with regards to produced species densities in a He-H_2O gas mixture, the use of advanced diagnostic techniques to measure those species, and the development of a plasma-chemical reaction mechanism, which accurately describes the observed variations of species densities, and could be used to identify their most important formation pathways. These aims are the first step in developing plasmas control strategies to tailor the properties of the studied plasma source, and other plasma sources operated in similar gas mixtures, for individual applications, in biomedicine, for example.

For the experimental detection of RS produced in the plasma, several advanced diagnostic techniques were applied. These are in particular VUV-Fourier-transform absorption spectroscopy, ultra-stable broad-band absorption spectroscopy in the gas phase, and picosecond two-photon laser induced fluorescence. These techniques are able to overcome the challenges of RS detection at atmospheric pressure, such as high collisional quenching, and they provide measurements with high spatial resolution. Using these techniques, absolute species densities of OH, O, and also N and NO in the plasma core, and O and H in the plasma effluent region were measured. Additionally, absorption spectroscopy on a aqueous plasma treated sample was used to measure absolute densities of H_2O_2 in both the liquid and gas phase. Parameter variations such as a variation of the humidity, air and oxygen content in the plasma showed potential for tailoring reactive species densities as these densities were found to be strongly dependent on the molecular gas admixtures.

The applied voltage was found to have a strong impact on NO densities, however, OH and H_2O_2 were relatively unaffected by the plasma power. With respect to applications

in biomedicine, the plasma power is a limited control parameter for tailoring densities, since increasing plasma powers typically also leads to increasing the gas temperature [30], which are undesired. Changing the plasma power was found to allow for a limited tuning of species densities in He-H_2O plasmas, since certain groups of species, such as purely oxygen containing species, were found in simulations to respond more strongly to a change in power than purely hydrogen containing species or mixed species.

The variety of measured species densities enables a reliable benchmark of simulation results within the uncertainty for both experiments and, likely, simulations. In order to fully quantify uncertainties arising from the simulation, a sensitivity analysis has to be carried out, which takes into account the uncertainties of all used reaction rate coefficients. A sensitivity analysis carried out in a He-O_2 plasma in previous work [103] revealed variations in species densities up to a factor 10 depending on the species and plasma conditions. Although such an analysis was not carried out in this work, it would be a very important task for future work.

A comparison of the simulated and experimental absolute densities as a function of H_2O content in the plasma are summarised in fig. 7.1. Generally, all investigated species show an increase in densities towards higher H_2O contents. An exception is the measurement of O in the μAPPJ using ps-TALIF, which also shows an increase towards lower admixtures of H_2O. Since this increase was not observed in the mod-μAPPJ, which is a closed source, it has been attributed to impurities present in the feed gas. These impurities are likely to enter the gas volume through leaks in the gas feed system, or via back diffusion of ambient air into the plasma channel, and were found to dominate the gas phase chemistry at low water admixtures. It is therefore important to consider the concentrations of impurities in the gas flow when treating biological or any other samples, particularly when only small amounts of molecules are purposefully added to the feed gas. It was also found that hydrogen and purely oxygen containing species can be tuned independently to some degree by fixing the amount of H_2O and changing the amount of O_2 in the feed gas, which is potentially relevant for biomedical applications of APPs.

Some species, particularly those mainly produced via electron impact dissociation of H_2O, such as OH and H, show an exceptional agreement in absolute densities for both simulation and experiment. Other species, such as O and H_2O_2, show larger discrepancies, up to a factor 3 and 6, respectively, under the investigated conditions. Possible reasons for this are the complex multi-step formation mechanisms of these species, which lead to an addition of uncertainties of the rate coefficients used, or some formation mechanisms that have not been taken into account. However, trends of simulation and experiments agree well for most species, and the agreement of absolute densities is still regarded as good taking into account the uncertainties in both simulation and experiment.

Given the good agreement between experiment and simulations, the main formation mechanisms for the different species of interest have been identified using pathway analysis of the simulation results. Some general conclusions were found. The first step in creating the reactive plasma chemistry is the dissociation of H_2O molecules by He metastables or

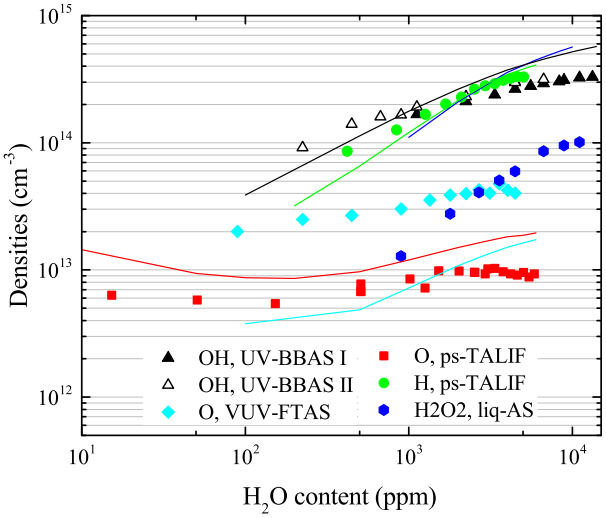

Fig. 7.1: Overview of simulated (lines) and experimental (scatter) reactive species densities for conditions discussed in chapters 4 to 6.

electrons. H_2O is also consumed through the formation of high order charged protonated clusters.

For low water admixtures or at the beginning of the channel, reactive species are created by fast reaction mechanisms including ions and electrons, whereas at high water admixtures and towards the end of the channel, neutral heavy particle reactions become more important. H and OH are formed quickly via electron impact dissociation of water, and approach a steady-state value within the plasma channel, whereas most other species do not. This may allow for the opportunity to tailor the reactive species content of such plasma sources by varying the plasma dimensions, particularly the length of the plasma channel. OH is a key species in H_2O containing plasmas, dominating the formation mechanisms of many species such as O and H_2O_2. It is also the main species responsible for the consumption of most investigated species due to its high reactivity.

In addition to the investigation of absolute species densities, quenching coefficients were measured close to the plasma nozzle using ps-TALIF. In TALIF investigations with nanosecond resolution, these coefficients are important to calculate the effective decay rate of species, which is an essential step to obtain absolute species densities, and are typically obtained from the literature. However, only very few publications exists that discuss quenching of excited states by H_2O molecules, and the results in these publications are often in disagreement. Therefore, measuring decay rates and quenching coefficients in situ at atmospheric pressure offers a great advantage.

With regard to the application of atmospheric pressure plasmas, the RS distribution in the effluent region is of great importance. Using H as an example, it was demonstrated in this work how RS can be measured with spatial resolution in the plasma effluent region using ps-TALIF. Such measurements are difficult to carry out accurately using conventional ns-TALIF as a result of gas mixing in the effluent region, which makes the calculation of accurate decay rates extremely challenging. Absolute H densities were found to extend

up to 7 mm downstream in the effluent at 1 slm gas flow in He. Radial and axial gas mixing with ambient are was found by evaluating the lifetimes of the H(n=3) excited state. Investigation of other species densities, or the influence of a treated surface are important steps for future investigations. The presence of a surface in the jet effluent could significantly change the gas dynamics and species distribution, compared to the “free jet configuration" that has been investigated in this work. Higher dimensional simulations could also be used to simulate the plasma and gas dynamics in the plasma effluent region without and with potential surfaces. The global model used in this work only has limited applicability in this region, because it does not take into account gas mixing with ambient air. This is demonstrated by the discrepancy in the spatial decay of H in the effluent which was found to be much smaller in the experiment than the simulation as a result of increased interactions with air which are not accounted for in the global model.

Appendix A Reaction set for He-H_2O chemistry

Tab. A.1: Electron collisions

No	E_{Thr}(eV)	Reaction	Rate[ab]	Ref.
Elastic scattering and momentum transfer				
1	0.00	$e + He \rightarrow He + e$	f(E)	[192]
2	0.00	$e + H_2O \rightarrow H_2O + e$	f(E)	[148]
3	0.00	$e + H_2 \rightarrow H_2 + e$	f(E)	[193]
4	0.00	$e + O_2 \rightarrow O_2 + e$	f(E)	[194]
Electron impact excitation and ionisation				
5	19.80	$e + He \rightarrow He^* + e$	f(E)	[192]
6	20.62	$e + He \rightarrow He^* + e$	f(E)	[192]
7	24.58	$e + He \rightarrow He^+ + e$	f(E)	[192]
8	4.77	$e + He^* \rightarrow He^+ + 2e$	f(E)	[126]
9	3.90	$e + He_2^* \rightarrow He_2^+ + 2e$	$2.06 \times 10^{-13} e^{-4.28/T_e}$	[195][c]
10	0.04	$e + H_2 \rightarrow H_2 + e$	f(E)	[193]
11	0.07	$e + H_2 \rightarrow H_2 + e$	f(E)	[193]
12	0.52	$e + H_2 \rightarrow H_2 + e$	f(E)	[193]
13	0.52	$e + H_2 \rightarrow H_2 + e$	f(E)	[193]
14	13.50	$e + OH \rightarrow OH^+ + 2e$	f(E)	[196]
15	0.20	$e + H_2O \rightarrow H_2O + e$	f(E)	[148]
16	0.45	$e + H_2O \rightarrow H_2O + e$	f(E)	[148]
17	0.47	$e + H_2O \rightarrow H_2O + e$	f(E)	[148]
18	13.50	$e + H_2O \rightarrow H_2O^+ + 2e$	f(E)	[148]
19	1.97	$e + O \rightarrow O(^1D) + e$	f(E)	[197]
20	4.19	$e + O \rightarrow O(^1S) + e$	f(E)	[197]
21	13.62	$e + O \rightarrow O^+ + 2e$	f(E)	[197]
22	11.65	$e + O(^1D) \rightarrow O^+ + 2e$	f(E)	[126][d]
23	9.43	$e + O(^1S) \rightarrow O^+ + 2e$	f(E)	[198][d]
24	0.02	$e + O_2 \rightarrow O_2 + e$	f(E)	[194]
25	0.19	$e + O_2 \rightarrow O_2 + e$	f(E)	[194]
26	0.19	$e + O_2 \rightarrow O_2 + e$	f(E)	[194]
27	0.38	$e + O_2 \rightarrow O_2 + e$	f(E)	[194]
28	0.38	$e + O_2 \rightarrow O_2 + e$	f(E)	[194]
29	0.57	$e + O_2 \rightarrow O_2 + e$	f(E)	[194]
30	0.75	$e + O_2 \rightarrow O_2 + e$	f(E)	[194]
31	0.98	$e + O_2 \rightarrow O_2(a^1\Delta) + e$	f(E)	[194]
32	1.63	$e + O_2 \rightarrow O_2(b^1\Sigma) + e$	f(E)	[194]
33	4.50	$e + O_2 \rightarrow O_2 + e$	f(E)	[194]

No	E_{Thr}(eV)	Reaction	Rate[ab]	Ref.
34	12.06	$e + O_2 \rightarrow O_2^+ + e$	f(E)	[194]
35	0.02	$e + O_2(a^1\Delta) \rightarrow O_2(a^1\Delta) + e$	f(E)	as 24[e]
36	0.19	$e + O_2(a^1\Delta) \rightarrow O_2(a^1\Delta) + e$	f(E)	as 25[e]
37	0.19	$e + O_2(a^1\Delta) \rightarrow O_2(a^1\Delta) + e$	f(E)	as 26[e]
38	0.38	$e + O_2(a^1\Delta) \rightarrow O_2(a^1\Delta) + e$	f(E)	as 27[e]
39	0.38	$e + O_2(a^1\Delta) \rightarrow O_2(a^1\Delta) + e$	f(E)	as 28[e]
40	0.57	$e + O_2(a^1\Delta) \rightarrow O_2(a^1\Delta) + e$	f(E)	as 29[e]
41	0.75	$e + O_2(a^1\Delta) \rightarrow O_2(a^1\Delta) + e$	f(E)	as 30[e]
42	0.65	$e + O_2(a^1\Delta) \rightarrow O_2(b^1\Sigma) + e$	f(E)	[199][f]
43	3.62	$e + O_2(a^1\Delta) \rightarrow O_2 + 2e$	f(E)	as 33[e]
44	11.08	$e + O_2(a^1\Delta) \rightarrow O_2^+ + e$	f(E)	as 34[e]
45	0.02	$e + O_2(b^1\Sigma) \rightarrow O_2(b^1\Sigma) + e$	f(E)	as 24[e]
46	0.19	$e + O_2(b^1\Sigma) \rightarrow O_2(b^1\Sigma) + e$	f(E)	as 25[e]
47	0.19	$e + O_2(b^1\Sigma) \rightarrow O_2(b^1\Sigma) + e$	f(E)	as 26[e]
48	0.38	$e + O_2(b^1\Sigma) \rightarrow O_2(b^1\Sigma) + e$	f(E)	as 27[e]
49	0.38	$e + O_2(b^1\Sigma) \rightarrow O_2(b^1\Sigma) + e$	f(E)	as 28[e]
50	0.57	$e + O_2(b^1\Sigma) \rightarrow O_2(b^1\Sigma) + e$	f(E)	as 29[e]
51	0.75	$e + O_2(b^1\Sigma) \rightarrow O_2(b^1\Sigma) + e$	f(E)	as 30[e]
52	2.87	$e + O_2(b^1\Sigma) \rightarrow O_2 + e$	f(E)	as 33[e]
53	10.43	$e + O_2(b^1\Sigma) \rightarrow O_2^+ + 2e$	f(E)	as 34[e]
Super-elastic collisions				
54	-19.80	$e + He^* \rightarrow He + e$	f(E)	[192][g]
55	-1.97	$e + O(^1D) \rightarrow O + e$	f(E)	[197][g]
56	-4.19	$e + O(^1S) \rightarrow O + e$	f(E)	[197][g]
57	-0.98	$e + O_2(a^1\Delta) \rightarrow O_2 + e$	f(E)	[194][g]
58	-1.63	$e + O_2(b^1\Sigma) \rightarrow O_2 + e$	f(E)	[194][g]
59	-0.65	$e + O_2(b^1\Sigma) \rightarrow O_2(a^1\Delta) + e$	f(E)	as 42[g]
Dissociation				
60	-17.90	$e + He_2^* \rightarrow 2\,He + e$	3.8×10^{-15}	[200]
61	13.50	$e + H_2O \rightarrow O(^1S) + 2\,H + e$	f(E)	[148, 201]
62	7.62	$e + H_2O \rightarrow H + OH + e$	f(E)	[148, 202]
63	13.00	$e + H_2O \rightarrow H_2 + O(^1D) + e$	$2.42 \times 10^{-14} T_e^{-0.062} e^{-22.42/T_e}$	[58][h]
64	8.80	$e + H_2 \rightarrow 2\,H + e$	f(E)	[203]
65	12.96	$e + OH \rightarrow O + H + e$	f(E)	[204][i]
66		$e + H_2O_2 \rightarrow 2\,OH + e$	2.36×10^{-15}	[189][j]
67	6.00	$e + O_2 \rightarrow O + O + e$	f(E)	[194]
68	8.40	$e + O_2 \rightarrow O(^1D) + O + e$	f(E)	[194]
69	10.00	$e + O_2 \rightarrow O(^1D) + O + e$	f(E)	[194]
70	5.02	$e + O_2(a^1\Delta) \rightarrow O + O + e$	f(E)	as 67
71	7.42	$e + O_2(a^1\Delta) \rightarrow O(^1D) + O + e$	f(E)	as 68[e]
72	9.02	$e + O_2(a^1\Delta) \rightarrow O(^1D) + O + e$	f(E)	as 69[e]
73	4.37	$e + O_2(b^1\Sigma) \rightarrow O + O + e$	f(E)	as 67
74	6.77	$e + O_2(b^1\Sigma) \rightarrow O(^1D) + O + e$	f(E)	as 68[e]
75	8.37	$e + O_2(b^1\Sigma) \rightarrow O(^1D) + O + e$	f(E)	as 69[e]
76	1.00	$e + O_3 \rightarrow O + O_2 + e$	$1.7 \times 10^{-14} T_e^{-0.57} e^{-2.48/T_e}$	[103, 205]

No	E_{Thr}(eV)	Reaction	Rate[ab]	Ref.
77	5.72	e + O_3 → $O(^1D)$ + $O_2(a^1\Delta)$ + e	$3.22 \times 10^{-13} T_e^{-1.18} e^{-9.17/T_e}$	[103, 205]
Dissociative ionisation				
78	17.50	e + H_2O → OH^+ + H + 2 e	f(E)	[148]
79	25.00	e + H_2O → O^+ + 2 H + 2 e	f(E)	[148]
80	17.00	e + O_2 → O^+ + O + 2 e	f(E)	[206]
81	16.02	e + $O_2(a^1\Delta)$ → O^+ + O + 2 e	f(E)	as 80[e]
82	15.37	e + $O_2(b^1\Sigma)$ → O^+ + O + 2 e	f(E)	as 80[e]
(Dissociative) Electron attachment				
83	5.30	e + H_2O → OH + H^-	f(E)	[148, 207]
84	4.43	e + H_2O → H_2 + O^-	f(E)	[148, 207]
85	4.30	e + H_2O → H + OH^-	f(E)	[148, 207]
86	0.00	e + H_2O_2 → H_2O + O^-	f(E)	[208]
87	0.00	e + H_2O_2 → OH + OH^-	f(E)	[208]
88	0.00	e + O_2 → O + O^-	f(E)	[194]
89	3.50	e + $O_2(a^1\Delta)$ → O + O^-	f(E)	[209]
90	2.85	e + $O_2(b^1\Sigma)$ → O + O^-	f(E)	as 89[e]
91	0.00	e + O_3 → O_2 + O^-	f(E)	[210]
92	0.00	e + O_3 → O_2^- + O	f(E)	[210]
Electron detachment				
93	2.70	e + O^- → O + e + e	f(E)	[211]
94	2.70	e + O_2^- → O_2 + e + e	f(E)	[211]
Recombination				
95	0.00	e + H_2O^+ → H + OH	$6.13 \times 10^{-14} T_e^{-0.5}$	[212, 213]
96	0.00	e + H_2O^+ → 2 H + O	$2.67 \times 10^{-14} T_e^{-0.5}$	[212, 213][k]
97	0.00	e + H_2O^+ → H_2 + O	$2.34 \times 10^{-14} T_e^{-0.5}$	[212, 213][k]
98	0.00	e + $H^+ \cdot (H_2O)$ → H + H_2O	$3.36 \times 10^{-14} T_e^{-1.0}$	[214]
99	0.00	e + $H^+ \cdot (H_2O)_2$ → H + 2 H_2O	$1.84 \times 10^{-12} T_e^{-0.08}$	[215]
100	0.00	e + $H^+ \cdot (H_2O)_3$ → 3 H_2O + H	$2.24 \times 10^{-12} T_e^{-0.08}$	[215]
101	0.00	e + $H^+ \cdot (H_2O)_4$ → 4 H_2O + H	3.6×10^{-12}	[215]
102	0.00	e + $H^+ \cdot (H_2O)_5$ → 5 H_2O + H	4.1×10^{-12}	[216]
103	0.00	e + $H^+ \cdot (H_2O)_6$ → 6 H_2O + H	5.13×10^{-12}	[216]
104	0.00	e + $H^+ \cdot (H_2O)_7$ → 7 H_2O + H	1.0×10^{-12}	[216]
105	0.00	e + $H^+ \cdot (H_2O)_8$ → 8 H_2O + H	4.1×10^{-12}	as 102
106	0.00	e + $H^+ \cdot (H_2O)_9$ → 9 H_2O + H	4.1×10^{-12}	as 102
107	0.00	e + $H_2O^+ \cdot (H_2O)$ → H + OH + H_2O	$9.63 \times 10^{-13} T_e^{-0.2}$	[214][lm]
108	0.00	e + O_2^+ → 2 O	f(E)	[217][n]
109	0.00	e + O_2^+ → O + $O(^1D)$	$8.17 \times 10^{-15} T_e^{-0.7}$	[218]
110	0.00	e + O_2^+ → 2 $O(^1D)$	$5.85 \times 10^{-15} T_e^{-0.7}$	[218]
111	0.00	e + $O_2^+ \cdot (H_2O)$ → O_2 + H_2O	$7.22 \times 10^{-13} T_e^{-0.2}$	[214]
112	0.00	e + O_4^+ → 2 O + O_2	$5.17 \times 10^{-14} T_e^{-1.0}$	[214]
113	0.00	e + O_4^+ → 2 O_2	$2.76 \times 10^{-13} T_e^{-0.5}$	[134]

[a] In m^3s^{-1} and m^6s^{-1} for two- and three-body collisions, respectively.
[b] f(E) means rate coefficients are calculated by the internal GlobalKin Boltzmann solver using cross sections obtained from the indicated literature.
[c] Calculated using Bolsig+ [219] assuming a Maxwell distribution function and cross sections from the given reference.
[d] Cross sections are calculated from an equation in this reference.
[e] As process from ground state but shifted and scaled.
[f] Born-Bethe fit to data in the cited reference.
[g] Obtained from reverse process by detailed balance.
[h] In the reference reaction rate were calculated using a Boltzmann solver [219] and cross sections obtained from the Morgan database [220] for a He/H_2O plasma.
[i] Cross sections are for dissociation of CO.
[j] Value is approximated in reference.
[k] Value is upper/lower limit in reference.
[l] Value is estimated in source.
[m] Calculated for $T_g = 300$K.
[n] $\sigma = 2.25 \times 10^{-19} 0.1/U$ m^2

Tab. A.2: Ion-ion chemistry

No	Reaction	Rate[a]	Ref.
Three-body collisions			
114 - 133	$A^+ + B^- + He \rightarrow A + B + He$	$2.0 \times 10^{-37} T_0^{-2.5}$	[134][bc]
134 - 138	$A_4^+ + B^- + He \rightarrow 2\ A_2 + B + He$	$2.0 \times 10^{-37} T_0^{-2.5}$	[134][bd]
139 - 150	$A^+ + OH^-\cdot(H_2O)_n + He \rightarrow A + OH + n\times H_2O + He$	$2.0 \times 10^{-37} T_0^{-2.5}$	[134][be]
151 - 153	$A_4^+ + OH^-\cdot(H_2O)_n + He \rightarrow 2\ A_2 + OH + n\times H_2O + He$	$2.0 \times 10^{-37} T_0^{-2.5}$	[134][bf]
154 - 189	$H^+\cdot(H_2O)_m + B^- + He \rightarrow m\times H_2O + H\cdot B$	$2.0 \times 10^{-37} T_0^{-2.5}$	[134][bg]
190 - 216	$H^+\cdot(H_2O)_m + OH^-\cdot(H_2O)_n + He \rightarrow (m+n+1)\times H_2O + He$	$2.0 \times 10^{-37} T_0^{-2.5}$	[134][bh]
217 - 225	$H^+\cdot(H_2O)_m + H_2O_2^- + He \rightarrow (m+1)\times H_2O + OH$	$2.0 \times 10^{-37} T_0^{-2.5}$	[134][bi]
226 - 230	$H_2O^+\cdot H_2O + B^- + He \rightarrow 2\ H_2O + B + He$	$2.0 \times 10^{-37} T_0^{-2.5}$	[134][bj]
231 - 233	$H_2O^+\cdot H_2O + OH^-\cdot(H_2O)_n + He \rightarrow (n+2)\times H_2O + OH + He$	$2.0 \times 10^{-37} T_0^{-2.5}$	[134][bk]
234 - 238	$O_2^+\cdot(H_2O) + B^- + He \rightarrow H_2O + O_2 + B$	$2.0 \times 10^{-37} T_0^{-2.5}$	[134][bj]
239 - 241	$O_2^+\cdot(H_2O) + OH^-\cdot(H_2O)_n + He \rightarrow (n+1)\times H_2O + O_2 + OH$	$2.0 \times 10^{-37} T_0^{-2.5}$	[134][bk]

[a] In m^6s^{-1}.
[b] Value estimated in reference.
[c] For A = O, O_2, OH, H_2O and B = O, O_2, H, OH, H_2O_2.
[d] For A = O and B = O, O_2, H, OH, H_2O_2.
[e] For A = O, O_2, OH, H_2O and n = 1..3.
[f] For A = O and n = 1..3.
[g] For m=1..9 and B = O, H, OH.
[h] For m=1..9 and n=1..3.
[i] For m=1..9.
[j] For B = O, O_2, H, OH, H_2O_2.
[k] For n=1..3.

Tab. A.3: Ion-neutral chemistry

No	Reaction	Rate[a]	Ref.
Two-body collisions - positive ions			
242	$He^+ + OH \rightarrow O^+ + H + He$	$1.1 \times 10^{-15} T_0^{-0.5}$	[135, 221]
243	$He^+ + H_2O \rightarrow H_2O^+ + He$	$6.05 \times 10^{-17} T_0^{-0.5}$	[135, 222]
244	$He^+ + H_2O \rightarrow OH^+ + H + He$	$2.86 \times 10^{-16} T_0^{-0.5}$	[135, 222]

No	Reaction	Rate[a]	Ref.
245	$He^+ + O \rightarrow O^+ + He$	5.00×10^{-17}	[117][b]
246	$He^+ + O_2 \rightarrow O^+ + O + He$	1.1×10^{-15}	[135, 223]
247	$He^+ + O_2 \rightarrow O_2^+ + He$	3.3×10^{-17}	[135, 223]
248	$He_2^+ + OH \rightarrow O^+ + H + 2\ He$	1.1×10^{-15}	as 242
249	$He_2^+ + H_2O \rightarrow H_2O^+ + 2\ He$	6.05×10^{-17}	as 243
250	$He_2^+ + H_2O \rightarrow H^+{\cdot}(H_2O) + 2\ He$	2.86×10^{-16}	as 244
251	$He_2^+ + O_2 \rightarrow O^+ + O + 2\ He$	1.0×10^{-15}	as 246
252	$He_2^+ + O_2 \rightarrow O_2^+ + 2\ He$	3.3×10^{-17}	as 247
253	$H^+{\cdot}(H_2O)_2\ (+ He) \rightarrow H^+{\cdot}(H_2O) + H_2O\ (+ He)$	$effective$	[124][c]
254	$H^+{\cdot}(H_2O)_3\ (+ He) \rightarrow H^+{\cdot}(H_2O)_2 + H_2O\ (+ He)$	$effective$	[124][c]
255	$H^+{\cdot}(H_2O)_4\ (+ He) \rightarrow H^+{\cdot}(H_2O)_3 + H_2O\ (+ He)$	$effective$	[124][c]
256	$H^+{\cdot}(H_2O)_5\ (+ He) \rightarrow H^+{\cdot}(H_2O)_4 + H_2O\ (+ He)$	$effective$	[124][c]
257	$H^+{\cdot}(H_2O)_6\ (+ He) \rightarrow H^+{\cdot}(H_2O)_5 + H_2O\ (+ He)$	$effective$	[124]
258	$H^+{\cdot}(H_2O)_7\ (+ He) \rightarrow H^+{\cdot}(H_2O)_6 + H_2O\ (+ He)$	$effective$	[124]
259	$H^+{\cdot}(H_2O)_8\ (+ He) \rightarrow H^+{\cdot}(H_2O)_7 + H_2O\ (+ He)$	4.15×10^5	est.
260	$H^+{\cdot}(H_2O)_9\ (+ He) \rightarrow H^+{\cdot}(H_2O)_8 + H_2O\ (+ He)$	9.00×10^1	est.
261	$OH^+ + H_2 \rightarrow H_2O^+ + H$	1.01×10^{-15}	[135, 224]
262	$OH^+ + OH \rightarrow H_2O^+ + O$	$7.0 \times 10^{-16} T_0^{-0.5}$	[135, 221]
263	$OH^+ + H_2O \rightarrow H_2O^+ + OH$	1.56×10^{-15}	[225]
264	$OH^+ + H_2O \rightarrow H^+{\cdot}(H_2O) + O$	1.27×10^{-15}	[225]
265	$OH^+ + O \rightarrow O_2^+ + H$	7.1×10^{-16}	[135, 221]
266	$OH^+ + O_2 \rightarrow O_2^+ + OH$	5.9×10^{-16}	[135, 224]
267	$H_2O^+ + H_2 \rightarrow H^+{\cdot}(H_2O) + H$	6.4×10^{-16}	[135, 226]
268	$H_2O^+ + OH \rightarrow H^+{\cdot}(H_2O) + O$	$6.9 \times 10^{-16} T_0^{-0.5}$	[135, 221]
269	$H_2O^+ + H_2O \rightarrow H^+{\cdot}(H_2O) + OH$	2.05×10^{-15}	[225]
270	$H_2O^+ + O \rightarrow O_2^+ + H_2$	4.0×10^{-17}	[135, 227]
271	$H_2O^+ + O_2 \rightarrow O_2^+ + H_2O$	3.3×10^{-16}	[228]
272	$H_2O^+{\cdot}H_2O + H_2O \rightarrow H^+{\cdot}(H_2O)_2 + OH$	1.4×10^{-15}	[214]
273	$H_2O^+{\cdot}H_2O + O_2(a^1\Delta) \rightarrow H^+{\cdot}(H_2O) + OH + O_2$	$1.0 \cdot 10^{-16}$	[229][b]
274	$O^+ + H_2 \rightarrow OH^+ + H$	1.7×10^{-15}	[135, 230]
275	$O^+ + OH \rightarrow OH^+ + O$	$3.6 \times 10^{-15} T_0^{-0.5}$	[135, 221]
276	$O^+ + OH \rightarrow O_2^+ + H$	$3.6 \times 10^{-15} T_0^{-0.5}$	[135, 221]
277	$O^+ + H_2O \rightarrow H_2O^+ + O$	3.2×10^{-15}	[230]
278	$O^+ + O_2 \rightarrow O_2^+ + O$	$2.0 \times 10^{-17} T_0^{-0.4}$	[231]
279	$O_2^+{\cdot}H_2O\ (+ He) \rightarrow O_2^+ + H_2O\ (+ He)$	$effective$	[124]
280	$O_2^+{\cdot}H_2O + H_2O \rightarrow H_2O^+{\cdot}H_2O + O_2$	1.0×10^{-15}	[214][b]
281	$O_4^+ + H_2O \rightarrow O_2^+{\cdot}H_2O + O_2$	1.7×10^{-15}	[232]
282	$O_4^+ + O \rightarrow O_2^+ + O_3$	3.0×10^{-16}	[214]
283	$O_4^+ + O_2(a^1\Delta) \rightarrow O_2^+ + 2\ O_2$	1.0×10^{-16}	[214][b]
284	$O_4^+ + O_2(b^1\Sigma) \rightarrow O_2^+ + 2\ O_2$	1.0×10^{-16}	as 283
	Two-body collisions - negative ions		
285	$H^- + He \rightarrow H + He + e$	$8.0 \times 10^{-18} T_0^{0.5}$	[39, 233]
286	$H^- + H_2O \rightarrow OH^- + H_2$	4.8×10^{-15}	[135, 234]
287	$OH^-{\cdot}(H_2O)_2 + He \rightarrow OH^-{\cdot}(H_2O) + H_2O + He$	$effective$	as 253
288	$OH^-{\cdot}(H_2O)_3 + He \rightarrow OH^-{\cdot}(H_2O)_2 + H_2O + He$	$effective$	as 254

No	Reaction	Rate[a]	Ref.
289	$H_2O_2^- + H_2O \rightarrow OH^-\cdot(H_2O) + OH$	1.0×10^{-17}	[235][d]
290	$O^- + H_2O \rightarrow OH^- + OH$	1.4×10^{-15}	[207]
291	$O^- + O_2 \rightarrow O_2^- + O$	1.0×10^{-18}	[103, 236]
292	$O^- + O_2(a^1\Delta) \rightarrow O_2^- + O$	$7.3 \times 10^{-16} e^{-890/T_g}$	[103, 237]
293	$O^- + O_2(a^1\Delta) \rightarrow O_3 + e$	6.1×10^{-16}	[103, 237]
294	$O^- + O_2(b^1\Sigma) \rightarrow O_2^- + O$	$7.3 \times 10^{-16} e^{-890/T_g}$	as 292
295	$O^- + O_3 \rightarrow O_2^- + O_2$	1.0×10^{-17}	[103, 236]
296	$O_2^- + O \rightarrow O^- + O_2$	$8.5 \times 10^{-17} T_0^{-1.7}$	[238][e]
297	$O_2^- + O \rightarrow O_3 + e$	$8.5 \times 10^{-17} T_0^{-1.7}$	[238][e]
Three-body collisions - positive ions			
298	$He^+ + 2He \rightarrow He_2^+ + He$	$1.4 \times 10^{-43} T_0^{-0.6}$	[239]
299	$H^+\cdot(H_2O) + H_2O$ (+ He) $\rightarrow H^+\cdot(H_2O)_2$ (+ He)	$effective$	[124, 240][c]
300	$H^+\cdot(H_2O)_2 + H_2O$ (+ He) $\rightarrow H^+\cdot(H_2O)_3$ (+ He)	$effective$	[124, 240][c]
301	$H^+\cdot(H_2O)_3 + H_2O$ (+ He) $\rightarrow H^+\cdot(H_2O)_4$ (+ He)	$effective$	[124, 240][c]
302	$H^+\cdot(H_2O)_4 + H_2O$ (+ He) $\rightarrow H^+\cdot(H_2O)_5$ (+ He)	$effective$	[124, 240][c]
303	$H^+\cdot(H_2O)_5 + H_2O$ (+ He) $\rightarrow H^+\cdot(H_2O)_6$ (+ He)	$effective$	[124, 240][c]
304	$H^+\cdot(H_2O)_6 + H_2O$ (+ He) $\rightarrow H^+\cdot(H_2O)_7$ (+ He)	$effective$	[124, 240][bc]
305	$H^+\cdot(H_2O)_7 + H_2O$ (+ He) $\rightarrow H^+\cdot(H_2O)_8$ (+ He)	2.08×10^{-18}	est.
306	$H^+\cdot(H_2O)_8 + H_2O$ (+ He) $\rightarrow H^+\cdot(H_2O)_9$ (+ He)	3.10×10^{-19}	est.
307	$O_2^+ + H_2O$ (+ He) $\rightarrow O_2^+\cdot H_2O$ (+ He)	$effective$	[124][c]
308	$O_2^+ + O_2$ (+ He) $\rightarrow O_4^+$ (+ He)	$effective$	[124][c]
Three-body collisions - negative ions			
309	$OH^- + H_2O + He \rightarrow OH^-\cdot(H_2O) + He$	8.0×10^{-42}	[241][f]
310	$OH^-\cdot(H_2O) + H_2O + He \rightarrow OH^-\cdot(H_2O)_2 + He$	2.5×10^{-43}	[241][f]
311	$OH^-\cdot(H_2O)_2 + H_2O + He \rightarrow OH^-\cdot(H_2O)_3 + He$	1.5×10^{-43}	[241][f]
312	$O^- + H_2O + He \rightarrow H_2O_2^- + He$	1.3×10^{-40}	[235]

[a] In m^3s^{-1} and m^6s^{-1} for two- and three-body collisions, respectively
[b] Value is estimated in reference.
[c] Effective rate coefficients calculated from pressure dependent rates as described by Sieck [124] for 1 atm and a temperature range 280-350 K, as described in the text.
[d] Value in an lower limit in reference.
[e] Estimated branching ratio.
[f] Collider gas is H_2O in reference.

Tab. A.4: Neutral chemistry

No	Reaction	Rate[a]	Ref.
Two-body collisions			
313	$He + O(^1D) \rightarrow O + He$	7.0×10^{-22}	[242][b]
314	$He + O(^1S) \rightarrow O + He$	7.0×10^{-22}	as 313
315	$He + O_2(a^1\Delta) \rightarrow O_2 + He$	8.0×10^{-27}	[243][b]
316	$He + O_2(b^1\Sigma) \rightarrow O_2(a^1\Delta) + He$	$1.0 \times 10^{-23} T_0^{0.5}$	[117][c]
317	$2He^* \rightarrow He + He^+ + e$	4.5×10^{-16}	[101, 200]
318	$2He^* \rightarrow He_2^+ + e$	1.05×10^{-15}	[101, 200]
319	$He^* + He_2^* \rightarrow 2\ He + He^+ + e$	5.0×10^{-16}	[200][f]
320	$He^* + He_2^* \rightarrow He + He_2^+ + e$	2.0×10^{-15}	[200][f]

No	Reaction	Rate[a]	Ref.
321	$He^* + OH \rightarrow OH^+ + He + e$	6.08×10^{-16}	as 322
322	$He^* + H_2O \rightarrow He + H_2O^+ + e$	6.08×10^{-16}	[244][d]
323	$He^* + H_2O \rightarrow He + OH^+ + H + e$	1.39×10^{-16}	[244][d]
324	$He^* + H_2O_2 \rightarrow He + OH^+ + OH + e$	6.08×10^{-16}	as 322
325	$He^* + O \rightarrow O^+ + He + e$	2.54×10^{-16}	as 326
326	$He^* + O_2 \rightarrow O_2^+ + He + e$	2.54×10^{-16}	[138]
327	$He^* + O_2(a^1\Delta) \rightarrow O_2^+ + He + e$	2.54×10^{-16}	as 326
328	$He^* + O_2(b^1\Sigma) \rightarrow O_2^+ + He + e$	2.54×10^{-16}	as 326
329	$He_2^* + H_2O \rightarrow 2\,He + H_2O^+ + e$	2.2×10^{-15}	[245]
330	$He_2^* + O \rightarrow O^+ + 2\,He + e$	3.6×10^{-16}	as 332
331	$He_2^* + O(^1D) \rightarrow O^+ + 2\,He + e$	3.6×10^{-16}	as 332
332	$He_2^* + O_2 \rightarrow O_2^+ + 2\,He + e$	3.6×10^{-16}	[245]
333	$H + HO_2 \rightarrow H_2 + O_2$	5.6×10^{-18}	[142]
334	$H + HO_2 \rightarrow 2\,OH$	7.2×10^{-17}	[142]
335	$H + HO_2 \rightarrow H_2O + O$	2.4×10^{-18}	[142]
336	$H + H_2O_2 \rightarrow H_2O + OH$	$1.7 \times 10^{-17} e^{-1800/T_g}$	[246]
337	$H + H_2O_2 \rightarrow H_2 + HO_2$	$2.8 \times 10^{-18} e^{-1890/T_g}$	[246]
338	$H + O_3 \rightarrow OH + O_2$	$1.4 \times 10^{-16} e^{-470/T_g}$	[247, 248]
339	$H_2 + OH \rightarrow H_2O + H$	$4.27 \times 10^{-19} T_0^{2.41} e^{-1240/T_g}$	[249]
340	$H_2 + O(^1D) \rightarrow OH + H$	1.2×10^{-16}	[142]
341	$H_2 + O_2(a^1\Delta) \rightarrow O_2 + H_2$	4.53×10^{-24}	[243]
342	$2\,OH \rightarrow H_2O + O$	$6.2 \times 10^{-20} T_0^{2.6} e^{945/T_g}$	[142]
343	$OH + HO_2 \rightarrow O_2 + H_2O$	$4.8 \times 10^{-17} e^{250/T_g}$	[142, 250, 251]
344	$OH + H_2O_2 \rightarrow HO_2 + H_2O$	$2.9 \times 10^{-18} e^{-160/T_g}$	[142]
345	$OH + O \rightarrow H + O_2$	$2.4 \times 10^{-17} e^{110/T_g}$	[142, 252, 253]
346	$OH + O(^1D) \rightarrow O_2 + H$	$2.4 \times 10^{-17} e^{110/T_g}$	as 345
347	$H_2O + O(^1D) \rightarrow 2\,OH$	2.14×10^{-16}	[142]
348	$H_2O + O(^1D) \rightarrow O + H_2O$	6.6×10^{-19}	[142][b]
349	$H_2O + O(^1D) \rightarrow O_2 + H_2$	2.2×10^{-18}	[142][b]
350	$H_2O + O(^1S) \rightarrow O + H_2O$	4.5×10^{-17}	[254]
351	$H_2O + O(^1S) \rightarrow O(^1D) + H_2O$	1.5×10^{-16}	[254]
352	$H_2O + O(^1S) \rightarrow 2\,OH$	3.05×10^{-16}	[254]
353	$H_2O + O_2(a^1\Delta) \rightarrow O_2 + H_2O$	5.6×10^{-24}	[243, 248]
354	$H_2O + O_2(b^1\Sigma) \rightarrow O_2 + H_2O$	$2.25 \times 10^{-18} e^{89/300}$	[255][e]
355	$H_2O + O_2(b^1\Sigma) \rightarrow O_2(a^1\Delta) + H_2O$	$2.25 \times 10^{-18} e^{89/300}$	[255][e]
356	$HO_2 + O \rightarrow OH + O_2$	$2.7 \times 10^{-17} e^{224/T_g}$	[142, 251]
357	$H_2O_2 + O(^1D) \rightarrow H_2O + O_2$	5.2×10^{-16}	[256]
358	$O + O(^1D) \rightarrow 2\,O$	8.0×10^{-18}	[257]
359	$O + O(^1S) \rightarrow 2\,O$	$3.33 \times 10^{-17} e^{-300/T_g}$	[117, 258][f]
360	$O + O(^1S) \rightarrow O(^1D) + O$	$1.67 \times 10^{-17} e^{-300/T_g}$	[117, 258][f]
361	$O(^1D) + O_2 \rightarrow O + O_2$	6.4×10^{-18}	[142]
362	$O(^1D) + O_2 \rightarrow O + O_2(b^1\Sigma)$	2.56×10^{-17}	[142]
363	$O(^1D) + O_3 \rightarrow 2O_2$	1.2×10^{-16}	[142]
364	$O(^1D) + O_3 \rightarrow O_2 + 2O$	1.2×10^{-16}	[142]
365	$O(^1S) + O_2(a^1\Delta) \rightarrow 3\,O$	3.2×10^{-17}	[259]

No	Reaction	Rate[a]	Ref.
366	$O(^1S) + O_2(a^1\Delta) \rightarrow O + O_2$	1.1×10^{-16}	[259][f]
367	$O(^1S) + O_2(a^1\Delta) \rightarrow O(^1D) + O_2(b^1\Sigma)$	2.9×10^{-17}	[259]
368	$O_2 + O_2(a^1\Delta) \rightarrow 2\ O_2$	$3.0 \times 10^{-24} e^{-200/T_g}$	[142]
369	$O_2 + O_2(b^1\Sigma) \rightarrow O_2 + O_2(a^1\Delta)$	$3.6 \times 10^{-23} T_0^{0.5}$	[117]
370	$2O_2(a^1\Delta) \rightarrow O_2(b^1\Sigma) + O_2$	$1.8 \times 10^{-24} T_0^{3.8} e^{700/T_g}$	[260, 261]
371	$O_2(b^1\Sigma) + O_3 \rightarrow O + 2\ O_2$	1.21×10^{-17}	[255][f]
372	$O_2(b^1\Sigma) + O_3 \rightarrow O_2 + O_3$	1.21×10^{-17}	[255][f]
373	$O_2(b^1\Sigma) + O_3 \rightarrow O_2(a^1\Delta) + O_3$	1.21×10^{-17}	[255][f]
Three-body collisions			
374	$2He + He^* \rightarrow He + He_2^* + e$	2.0×10^{-46}	[262]
375	$He + He^* + H_2O \rightarrow H_2O^+ + 2\ He + e$	1.48×10^{-41}	[244][d]
376	$He + He^* + O \rightarrow O^+ + 2He + e$	8.2×10^{-42}	as 377
377	$He + He^* + O_2 \rightarrow O_2^+ + 2\ He + e$	8.2×10^{-42}	[139]
378	$He + H + H \rightarrow H_2 + He$	$6.04 \times 10^{-45} T_0^{-1.0}$	[246, 248][g]
379	$He + H + OH \rightarrow H_2O + He$	$1.42 \times 10^{-43} T_0^{-1.527} e^{-185/T_g}$	[263]
380	$He + H + O \rightarrow OH + He$	$4.36 \times 10^{-44} T_0^{-1.0}$	[264][c]
381	$He + H + O(^1D) \rightarrow OH + He$	$4.36 \times 10^{-44} T_0^{-1.0}$	as 380
382	$(He +)\ H + O_2 \rightarrow HO_2\ (+ He)$	$effective$	[142][g]
383	$(He +)\ 2OH \rightarrow H_2O_2\ (+ He)$	$effective$	[142][h]
384	$He + 2O \rightarrow O_2 + He$	$5.2 \times 10^{-47} e^{900/T_g}$	[264]
385	$He + O + O_2 \rightarrow O_3 + He$	$6.0 \times 10^{-46} T_0^{-2.4}$	[247]

[a] In m^3s^{-1} and m^6s^{-1} for two- and three-body collisions, respectively.
[b] Value in an upper limit in reference.
[c] Estimated value in reference.
[d] Branching ratios taken from Sanders [265]
[e] With branching ration 1:1 for products.
[f] Estimated branching ratio.
[g] Third body is Ar instead of He in reference.
[h] Effective rate coefficients calculated from pressure dependent rates as described by Carstensen and Dean [266] for 1 atm and a temperature range 280-350 K.

Appendix B Additional reactions accounting for air impurities

Tab. B.1: Electron collisions

No	E_{Thr} (eV)	Reaction	Rate[ab]	Ref.
Elastic scattering and momentum transfer				
386	0.00	$e + N_2 \rightarrow N_2 + e$	f(E)	[267]
Electron impact excitation and ionisation				
387	2.38	$e + N \rightarrow N(^2D) + e$	f(E)	[268]
388	3.57	$e + N \rightarrow N(^2P) + e$	f(E)	[268]
389	14.55	$e + N \rightarrow N^+ + 2e$	f(E)	[269]
390	1.19	$e + N(^2D) \rightarrow N(^2P) + e$	f(E)	[268]
391	12.17	$e + N(^2D) \rightarrow N^+ + 2e$	f(E)	[126]
392	0.02	$e + N_2 \rightarrow N_2 + e$	f(E)	[267]
393	0.29	$e + N_2 \rightarrow N_2 + e$	f(E)	[267]
394	0.57	$e + N_2 \rightarrow N_2 + e$	f(E)	[267]
395	0.86	$e + N_2 \rightarrow N_2 + e$	f(E)	[267]
396	1.13	$e + N_2 \rightarrow N_2 + e$	f(E)	[267]
397	1.41	$e + N_2 \rightarrow N_2 + e$	f(E)	[267]
398	1.68	$e + N_2 \rightarrow N_2 + e$	f(E)	[267]
399	15.50	$e + N_2 \rightarrow N_2^+ + 2e$	f(E)	[267]
400	9.26	$e + NO \rightarrow NO^+ + 2e$	f(E)	[270]
Super-elastic collisions				
401	-2.38	$e + N(^2D) \rightarrow N + e$	f(E)	as 387[c]
402	-3.57	$e + N(^2P) \rightarrow N + e$	f(E)	as 388[c]
Dissociation				
403	12.25	$e + N_2 \rightarrow N + N(^2D) + e$	f(E)	[271]
404	6.77	$e + NO \rightarrow O + N + e$	f(E)	[272]
405	0.00	$e + NO_2 \rightarrow O + NO + e$	$5.6 \times 10^{-15} e^{-3.11/T_e}$	[273]
406	0.00	$e + N_2O \rightarrow O + N_2 + e$	$1.4 \times 10^{-15} e^{-1.67/T_e}$	[273]
407	0.00	$e + N_2O \rightarrow N + NO + e$	$1.0 \times 10^{-16} e^{-4.93/T_e}$	[273]
408	0.00	$e + N_2O \rightarrow O^* + N_2 + e$	$1.2 \times 10^{-15} e^{-3.46/T_e}$	[273]
409	5.60	$e + NH \rightarrow H + N + e$	f(E)	as 412
410	5.60	$e + NH_2 \rightarrow NH + H + e$	f(E)	as 412
411	8.90	$e + NH_2 \rightarrow N + 2H + e$	f(E)	as 413
412	5.60	$e + NH_3 \rightarrow NH_2 + H + e$	f(E)	[274]

No	E_{Thr} (eV)	Reaction	Rate[ab]	Ref.
413	8.90	$e + NH_3 \rightarrow NH + 2H + e$	f(E)	[274]
Dissociative ionisation				
414	21.31	$e + N_2 \rightarrow N^+ + N + 2e$	f(E)	[275]
415	20.17	$e + NO \rightarrow O^+ + N + 2e$	f(E)	[270]
416	21.09	$e + NO \rightarrow N^+ + O + 2e$	f(E)	[270]
417	13.00	$e + NO_2 \rightarrow NO^+ + O + 2e$	f(E)	[270]
418	17.70	$e + NH \rightarrow N^+ + H + 2e$	f(E)	[276]
(Dissociative) Electron attachment				
419	4.50	$e + NH_2 \rightarrow NH + H^-$	f(E)	as 420
420	4.50	$e + NH_3 \rightarrow NH_2 + H^-$	f(E)	[193]
Recombination				
421	0.00	$e + N^+ \rightarrow N$	f(E)	[d]
422	0.00	$e + N_2^+ \rightarrow 2N$	f(E)	[217][e]
423	0.00	$e + N_4^+ \rightarrow 2N + N_2$	$3.13 \times 10^{-13} T_e^{-0.41}$	[277, 278]
424	0.00	$e + N_4^+ \rightarrow 2N_2$	$3.22 \times 10^{-13} T_e^{-0.5}$	[134][f]
425	0.00	$e + NO^+ \rightarrow NO$	$3.10 \times 10^{-19} T_e^{-0.7}$	[279][fg]
426	0.00	$e + NO^+ \rightarrow O + N$	$1.66 \times 10^{-15} T_e^{-1.5}$	[134][f]
427	0.00	$e + NO^+ \rightarrow O + N(^2D)$	$7.76 \times 10^{-15} T_e^{-0.5}$	[279][fg]

[a] In m^3s^{-1} and m^6s^{-1} for two- and three-body collisions, respectively.
[b] f(E) means rate coefficients are calculated by the internal Boltzmann solver using cross sections obtained from the indicated literature.
[c] As process from ground state but shifted and scaled.
[d] $\sigma = 7.2 \times 10^{-25}/E$ m^2
[e] $\sigma = 5.0 \times 10^{-19}(0.1/E)^{1.15}$ m^2
[f] Calculated for $T_g = 300$K.
[g] Value is estimated in source.

Tab. B.2: Ion-ion chemistry

No	Reaction	Rate[a]	Ref.
Three-body collisions			
428 - 442	$A^+ + B^- + He \rightarrow A + B + He$	$2.0 \times 10^{-37} T_0^{-2.5}$	[134][bc]
443 - 447	$A_4^+ + B^- + He \rightarrow 2\ A_2 + B + He$	$2.0 \times 10^{-37} T_0^{-2.5}$	[134][bd]
448 - 456	$A^+ + OH^- \cdot (H_2O)_n + He \rightarrow A + OH + n \cdot H_2O + He$	$2.0 \times 10^{-37} T_0^{-2.5}$	[134][be]
457 - 459	$A_4^+ + OH^- \cdot (H_2O)_n + He \rightarrow 2\ A_2 + OH + n \cdot H_2O + He$	$2.0 \times 10^{-37} T_0^{-2.5}$	[134][bf]

[a] In m^6s^{-1}.
[b] Value estimated in reference.
[c] For A = N, N_2, NO, and B = O, O_2, H, OH, H_2O_2.
[d] For A = N and B = O, O_2, H, OH, H_2O_2.
[e] For A = N, N_2, NO and n = 1..3.
[f] For A = N and n = 1..3.

Tab. B.3: Ion-neutral chemistry

No	Reaction	Rate[a]	Ref.
Two-body collisions - positive ions			

No	Reaction	Rate[a]	Ref.
460	$He^+ + N_2 \rightarrow N^+ + N + He$	9.6×10^{-16}	[135, 223]
461	$He^+ + N_2 \rightarrow N_2^+ + He$	6.4×10^{-16}	[135, 223]
462	$He^+ + NO \rightarrow N^+ + O + He$	1.4×10^{-15}	[135, 280]
463	$He^+ + NO \rightarrow O^+ + N + He$	2.0×10^{-16}	[135, 280]
464	$He^+ + NH_2 \rightarrow N^+ + H_2 + He$	$8.0 \times 10^{-16} T_0^{-0.5}$	[135, 221]
465	$He_2^+ + N_2 \rightarrow N_2^+ + 2He$	6.4×10^{-16}	as 460
466	$He_2^+ + NO \rightarrow N^+ + O + 2He$	1.4×10^{-15}	as 462
467	$He_2^+ + NO \rightarrow O^+ + N + 2He$	2.0×10^{-16}	as 463
468	$OH^+ + N \rightarrow NO^+ + H$	8.9×10^{-16}	[135, 221]
469	$OH^+ + NO \rightarrow NO^+ + OH$	3.59×10^{-16}	[135, 224]
470	$H_2O^+ + NO \rightarrow NO^+ + H_2O$	2.7×10^{-16}	[135, 232]
471	$O_2^+(H_2O) + NO \rightarrow NO^+ + H_2O + O_2$	5.3×10^{-16}	[124]
472	$O^+ + N_2 \rightarrow NO^+ + N$	1.2×10^{-18}	[230, 281]
473	$O_2^+ + N \rightarrow NO^+ + O$	1.2×10^{-16}	[135, 282]
474	$O_2^+ + NO \rightarrow NO^+ + O_2$	4.5×10^{-16}	[281]
475	$N^+ + H_2O \rightarrow H_2O^+ + N$	$2.8 \times 10^{-15} T_0^{-0.5}$	[135, 230, 283]
476	$N^+ + OH \rightarrow OH^+ + N$	$3.7 \times 10^{-16} T_0^{-0.5}$	[135, 221]
477	$N^+ + O_2 \rightarrow O_2^+ + N$	3.11×10^{-16}	[135, 230, 283]
478	$N^+ + NO \rightarrow N_2^+ + O$	7.9×10^{-17}	[135, 230, 283]
479	$N_2^+ + H_2O \rightarrow OH^+ + N$	$2.3 \times 10^{-15} T_0^{-0.5}$	[135, 230]
480	$N_2^+ + OH \rightarrow OH^+ + N_2$	$6.3 \times 10^{-16} T_0^{-0.5}$	[135, 221]
481	$N_2^+ + O \rightarrow O^+ + N_2$	1.0×10^{-17}	[135, 284]
482	$N_2^+ + O \rightarrow NO^+ + N$	1.3×10^{-16}	[135, 284]
483	$N_2^+ + O_2 \rightarrow O_2^+ + N_2$	5.0×10^{-17}	[135, 230]
484	$N_4^+ + H_2O \rightarrow H_2O^+ + 2N_2$	3.0×10^{-15}	[285]
485	$N_4^+ + O_2 \rightarrow O_2^+ + 2N_2$	2.5×10^{-16}	[285]
Two-body collisions - negative ions			
486	$H^- + NH \rightarrow NH_2 + e$	1.0×10^{-16}	[135, 221]
487	$H^- + NH_2 \rightarrow NH_3 + e$	1.0×10^{-15}	[135, 221]
Three-body collisions - positive ions			
488	$N_2^+ + N_2$ (+ He) $\rightarrow N_4^+$ (+ He)	$effective$	[124]

[a] In m^3s^{-1} and m^6s^{-1} for two- and three-body collisions, respectively

Tab. B.4: Neutral chemistry

No	Reaction	Rate[a]	Ref.
Two-body collisions			
489	$He^* + N_2 \rightarrow N_2^+ + He + e$	6.8×10^{-17}	[286]
490	$He_2^* + N_2 \rightarrow N_2^+ + 2He + e$	6.8×10^{-17}	as 489
491	$H + NO_2 \rightarrow NO + OH$	$4.0 \times 10^{-16} e^{-340/T_g}$	[247]
492	$H + NO_3 \rightarrow NO_2 + OH$	1.1×10^{-16}	[248, 287]
493	$H + HNO \rightarrow NO + H_2$	$4.5 \times 10^{-17} T_0^{-0.72} e^{-329/T_g}$	[135, 288]
494	$H_2 + N(^2D) \rightarrow NH + N$	$4.2 \times 10^{-17} e^{-105/T_g}$	[248, 289]
495	$OH + NO_3 \rightarrow NO_2 + HO_2$	2.0×10^{-17}	[142, 248]

No	Reaction	Rate[a]	Ref.
496	$OH + NH \rightarrow N + H_2O$	3.09×10^{-18}	[290]
497	$OH + NH \rightarrow HNO + H$	3.32×10^{-17}	[290]
498	$OH + NH_2 \rightarrow NH + H_2O$	$1.35 \times 10^{-18} T_0^{1.25} e^{43.5/T_g}$	[135]
499	$OH + NH_2 \rightarrow NH_3 + O$	$2.08 \times 10^{-19} T_0^{0.76} e^{-262/T_g}$	[135]
500	$OH + NH_3 \rightarrow NH_2 + H_2O$	$1.47 \times 10^{-19} T_0^{2.05} e^{-7/T_g}$	[135]
501	$OH + HNO \rightarrow NO + H_2O$	$6.17 \times 10^{-18} T_0^{1.23} e^{44.3/T_g}$	[135]
502	$OH + HNO_2 \rightarrow NO_2 + H_2O$	$2.5 \times 10^{-18} e^{260/T_g}$	[142]
503	$OH + HNO_3 \rightarrow NO_3 + H_2O$	$1.5 \times 10^{-19} e^{260/T_g}$	[142]
504	$H_2O + N(^2D) \rightarrow NH + OH$	1.4×10^{-17}	[289][b]
505	$H_2O + N(^2D) \rightarrow H + HNO$	1.4×10^{-17}	[289][b]
506	$H_2O + N(^2D) \rightarrow H_2 + NO$	1.4×10^{-17}	[289][b]
507	$H_2O + N(^2P) \rightarrow NH + OH$	1.9×10^{-19}	[291][b]
508	$H_2O + N(^2P) \rightarrow H + HNO$	1.9×10^{-19}	[291][b]
509	$H_2O + N(^2P) \rightarrow H_2 + NO$	1.9×10^{-19}	[291][b]
510	$O + NO_2 \rightarrow O_2 + NO$	$5.1 \times 10^{-18} e^{198/T_g}$	[142]
511	$O + NO_3 \rightarrow O_2 + NO_2$	1.7×10^{-17}	[142]
512	$O + NH \rightarrow NO + H$	1.7×10^{-16}	[290][c]
513	$O + NH \rightarrow OH + N$	5.0×10^{-18}	[290][c]
514	$O + NH_2 \rightarrow HNO + H$	$6.3 \times 10^{-17} T_0^{-0.1}$	[135, 136]
515	$O + NH_2 \rightarrow OH + NH$	$7.0 \times 10^{-18} T_0^{-0.1}$	[135, 136]
516	$O + HNO \rightarrow NO + OH$	$3.8 \times 10^{-17} T_0^{-0.08}$	[135, 292]
517	$O(^1D) + NO_2 \rightarrow O_2 + NO$	7.3×10^{-17}	[293][b]
518	$O(^1D) + NO_2 \rightarrow O_2(a^1\Delta) + NO$	7.3×10^{-17}	[293][b]
519	$O(^1D) + NO_2 \rightarrow O_2(b^1\Sigma) + NO$	7.3×10^{-17}	[293][b]
520	$O(^1D) + N_2 \rightarrow O + N_2$	$2.15 \times 10^{-17} e^{110/T_g}$	[142]
521	$O(^1D) + N_2O \rightarrow O + N_2O$	6.0×10^{-18}	[142]
522	$O(^1D) + N_2O \rightarrow 2NO$	7.6×10^{-17}	[142]
523	$O(^1D) + N_2O \rightarrow N_2 + O_2$	4.3×10^{-17}	[142]
524	$O(^1S) + NO \rightarrow O + NO$	1.98×10^{-16}	[254]
525	$O(^1S) + NO \rightarrow O(^1D) + NO$	3.52×10^{-16}	[254]
526	$O_2 + N(^2D) \rightarrow O + NO$	$2.3 \times 10^{-18} e^{-185/T_g}$	[289]
527	$O_2 + N(^2D) \rightarrow O(^1D) + NO$	$7.4 \times 10^{-18} e^{-185/T_g}$	[289]
528	$O_2 + N(^2P) \rightarrow O + NO$	$1.0 \times 10^{-18} e^{-60/T_g}$	[289]
529	$O_2 + N(^2P) \rightarrow O(^1D) + NO$	$1.0 \times 10^{-18} e^{-60/T_g}$	[289]
530	$O_2 + N(^2P) \rightarrow O(^1S) + NO$	$1.0 \times 10^{-18} e^{-60/T_g}$	[289]
531	$O_3 + N(^2D) \rightarrow O_2 + NO$	1.0×10^{-16}	[291][d]
532	$O_3 + N(^2D) \rightarrow O + O_2 + N$	1.0×10^{-16}	est.
533	$N + NO \rightarrow N_2 + O$	$2.1 \times 10^{-17} e^{100/T_g}$	[247]
534	$N + NO_2 \rightarrow N_2O + O$	$5.8 \times 10^{-18} e^{220/T_g}$	[247]
535	$N + NO_2 \rightarrow 2NO$	$4.5 \times 10^{-18} e^{220/T_g}$	[247][e]
536	$N + NH \rightarrow H + N_2$	$1.95 \times 10^{-17} T_0^{0.51} e6{-}0.08/T_g$	[294]
537	$N(^2D) + NO \rightarrow O + N_2$	2.0×10^{-17}	[289][b]
538	$N(^2D) + NO \rightarrow O(^1D) + N_2$	2.0×10^{-17}	[289][b]
539	$N(^2D) + NO \rightarrow O(^1S) + N_2$	2.0×10^{-17}	[289][b]
540	$N(^2D) + N_2O \rightarrow NO + N_2$	$5.75 \times 10^{-18} e^{-570/T_g}$	[289][b]

No	Reaction	Rate[a]	Ref.
541	$N(^2D) + N_2O \rightarrow O + N + N_2$	$5.75 \times 10^{-18} e^{-570/T_g}$	[289][b]
542	$N(^2P) + NO \rightarrow N + NO$	2.9×10^{-17}	[289]
543	$NO_2 + NH \rightarrow HNO + NO$	$2.44 \times 10^{-17} T_0^{-1.94} e^{-56.9/T_g}$	[135, 295]
544	$NO_2 + NH \rightarrow N_2O + OH$	$1.7 \times 10^{-17} T_0^{-1.94} e^{-56.9/T_g}$	[135, 295]
545	$2NH \rightarrow NH_2 + N$	$1.83 \times 10^{-19} T_0^{1.8} e^{70/T_g}$	[135]
546	$NH_2 + NO \rightarrow N_2 + H_2O$	$4.27 \times 10^{-17} T_0^{-2.5} e^{-331/T_g}$	[135]
547	$NH_2 + NO \rightarrow N_2 + OH + H$	1.49×10^{-18}	[135]
Three-body collisions			
548	$H + N + He \rightarrow NH + He$	4.75×10^{-44}	[296]
549	$H + NO + He \rightarrow HNO + He$	$5.04 \times 10^{-44} T_0^{-1.32} e^{-370/T_g}$	[297]
550	$OH + NO + He \rightarrow HNO_2 + He$	$effective$	[142]
551	$OH + NO_2 (+ He) \rightarrow HNO_3 (+ He)$	$effective$	[142]

[a] In m^3s^{-1} and m^6s^{-1} for two- and three-body collisions, respectively.
[b] Estimated branching ratio.
[c] Value for 298 K.
[d] Estimated value in reference.
[e] Value from this reference was corrected according to branching ratio found by Phillips and Schiff [298].

Appendix C L-state mixing in atomic hydrogen

The importance of L-state mixing for typical experimental conditions investigated in this work is investigated using a model proposed by Preppernau et al [178]. In this model, the rate of change in density of the different sub-levels is calculated taking into account a radiative decay, quenching, and L-state mixing.

$$\begin{aligned}
\frac{\mathrm{d}n_\mathrm{s}}{\mathrm{d}t} &= -n_\mathrm{s}\left(\tau_\mathrm{s}^{-1} + n_\mathrm{q}\left(8k_\mathrm{mix} + k_\mathrm{q}\right)\right) + 1n_\mathrm{q}k_\mathrm{mix}\left(n_\mathrm{p} + n_\mathrm{d}\right) \\
\frac{\mathrm{d}n_\mathrm{p}}{\mathrm{d}t} &= -n_\mathrm{p}\left(\tau_\mathrm{p}^{-1} + n_\mathrm{q}\left(6k_\mathrm{mix} + k_\mathrm{q}\right)\right) + 3n_\mathrm{q}k_\mathrm{mix}\left(n_\mathrm{s} + n_\mathrm{d}\right) \\
\frac{\mathrm{d}n_\mathrm{d}}{\mathrm{d}t} &= -n_\mathrm{d}\left(\tau_\mathrm{d}^{-1} + n_\mathrm{q}\left(4k_\mathrm{mix} + k_\mathrm{q}\right)\right) + 5n_\mathrm{q}k_\mathrm{mix}\left(n_\mathrm{s} + n_\mathrm{p}\right)
\end{aligned} \tag{C.1}$$

where k_mix is a background gas specific mixing coefficient. From this set of differential equations, a radiative rate from the n=3 level can be calculated

$$R(t) = \frac{b_\mathrm{s}}{\tau_\mathrm{s}}n_\mathrm{s}(t) + \frac{b_\mathrm{p}}{\tau_\mathrm{p}}n_\mathrm{p}(t) + \frac{b_\mathrm{d}}{\tau_\mathrm{d}}n_\mathrm{d}(t) \tag{C.2}$$

where b are the branching ratios for the fluorescence decay from each sub-level. The 3s and 3d states can only decay into the 2p state, as indicated in fig. 5.2. Therefore, b_s and b_d are set to one. From the 3p state, approximately 88% decays into the 1s ground state, and is not detectable in the experiment. Therefore, b_p is set to 0.12. $R(t)$ can be normalised to the value of $R_0 = R(t=0) = 5.73 \times 10^7$ s^{-1}.

Figure C.1 shows the normalised populations of the H(n=3) sub-levels, and the normalised H(n=3) decay rate, taking into account different depopulation mechanisms. In the calculations, a pressure of 1 bar He, 315 K gas temperature, and the values $k_\mathrm{q} = 0.317 \times 10^{-1}$ cm^{3}s^{-1} and $k_\mathrm{mix} = 0.07 \times 10^{-1}$ cm^{3}s^{-1} [89] are assumed.

If only radiative decay is taken into account (fig. C.1 (a)), the 3s and 3d state start off with a relative population of 12 and 88% respectively, and decay with their own lifetimes, which are 159 and 15.6 ns. The 3p state is not populated by the laser radiation. The overall lifetime of the n=3 state is therefore dominated by the 3d state, due to its higher population. If quenching and radiative emission are considered together (fig. C.1 (c)) both the 3d and 3s states are depopulated much faster, with a time constant more than 10 times larger.

If L-state mixing is considered without taking into account quenching (fig. C.1 (b)), a population of the 3p state takes place in the first few nanoseconds after population of the 3d and 3s states. The sub-level densities therefore do not follow exponential trends until an equilibrium between the populations is reached. The equilibrium densities are defined by the statistical weights of the different sub-levels: they are 55.55% (3d), 33.33% (3p) and 11.11% (3s). From the model, 56.8%, 31.4% and 11.8% are obtained, in good agreement with the theoretical values. The overall lifetime is calculated in the equilibrium region as 10.5 ns, which is shorter than the lifetime obtained for radiative contribution only due to the short lifetime of the 3p state. By taking into account all three processes (fig. C.1 (d)), the equilibrium overall lifetime is shortened to 1.2 ns. This is in very

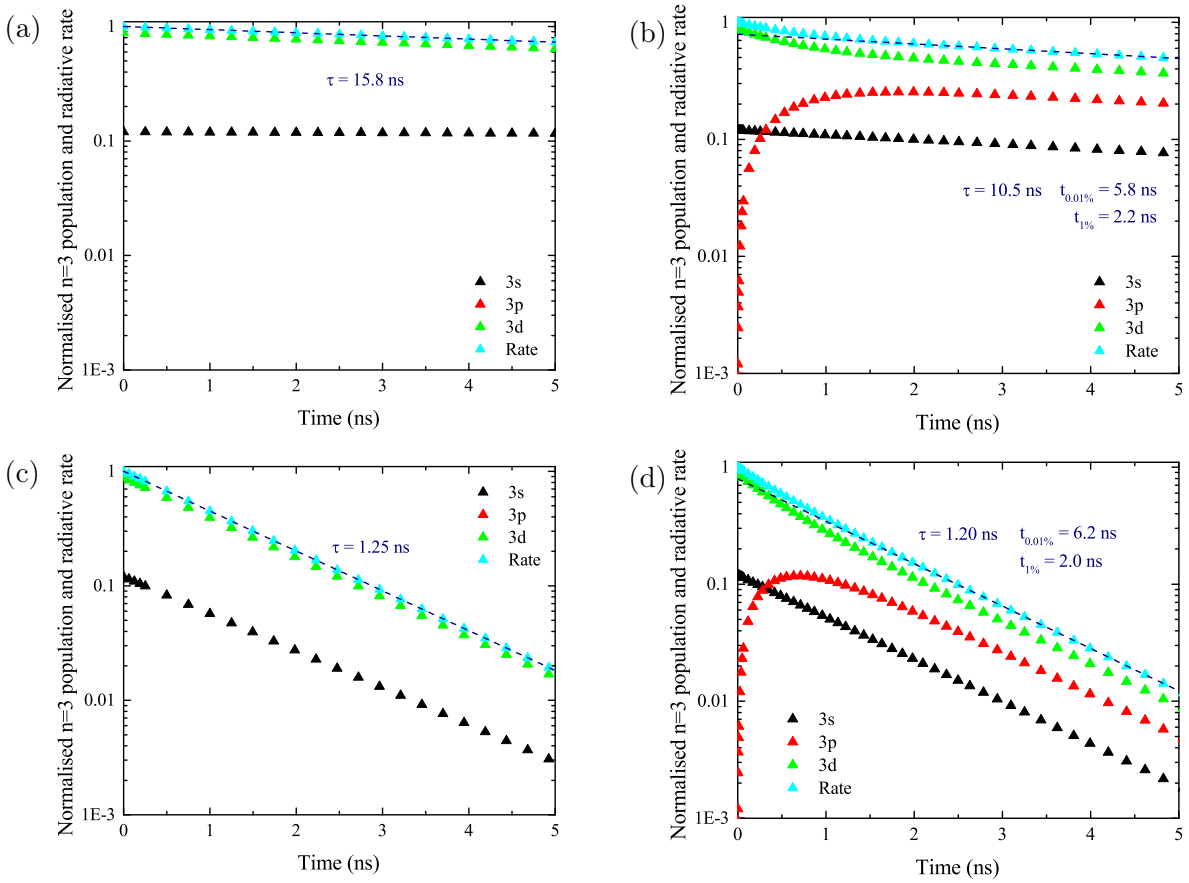

Fig. C.1: Normalised n=3 sub-level densities and effective decay rate taking into account different depopulation mechanisms: (a) only radiative decay, (b) radiative decay and L-state mixing, (c) radiative decay and quenching, (d) all three processes. Also shown is the time after which an equilibrium between the different processes is established (for a relative rate change smaller than 1% and 0.01%), and the lifetime obtained from an exponential fit in this equilibrium region.

good agreement with an experimentally determined lifetime of 0.97 ns in a pure He flow, where the detected H is produced from impurities only, as it will be discussed in section 5.2. Only on very small timescales after the laser pulse, the decay rate deviates from an exponential decay, due to the internal redistribution of the H(n=3) state.

Appendix D Titration of H_2O_2 solution

Commercial H_2O_2 solutions typically do not have a strictly defined concentration, which is necessary for the absolute calibration of the conducted experiments. Additionally, H_2O_2 solution decomposes over time, especially under the influence of light or heat, and should therefore not be used over a long period of time.

In order to check the concentration of the used H_2O_2 solution, 10% solution was titrated using 0.025 M potassium permanganate solution. For this experiment, three different solutions have to be prepared:

1. **10% H_2O_2 solution.** This solution is prepared by mixing 1 part of commercial 30% H_2O_2 solution with 2 parts of H_2O .
2. **Sulfuric acid solution.** Concentrated H_2SO_4 is diluted 6 times to create a 3 M solution.
3. **Potassium permanganate solution.** Combine 2.015 g of $KMnO_4$ powder (Alfa Aesar, 98%) with 0.5 l of H_2O to create a 0.025 M solution.

1 ml of the H_2O_2 solution is then mixed with 20 ml of H_2O and 10 ml of the Sulfuric acid solution in an Erlenmeyer flask.

The permanganate ion reacts with the H_2O_2 solution in the following balance equation:

$$2MnO_4^- + 6H^+ + 5H_2O_2 \rightarrow 5O_2 + 2Mn^{2+} + 8H_2O \tag{D.1}$$

While the permanganate aqueous complex MnO_4^- dyes the liquid dark purple, the reactants (right hand side of eq. D.1) are clear of colour. The permanganate solution is slowly added to 10% H_2O_2 solution and reacts with H_2O_2 , leaving a clear solution, until all H_2O_2 molecules have reacted with MnO_4^-. After that the solution starts colouring purple, because the MnO_4^- starts getting accumulated in the solution.

By measuring the amount of added $KMnO_4$ solution $V_{KMnO_4} = 48$ ml and taking into account the molarity of the solution, the amount of MnO_4^+ ions can be calculated as $c_{MnO_4^-} = 1.2 \times 10^{-3}$ mol. From eq. D.1 it is clear that the molar ratio of MnO_4^- and H_2O_2 is 2.5. Therefore, the titrated amount of H_2O_2 can be determined as 3.0×10^{-3} mol. Multiplication with the molar mass of H_2O_2 $m_{hydper} = 34.01 \frac{g}{mol}$ and dividing by the weight of 1 ml of H_2O_2 solution $w_{H_2O_2} = 1.015$ g leads to a H_2O_2 concentration of 10.05% in the solution. Therefore, the concentration of the commercial H_2O_2 solution is 30.15%.

Common symbols used in equations

This table is a collection of symbols, abbreviaions and subscripts which are used throughout this manuscript.

Symbol	Name
Subscripts used throughout this document.	
i	any
j	ions
e	electrons
n	neutrals
g	gas
Symbols used throughout this document.	
A	Absorbance
A_a	Arrhenius A coefficient
A_flow	Cross sectional area of plasma
A_s	Surface area of reactor in contact with plasma
f_i	Return fraction for species i
c	Speed of light
D_i	Diffusion constant for species i
E	Energy
E_a	Activation energy
E_t	Threshold energy
e	Elementary charge
F_i	Flow rate for species i
g	statistical weight
I	Current amplitude
k	Reaction rate coefficient
k_B	Boltzmann constant
l	Absorption length
N_A	Avogadro constant
n_i	Volume density for species i
P_d	Power deposited in Plasma
p	Pressure

Symbol	Name
R	Rate
r	Radius
S_i	Source term for species i
t	Time
T	Transmission
T_i	Temperature for species i
T_0	relative temperature $\frac{T_\mathrm{g}}{300}$
U	Voltage amplitude
V_p	Plasma volume
v_x	Velocity in x-direction
α	Absorption coefficient
ε_a^i	Electron affinity for species i
γ	Sticking coefficient
Λ	Diffusion length
λ	Wavelength
μ_j	Ion mobility for species j
ν	Collision frequency
ϕ	Line profile
ρ	Mass density
σ	Cross section
τ_P	Time scale of interest for PumpKin simulations

Symbols denoting specific species.

H	H(n=1) - Ground state of atomic hydrogen
H*	H(n=3) - Laser excited state of atomic hydrogen for TALIF measurements
O	$\sum_J$ O($2p^4\ ^3P_J$) - Ground state of atomic oxygen
O*	$\sum_J$ O($3p\ ^3P_J$) - Laser excited state of atomic oxygen for TALIF measurements

References

[1] E. Kvam, B. Davis, F. Mondello, and A. L. Garner. *Antimicrob. Agents Chemother.* **56** (2012) 2028–2036.

[2] A. Privat-Maldonado, D. O'Connell, E. Welch, R. Vann, and M. W. van der Woude. *Sci. Rep.* **6** (2016) 35646.

[3] J. H. Park, N. Kumar, D. H. Park, M. Yusupov, E. C. Neyts, C. C. W. Verlackt, A. Bogaerts, M. H. Kang, H. S. Uhm, E. H. Choi, and P. Attri. *Sci. Rep.* **5** (2015) 13849.

[4] A. M. Hirst, F. M. Frame, N. J. Maitland, and D. O'Connell. *IEEE Trans. Plasma Sci.* **42** (2014) 2740–2741.

[5] A. M. Hirst, M. S. Simms, V. M. Mann, N. J. Maitland, D. O'Connell, and F. M. Frame. *Br. J. Cancer* **112** (2015) 1536–1545.

[6] D. O'Connell, L. J. Cox, W. B. Hyland, S. J. McMahon, S. Reuter, W. G. Graham, T. Gans, and F. J. Currell. *Appl. Phys. Lett.* **98** (2011) 043701.

[7] A. R. Gibson, H. O. McCarthy, A. A. Ali, D. O'Connell, and W. G. Graham. *Plasma Processes Polym.* **11** (2014) 1142–1149.

[8] S. Vermeylen, J. De Waele, S. Vanuytsel, J. De Backer, J. Van der Paal, M. Ramakers, K. Leyssens, E. Marcq, J. Van Audenaerde, E. L. J. Smits, S. Dewilde, and A. Bogaerts. *Plasma Processes Polym.* **13** (2016) 1195–1205.

[9] K. Wende, P. Williams, J. Dalluge, W. Van Gaens, H. Aboubakr, J. Bischof, T. von Woedtke, S. M. Goyal, K.-D. Weltmann, A. Bogaerts, M. Masur, and P. J. Bruggeman. *Biointerphases* **10** (2015) 029518.

[10] M. Laroussi. *IEEE Trans. Plasma Sci.* **30** (2002) 1409–1415.

[11] M. Laroussi. *Plasma Process. Polym.* **2** (2005) 391–400.

[12] R. E. J. Sladek and E. Stoffels. *J. Phys. D: Appl. Phys.* **38** (2005) 1716–1721.

[13] A. M. Hirst, F. M. Frame, N. J. Maitland, and D. O'Connell. *BioMed Res. Int.* **2014** (2014) 1–15.

[14] E. A. Ratovitski, X. Cheng, D. Yan, J. H. Sherman, J. Canady, B. Trink, and M. Keidar. *Plasma Processes Polym.* **11** (2014) 1128–1137.

[15] M. Vandamme, E. Robert, S. Lerondel, V. Sarron, D. Ries, S. Dozias, J. Sobilo, D. Gosset, C. Kieda, B. Legrain, J. M. Pouvesle, and A. Le Pape. *Int. J. Cancer* **130** (2011) 2185–2194.

[16] G. Isbary, J. Heinlin, T. Shimizu, J.L. Zimmermann, G. Morfill, H.-U. Schmidt, R. Monetti, B. Steffes, W. Bunk, Y. Li, T. Klaempfl, S. Karrer, M. Landthaler, and W. Stolz. *Br. J. Dermatol.* **167** (2012) 404–410.

[17] A. V. Nastuta, I. Topala, C. Grigoras, V. Pohoata, and G. Popa. *J. Phys. D: Appl. Phys.* **44** (2011) 105204.

[18] R. S. Tipa and G. M. W. Kroesen. *IEEE Trans. Plasma Sci.* **39** (2011) 2978–2979.

[19] K. R. Stalder and J. Woloszko. *Contrib. Plasma Phys.* **47** (2007) 64–71.

[20] G. Fridman, G. Friedman, A. Gutsol, A. B. Shekhter, V. N. Vasilets, and A. Fridman. *Plasma Process. Polym.* **5** (2008) 503–533.

[21] M. G. Kong, G. Kroesen, G. Morfill, T. Nosenko, T. Shimizu, J. van Dijk, and J. L. Zimmermann. *New J. Phys.* **11** (2009) 115012.

[22] T. von Woedtke, S. Reuter, K. Masur, and K.-D. Weltmann. *Phys. Rep.* **530** (2013) 291–320.

[23] S. Schneider, J.-W. Lackmann, D. Ellerweg, B. Denis, F. Narberhaus, J. E. Bandow, and J. Benedikt. *Plasma Process. Polym.* **9** (2011) 561–568.

[24] S. Schneider, J.-W. Lackmann, F. Narberhaus, J. E. Bandow, B. Denis, and J. Benedikt. *J. Phys. D: Appl. Phys.* **44** (2011) 295201.

[25] J.-W. Lackmann, S. Schneider, E. Edengeiser, F. Jarzina, S. Brinckmann, E. Steinborn, M. Havenith, J. Benedikt, and J. E. Bandow. *Journal of The Royal Society Interface* **10** (2013) 20130591.

[26] D. B. Graves. *J. Phys. D: Appl. Phys* **45** (2012) 263001.

[27] J. Van der Paal, S. Aernouts, A. C. T. van Duin, E. C. Neyts, and A. Bogaerts. *J. Phys. D: Appl. Phys.* **46** (2013) 395201.

[28] U. Pliquett, R.P. Joshi, V. Sridhara, and K.H. Schoenbach. *Bioelectrochemistry* **70** (2007) 275–282.

[29] S. A. Norberg, E. Johnsen, and M. J. Kushner. *J. Phys. D: Appl. Phys.* **49** (2016) 185201.

[30] J. Golda, J. Held, B. Redeker, M. Konkowski, P. Beijer, A. Sobota, G. Kroesen, N. St. J. Braithwaite, S. Reuter, M. M. Turner, T. Gans, D. O'Connell, and V. Schulz-von der Gathen. *J. Phys. D: Appl. Phys.* **49** (2016) 084003.

[31] COST European Cooperation in Science and Technology. *http://www.cost.eu/*.

[32] K.-D. Weltmann, E. Kindel, R. Brandenburg, C. Meyer, R. Bussiahn, C. Wilke, and T. von Woedtke. *Contrib. Plasma Phys.* **49** (2009) 631–640.

[33] E. Robert, E. Barbosa, S. Dozias, M. Vandamme, C. Cachoncinlle, R. Viladrosa, and J. M. Pouvesle. *Plasma Processes Polym.* **6** (2009) 795–802.

[34] C. Tendero, C. Tixier, P. Tristant, J. Desmaison, and P. Leprince. *Spectrochim. Acta B* **61** (2006) 2–30.

[35] A. M. Hirst, F. M. Frame, M. Arya, N. J. Maitland, and D. O'Connell. *Tumor Biology* **37** (2016) 7021–7031.

[36] A. F. H. van Gessel, K. M. J. Alards, and P. J. Bruggeman. *J. Phys. D: Appl. Phys.* **46** (2013) 265202.

[37] C. Douat, S. Hübner, R. Engeln, and J. Benedikt. *Plasma Sources Sci. Technol.* **25** (2016) 025027.

[38] A. V. Pipa, S. Reuter, R. Foest, and K.-D. Weltmann. *J. Phys. D: Appl. Phys.* **45** (2012) 085201.

[39] D. X. Liu, P. Bruggeman, F. Iza, M. Z. Rong, and M. G. Kong. *Plasma Sources Sci. Technol.* **19** (2010) 025018.

[40] P. Bruggeman, G. Cunge, and N. Sadeghi. *Plasma Sources Sci. Technol.* **21** (2012) 035019.

[41] A. Schmidt-Bleker, J. Winter, S. Iseni, M. Dünnbier, K.-D. Weltmann, and S. Reuter. *J. Phys. D: Appl. Phys.* **47** (2014) 145201.

[42] J. Winter, K. Wende, K. Masur, S. Iseni, M. Dünnbier, U. Hammer, H. Tresp, K.-D. Weltmann, and S. Reuter. *J. Phys. D: Appl. Phys.* **46** (2013) 295401.

[43] S. Große-Kreul, S. Hübner, S. Schneider, A. von Keudell, and J. Benedikt. *EPJ Techn. Instrum.* **3** (2016) 1–16.

[44] J. Benedikt, D. Schröder, S. Schneider, G. Willems, A. Pajdarová, J. Vlček, and V. Schulz-von der Gathen. *Plasma Sources Sci. Technol.* **25** (2016) 045013.

[45] P. Bruggeman, F. Iza, P. Guns, D. Lauwers, M. G Kong, Y. A. Gonzalvo, C. Leys, and D. C. Schram. *Plasma Sources Sci. Technol.* **19** (2009) 015016.

[46] G. Dilecce, P. F. Ambrico, M. Simek, and S. De Benedictis. *Chem. Phys.* **398** (2012) 142–147.

[47] G. Dilecce, P. F. Ambrico, M. Simek, and S. De Benedictis. *J. Phys. D: Appl. Phys.* **45** (2012) 125203.

[48] T. Verreycken, N. Sadeghi, and P. J. Bruggeman. *Plasma Sources Sci. Technol.* **23** (2014) 045005.

[49] P. Bruggeman, F. Iza, D. Lauwers, and Y. A. Gonzalvo. *J. Phys. D: Appl. Phys.* **43** (2009) 012003.

[50] Z. Abd-Allah, D. A. G. Sawtell, K. McKay, G. T. West, P. J. Kelly, and J. W. Bradley. *J. Phys. D: Appl. Phys.* **48** (2015) 085202.

[51] C. A. Vasko, D. X. Liu, E. M. van Veldhuizen, F. Iza, and P. J. Bruggeman. *Plasma Chem. Plasma Process.* **34** (2014) 1081–1099.

[52] D. X. Liu, F. Iza, X. H. Wang, M. G. Kong, and M. Z. Rong. *Appl. Phys. Lett.* **98** (2011) 221501.

[53] K. McKay, D. X. Liu, M. Z. Rong, F. Iza, and M. G. Kong. *J. Phys. D: Appl. Phys.* **45** (2012) 172001.

[54] T. Murakami, K. Niemi, T. Gans, D. O'Connell, and W. G. Graham. *Plasma Sources Sci. Technol.* **22** (2013) 015003.

[55] T. Murakami, K. Niemi, T. Gans, D. O'Connell, and W. G. Graham. *Plasma Sources Sci. Technol.* **22** (2013) 045010.

[56] T. Murakami, K. Niemi, T. Gans, D. O'Connell, and W. G. Graham. *Plasma Sources Sci. Technol.* **23** (2014) 025005.

[57] K. Ding and M. A. Lieberman. *J. Phys. D: Appl. Phys.* **48** (2014) 035401.

[58] K. Ding, M. A. Lieberman, and A. J. Lichtenberg. *J. Phys. D: Appl. Phys.* **47** (2014) 305203.

[59] Y. Gorbanev, D. O'Connell, and V. Chechik. *Chem. Eur. J.* **22** (2016) 3496–3505.

[60] S. Yonemori and R. Ono. *J. Phys. D: Appl. Phys* **47** (2014) 125401.

[61] P. J. Bruggeman, M. J. Kushner, B. R. Locke, J. G. E. Gardeniers, W. G. Graham, D. B. Graves, R. C. H. M. Hofman-Caris, D. Maric, J. P. Reid, E. Ceriani, D. Fernandez Rivaz, J. E. Foster, S. C. Garrick, Y. Gorbanev, S. Hamaguchi, F. Iza, H. Jablonowski, E. Klimova, J. Kolb, F. Krcma, P. Lukes, Z. Machala, I. Marinov, D. Mariotti, S. Mededovic Thagard, D. Minakata, E. C. Neyts, J. Pawlatt, Y. L. Petrovic, R. Pflieger, S. Reuter, D. C. Schram, S. Schröter, M. Shiraiwa, B. Tarabová, P. A. Tsai, J. R. R. Verlet, T. von Woedtke, K. R. Wilson, K. Yasui, and G. Zvereva. *Plasma Sources Sci. Technol.* **25** (2016) 053002.

[62] S. Reuter, J. S. Sousa, G. D. Stancu, and J.-P. H. van Helden. *Plasma Sources Sci. Technol.* **24** (2015) 054001.

[63] R. Ono. *J. Phys. D: Appl. Phys.* **49** (2016) 083001.

[64] C. Hibert, I. Gaurand, O. Motret, and J. M. Pouvesle. *J. Appl. Phys.* **85** (1999) 7070–7075.

[65] J. Winter, M. Dünnbier, A. Schmidt-Bleker, A. Meshchanov, S. Reuter, and K.-D. Weltmann. *J. Phys. D: Appl. Phys.* **45** (2012) 385201.

[66] K. Niemi, D. O'Connell, N. de Oliveira, D. Joyeux, L. Nahon, J. P. Booth, and T. Gans. *Appl. Phys. Lett.* **103** (2013) 034102.

[67] C. Wang and N. Srivastava. *Euro. Phys. J. D* **60** (2010) 465–477.

[68] J. Winter, H. Tresp, M. U. Hammer, S. Iseni, S. Kupsch, A. Schmidt-Bleker, K. Wende, M. Dünnbier, K. Masur, K.-D. Weltmann, and et al. *J. Phys. D: Appl. Phys.* **47** (2014) 285401.

[69] M. G. H. Boogaarts, S. Mazouffre, G. J. Brinkman, H. W. P. van der Heijden, P. Vankan, J. A. M. van der Mullen, D. C. Schram, and H. F. Döbele. *Rev. Sci. Instrum.* **73** (2002) 73–86.

[70] H. F. Döbele, T. Mosbach, K. Niemi, and V. Schulz-von der Gathen. *Plasma Sources Sci. Technol.* **14** (2005) S31–S41.

[71] A. F. H. van Gessel, S. C. van Grootel, and P. J. Bruggeman. *Plasma Sources Sci. Technol.* **22** (2013) 055010.

[72] H. W. P. van der Heijden, M. G. H. Boogaarts, S. Mazouffre, J. A. M. van der Mullen, and D. C. Schram. *Phys. Rev. E* **61** (2000) 4402–4409.

[73] N. Knake, D. Schröder, J. Winter, and V. Schulz-von der Gathen. *Journal of Physics: Conference Series* **227** (2010) 012020.

[74] N. Knake and V. Schulz-von der Gathen. *Eur. Phys. J. D* **60** (2010) 645–652.

[75] M. Mrkvičková, J. Ráhel, P. Dvořák, D. Trunec, and T. Morávek. *Plasma Sources Sci. Technol.* **25** (2016) 055015.

[76] K Niemi, V. Schulz-von der Gathen, and H. F. Döbele. *Plasma Sources Sci. Technol.* **14** (2005) 375–386.

[77] A. Nikiforov, L. Li, N. Britun, R. Snyders, P. Vanraes, and C. Leys. *Plasma Sources Sci. Technol.* **23** (2014) 015015.

[78] R. Ono, Y. Yamashita, K. Takezawa, and T. Oda. *J. Phys. D: Appl. Phys.* **38** (2005) 2812–2816.

[79] S. Reuter, K. Niemi, V. Schulz-von der Gathen, and H. F. Döbele. *Plasma Sources Sci. Technol.* **18** (2009) 015006.

[80] S. Reuter, J. Winter, A. Schmidt-Bleker, D. Schröder, H. Lange, N. Knake, V. Schulz-von der Gathen, and K.-D. Weltmann. *Plasma Sources Sci. Technol.* **21** (2012) 024005.

[81] D. Schröder, H. Bahre, N. Knake, J. Winter, T. de los Arcos, and V. Schulz-von der Gathen. *Plasma Sources Sci. Technol.* **21** (2012) 024007.

[82] E. Wagenaars, T. Gans, D. O'Connell, and K. Niemi. *Plasma Sources Sci. Technol.* **21** (2012) 042002.

[83] S. Yatom, Y. Luo, Q. Xiong, and P. J. Bruggeman. *Journal of Physics D: Applied Physics* **50** (2017) 415204.

[84] J. Conway, G. S. Gogna, C. Gaman, M. M. Turner, and S. Daniels. *Plasma Sources Sci. Technol.* **25** (2016) 045023.

[85] V. Schulz-von der Gathen, L. Schaper, N. Knake, S. Reuter, K. Niemi, T. Gans, and J. Winter. *J. Phys. D: Appl. Phys.* **41** (2008) 194004.

[86] J. B. Schmidt, B. Sands, J. Scofield, J. R. Gord, and S. Roy. *Plasma Sources Sci. Technol.* **26** (2017) 055004.

[87] W. D. Kulatilaka, J. R. Gord, V. R. Katta, and S. Roy. *Opt. Lett.* **37** (2012) 3051.

[88] J. B. Schmidt, B. L. Sands, W. D. Kulatilaka, S. Roy, J. Scofield, and J. R. Gord. *Plasma Sources Sci. Technol.* **24** (2015) 032004.

[89] J. B. Schmidt, S. Roy, W. D. Kulatilaka, I. Shkurenkov, I. V. Adamovich, W. R. Lempert, and J. R. Gord. *J. Phys. D: Appl. Phys.* **50** (2016) 015204.

[90] D. Riés, G. Dilecce, E. Robert, P. F. Ambrico, S. Dozias, and J.-M. Pouvesle. *J. Phys. D: Appl. Phys.* **47** (2014) 275401.

[91] T. Verreycken and P. J. Bruggeman. *Plasma Chem. Plasma Process.* **34** (2014) 605–619.

[92] I. Yagi, R. Ono, T. Oda, and K. Takaki. *Plasma Sources Sci. Technol.* **24** (2014) 015002.

[93] S. Yonemori, Y. Nakagawa, R. Ono, and T. Oda. *J. Phys. D: Appl. Phys* **45** (2012) 225202.

[94] O. Johansson, J. Bood, B. Li, A. Ehn, Z.S. Li, Z.W. Sun, M. Jonsson, A.A. Konnov, and M. Aldén. *Combust. Flame* **158** (2011) 1908–1919.

[95] D. Ellerweg, J. Benedikt, A. von Keudell, N. Knake, and V. Schulz-von der Gathen. *New J. Phys.* **12** (2010) 013021.

[96] G. Willems, J. Benedikt, and A. von Keudell. *J. Phys. D: Appl. Phys.* **50** (2017) 335204.

[97] D. Ellerweg, A. von Keudell, and J. Benedikt. *Plasma Sources Sci. Technol.* **21** (2012) 034019.

[98] D. Maletić, N. Puač, S. Lazović, G. Malović, T. Gans, V. Schulz-von der Gathen, and Z. Lj. Petrović. *Plasma Physics and Controlled Fusion* **54** (2012) 124046.

[99] A. Hurlbatt, A. R. Gibson, S. Schröter, J. Bredin, A. P. S. Foote, P. Grondein, D. O'Connell, and T. Gans. *Plasma Process. Polym.* **14** (2016) 1600138.

[100] K. Niemi, T. Gans, and D. O'Connell. *Plasma Sources Sci. Technol.* **22** (2013) 032001.

[101] K. Niemi, J. Waskoenig, N. Sadeghi, T. Gans, and D. O'Connell. *Plasma Sources Sci. Technol.* **20** (2011) 055005.

[102] G. Y. Park, Y. J. Hong, H. W. Lee, J. Y. Sim, and J. K. Lee. *Plasma Process. Polym.* **7** (2010) 281–287.

[103] M. M. Turner. *Plasma Sources Sci. Technol.* **24** (2015) 035027.

[104] M. M. Turner. *Plasma Sources Sci. Technol.* **25** (2016) 015003.

[105] W. Van Gaens and A. Bogaerts. *J. Phys. D: Appl. Phys.* **47** (2014) 079502.

[106] W. Van Gaens, S. Iseni, A. Schmidt-Bleker, K. D. Weltmann, S. Reuter, and A. Bogaerts. *New J. Phys.* **17** (2015) 033003.

[107] S. Kelly and M. M. Turner. *J. Appl. Phys.* **114** (2013) 123301.

[108] S. Kelly and M. M.Turner. *Plasma Sources Sci. Technol.* **23** (2014) 065013.

[109] A. M. Lietz and M. J. Kushner. *J. Phys. D: Appl. Phys.* **49** (2016) 425204.

[110] J. Waskoenig, K. Niemi, N. Knake, L. M. Graham, S. Reuter, V. Schulz-von der Gathen, and T. Gans. *Plasma Sources Sci. Technol.* **19** (2010) 045018.

[111] B. Niermann, T. Hemke, N. Y. Babaeva, M. Böke, M. J. Kushner, T. Mussenbrock, and J. Winter. *J. Phys. D: Appl. Phys.* **44** (2011) 485204.

[112] S. Kelly, J. Golda, M. M. Turner, and V. Schulz-von der Gathen. *J. Phys. D: Appl. Phys.* **48** (2015) 444002.

[113] W. Van Gaens, P. J. Bruggeman, and A. Bogaerts. *New J. Phys.* **16** (2014) 063054.

[114] L. Nahon, N. de Oliveira, G. A. Garcia, J.-F. Gil, B. Pilette, O. Marcouillé, B. Lagarde, and F. Polack. *J. Synchrotron Rad.* **19** (2012) 508–520.

[115] O. A. Alduchov and R. E. Eskridge. *J. Appl. Meteor.* **35** (1996) 601–609.

[116] Andrea Pogány, Steven Wagner, Olav Werhahn, and Volker Ebert. *Appl. Spectrosc.* **69** (2015) 257–268.

[117] D. S. Stafford and M. J. Kushner. *J. Appl. Phys.* **96** (2004) 2451–2465.

[118] A. H. Markosyan, A. Luque, F. J. Gordillo-Vázquez, and U. Ebert. *Comput. Phys. Commun.* **185** (2014) 2697–2702.

[119] R. Dorai, K. Hassouni, and M. J. Kushner. *J. Appl. Phys.* **88** (2000) 6060–6071.

[120] R. Dorai and M. J. Kushner. *J. Phys. D: Appl. Phys.* **36** (2003) 666–685.

[121] J. R. Roth. *Industrial Plasma Processing*. IOP Publishing: Bristol and Philadelphia, 1995.

[122] A. West. *Optical and electrical diagnostics of atmospheric pressure plasma jets*. PhD thesis, University of York, 2016.

[123] S. Hofmann, A. F. H. van Gessel, T. Verreycken, and P. Bruggeman. *Plasma Sources Sci. Technol.* **20** (2011) 065010.

[124] L. Wayne Sieck, John T. Heron, and David S. Green. *Plasma Chem. Plasma Process.* **20** (2000) 235–258.

[125] M. Gryziński. *Phys. Rev.* **113** (1959) 374–383.

[126] L. Vriens. *Physical Letters* **5** (1964) 260–261.

[127] I. A. Soloshenko, V. V. Tsiolko, V. A. Khomich, V. Y. Bazhenov, A. V. Ryabtsev, A. I. Schedrin, and I. L. Mikhno. *IEEE Trans. Plasma Sci.* **30** (2002) 1440–1444.

[128] T. M. Miller, N. S. Shuman, and A. A. Viggiano. *J. Chem. Phys.* **136** (2012) 204306.

[129] M.R. Flannery. *Chem. Phys. Lett.* **80** (1981) 541–546.

[130] D. R. Bates and I. Mendas. *P. Roy. Soc. A: Math. Phys.* **359** (1978) 287–301.

[131] H. S. Lee and R. Johnsen. *J. Chem. Phys.* **90** (1989) 6328–6334.

[132] S. P. Mezyk, R. Cooper, and J. Sherwell. *The Journal of Physical Chemistry* **93** (1989) 8187–8193.

[133] H. Jungblut, D. Hansen, and W. F. Schmidt. *IEEE Transaction on Electrical Insulation* **24** (1989) 343–348.

[134] I. A. Kossyi, A. Y. Kostinsky, A. A. Matveyev, and V. P. Silakov. *Plasma Sources Sci. Technol.* **1** (1992) 207–220.

[135] D. McElroy, C. Walsh, A. J. Markwick, M. A. Cordiner, K. Smith, and T. J. Millar. *A&A* **550** (2013) A36.

[136] V. Wakelam, E. Herbst, J.-C. Loison, I. W. M. Smith, V. Chandrasekaran, B. Pavone, N. G. Adams, M.-C. Bacchus-Montabonel, A. Bergeat, K. Béroff, V. M. Bierbaum, M. Chabot, A. Dalgarno, E. F. van Dishoek, E. Faure, W. D. Geppert, D. Gerlich, D. Galli, E. Hébard, F. Hersant, K. M. Hickson, P. Honvault, S. J. Klippenstein, S. Le Picard, G. Nyman, P. Pernot, S. Schlemmer, F. Selsis, I. R. Sims, D. Talbi, J. Tennyson, J. Troe, R. Wester, and L. Wiesenfeld. *Astrophys. J., Suppl. Ser.* **199** (2012) 21.

[137] J. M. Pouvesle, A. Bouchoule, and J. Stevefelt. *J. Chem. Phys.* **77** (1982) 817–825.

[138] J. M. Pouvesle, A. Khacef, J. Stevefelt, H. Jahani, V. V. Gylys, and C. B. Collins. *J. Chem. Phys.* **88** (1988) 3061–3071.

[139] G. Myers and A. J. Cunningham. *J. Chem. Phys.* **67** (1977) 3352–3359.

[140] F. W. Lee. *J. Chem. Phys.* **65** (1976) 5189.

[141] J. Li, Z. Zhao, and F. L. Kazakov, A.and Dryer. *Int. J. Chem. Kinet.* **36** (2004) 566–575.

[142] R. Atkinson, D. L. Baulch, R. A. Cox, J. N. Crowley, R. F. Hampson, R. G. Hynes, M. E. Jenkin, M. J. Rossi, and J. Troe. *Atmos. Chem. Phys.* **4** (2004; IUPAC Task Group on Atmospheric Chemical Kinetic Data Evaluation, http://iupac.pole-ether.fr) 1461–1738, Vol 1.

[143] R. Forster, M. Frost, D. Fulle, H. F. Hamann, H. Hippler, A. Schlepegrell, and J. Troe. *J. Chem. Phys.* **103** (1995) 2949–2958.

[144] B.F. Gordiets, C.M. Ferreira, V.L. Guerra, J.M.A.H. Loureiro, J. Nahorny, D. Pagnon, M. Touzeau, and M. Vialle. *IEEE Trans. Plasma Sci.* **23** (1995) 750–768.

[145] I. Méndez, F. J. Gordillo-Vazquez, V. J. Herrero, and I. Tanarro. *J. Phys. Chem. A* **110** (2006) 6060–6066.

[146] R. Lehmann. *J. Atmos. Chem.* **47** (2004) 45–78.

[147] H. J. Forman, J. M. Fukuto, T. Miller, H. Zhang, A. Rinna, and S. Levy. *Arch. Biochem. Biophys.* **477** (2008) 183–195.

[148] Y. Itikawa and N. Mason. *J. Phys. Chem. Ref. Data* **34** (2005) 1–22.

[149] M. B. Schulman, F. A. Sharpton, S. Chung, C. C. Lin, and L. W. Anderson. *Phys. Rev. A* **32** (1985) 2100–2116.

[150] G. R. Möhlmann, F.J. De Heer, and J. Los. *Chem. Phys.* **25** (1977) 103–116.

[151] N. de Oliveira, M. Roudjane, D. Joyeux, D. Phalippou, J.-C. Rodier, and L. Nahon. *Nature Photon* **5** (2011) 149–153.

[152] H. Keller-Rudek, G. K. Moortgat, R. Sander, and R. Sörensen. *Earth System Science Data* **5** (2013) 365–373.

[153] W.F. Chan, G. Cooper, and C.E. Brion. *Chem. Phys.* **178** (1993) 387–400.

[154] M. Foucher, D. Marinov, E. Carbone, P. Chabert, and J.-P. Booth. *Plasma Sources Sci. Technol.* **24** (2015) 042001.

[155] G. H. Dieke and H. M. Crosswhite. *J. Quant. Spectrosc. Radiat. Transfer* **2** (1962) 97–199.

[156] L. Earls. *Phys. Rev.* **48** (1935) 423–424.

[157] K. R. German. *J. Chem. Phys.* **62** (1975) 2584–2587.

[158] A. Goldman and J. R. Gillis. *J. Quant. Spectrosc. Radiat. Transfer* **25** (1981) 111–135.

[159] C. M. Western. *Journal of Quantitative Spectroscopy and Radiative Transfer* (2016).

[160] K. P. Huber, G. Herzberg (data prepared by J. W. Gallagher, and R. D. Johnson III). *"Constants of Diatomic Molecules" in NIST Chemistry WebBook, NIST Standard Reference Database Number 69.* National Institute of Standards and Technology, Gaithersburt, MD, 20899, retrieved September 14, 2016.

[161] E. A. Moore and W. G. Richards. *Phys. Scr.* **3** (1971) 223–230.

[162] N. Knake and V. Schulz-von der Gathen. *Eur. Phys. J. D* **60** (2010) 645–652.

[163] H. H. H. W. Schmidt and U. Walter. *Cell* **78** (1994) 919–925.

[164] M. B. Witte and A. Barbul. *The American Journal of Surgery* **183** (2002) 406–412.

[165] J.-D. Luo and A. F. Chen. *Acta Pharmacol. Sin.* **26** (2005) 259–264.

[166] M. R. Schäffer, U. Tantry, S. S. Gross, H. L. Wasserkrug, and A. Barbul. *J. Surg. Res.* **63** (1996) 237–240.

[167] J. R. Reisel, C. D. Carter, and N. M. Laurendeau. *Journal of Quantitative Spectroscopy and Radiative Transfer* **47** (1992) 43–54.

[168] V. Guerra and J. Loureiro. *J. Phys. D: Appl. Phys.* **28** (1995) 1903–1918.

[169] V. Guerra and J. Loureiro. *Plasma Sources Sci. Technol.* **6** (1997) 373–385.

[170] C. D. Pintassilgo, O. Guaitella, and A. Rousseau. *Plasma Sources Sci. Technol.* **18** (2009) 025005.

[171] C. D. Pintassilgo, V. Guerra, O. Guaitella, and A. Rousseau. *Plasma Sources Sci. Technol.* **19** (2010) 055001.

[172] K. Niemi. *Nachweis leichter Atome in reaktiven Plasmen mittels Zweiphotonen laserinduzierter Fluoreszenzspektroskopie unter besonderer Berücksichtigung der Absolutkalibrierung.* PhD thesis, Universität Duisburg-Essen, 2003.

[173] K. Niemi, V. Schulz-von der Gathen, and H. F. Döbele. *J. Phys. D: Appl. Phys.* **34** (2001) 2330–2335.

[174] A. Goehlich, T. Kawetzki, and H. F. Döbele. *J. Chem. Phys.* **108** (1998) 9362–9370.

[175] K. D. Bonin and T. J. McIlrath. *J. Opt. Soc. Am. B* **1** (1984) 52.

[176] A. Kramida, Yu. Ralchenko, J. Reader, [Online]. Available: http://physics.nist.gov/asd [2016, December 15]. National Institute of Standards and NIST ASD Team. *NIST Atomic Spectra Database* (ver. 5.3), and MD. Technology, Gaithersburg.

[177] H. Horiguchi. *J. Chem. Phys.* **75** (1981) 1207–1218.

[178] B.L Preppernau, K Pearce, A Tserepi, E Wurzberg, and Terry A Miller. *Chem. Phys.* **196** (1995) 371–381.

[179] E. U. Condon and G. H. Shortley. *Theory of atomic spectra.* The syndics of the Cambridge University Press, 1951.

[180] R. S. F. Chang, H. Horiguchi, and D. W. Setser. *J. Chem. Phys.* **73** (1980) 778–790.

[181] A. S. Siegman. *Lasers.* University Science Books, 55D Gate Five Road, Sausalito, CA 94965, 1986.

[182] D. Marinov, C. Drag, C. Blondel, O. Guaitella, J. Golda, B. Klarenaar, R. Engeln, V. Schulz-von der Gathen, and J.-P. Booth. *Plasma Sources Sci. Technol.* **25** (2016) 06LT03.

[183] T. I. Quickenden, S. M. Trotman, J. A. Irvin, and D. F. Sangster. *J. Chem. Phys.* **71** (1979) 497–501.

[184] U. Meier, K. Kohse-Höinghaus, and Th. Just. *Chem. Phys. Lett.* **126** (1986) 567–573.

[185] J. Bittner, K. Kohse-Höinghaus, U. Meier, and Th. Just. *Chem. Phys. Lett.* **143** (1988) 571–576.

[186] N. Knake, K. Niemi, S. Reuter, V. Schulz-von der Gathen, and J. Winter. *Appl. Phys. Lett.* **93** (2008) 131503.

[187] R. M. Sellers. *Analyst* **105** (1980) 950–954.

[188] O. Maass and W. H. Hatcher. *J. Am. Chem. Soc.* **42** (1920) 2548–2569.

[189] I. A. Soloshenko, V. V. Tsiolko, S. S. Pogulay, A. G. Terent'yeva, V. Y. Bazhenov, A. I. Shchedrin, A. V. Ryabtsev, and A. I. Kuzmichev. *Plasma Sources Sci. Technol.* **16** (2007) 56–66.

[190] T. Kozák and A. Bogaerts. *Plasma Sources Sci. Technol.* **23** (2014) 045004.

[191] L. D. Pietanza, G. Colonna, G. D'Ammando, A. Laricchiuta, and M. Capitelli. *Chem. Phys.* **468** (2016) 44–52.

[192] Biagi v8.9 database, www.lxcat.net, retrieved March 2016.

[193] M. Hayashi. *Le Journal de Physique Colloques* **40** (1979) C7/45–46.

[194] A. V. Phelps. Technical report, University of Colorado, 1985.

[195] M. R. Flannery, K. J. McCann, and N. W. Winter. *J. Phys. B: At. Mol. Phys.* **14** (1981) 3789–3796.

[196] R. Riahi, P. Teulet, Z. Ben Lakhdar, and A. Gleizes. *Eur. Phys. J. D* **40** (2006) 223–230.

[197] R. R. Laher and F. R. Gilmore. *J. Phys. Chem. Ref. Data* **19** (1990) 277–305.

[198] M. Gryziński. *Phys. Rev.* **138** (1965) A336–A358.

[199] R. I. Hall and S. Trajmar. *J. Phys. B: At. Mol. Phys.* **8** (1975) L293–L296.

[200] R. Deloche, P. Monchicourt, M. Cheret, and F. Lambert. *Phys. Rev. A* **13** (1976) 1140–1176.

[201] W. Kedzierski, J. Derbyshire, C. Malone, and J. W. McConkey. *J. Phys. B: At., Mol. Opt. Phys.* **31** (1998) 5361–5368.

[202] T. Harb, W. Kedzierski, and J. W. McConkey. *J. Chem. Phys.* **115** (2001) 5507–5512.

[203] S. J. B. Corrigan. *J. Chem. Phys.* **43** (1965) 4381–4386.

[204] W. Liu and G. A. Victor. *Astrophys. J.* **435** (1994) 909–919.

[205] M. Gupta and K. L. Baluja. *J. Phys. B: At., Mol. Opt. Phys.* **38** (2005) 4057–4073.

[206] E. Krishnakumar and S.K. Srivastava. *Int. J. of Mass Spectrom. Ion Process.* **113** (1992) 1–12.

[207] C. E. Melton and G. A. Neece. *J. Am. Chem. Soc.* **93** (1971) 6757–6759.

[208] D. Nandi, E. Krishnakumar, A. Rosa, W.-F. Schmidt, and E. Illenberger. *Chem. Phys. Lett.* **373** (2003) 454–459.

[209] P. D. Burrow. *J. Chem. Phys.* **59** (1973) 4922–4931.

[210] S. Matejcik, A. Kiendler, P. Cicman, J. Skalny, P. Stampfli, E. Illenberger, Y. Chu, A. Stamatovic, and T. D. Märk. *Plasma Sources Sci. Technol.* **6** (1997) 140–146.

[211] H. Deutsch, P. Scheier, K. Becker, and T. D. Märk. *Chem. Phys. Lett.* **382** (2003) 26–31.

[212] P. M. Mul, J. W. McGowan, P. Defrance, and J. B. A. Mitchell. *J. Phys. B: At. Mol. Phys.* **16** (1983) 3099–3107.

[213] B. R. Rowe, F. Vallée, J. L. Queffelec, J. C. Gomet, and M. Morlais. *J. Chem. Phys.* **88** (1988) 845–850.

[214] M. H. Bortner and T. Baurer. *Defense Nuclear Agency reaction rate handbook, revision no. 7.* DaD Nuclear Information and Analysis Center, 7 edition, 1979.

[215] C.-M. Huang, M. Whitaker, M. A. Biondi, and R. Johnsen. *Phys. Rev. A* **18** (1978) 64–67.

[216] M. T. Leu, Manfred A. Biondi, and R. Johnsen. *Phys. Rev. A* **7** (1973) 292–298.

[217] J. B. A. Mitchell. *Phys. Rep.* **186** (1990) 215–248.

[218] R. Peverall, S. Rosén, J. R. Peterson, M. Larsson, A. Al-Khalili, L. Vikor, J. Semaniak, R. Bobbenkamp, A. Le Padellec, A. N. Maurellis, and et al. *J. Chem. Phys.* **114** (2001) 6679–6689.

[219] G. J. M. Hagelaar and L. C. Pitchford. *Plasma Sources Sci. Technol.* **14** (2005) 722–733.

[220] Morgan (Kinema Research & Software) database, www.lxcat.net, retrieved on April 13, 2016.

[221] S. S. Prasad and W. T. Huntress Jr. *Astrophys. J., Suppl. Ser.* **43** (1980) 1–35.

[222] G. Mauclaire, R. Derai, and R. Marx. *International Journal of Mass Spectrometry and Ion Physics* **26** (1978) 289–301.

[223] N. G. Adams and D. Smith. *J. Phys. B: At. Mol. Phys.* **9** (1976) 1439–1451.

[224] J. D. C. Jones, K. Birkinshaw, and N. D. Twiddy. *Chem. Phys. Lett.* **77** (1981) 484–488.

[225] W. T. Huntress. *J. Chem. Phys.* **59** (1973) 4742–4756.

[226] A. B. Rakshit and P. Warneck. *Journal of the Chemical Society, Faraday Transactions 2* **76** (1980) 1084–1094.

[227] A. A. Viggiano, D. L. Albritton, F. C. Fehsenfeld, N. G. Adams, D. Smith, and F. Howorka. *Astrophys. J.* **236** (1980) 492–497.

[228] V. G. Anicich. *J. Phys. Chem. Ref. Data* **22** (1993) 1469–1569.

[229] R. J. Vidmar and K. R. Stalder. Technical report, University of Nevada, Reno, 2004.

[230] D. Smith, N. G. Adams, and T. M. Miller. *J. Chem. Phys.* **69** (1978) 308–318.

[231] M. McFarland. *J. Chem. Phys.* **59** (1973) 6620–6628.

[232] A. B. Rakshit and P. Warneck. *J. Chem. Phys.* **73** (1980) 5074–5080.

[233] R. L. Champion, L. D. Doverspike, and S. K. Lam. *Phys. Rev. A* **13** (1976) 617–621.

[234] O. Martinez, Z. Yang, N. J. Demarais, T. P. Snow, and V. M. Bierbaum. *Astrophys. J.* **720** (2010) 173–177.

[235] F. C. Fehsenfeld and E. E. Ferguson. *J. Chem. Phys.* **61** (1974) 3181–3191.

[236] Y. Ikezoe, S. Matsuoka, M. Takebe, and A. Viggiano. *Gas Phase Ion-Molecule Reaction Rate Constants Through 1986.* Maruzen Company Ltd., 1987.

[237] A. Midey, I. Dotan, and A. A. Viggiano. *J. Phys. Chem. A* **112** (2008) 3040–3045.

[238] S. G. Ard, J. J. Melko, B. Jiang, Y. Li, N. S. Shuman, H. Guo, and A. A. Viggiano. *J. Chem. Phys.* **139** (2013) 144302.

[239] H. Böhringer, W. Glebe, and F. Arnold. *J. Phys. B: At. Mol. Phys.* **16** (1983) 2619–2626.

[240] Y. K. Lau, S. Ikuta, and P. Kebarle. *J. Am. Chem. Soc.* **104** (1982) 1462–1469.

[241] J. de Urquijo, A. Bekstein, G. Ruiz-Vargas, and F. J. Gordillo-Váquez. *J. Phys. D: Appl. Phys.* **46** (2012) 035201.

[242] R. F. Heidner III and D. Husain. *Int. J. Chem. Kinet.* **6** (1974) 77–87.

[243] F. D. Findlay. *J. Chem. Phys.* **55** (1971) 545–551.

[244] C. B. Collins and F. W. Lee. *J. Chem. Phys.* **70** (1979) 1275–1285.

[245] J. M. Pouvesle, J. Stevefelt., W. Lee, H. R. Jahani, V. T. Gylys, and C. B. Collins. *J. Chem. Phys.* **83** (1985) 2836–2839.

[246] D. L. Baulch, C. J. Cobos, R. A. Cox, C. Esser, P. Frank, Th. Just, J. A. Kerr, M. J. Pilling, J. Troe, R. W. Walker, and et al. *J. Phys. Chem. Ref. Data* **21** (1992) 411–734.

[247] J. B. Burkholder, S. P. Sander, J. Abbatt, J. R. Barker, R. E. Huie, C. E. Kolb, M. J. Kurylo, V. L. Orkin, D. M. Wilmouth, and P. H. Wine. *JPL Publication 15-10, Jet Propulsion Laboratory, Pasadena* (2015). http://jpldataeval.jpl.nasa.gov/.

[248] J. A. Manion, R. E. Huie, R. D. Levin, D. R. Burgess Jr., V. L. Orkin, W. Tsang, W. S. McGivern, J. W. Hudgens, V. D. Knyazev, D. B. Atkinson, E. Chai, A. M. Tereza, C.-Y. Lin, T. C. Allison, W. G. Mallard, F. Westley, J. T. Herron, R. F. Hampson, and D. H. Frizzell, NIST Chemical Kinetics Database, NIST Standard Reference Database 17, Version 7.0 (Web Version), Release 1.6.8, Data version 2015.12. National Institute of Standards and Technology, Gaithersburg, Maryland, 20899-8320. Web address: http://kinetics.nist.gov/.

[249] V. L. Orkin, S. N. Kozlov, G. A. Poskrebyshev, and M. J. Kurylo. *J. Phys.Chem. A* **110** (2006) 6978–6985.

[250] L. F. Keyser. *J. Phys. Chem.* **92** (1988) 1193–1200.

[251] D. L. Baulch, C. T. Bowman, C. J. Cobos, R. A. Cox, Th. Just, J. A. Kerr, M. J. Pilling, D. Stocker, J. Troe, W. Tsang, and R. W. Walker. *J. Phys. Chem. Ref. Data* **34** (2005) 757–1397.

[252] R. S. Lewis and R. T. Watson. *J. Phys. Chem.* **84** (1980) 3495–3503.

[253] M. J. Howard and I. W. M. Smith. *Journal of the Chemical Society, Faraday Transactions 2* **77** (1981) 997–1008.

[254] T. G. Slanger and G. Black. *J. Chem. Phys.* **68** (1978) 989–997.

[255] E. J. Dunlea, R. K. Talukdar, and A. R. Ravishankara. *J. Phys.Chem. A* **109** (2005) 3912–3920.

[256] I.S. Fletcher and D. Husain. *Revue canadienne de chimie* **54** (1976) 1765–1770.

[257] V. J. Abreu, J. H. Yee, S. C. Solomon, and A. Dalgarno. *Planet. Space Sci.* **34** (1986) 1143–1145.

[258] K. Schofield. *Journal of Photochemistry* **9** (1978) 55–68.

[259] T. G. Slanger and G. Black. *J. Chem. Phys.* **75** (1981) 2247–2251.

[260] R. G. Derwent and B. A. Thrush. *Transactions of the Faraday Society* **67** (1971) 2036–2043.

[261] R. F. Heidner III, C. E. Gardner, T. M. El-Sayed, G. I. Segal, and J. V. V. Kasper. *J. Chem. Phys.* **74** (1981) 5618–5626.

[262] G. Myers and A. J. Cunningham. *J. Chem. Phys.* **67** (1977) 247–253.

[263] S. R. Sellevåg, Y. Georgievskii, and J. A. Miller. *J. Phys.Chem. A* **112** (2008) 5085–5095.

[264] W. Tsang and R. F. Hampson. *J. Phys. Chem. Ref. Data* **15** (1986) 1087–1222.

[265] R.A. Sanders and E.E. Muschlitz. *International Journal of Mass Spectrometry and Ion Physics* **23** (1977) 99–108.

[266] H.-H. Carstensen and A.M. Dean. *Comprehensive Chemical Kinetics* (2007) 101–184.

[267] Y. Itikawa, M. Hayashi, A. Ichimura, K. Onda, K. Sakimoto, K. Takayanagi, M. Nakamura, H. Nishimura, and T. Takayanagi. *J. Phys. Chem. Ref. Data* **15** (1986) 985–1010.

[268] R. J. W. Henry, P. G. Burke, and A.-L. Sinfailam. *Phys. Rev.* **178** (1969) 218–225.

[269] A. C. H. Smith, E. Caplinger, R. H. Neynaber, Erhard W. Rothe, and S. M. Trujillo. *Phys. Rev.* **127** (1962) 1647–1649.

[270] B. G. Lindsay, M. A. Mangan, H. C. Straub, and R. F. Stebbings. *J. Chem. Phys.* **112** (2000) 9404–9410.

[271] P. C. Cosby. *J. Chem. Phys.* **98** (1993) 9544–9553.

[272] L. Josić, T. Wróblewski, Z. Lj. Petrović, J. Mechlińska-Drewko, and G. P. Karwasz. *Chem. Phys. Lett.* **350** (2001) 318–324.

[273] M. Castillo, V. J. Herrero, I. Méndez, and I. Tanarro. *Plasma Sources Science and Technology* **13** (2003) 39–47.

[274] Hayashi database, www.lxcat.net, retrieved on March 16, 2017.

[275] T. Tabata, T. Shirai, M. Sataka, and H. Kubo. *Atomic Data and Nuclear Data Tables* **92** (2006) 375–406.

[276] V. Tarnovsky, H. Deutsch, and K. Becker. *Int. J. of Mass Spectrom. Ion Process.* **167-168** (1997) 69–78.

[277] M. Whitaker, M. A. Biondi, and R. Johnsen. *Phys. Rev. A* **24** (1981) 743–745.

[278] F. J. Gordillo-Vázquez. *J. Phys. D: Appl. Phys.* **41** (2008) 234016.

[279] M. H. Bortner and T. Baurer. *Defence nuclear agency reaction rate handbook, second edition.* DaD Nuclear Information and Analysis Center, 1972.

[280] V. G. Anicich, J. B. Laudenslager, W. T. Huntress, and J. H. Futrell. *J. Chem. Phys.* **67** (1977) 4340–4350.

[281] T. J. Millar, P. R. A. Farquhar, and K. Willacy. *Astron. Astrophys. Suppl. Ser.* **121** (1997) 139–185.

[282] P. D. Goldan. *J. Chem. Phys.* **44** (1966) 4095–4103.

[283] N. G. Adams, D. Smith, and J. F. Paulson. *J. Chem. Phys.* **72** (1980) 288.

[284] M. McFarland, D. L. Albritton, F. C. Fehsenfeld, E. E. Ferguson, and A. L. Schmeltekopf. *J. Geophys. Res.* **79** (1974) 2925–2926.

[285] D. L. Albritton. *Atomic Data and Nuclear Data Tables* **22** (1978) 1–89.

[286] T. Ueno and Y. Hatano. *Chem. Phys. Lett.* **40** (1976) 283–286.

[287] R. B. Boodaghians, C. E. Canosa-Mas, P. J. Carpenter, and R. P. Wayne. *Journal of the Chemical Society, Faraday Transactions 2* **84** (1988) 931–948.

[288] M. R. Soto and M. Page. *J. Chem. Phys.* **97** (1992) 7287–7296.

[289] J. T. Herron. *J. Phys. Chem. Data* **28** (1999) 1453–1483.

[290] N. Cohen and K. R. Westberg. *J. Phys. Chem. Ref. Data* **20** (1991) 1211–1311.

[291] J. T. Herron and D. S. Green. *Plasma Chem. Plasma Process.* **21** (2001) 459–481.

[292] S. Inomata and N. Washida. *J. Phys.Chem. A* **103** (1999) 5023–5031.

[293] R. F. Heidner III and D. Husain. *Int. J. Chem. Kinet.* **5** (1973) 819–831.

[294] P. J. S. B. Caridade, S. P. J. Rodrigues, F. Sousa, and A. J. C. Varandas. *J. Phys.Chem. A* **109** (2005) 2356–2363.

[295] J. A. Harrison, A. R. Whyte, and L. F. Phillips. *Chem. Phys. Lett.* **129** (1986) 346–352.

[296] R. L. Brown. *Int. J. Chem. Kinet.* **5** (1973) 663–668.

[297] W. Tsang and J. T. Herron. *J. Phys. Chem. Ref. Data* **20** (1991) 609–663.

[298] L. F. Phillips and H. I. Schiff. *J. Chem. Phys.* **42** (1965) 3171–3174.